Effect of ultra-short laser nanostructuring of material surfaces on the evolution of their thermoelectric properties

Abderazek Talbi

Centre Val de Loire UNIVERSITÉ **UNIVERSITÉ D'ORLÉANS**

UNIVERSITE D'ORLEANS

ÉCOLE DOCTORALE
ENERGIE, MATERIAUX, SCIENCES DE LA TERRE ET DE L'UNIVERS

Groupe de Recherche sur l'Energétique des Milieux Ionisées

THÈSE présentée par :

Abderazek TALBI

soutenue le : 11/12/2017

pour obtenir le grade de : **Docteur de l'université d'Orléans**

Discipline/ Spécialité : Energie - Matériaux

Effect of ultra-short laser nanostructuring of materials surfaces on the evolution of their thermoelectric properties

THÈSE dirigée par :

Chantal BOULMER-LEBORGNE Professeure des universités, GREMI, Université d'Orléans
Nadjib SEMMAR Professeur des universités, GREMI, Université d'Orléans

RAPPORTEURS:

Joerg KRUEGER Docteur, BAM Federal Institute for Materials Research and Testing
Maria DINESCU Docteure**, National** Institute for Lasers

JURY

Florence GARRELIE Professeure des universités, LHC, Université de St-Etienne
Gerard O'CONNOR Docteur, NCLA, Université de NUI Galway
Chantal BOULMER-LEBORGNE Professeure des universités, GREMI, Université d'Orléans
Arnaud STOLZ Maitre de conférences, GREMI, Université d'Orléans
Joerg KRUEGER Docteur, BAM Federal Institute for Materials Research and Testing
Maria DINESCU Docteure, National Institute for Lasers

A mes parents,

Table of contents

General introduction

According to a recent study published in the International Energy Outlook 2016 [1], a strong growing demand of energy is expected in the next three decades. By 2040, the total world energy consumption is going to reach an astronomic amount of 815.10^{24} British thermal units (Btu) compared to 549.10^{24} Btu consumption registered in 2012 (Fig.1). In other words, world is going to be faced to an aggressive increase of approximatively 48 % of total energy consumption within this period [1]. To satisfy the higher amount of energy needs, different primary sources of energy are currently explored that could be divided in two main categories:

- Fossil fuels: Natural gas (tight gas, shale gas, and coalbed methane), liquid fuels (mostly petroleum), Coal.
- Renewable energy sources: solar cells and fuel cells, hydropower, thermoelectric generators, wind and geothermal energy.

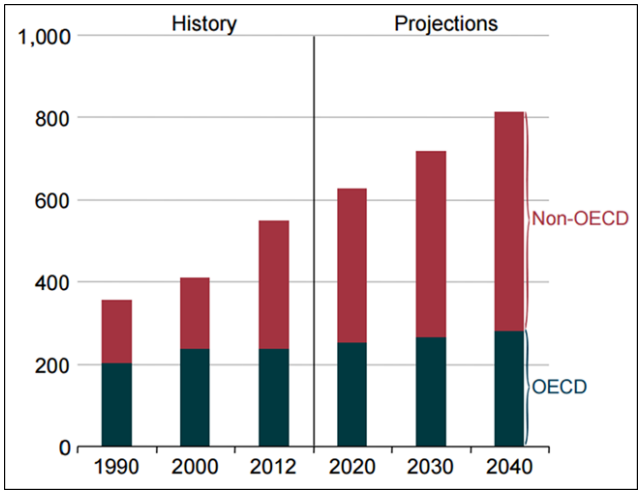

Figure.1. Total world energy consumption, 1990–2040 (10^{24} Btu)*[1]

*In Fig.1. OECD corresponds to the Organization for Economic Cooperation and Development members and (non-OECD) to nonmembers [1].

A significant increase of world energy consumption from all sources is then anticipated over the projection period (Fig.2). From today until at least 2030, the fossil fuels will dwell the most consumed energy source [2]. However, such situation will not remain long time face to a parallel decrease of their reserves that expected to run out by 2100. Face to the fuel depletion problem, renewable energy sources will play the key role to resolve the energy crisis in future. Current predications confirm this and expect that renewables will be the world's strongest-growing energy

source in the three next decades with an average increase estimation of 2.6% per year over period between 2012 and 2040. However, renewable energy conversion commercialization remains limited due to their relatively limited efficiency, high cost and bad long-term stability.

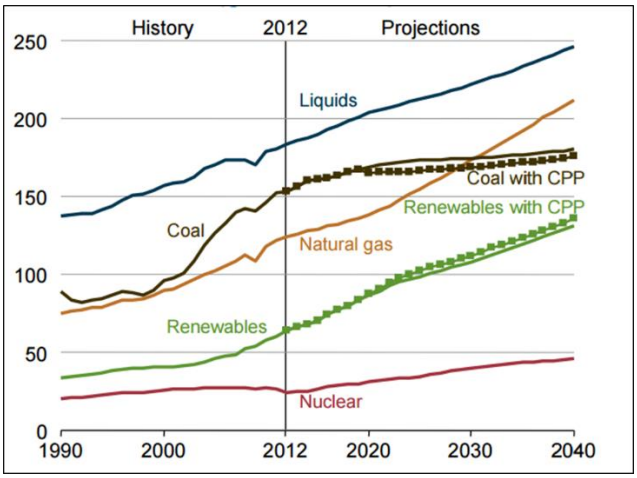

Figure.2. Total world energy consumption by energy source, 1990–2040 (10^{24} Btu) [1]

Among the different end-use energy, electricity is the most consumed one with consumption reached 18.1 % from world total final consumption in 2012 [3]. Being generated through several sources mainly coal, nuclear, natural gas and renewables, the electricity generation is faced to a huge challenge because the decrease of fuel reserves. Therefore, the research of new sources or the enhancement of efficiency, the stability and reduce the cost of all type of renewable sources is highly demanded today.

Currently, the most renewables energy conversion used for electricity generation are hydroelectric, wind, solar, and biomass. In this context, thermoelectric energy conversion presents as promising alternative power source due to its ability to convert the electricity into heat and vice-versa [4]. This means the possibility to use the waste thermal energies to generate useful electrical energy. For example, according to statistics reported in US, 191 million vehicles dissipate about 66% of their energy in the form of heat through emission which represents about 36 TWh of waste thermal energy per year [5]. The big idea, aiming to convert the huge amount of waste heat generated everywhere around us by automotive, industry, machines and even human body into a usable electrical energy using TE generators, makes thermoelectric research a field attracting much attention for its wide area of applications.

Although, macro-thermoelectric devices are the most developed since their introduction in the 1960's, thermoelectric technology can provide a potential application in microelectronic field today.

This requires the miniaturization of these devices in order to be addressed to solve the thermal problems in microelectronic such as microelectronic circuits cooling (computer and optoelectronic devices). In addition, micro-thermoelectric devices can be used in the fabrication of low-power energy source for microelectronic and microelectromechanical systems (MEMS) [6][7]. Since the MEMS based devices have an electrical power consumption in order of µWatt, this needed power can be supplied by TE devices. As example of MEMS based TE devices, fig.3. displays a picture of MEMS based TE power generator designed by J. Xie et al [8]. With a size of 1 cm², this generator provides an open circuit voltage of 16.7 V and an output power of 1.3 µW for relatively very small temperature difference of 5 K.

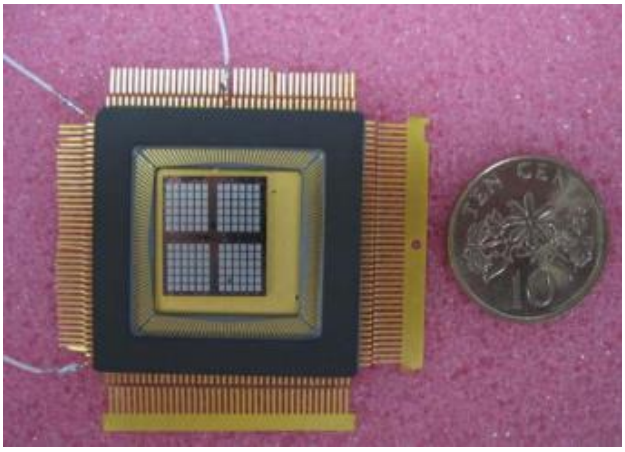

Figure.3. MEMS based TE power generator assembled in ceramic package and placed beside a Singapore ten-cent coin [8].

In spite of the promising area applications of macro-thermoelectric devices as well as the micro devices, the low efficiency showed by these thermoelectric generators which is limited to 10 % and 25 % for mid and high temperature thermoelectric respectively compared to 40% and 60% of efficiency reached by solar and fuel cell respectively makes the commercialization of TE modules very limited [9]. The efficiency of TE material is estimated through a quantity so-called the figure of merit ZT which is function of TE properties such as Seebeck coefficient, Electrical, thermal conductivity and temperature [10] (more details in first chapter). Today, the common TE devices commercialized are based on expensive and toxic bulk materials such Bi_2Te_3 based alloys that show a high ZT values about 1 [11]. In order to improve the commercialization of TE devices, several efforts are focusing on the synthesis of alternative TE materials inexpensive and more environmentally friendly such as conductive polymer and oxides and also enhancement of their TE properties through different approaches such as nanostructuring and doping [12][13].

Several ways of nanostructuring were extensively investigated and explored in the literature in order to enhance the TE material efficiency [5][14] through using complex structures, nanocomposites, nano-wires, thin film, nano-inclusions…. However, among the several nanostructuring ways existing in the literature, laser nanostructuring material surface has never been explored and tested to enhance the TE properties. Thus, in this thesis, we aim to investigate the laser nanostructuring method as new useful way that may change (hopefully enhance) the TE properties of materials. The interesting results achieved in the literature concerning the laser nanostructuring of material surfaces topic show different shape (lines, dots and spikes), symmetry (1D and 2D) and size (few ten to hundreds nm) of nanostructures developed on wide variety of materials under different laser radiations conditions, encourage us to employ this method in order to enhance the TE properties of materials [15][16][17].

To achieve our goals, two TE materials are investigated in this work:

- Mesoporous silicon (MeP-Si) bulk (thickness of 50 µm): This material was chosen for its promising TE properties (low thermal conductivity ~15 to 30 times lower than the crystallized silicon and large Seebeck coefficient) and for its remarkable surface (presence of nanopores);
- Titanium oxide (TiO_x) thin film (thickness about 500 nm): This material is widely used in devices for harvesting energy (photovoltaic, photo-catalyst) for its good stability at high temperature and its low negative environmental;

This manuscript is divided into five chapters:

I. The first chapter will present the state of art of TE materials and the laser nanostructuring. Firstly, we present the fundamental principles of thermoelectricity then theoretical predictions and experimental strategies reported in the literature in order to enhance the TE properties of materials. In second part, we discuss the fundamental principles of laser-matter interactions and the different mechanisms involved in the formation of laser induced periodic surface structures (LIPSS).

II. The second chapter deals with an experimental investigation of micro/nanostructuring of MeP-Si under picosecond laser irradiation. We investigate the irradiation of MeP-Si under mainly two regimes depending on the laser dose. In the first regime and under particular laser irradiation conditions (low fluence and high number of pulses), the generation of LIPSS,

nanoparticles, melted regions and amorphous phase is achieved. In the second regime and by increasing the fluence, different structures can develop in form of micro-spikes.

III. The third chapter provides the results of interaction femtosecond laser with MeP-Si and titanium oxide thin films by using two femtosecond lasers at two wavelength in UV and IR. We start by a comparative study of the MeP-Si response under laser radiation in ps and fs time scale. Then, we study the nanostructuring of large area of MeP-Si (up to 25x25 mm^2). In the last section, we focus in studying of TiOx on single laser spot as well as large surface area.

IV. The fourth chapter is divided into two parts. The first one deals with the validation of a new experimental setup for thermoelectric properties measurements based on CO_2 laser heating. In the second part, we provide the first results showing the evaluation of TE properties of MeP-Si and TiOx thin film with laser nanostructuring.

V. In the last chapter, we discuss the formation of exotic and complex structures on thin films samples (TiOx and polymer) under femtosecond laser irradiation. Such structures seem to be observed for the first time in the present work.

References

[1] U.S. Energy Information Administration, International Energy Outlook 2016, vol 0484(2016), no May 2016. 2016.

[2] International Energy Agency, World Energy Outlook 2014. 2014.

[3] IEA, "Key World Energy Statistics 2014", 2014.

[4] J. Tervo, A. Manninen, R. Ilola, "State-of-the-art of thermoelectric materials processing", report, 2009.

[5] H. Alam, S. Ramakrishna, "A review on the enhancement of figure of merit from bulk to nano-thermoelectric materials", Nano Energy, vol 2, no 2, 190–212, 2013.

[6] C. A. Gould, N. Y. A. Shammas, S. Grainger, I. Taylor, "Thermoelectric cooling of microelectronic circuits and waste heat electrical power generation in a desktop personal computer", Mater. Sci. Eng. B, vol 176, no 4, 316–325, 2011.

[7] C. A. Gould, N. Y. A. Shammas, S. Grainger, I. Taylor, "A Comprehensive Review of Thermoelectric Technology , Micro-electrical and Power Generation Properties", PROC. 26th INTERNATIONAL CONFERENCE ON MICROELECTRONICS (MIEL 2008), 11–14, 2008.

[8] J. Xie, C. Lee, H. Feng, "Design , Fabrication , and Characterization of CMOS MEMS-Based Thermoelectric Power Generators", Journal of microelectromechanical systems, vol 19, no 2, 317–324, 2010.

[9] C. Gayner, K. K. Kar, "Recent advances in thermoelectric materials", Progress in Materials Science, vol 83. 330–382, 2016.

[10] J. Jarman, E. Khalil, E. Khalaf, "Energy Analyses of Thermoelectric Renewable Energy Sources", Open J. Energy Effic., vol 2013, no December, 173–189, 2013.

[11] F. D. Rosi, B. Abeles, R. V. Jensen, "Materials for thermoelectric refrigeration", J. Phys. Chem. Solids, vol 10, no 2, 191–200, 1959.

[12] N. Van Nong, N. Pryds, S. Linderoth, M. Ohtaki, "Enhancement of the thermoelectric performance of p-type layered oxide Ca3Co4O9+δ through heavy doping and metallic

nanoinclusions", Adv. Mater., vol 23, no 21, 2484–2490, 2011.

[13] J. R. Szczech, J. M. Higgins, S. Jin, "Enhancement of the thermoelectric properties in nanoscale and nanostructured materials", J. Mater. Chem., vol 21, no 12, 4037, 2011.

[14] R. Mohanraman, T.-W. Lan, T.-C. Hsiung, D. Amada, P.-C. Lee, M.-N. Ou, Y.-Y. Chen, "Engineering Nanostructural Routes for Enhancing Thermoelectric Performance: Bulk to Nanoscale", Front. Chem., vol 3, no November, 1–9, 2015.

[15] R. Le Harzic, D. Dörr, D. Sauer, M. Neumeier, M. Epple, H. Zimmermann, F. Stracke, "Formation of Periodic Nanoripples on Silicon and Germanium Induced by Femtosecond Laser Pulses", Phys. Procedia, vol 12, 29–36, 2011.

[16] S. Höhm, A. Rosenfeld, J. Krüger, J. Bonse, "Femtosecond laser-induced periodic surface structures on silica", J. Appl. Phys., vol 112, no 1, 14901, 2012.

[17] T. T. D. Huynh, M. Vayer, A. Sauldubois, A. Petit, N. Semmar, "Evidence of liquid phase during laser-induced periodic surface structures formation induced by accumulative ultraviolet picosecond laser beam", Appl. Phys. Lett., vol 107, no 19, 2015.

[18] Z. Huang, J. E. Carey, M. Liu, X. Guo, E. Mazur, J. C. Campbell, "Microstructured silicon photodetector", Appl. Phys. Lett., vol 89, no 3, 3–5, 2006.

[19] B. Tan, K. Venkatakrishnan, "A femtosecond laser-induced periodical surface structure on crystalline silicon", J. Micromechanics Microengineering, vol 16, no 5, 1080–1085, 2006.

Chapter I: State of the art

A. Thermoelectric research

The first discovery of thermoelectric effect dates to 1821, when Thomas Seebeck noticed the generation of voltage when two connected dissimilar conductors are subjected to two different temperatures [1]. Firstly, Seebeck explained this effect as a magnetic field induced by the temperature gradient in interaction with the earth's magnetic field and then he called this physical phenomenon as thermo-magnetic effect. Later, it was understood that another effect is produced leading to converting the temperature difference to an electrical voltage. This effect is defined today by thermoelectric effect [2].

I. Thermoelectric effects:

1. Seebeck effect

When a material is subjected to a gradient of temperature, electrons in the hot side have a kinetic energies higher than those located in the cold side. As result of this difference, electrons diffuse from high side to the cold one leaving holes as illustrated in Fig.I.1.

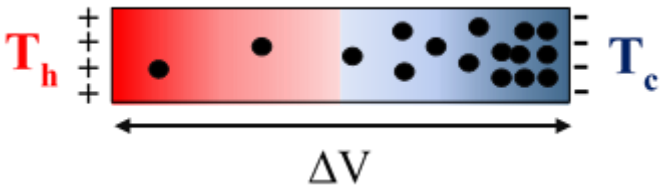

Figure.I.1. Schematic of electrons diffusion from the hot to the cold side of materials.

This phenomenon is called Seebeck effect. The magnitude of material to produce a voltage from temperature gradient is evaluated by Seebeck coefficient S which represents the ratio of the induced voltage and the temperature difference.

By convention S is defined as [3]:

$$S\left(\frac{\mu V}{K}\right) = \frac{dV}{dT} = \frac{V_c - V_h}{T_h - T_c} \qquad Eq.I.1$$

Where V_c: Potential on the cold side, V_h: Potential on the hot side, Tc: the temperature of the cold side and T_h is the temperature of the hot side.

By convention, the sign of S is negative for N type materials when the electrons migrate from the hot side to the cold one. As for P type materials, the values of S are positive and in this case the holes will diffuse from the hot side to the cold side of the material [3].

2. Peltier effect

Thirteen years after the discovery of the Seebeck effect, Jean Charles Athanase Peltier highlighted the opposite effect to that of Seebeck. Indeed, when an electric current is applied through a circuit formed by two different materials A and B, the junction between is heated due to Peltier effect [4]. The Peltier coefficient Π is defined by:

$$\Pi = \frac{Q}{I} \qquad Eq.I.2$$

Where Q is the heat flow and I is the injected electric current.

3. Thomson effect

Seebeck and Peltier effects are combined in a third thermoelectric effect known by Thomson effect and presented by Lord Kelvin in 1851. This effect describes the heating and/or cooling of a homogeneous material when an electric current is injected and in the presence of a temperature gradient [5]. This can be observed, for example, by the variation of the Seebeck coefficient as a function of the temperature at which it was measured. The heat generated or absorbed can be determined from the following formula:

$$\frac{dQ}{dx} = \tau . I . \frac{dI}{dx} \qquad Eq.I.3$$

Where x is the spatial coordinate and τ the Thomson coefficient of the material.

4. Joule effect

The propagation of an electric current in a material induces the generation of a heat flux Q_{Joule} per unit area, as given by the following formula:

$$Q_{Joule} = RI^2 \qquad Eq.I.4$$

Where R is the resistivity of the material.

Joule effect seems to be similar to Peltier one. However, this is not true. In fact, the Joule effect leads only to an increase in the temperature of the material whereas the Peltier effect allows the creation of

a temperature difference. Moreover, the Joule effect is irreversible, contrary to Peltier effect, which is reversible.

II. Thermoelectric modules

1. Presentation

Thermoelectric devices can be classified into two main categories depending on the intended application. The first category concerns the TE generators (TEG) allowing the production of electrical power from a temperature gradient. These generators ensure the production of clean electrical energy [6]. Their principle of operation consists in recycling the heat supplied and lost in the combustion processes in order to re-use and transforming it into useful energy. The second category includes the modules used for refrigeration applications. TE refrigerators allow the generation of a heat flux when they are covered by an electric current through Peltier effect [1]. These devices offer many advantages over conventional systems such as autonomy (these devices can be integrated into mobile systems thanks to the absence of compression-relaxation cycles) and the non-use of harmful gases (Freon) [7].

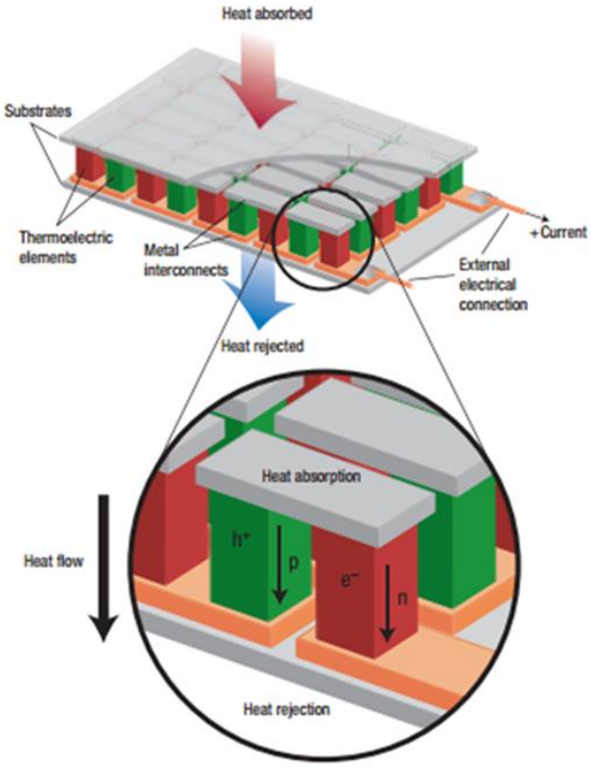

Figure.I.2. TE module showing the heat flow and the charge carrier diffusion [6]**.**

All TE modules (generators and refrigerators) exhibit a similar architecture (Fig.I.2.), based on the assembly of two different materials distinguished by the type of charge carriers (electrons or holes) resulting a couple of materials whose Seebeck coefficient (S) sign is different N ($S < 0$) and P ($S > 0$).

These materials are connected, electrically in series and thermally in parallel, by a conductive material with Seebeck coefficient close to zero (copper, for example). In the case of a TE generator, when one extremity of the module is heated while the other one is cooled, the charge carriers will diffuse from the hot side to the cold, this causes the induction electric power. While for TE refrigerators, the process is triggered through the application of an electrical current that will induce a flow of charge carriers from one side to the other one. This results a decrease of temperature of the side which has transferred the charge carriers [4].

2. Conversion efficiency

The maximum efficiency of a TE refrigerator represents the ratio between the quantities of absorbed heat on the electric power supplied. Its expression is given as follows [1][8]:

$$\eta = \frac{Qc}{W} = \left(\frac{Th}{Th - Tc}\right)\frac{\sqrt{1 + ZpnTm} - \frac{Th}{Tc}}{1 + \sqrt{1 + ZpnTm}} \qquad Eq.I.5$$

By analogy with TE refrigerators, the maximum efficiency of a TE generator can be defined by the ratio of the generated electrical power and the heat flow. It can be expressed as [1]:

$$\eta = \frac{W}{Qh} = \left(\frac{Th - Tc}{Th}\right)\frac{\sqrt{1 + ZpnTm} - 1}{\sqrt{1 + ZpnTm} + \frac{Tc}{Th}} \qquad Eq.I.6$$

Where:

T_h: hot temperature and T_c: cold temperature;

$Z_{pn}T_m$: figure of merit of the PN junction at $T_m = (Tc + Th)/2$.

$$ZpnTm = \frac{(Sp - Sn)^2}{\sqrt{\frac{\kappa_p}{\sigma_p}} + \sqrt{\frac{\kappa_n}{\sigma_n}}}Tm \qquad Eq.I.7$$

III. Figure of merit

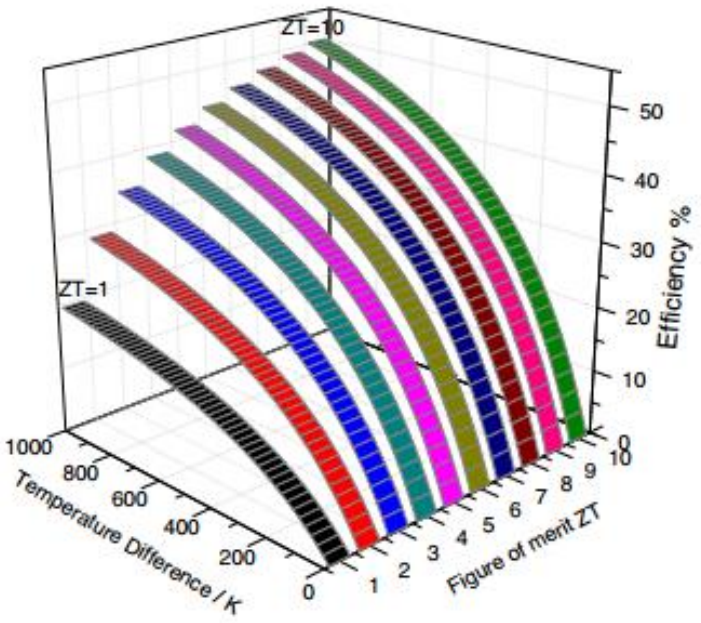

Figure.I.3. TE efficiency conversion as function of figure of merit ZT and temperature T [9]**.**

According to the efficiency conversion formulas of TE modules given above, it can be deduced that the TE performance of these modules and therefore of the used TE materials depends directly on the figure of merit ZT (see Fig.I.3.) which is a function of TE properties of materials. Therefore an ideal TE material should have important Seebeck coefficient S, good electrical conductivity σ and low thermal conductivity κ [10].

$$ZT = \frac{S^2\sigma}{\kappa}T \qquad Eq.I.8$$

Where

S: the Seebeck coefficient which can be expressed according to Mott as follows [11]:

$$S = \frac{\Pi^2 k_B}{3q} k_B T \left(\frac{d\left[\ln(\sigma(E))\right]}{dE}\right)_{E=E_F} \qquad Eq.I.9$$

$$S = \frac{\Pi^2 k_B}{3q} k_B T \left(\frac{1}{n}\frac{dn(E)}{dE} + \frac{1}{\mu}\frac{d\mu(E)}{dE}\right)_{E=E_F} \qquad Eq.I.10$$

σ: the electrical conductivity which can be defined as [11]:

$$\sigma = n(E)q\mu(E) \qquad Eq.I.11$$

κ: the thermal conductivity which can be considered as the sum of two contributions, the first one is attributed to the lattice κ_{lat} and the second one is attributed to the electrons κ_e. κ is proportional to the electrical conductivity according to the Wiedemann's law [12]. (Eq.I.12 and I.13).

$$\kappa = \kappa_e + \kappa_{Lat} \qquad Eq.I.12$$

$$\kappa = \kappa_e + L\sigma T \qquad Eq.I.13$$

Where:

k_B is the Boltzmann coefficient, n(E) is the density of charge carriers or states (D.O.S) at the energy level E, q is the carrier charge, μ(E) is the mobility of charge carriers and L is the Lorentz number.

IV. Optimizing of thermoelectric materials

As mentioned above, the efficiency conversion of TE devices can be estimated by the figure of merit ZT. Therefore, the current research efforts focusing on maximizing the TE modules performance, are based on optimization of TE properties of materials. Although, this seems to be evident and assumed that the solution is to find the good TE material presenting a very good TE properties, however, the interdependence between these three TE properties involved in the calculation of ZT (S, σ and κ) makes their optimization a real challenge. In other words, it is very difficult to modify one TE property without disturbing or destroying the two others.

The correlation between TE properties can be manifested mainly by the Wiedemann-Franz law and the Mott relation (Eq.I.10 and I.11). The Mott relation, describing the expression of S (Eq.I.9 and I.10), displays that S is inversely proportional to the charge carrier density n. This means that higher values of S are obtained for insulator and lightly doped semiconductors and that the increase of the charge carrier density leads to a decrease of S (Fig.I.4). In contrast, to ensure good electrical conductivity σ (Eq.I.11), the concentration of charge carriers n should be as large as possible (fig.I.4). Therefore, due to the opposite variations of S and σ, the maximizing of the quantity $S^2\sigma$ (known in the literature by the power factor) consists to define the field of charge carrier densities offering the maximum values of the factor of power. For most of semiconductors this range is found to extend from 10^{19} to 10^{20} cm^{-3} as shown in Fig.I.4 [13][14]. The second relation between TE properties can be evidenced by the Wiedemann-Franz law (Eq.I.13) assuming that thermal conductivity is a function of electrical conductivity since its electrical contribution κ_{lat} is directly proportional to σ. Thus, having a material showing simultaneously a good electrical conductivity and a low thermal conductivity is very difficult.

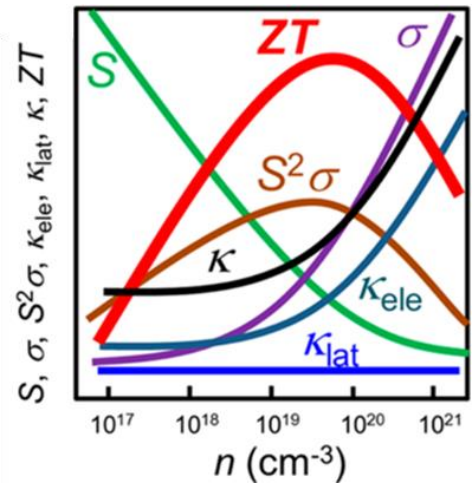

Figure.I.4. Variation of different TE properties versus the charge carrier density [14]**.**

V. Enhancement of TE properties by nanostructuring

The research for high-performance TE materials to build the first TE devices in the twentieth century was based on a "simple" choice of material exhibiting the largest ZT value among a wide range of solid semiconductors or alloys. The best TE materials found are known today by conventional materials [15] as the bismuth tellurium (Bi_2Te_3) which is considered as the best TE semiconductor presenting a ZT ~ 1 at 300 K [16]. Thus it was used to manufacture the first TE devices whose conversion efficiency did not exceed 7% [4][16]. Because of this low conversion efficiency, the high cost of the synthesis, the toxicity and the poor stability at high temperatures of these materials, TE research was obviously neglected in the following years (1960-1990). In 1993, a new concept has been appeared giving a new theoretical investigation predicting the possibility to considerably enhance the TE properties and to better control separately these properties [17][18]. This concept proposed by Dresselhaus, is the nanostructuring based on the dimension reduction of materials from bulk (3D) to thin film (2D), wire (1D) and dot (0D). When the dimension of materials is reduced by nanostructuring, there is a new physical phenomenon offering the possibility of varying "independently" S, σ and κ. In theory, the improvement of ZT by nanostructuring is mainly based on two effects:

- ✓ Quantum confinement effect on electronic density of states allowing the improvement of Seebeck coefficient.
- ✓ Scattering of phonons leading to thermal conductivity reduction.

1. Seebeck coefficient enhancement by nanostructuring

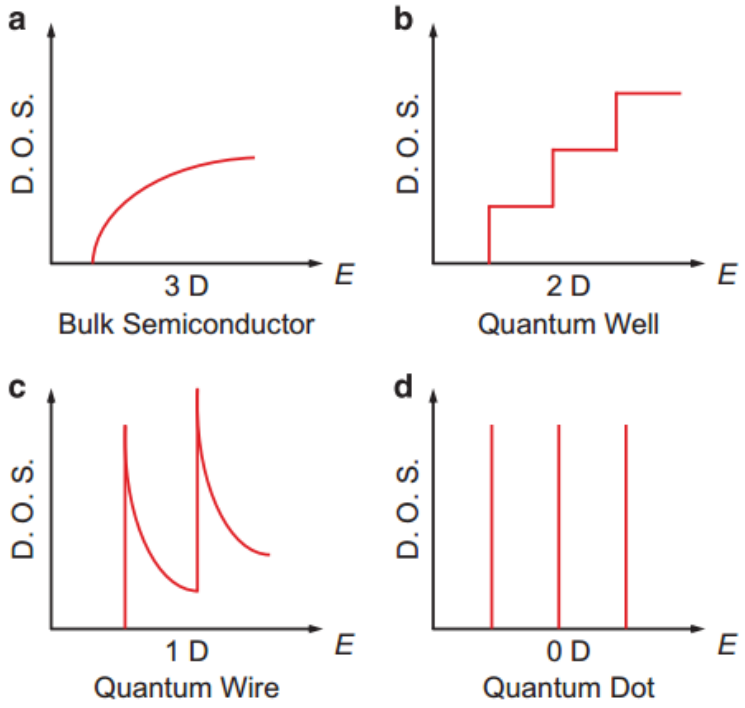

Figure.I.5. Electronic density of states of bulk (a), well (b), wire (c) and dot semiconductor (d) [2].

The reduction of materials dimensionality from bulk to nanostructures leads to an enhancement of density of states given by the presence of peaks exhibiting the quantum confinement as displayed in Fig.I.5 [19][20]. As S is directly proportional to the derivative of the density of states that depends on the energy as shown by the Mott formula in Eq.I.9, the enhancement of the state density allows to increase S. For this purpose, Robert. Y and coauthors [21], have achieved an experimental work based on the synthesis of nanostructured PbSe in the form of quantum dots with diameters varying from 5 to 9 nm. As a result of the reduction of size, the authors observed an important increase of Seebeck coefficient from 600 µV/k for bulk PbSe to respectively 700 and 1150 µV/k for PbSe dots of 8.6 and 4.8 nm in diameter as shown in Fig.I.6. This work assumes that this improvement of S is attributed to the enhancement of the density of states by nanostructuring.

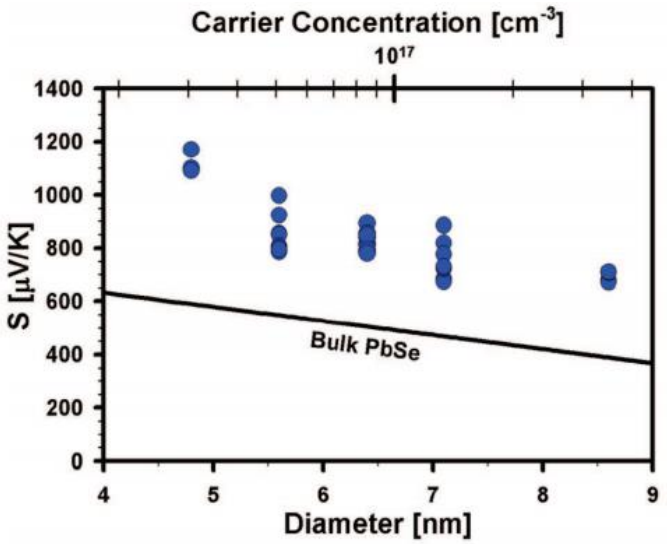

Fig.I.6. Seebeck coefficient of PbSe depending on the size of material [21]**.**

2. Thermal conductivity reduction by nanostructuring

As mentioned previously the thermal conductivity has two contributions κ_e and κ_{lat}. Thus, in order to reduce the thermal conductivity without deteriorating the electrical conductivity, the reduction of thermal conductivity involves the decrease of lattice thermal conductivity $\kappa_{lat.}$ This can be provided through nanostructuring method. Similar to the quantum confinement on carriers leading to enhancement of Seebeck coefficient, the quantum confinement on phonons allows also to decrease the lattice thermal conductivity and therefore the total thermal conductivity [22]. When the dimension of material is significantly reduced, the scattering of phonons at the interfaces and grain boundaries becomes very important [11][23][24]. The variation of electrical thermal conductivity κ_e with nanostructuring can be neglected because the mean free path of electrons (l_e) is lower than the characteristic length scale of material d (d refers to the size of nanostructured material which can be the thickness of quantum well and the diameter of quantum wire or dot). While, the mean free path of phonons (l_φ) is limited by d (as given in Eq.I.13) [16].

$$l_e \ll d \sim l_\varphi \qquad Eq.I.13$$

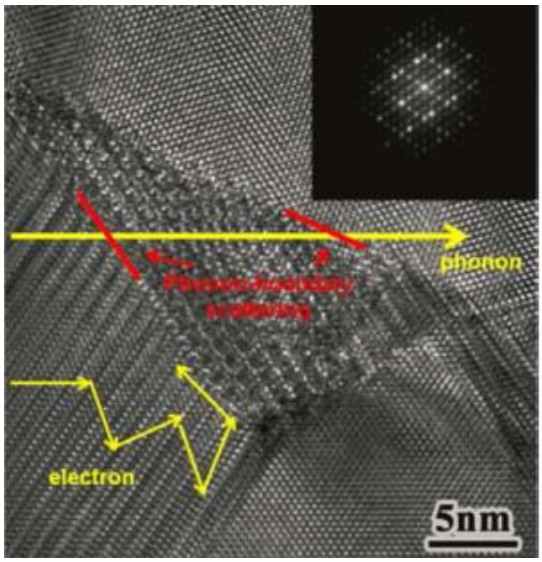

Figure.I.7. Scheme of dominant scattering of phonons in nanocrystalline silicon at the interfaces and grain boundaries [6].

As example, in the case of crystal silicon (doping concentration in the range of 1-2%), the mean free path of electrons is roughly in the range of a few nanometers while the mean free path of phonons is in the micrometer scale (see Fig.I.7.)[25]. In reference [26], the thermal conductivities of single-crystalline silicon nanowires having different diameters are measured. Two important results that match very well with the theoretical predictions are obtained. The first one points out the huge reduction of thermal conductivity at 300 K from (150 W/m.K) for bulk silicon to (5-40 W/m.K) for nanowire with 115 nm diameter. The second one displays the direct dependence between the thermal conductivity and the nanowire diameter as reported in Fig.I.8, suggesting the significant phonon scattering process with the wire diameter lowering.

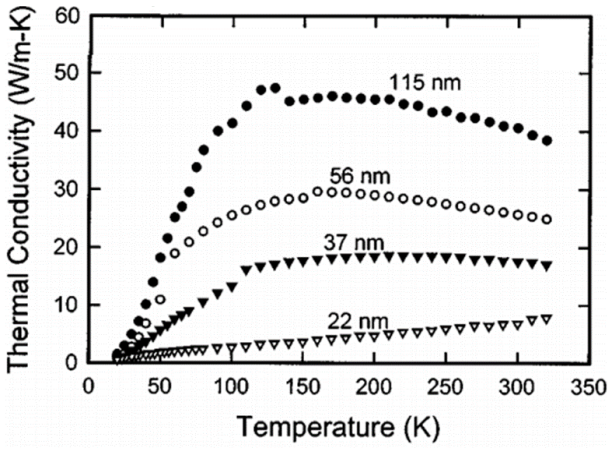

Figure.I.8. Thermal conductivities of single-crystalline nanowires as a function of temperature and diameter [7].

In this part, a brief picture of the current state of the art of thermoelectric research is presented. It is clearly understood that the current research efforts in this field are focusing in the enhancement of

thermoelectric properties though mainly nanostructuring way. Different nanostructuring ways were investigated in literature from super-lattices, nanowires, quantum dots, grain sizing, nanocomposites and nano-inclusions [27][2] etc. In this context, ultrashort lasers can be utilized to generate different nanostructures mainly on material surface that could contribute strongly to enhance the TE properties of materials. Although this method was widely investigated in the two last decades, it has never been employed directly in order to evaluate its effect on TE property evolution. To our knowledge the only one publication available on laser surface treatment in relation with TE field is the one reported by T.Y. Hwang et al. [28], in which they have studied the role of laser surface texturing on the enhancement of solar-driven thermoelectric generator efficiency by improving the surface absorbance in UV. However no investigation on its effect on the TE properties was achieved. Thus, the purpose of this thesis is to investigate this effect. Thus a great part of the work has been focused on the laser induced periodic surface structure formation.

VI. Materials investigated in this thesis

As discussed in paragraph V, the best TE materials so-called conventional materials such Bi_2Te_3 and PbTe alloys are known to be toxic, rare and unstable at high temperatures [29]. This makes their synthesis and manufacturing processes very complicated and expensive. Thus, the current thermoelectric research activities are based on improving the TE properties of other types of materials such oxides and semiconductors offering a relatively low manufacturing cost, no-toxicity risks and a good stability at high temperature [19][30]. Two materials have been chosen to carry out our fundamental investigation of the role of laser structuring on the evolution of TE properties of materials. These materials are bulk mesoporous silicon MeP-Si (50 µm thick) and titanium oxide thin films $TiO_{1.6}$ (500 nm), as they are well known in our laboratory[31][32][33]. Additionally, their increasing employment in microelectronics and photovoltaics need to check other complementary intrinsic energy sources for micro and nano-systems.

1. Mesoporous silicon MeP-Si

Bulk silicon shows a very limited ZT about 0.01 at room temperature due to its high thermal conductivity (~ 150 W/m.K)[34]. In order to reduce this value, different nanostructuring ways were tested leading to the fabrication of nanostructured silicon mainly in form of nanowire and porous silicon exhibiting a good ZT values reaching 0.4 at room temperature [35][36][37]. The thermal properties of MeP-Si have been studied in GREMI [32]. It has been shown that a huge reduction of its thermal conductivity is obtained when porosity and thickness of MeP-Si samples are increasing (Tab.I.1.). These results appear to be in good agreement with literature [34][37]. This reduction is

explained by the presence of porosity, Si-O, Si-H bonds formed during electrochemical etching process [32].

Sample	Thickness (µm)	Porosity (%)	Thermal conductivity ($W.m^{-1}.K^{-1}$)
MeP-Si (1)	0.2	28	8.0 ± 0.8
MeP-Si (2)	1	32	7.0 ± 0.4
MeP-Si (3)	10	34	7.0 ± 0.7
MeP-Si (4)	50	41	5.0 ± 0.5

Table.II.1. Thermal conductivity of different MeP-Si samples (porosity and thickness).

2. Titanium oxide thin film ($TiO_{1.6}$)

Metal oxides have been recently proposed as a promising materials for thermoelectric field since they are abundant and stable at higher temperatures [38]. Among the different thermoelectric oxides investigated in literature (cobaltites, zinc oxide etc.) [39][40][41], titanium dioxide is known to be a well matured engineered oxide material since it is widely used for many promising applications on energy and environmental fields such as photovoltaics, photo-catalysis, photo-electrochromic and sensors. The recent development efforts in the synthesis research of this material, are focused in the downsizing of the material to nano-scaled structures through TiO_x such as nanoparticles and nanowires. Recently, the non-stoichiometric titanium oxides (TiO_{2-x}) have demonstrated a promising ZT of 0.1 at 10 K [19]. Thus TiO_{2-x} thin films have been chosen to be the second material of this investigation. The films were prepared in GREMI, the x value of their stoichiometry has been estimated from Rutherford backscattering spectrometry (RBS) technic and was ranging in 0.2 to 0.4 values.

B. Laser Induced Periodic Surface Structures

I. Ultrashort pulse laser irradiation of solids

1. Absorption of photons

During ultrashort pulse laser irradiation of materials, wide variety of physical processes can occur like heating, melting, ablation and plasma generation etc. The mechanisms of pulse photon energy absorption depend strongly on the kind of material (metal, semiconductor or insulator). These materials differ in their characteristic energy band structure. The band structure or metal characterized by overlapping valence and conduction bands whereas semiconductor has a filled valence band and an empty conduction band separated by a small band gap (typically < 4 eV), while insulator band gap is much larger (Fig.I.9.). In metals, the laser pulse energy absorption is usually dominated by free electrons due to inverse Bremsstrahlung process. Free electrons absorb the photons energy and then share it with other electrons through electron-electron collisions. For semiconductors, electrons are excited from the valence band to the conduction band in one step as far as the photons energy exceeds the band gap or less likely several photons with lower energies than gap, can be simultaneously absorbed. For insulators, the direct excitation of electrons from the valence to the conduction band is not possible due to their large band gap (larger than any photon energy). Several photons adding their energy must be simultaneously absorbed to excite a valence electron to conduction band. However, due to the high density of photons delivered in each laser ultrashort pulse (high peak power), the electron excitation can be produced by multiphoton ionization then inelastic electron collisions contribute to avalanche ionization [42]. The probability of these ionization processes increases with the number of photons if delivered in a very short time (in order to have a simultaneous absorption of photons) that means that increases with the laser energy density (fluence J/cm^2).

In these cases, once the electrons are excited, their energy is transferred to the lattice through electron-phonon coupling [43].

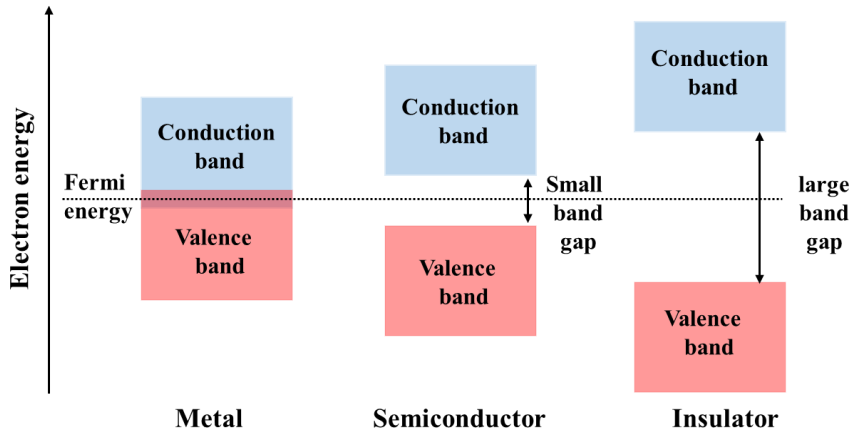

Figure.I.9. Schematic of energy band structures of metal, semiconductor and insulator.

2. Relaxation electron-phonon: Two temperature model

The ultrashort pulse duration implies that after electron excitation, electrons are not in thermal equilibrium for a few 100 fs up to the picosecond regime. The duration time, called "electronic thermalization" describes the time during which the laser energy, absorbed by free electrons, is distributed to other free electrons by electron-electron collisions. By this way the mean free electron temperature is increased (electron temperature can raise up to tens of thousands kelvins) [44]. At this point free electron has reached thermal equilibrium, then relax their energy by electron-phonon collisions with lattice. This leads to electron cooling and lattice heating. This stage is known by "electron-lattice relaxation". Finally, thermal equilibrium between free electrons and lattice will be reached within few picoseconds [45]. This sequence is widely accepted to describe the physical mechanisms involved during ultrashort irradiation of materials especially for metals because the presence of intrinsic free electrons allowing the initiation of this process. However, even in the case of semiconductors and insulators, this description stays available as multi-photoionization process can produce a high density of free electrons due to the high density of laser photons in a very short delay time allowing the simultaneous absorption of several photons by valence electrons [46]. The electron and lattice thermalization behaviors can be modeled by the two-temperature model evidenced by the following two coupled equations (eq.I.14 and I.15) [47][48][49]:

$$C_e \frac{\partial T_e(t,x,z)}{\partial t} = \nabla(K_e(T_e).\nabla T_e) - \gamma_{ei}(T_e - T_i) + S(t,x,z) \qquad Eq.I.14$$

$$C_i \frac{\partial T_i(t,x,z)}{\partial t} = \nabla(K_i(T_i).\nabla T_i) + \gamma_{ei}(T_e - T_i) \qquad Eq.I.15$$

With

$$S(z,t) = \alpha . A . I(t) \exp(-\alpha z) \qquad Eq.I.16$$

Where

T_e and T_i are electron and lattice temperatures (K);

C_e and C_i are the specific heat capacities of electrons and lattice (J m^{-3} K^{-1});

K_e and K_i is the thermal conductivity of electrons and lattice (W m^{-1} K^{-1});

$\gamma_{ei} = \frac{C_e}{\tau_e}$ is the electron-phonon coupling parameter (W.m^{-3}.K^{-1}), where τ_e is the electron-phonon collision time (or electron cooling time);

$S(z,t)$ is the source term describing the laser energy deposition, where I is the laser intensity, A is the percentage of absorbed photons and α is the absorption coefficient (cm^{-1}).

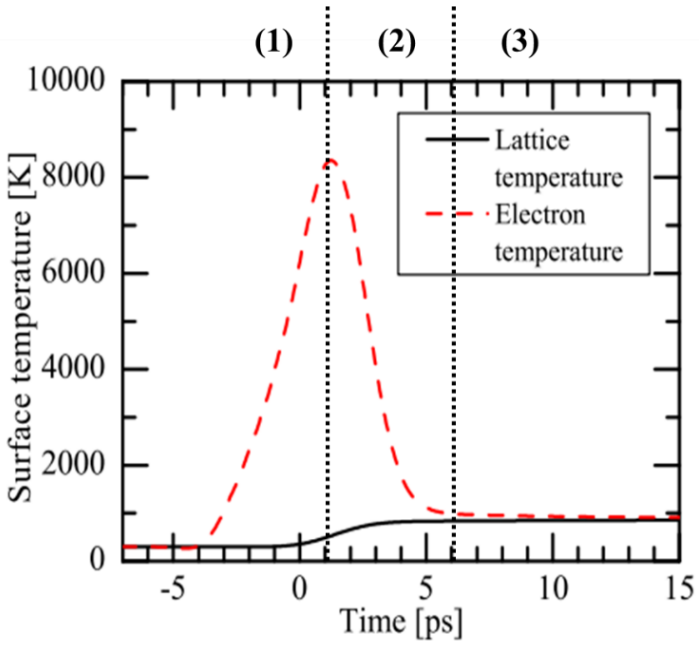

Figure.I.10. Simulation of electron and lattice temperature evolution for silicon irradiated by picosecond laser (3 ps of pulse duration) at 1030nm and a fluence per pulse of 0.58 J/cm² [50]**.**

As an example, Fig.I.10. presents the evolution of electron and lattice temperatures as a function of time, calculated in silicon according to the two temperature model. A laser pulse of 3 ps duration (centered at t=0) and a fluence F of 0.58 J/cm² was used. First, the electrons are strongly superheated in few hundred fs during the "electronic thermalization" time and their temperature reaches roughly 8000 K (1). Then, energy exchange from electrons to phonons takes place within few picoseconds through electron-phonon coupling (2) and at the end a thermal equilibrium between electrons and

lattice is reached in few to ten ps resulting in the heating of silicon from 300K to roughly 900K (3) [50].

3. Thermal and non-thermal regimes: Ablation and melting

During ultrashort laser radiation, melting and ablation processes can occur under two regimes that are strongly depending on the beam fluence. As discussed above, after laser irradiation, the thermal equilibrium is reached when electrons transfer their energy (absorbed from the pulse) to the lattice, which means that material reached a global temperature (within few ps). If this global temperature exceeds the melting point, thermal melting process takes place. If this temperature is larger than the boiling point the target will be evaporated and thus ablated. This means that melting and ablation occur after electron-phonon relaxation (after a tens of picosecond). This regime refers to thermal one with thermal melting followed by ablation by evaporation.

In contrast, when the laser fluence is very high (two times higher than the thermal threshold fluence ~ J/cm² [51]), the density of highly excited electrons by absorption of photons is very large and electron thermalization by electron-electron collisions does not occur. There is a nonequilibrium state. High-energy electrons cause the direct ionization of the lattice yielding to bond breaking and disordering of material thus to phase transformation and material ejection (non-thermal melting and non-thermal ablation). These processes take place within 1 ps or less (few hundreds of femtosecond), before the thermal equilibrium (where $T_e >> T_i$) is reached and the lattice remained cold. The bond weakening and breaking on femtosecond time scale is visualized in (Fig.I.11.) [52] which displays the results obtained by a simulation study (ab-initio molecular dynamics) of silicon strongly excited (14.1 % of valence electrons are excited) by femtosecond laser. After 450 fs, covalent bond get destroyed and molten silicon is formed. This regime is known by non-thermal regime or ultrafast regime.

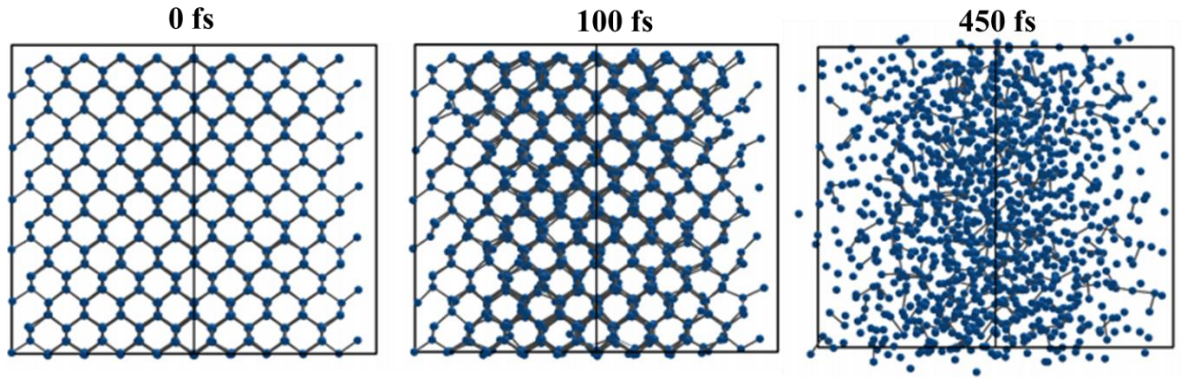

Figure.I.11. Snapshots of one ab-initio molecular-dynamics of silicon after intense femtosecond laser excitation [19].

4. Ablation fluence threshold and incubation effect

Pulsed laser ablation process has attracted a great attention since it plays a key role in different fields such as, pulsed laser deposition, nanoparticles generation, laser induced plasma spectrometry and surface texturing. As outlined above, this phenomenon can be described by the removal or ejected material from the target surface and can be considered as a result of phase explosion phenomenon which is, by definition, a transition from heating liquid (melting) to material vapor, cluster and droplets [53][51]. The single pulse ablation fluence threshold, $F_{th}(1)$, refers thus to the fluence required to initiate the material removal (melting, damage and LIPSS formation) after irradiation by 1 pulse (usually in the range of few hundreds to few thousands of mJ/cm²). This parameter depends strongly on the kind of irradiated material (as absorption coefficient α, inversely proportional to photon wavelength, is directly bound to material characteristics) and on the laser pulse duration time. The threshold fluence usually decreases with changing the radiation wavelength from IR to UV due to the enhancement of material absorption. In ref [50], the irradiation of bulk silicon by 3 ps laser at three different radiation wavelengths 1030, 515 and 343 nm, causes a decreasing of the ablation threshold fluence values as respectively, 240, 220 and 100 mJ/cm². Moreover, threshold fluence decreases by reducing the pulse duration because the increasing of photon number per second allowing multiphoton ionization process and the reduction of energy losses by thermal diffusion (thermal diffusion starts to take place for laser pulse duration time larger than 10 ps) [49][54].

If the applied laser fluence F is lower than the single-pulse ablation (melting, damage and LIPSS) threshold $F_{th}(1)$, ablation process may occur by increasing the laser dose by increasing the number of pulses N. Because F is lower than $F_{th}(1)$, this fluence cannot initiate the ablation process but it can heat and induce some defects on the surface of material like chemical modifications (oxidation) and structural deformations (stress, dislocations) etc. Pulse after pulse, these defects accumulate and may lead to the initiation of ablation (melting, damage and LIPSS) formation. This phenomenon is known by accumulation or "incubation effect" [55][56]. This means that F_{th} decreases with increasing N.

In the case of metals and semiconductors [56][57][58][59], the behavior of incubation effect can be often modeled and described mathematically as follows:

$$F_{th}(N) = F_{th}(1).N^{(S-1)} \qquad Eq.I.17$$

Where:

$F_{th}(N)$ refers to the fluence threshold after N pulses and S is the incubation coefficient which qualifies the accumulation behavior of each material.

The values of S are typically ranging in 0.8 to 0.95 (for metals and semiconductors).

S<1, corresponds to incubation effect as described above and in this case low values of S mean a very important incubation effect [54].

S=1, means the fluence threshold is constant and independent on N (no incubation effect). This supposes, for a fluence lower than $F_{th}(1)$, there is no modification on the material [54].

S>1, In this case the fluence threshold increases with N. Material properties are modified by laser irradiation and cannot be ablated [54].

As an example from literature, C. S. R. Nathala et al. [59] have studied the incubation effect behavior of silicon when irradiated by fs laser beam with varied pulse durations. Their findings are illustrated in Fig.I.12. This figure illustrates the decreasing of ablation threshold with the reducing of the pulse duration time for a silicon target irradiated by a fs laser beam with pulse duration varying in 10-550 fs range. Moreover the incubation effect is evidenced and author results match very well with the model given in Eq.I.17. The incubation coefficient S, extracted from Fig.I.12 curves, is found to be 0.82, 0.83, 0.84 and 0.84 for respectively 10, 30, 250 and 550 fs pulse duration times, [59]. It appears that incubation effect becomes very important with reducing the pulse laser duration.

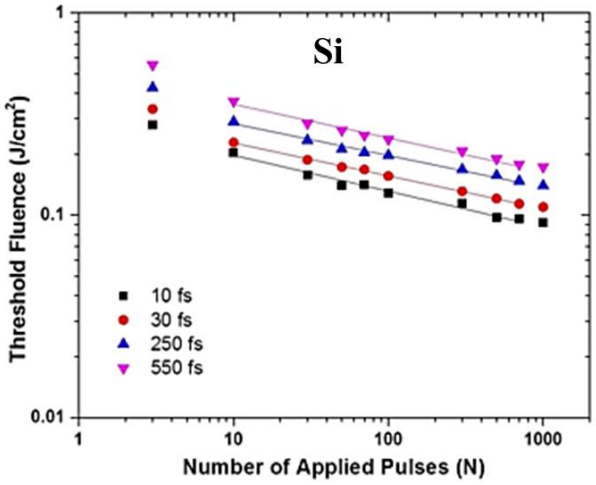

Figure.I.12.Threshold fluence vs the number of pulses on a silicon irradiated by fs laser beam [59]**.**

In the case of insulators, the incubation behavior seems to be more complicated due to the "complex" nonlinear processes involving in the first stage of pulse absorption process (electron excitation). their incubation behavior can be modeled as following [60][61][62]:

$$F_{th}(N) = F_{th}(\infty) + [F_{th}(1) - F_{th}(\infty)]e^{k(N-1)} \qquad Eq.I.18$$

Where, $F_{th}(\infty)$ is the largest fluence that can be applied without causing sample damage and k is related to incubation degree. Fig.I.13. displays the incubation behavior of SiO_2. The ablation threshold decreases sharply with increasing N (from 3.5 to 1 J/cm² within few tens of pulses) until it reaches a plateau value before 50 pulses [63].

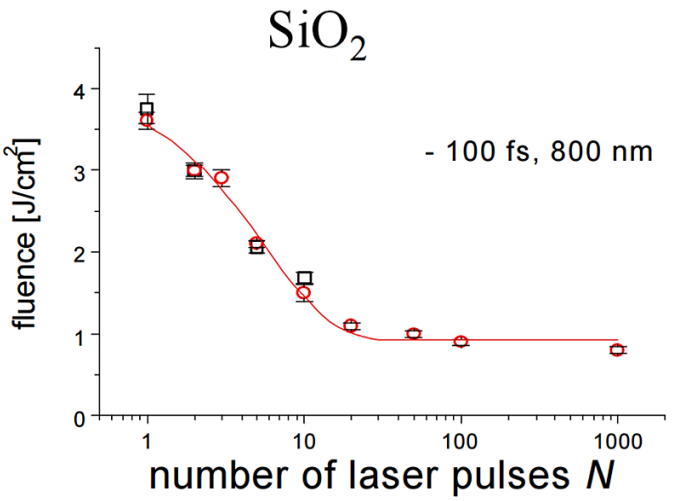

Figure.I.13. Semilog-arithmetic plot of the ablation threshold versus laser shot numbers in fused silica irradiated by 100 fs @ 800 nm [63]**.**

II. Laser induced periodic surface structures (LIPSS)

After the brief summary, on the ultra-short laser-matter interaction, described above, this part will focus on the investigation of LIPSS formation phenomenon which can be considered as a result of different combined processes from laser pulse absorption to material melting and ablation. The first observation of LIPSS has been related in 1965 by Birnbaum who evidenced the generation of micro-nano- structures produced on semiconductor surfaces after irradiation by Ruby lasers [64]. Since this date, this phenomenon has been extensively investigated on a wide variety of bulk or thin film materials (conductors, semi-conductors, insulators) [65][66][67]. Different kind of laser beams were utilized : continuous or pulsed emission in a large spectrum from UV to IR wavelength [68][69][70][71][72]. However, despite the large numerous of LIPSS studies being available today, their formation mechanisms are not yet fully reveled. The present part aims to give a brief presentation of the existing state of the art on the main parameters and physical phenomena involving in LIPSS generation.

1. Different LIPSS types

Several types of LIPSS have been observed due to the different laser and material parameters. These different types can be distinguished as function of their shape, size and period.

1.1. HSFL and LSFL

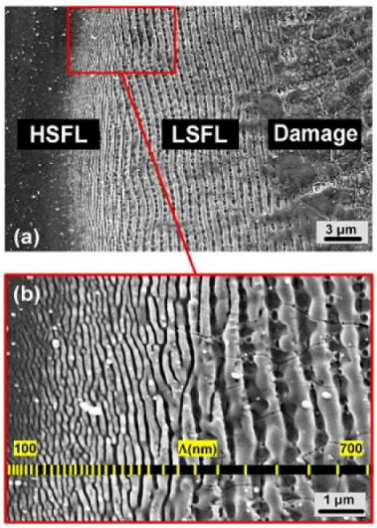

Figure.I.14. SEM images of LSFL and HSFL produced on ZnO surface irradiated by fs laser beam @ 800nm [73]**.**

Low Spatial Frequency (LSFL) LIPSS and High Spatial Frequency (HSFL) LIPSS are the main type of LIPSS observed and studied in literature. They are usually described as periodic ripples, periodic lines or periodic crests and valleys generated on the material surface (as seen in Fig.I.14.). LSFL and HSFL differ by their period. The LSFL period λ_{LSFL} is generally close to the beam wavelength λ, generally ripples presenting a period varying in 0.6λ-λ are considered as LSFL [74][75]. On the contrary, HSFL refer to ripples having a period significantly smaller than the beam wavelength ($\lambda_{HSFL} < 0.5\lambda$) [73] (Fig.I.14.).

1.2. Dots or droplets

A new type of LIPSS has been recently observed on thin film surfaces forming dot organizations. Circular shaped nanostructures have been observed on copper [69][76], polymer and titanium oxide [77] thin films. They can be organized in different ways such as well-defined lines that can be considered as LSFL and/or HSFL (Fig.I.15.a), or in more complex organization like symmetric hexagonal figures (Fig.I.15.b).

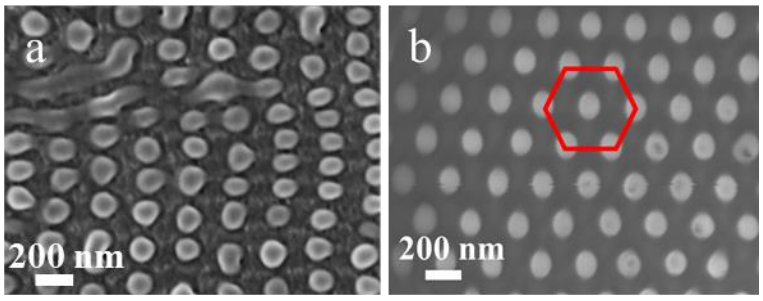

Figure.I.15. a) dots formed on copper thin film by 266 nm ps irradiation, b) hexagonal dots organization formed on polymer thin film by 266 nm fs irradiation.

1.3. Spikes

This type of LIPSS is characterized by its shape (conical, pyramid etc.) and its micrometer size which can vary from one to few tens of micrometers (Fig.I.16.a) [78][79]. They are usually observed on bulk material surfaces (especially semiconductors) irradiated by relatively high fluences that can reach few kJ/cm². This type of structures was extensively investigated on silicon surfaces in order to enhance its optical absorption especially in IR range through total internal light reflection [80][81]. Spiked silicon is widely called "black silicon" well known for its very high light absorption power (Fig.I.16.b).

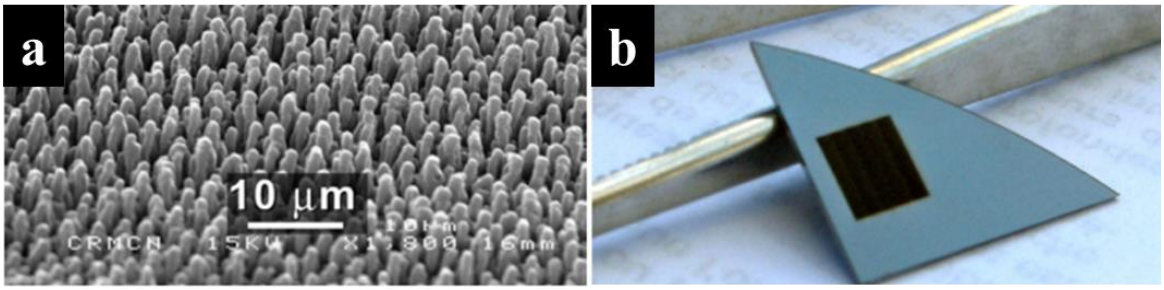

Figure.I.16. (a) SEM view of conical spikes formed on silicon by fs irradiation, (b) black silicon sample [82]**.**

2. Laser parameters and LIPSS formation

Like any other laser process (ablation, melting…), LIPSS formation process depends strongly on laser dose (fluence and number of pulses). It is accepted that the LIPSS formation fluence threshold, after one or few pulses, is very close the ablation threshold (it is generally slightly above the ablation threshold) [74][75]. The LIPSS threshold can be reduced by incubation effect as mentioned above for the ablation threshold. However, another parameter to be considered is the beam polarization. It has been observed that beam polarization controls very well the orientation of LIPSS especially HSFL and LSFL [67]. LSFL orientation is usually perpendicular to beam polarization [83] excepted in the case of some dielectric materials (like SiO_2 and $BaFe_2$) where their orientation is generally parallel to the polarization [84]. While, HSFL orientation can be either parallel or perpendicular to the beam polarization (Fig.I.17) [84][85].

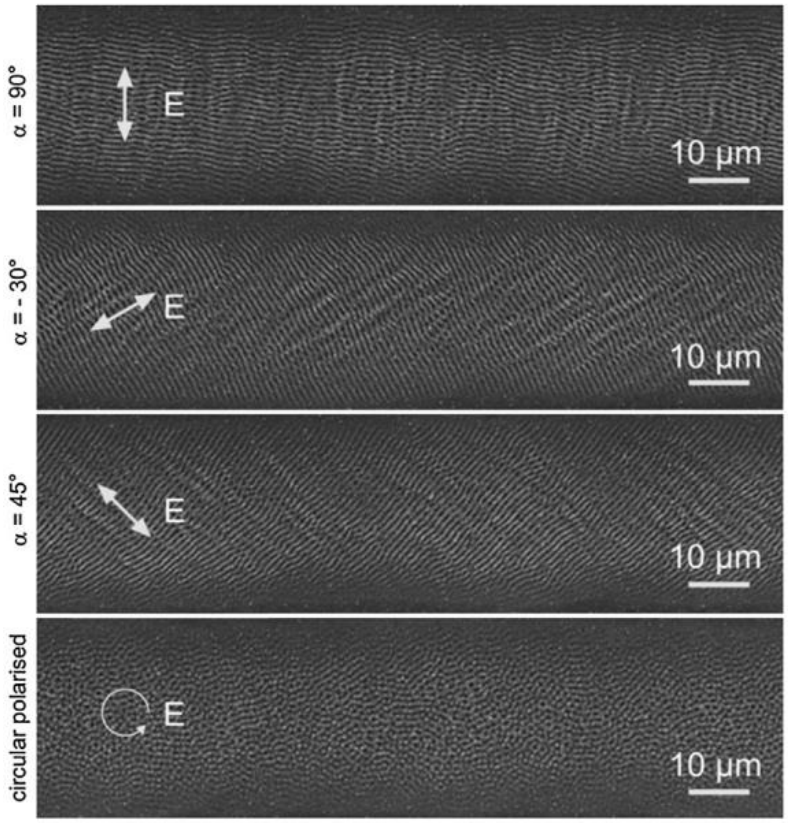

Figure.I.17. Dependence of LSFL orientation (formed by fs laser on stainless steel samples) with the laser beam polarization (here it is perpendicular to the polarization) [86]**.**

1. LIPSS formation mechanisms

The physical phenomenon explaining the LIPSS formation remains not completely understood yet. In summary, there are mainly two approaches proposed to explain the origin of LIPSS generation. The first one is known by classical model and is based on an optical approach. The second one assumes that the target plays a key role in LIPSS formation and is known by self-organization approach [87].

1.1. Classical model based on an optical approach

This model has been firstly proposed by Emmony et al, then was extended by Sipe et al, and improved by Bonse et al. [88][89][90]. It is assumed that LIPSS result of interferences produced between the incident laser beam and the excited electromagnetic surface waves. These waves can be generated from the beam scattering due to the surface roughness and defects and/or surface plasmons polaritons that can be defined as collective longitudinal oscillation of electrons [91][87]. These generated interferences can induce a periodic oscillations in the free electron density close to the sample surface leading to a periodic oscillations in the electron temperature profile [92]. As electrons

transfer their energy to the lattice, the oscillations of electrons temperature profile cause a spatial modulation of target surface temperature i.e. a spatial modulation in the laser deposited energy. The modulated heating yields to local material transformations (melting, liquid spallation, evaporation and ablation) resulting in the formation of periodic structures on the surface [92] like lithography process shown in Fig.I.18. This model can only explain the formation of nanostructures with a period close to the beam wavelength (LSFL). This approach is available when considering a large free electron density in material as metal, for semiconductors and insulators, this approach assumes a high multi-photon ionization process efficiency that occurs for ultra-short pulse laser.

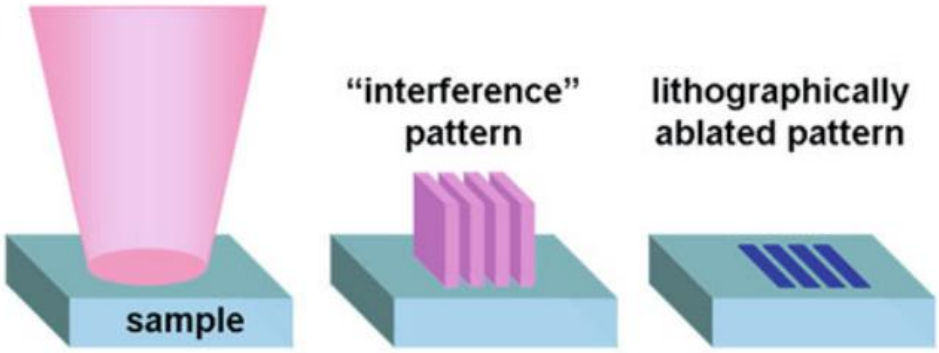

Figure.I.18.Schematic of LIPSS growth by interference model [93]**.**

1.2. Self-organization model

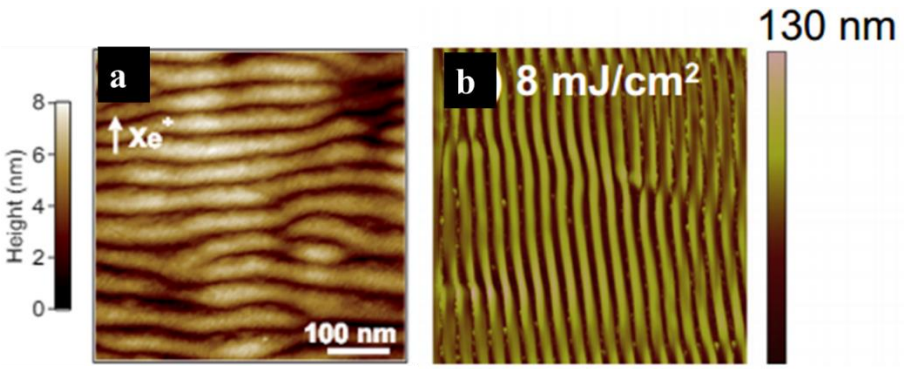

Figure.I.19. a) Periodic pattern on alumina surfaces produced by ion-beam sputtering[94]***, LIPSS formed on polymer surface by fs laser***[95]**.**

This model is developed by Reif et al [93][96]. and is the direct consequence of their observation of similarities in micro- nano- structures obtained on target surfaces after ion-beam or laser beam sputtering. The formation of these structures due to ion beam sputtering is generally attributed to a self-organization model which is a universal phenomenon [94]. This model assumes that a physical system strongly disturbed and driven very far from the thermodynamic equilibrium state

(instabilities) modifies its organization to recover a new thermodynamic equilibrium (stable state): the relaxation of instabilities results in the formation of pattern as shown in Fig.I.20. In this context, Reif et al [97]. proposed to adopt this model to explain the LIPSS formation mechanism. As ultrashort laser irradiation induces a non-equilibrium state in the material due to the strong excitation of electrons causing the weakening and breaking of atomic bonds, the lattice organization is highly disturbed. In order to reach a new thermodynamic equilibrium state, the system relaxes by a macroscopic material removal and a surface reorganization leading to the apparition of some periodic structures.

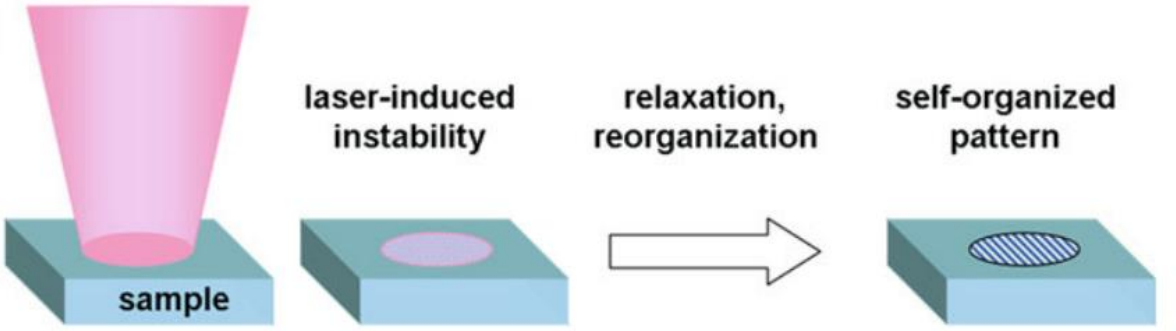

Figure.I.20. Illustration of LIPSS formation through self-organization model [93]**.**

C. Conclusion

A partial state of the art of TE materials was presented. Due to the toxicity and expensive manufacturing cost of TE conventional materials (Bi_2Te_3, PbTe etc.), the current TE research efforts are focusing on the improvement of TE properties of other no-toxic and abundant materials. Nanostructured materials were widely studied and a huge enhancement of figure of merit after nanostructuring has been observed. In order to explore a new nanostructuring way for TE properties improvement, laser surface nanostructuring method was proposed. The principle physical phenomena involved in ultra-short laser-matter interaction and the LIPSS's state of the art were presented. As the LIPSS formation mechanism remains not well-understood, experimental studies based on LIPSS formation on two new materials (have not been yet studied for LIPSS formation) will be the subject of chapter II and III of this manuscript. To point out the effect of this new nanostructuring way, the evaluation of Seebeck coefficient and electrical conductivity with LIPSS will be presented in chapter IV. Lastly, the formation of complex and exotic structures on thin film surfaces is discussed in the last chapter

References

[1] X. Zhang, L. Zhao, "ScienceDirect Thermoelectric materials : Energy conversion between heat and electricity", J. Mater, vol 1, no 2, 92–105, 2015.

[2] C. Gayner, K. K. Kar, "Recent advances in thermoelectric materials", Progress in Materials Science, vol 83. 330–382, 2016.

[3] G. Pennelli, "Review of nanostructured devices for thermoelectric applications", J. Nanotechnol, 1268–1284, 2014.

[4] G. Skomedal, "Thermoelectric Material for Waste Heat Recovery ", Report, ENE601 autumn 2013.

[5] J. C. Zheng, "Recent advances on thermoelectric materials", Front. Phys. China, vol 3, no 3, 12, 2011.

[6] G. J. Snyder, E. S. Toberer, "Complex thermoelectric materials", Nat. Mater, vol 7, no 2, 105–114, 2008.

[7] J. Jarman, E. Khalil, E. Khalaf, "Energy Analyses of Thermoelectric Renewable Energy Sources", J. Energy Effic., vol 2013, no December, 173–189, 2013.

[8] H. Seok, W. Liu, G. Chen, C. Chu, Z. Ren, "Relationship between thermoelectric figure of merit and energy conversion efficiency", PNAS, vol 112, no 27, 8205–8210, 2015.

[9] X. Chen, P. Lin, K. Zhang, H. Baumgart, B. Geist, "Seebeck Coefficient Enhancement of ALD PbTe / PbSe Nanolaminate Structures Deposited inside Porous Silicon", ECS Journal of Solid State Science and Technology, vol 5, no 9, 2016.

[10] Z. G. Chen, G. Hana, L. Yanga, L. Cheng, J. Zou, "Nanostructured thermoelectric materials: Current research and future challenge", Progress in Natural Science: Materials International, vol 22, no 6. 535–549, 2012.

[11] J. Mao, Z. Liu, Z. Ren, "Size effect in thermoelectric materials", npj Quantum Mater., vol 1, no August, 16028, 2016.

[12] H. Alam, S. Ramakrishna, "A review on the enhancement of figure of merit from bulk to nano-thermoelectric materials", Nano Energy, vol 2, no 2, 190–212, 2013.

[13] J. R. Szczech, J. M. Higgins, S. Jin, "Enhancement of the thermoelectric properties in nanoscale and nanostructured materials", J. Mater. Chem., vol 21, no 12, 4037, 2011.

[14] G. Tan, L. Zhao, M. G. Kanatzidis, "Rationally Designing High-Performance Bulk Thermoelectric Materials", Chem. Rev., 116, 12123−12149, 2016.

[15] L. D. Zhao, S. H. Lo, J. He, H. Li, K. Biswas, J. Androulakis, C. I. Wu, T. P. Hogan, D. Y. Chung, V. P. Dravid, M. G. Kanatzidis, "High performance thermoelectrics from earth-abundant materials: Enhanced figure of merit in PbS by second phase nanostructures", J. Am. Chem. Soc., vol 133, no 50, 20476–20487, 2011.

[16] J. P. Heremans, "Low-Dimensional Thermoelectricity", Proceedings of the XXXIV International School of Semiconducting Compounds, vol 108, no 4, 609–634, 2005.

[17] M. Saleemi, "Nano - Engineered Thermoelectric Materials for Waste Heat Recovery", Ph.D

thesis, KTH Royal Institute of Technology Stockholm, Sweden, 2014.

[18] L. D. Hicks, T. C. HarmanM, S. Dresselhaus, "Use of quantum-well from nonconventional superlattices to obtain a high figure of merit thermoelectric materials", Appl. Phys. Lett. 63 (23), 1993.

[19] S. Walia, S. Balendhran, H. Nili, S. Zhuiykov, G. Rosengarten, Q. H. Wang, M. Bhaskaran, S. Sriram, M. S. Strano, K. Kalantar-zadeh, "Transition metal oxides – Thermoelectric properties", Prog. Mater. Sci., vol 58, no 8, 1443–1489, 2013.

[20] Y. Zhang, G. D. Stucky, "Heterostructured Approaches to Efficient Thermoelectric Materials", Chem. Mater, 26, 837−848, 2014.

[21] R. Y. Wang, J. P. Feser, J. Lee, D. V Talapin, R. Segalman, A. Majumdar, "Enhanced Thermopower in PbSe Nanocrystal Quantum Dot Superlattices", NANO LETTERS, Vol. 8, No. 8 2283-2288, 2008.

[22] D. Baillis, J. Randrianalisoa, "Prediction of thermal conductivity of nanostructures: Influence of phonon dispersion approximation", Int. J. Heat Mass Transf., vol 52, no 11–12, 2516–2527, 2009.

[23] J. Minnich, M. S. Dresselhaus, Z. F. Ren, G. Chen, "Bulk nanostructured thermoelectric materials: current research and future prospects", Energy Env. Sci, vol 2, no 5, 466–479, 2009.

[24] Y. Lan, A. J. Minnich, G. Chen, Z. Ren, "Enhancement of thermoelectric figure-of-merit by a bulk nanostructuring approach", Adv. Funct. Mater., vol 20, no 3, 357–376, 2010.

[25] A. Ali, Y. Chen, V. Vasiraju, G. Schierning, R. Chavez, R. Schmechel, B. Balke, G. Rogl, P. Rogl, "Concepts for medium-high to high temperature thermoelectric heat-to-electricity conversion : a review of selected materials and basic considerations of module design", Transl. Mater. Res. 2, 025001, 2016.

[26] D. Li, P. Kim, "Thermal conductivity of individual silicon nanowires", Appl. Phys. Lett., vol 83, no 14, 2934–2936, 2003.

[27] R. Mohanraman, T. W. Lan, T. C. Hsiung, D. Amada, P. C. Lee, M. N. Ou, Y. Y. Chen, "Engineering Nanostructural Routes for Enhancing Thermoelectric Performance: Bulk to Nanoscale", Front. Chem., vol 3, no November, 1–9, 2015.

[28] T. Y. Hwang, A. Y. Vorobyev, C. Guo, "Enhanced efficiency of solar-driven thermoelectric generator with femtosecond laser- textured metals", Optic Express, vol 19, no July, 824–829, 2011.

[29] Y. Wu, S. W. Finefrock, H. Yang, "Nanostructured thermoelectric: Opportunities and challenges", Nano Energy, vol 1, no 5, 651–653, 2012.

[30] G. Kieslich, G. Cerretti, I. Veremchuk, R. P. Hermann, M. Panthofer, J. Grin, W. Tremel, "A chemists view: Metal oxides with adaptive structures for thermoelectric applications", Phys. Status Solidi Appl. Mater. Sci., vol 213, no 3, 808–823, 2016.

[31] N. Semmar, L. Coudron, G. Gautier, A. Petit, M. Gaillard, J. Mathias, E. Millon, "Thermal conductivity measurement of porous silicon by pulsed-photothermal method method is based on a pulsed-laser source in the nanosecond regime . A 1D analytical model is coupled with the PPT", Appl. Phys. 44 355401, 2011.

[32] A. Melhem, D. De Sousa Meneses, C. Andreazza-Vignolle, T. Defforge, G. Gautier, N. Semmar, “Structural, Optical and Thermal Analysis of n-type Mesoporous Silicon Prepared by Electrochemical Etching”, J. Phys. Chem. C, 2015.

[33] C. Tchiffo-tameko, C. Cachoncinlle, J. Perriere, M. Nistor, A. Petit, O. Aubry, R. P. Casero, E. Millon, “IR emission and electrical conductivity of Nd / Nb-codoped TiO x (1 . 5 < x < 2) thin films grown by pulsed-laser deposition”, Appl. Surf. Sci., vol 389, 1062–1068, 2016.

[34] J. Tang, H. Wang, D. H. Lee, M. Fardy, Z. Huo, T. P. Russell, P. Yang, “Holey Silicon as an Efficient Thermoelectric Material”, Nano Lett. 10, 4279–4283, 2010.

[35] K. Valalaki, P. Benech, A. G. Nassiopoulou, “High Seebeck Coefficient of Porous Silicon : Study of the Porosity Dependence”, Nanoscale Res. Lett., 2016.

[36] M. Jang, Y. Park, M. Jun, “The Characteristics of Seebeck Coefficient in Silicon Nanowires Manufactured by CMOS Compatible Process”, Nanoscale Res Lett, 1654–1657, 2010.

[37] J. de Boor, D. S. Kim, X. Ao, M. Becker, N. F. Hinsche, I. Mertig, P. Zahn, V. Schmidt, “Thermoelectric properties of porous silicon”, Appl. Phys. A, vol 107, no 4, 789–794, 2012.

[38] S. Harada, K. Tanaka, H. Inui, S. Harada, K. Tanaka, H. Inui, “Thermoelectric properties and crystallographic shear structures in titanium oxides of the Magnèli phases”, Journal of Applied Physics 108, 083703, 2010.

[39] K. Koumoto, Y. Wang, R. Zhang, A. Kosuga, R. Funahashi, “Oxide Thermoelectric Materials: A Nanostructuring Approach”, Annu. Rev. Mater. Res., vol 40, no 1, 363–394, 2010.

[40] M. Sondergaard, E. D. Bojesen, K. A. Borup, S. Christensen, M. Christensen, B. B. Iversen, “Sintering and annealing effects on ZnO microstructure and thermoelectric properties”, Acta Mater., vol 61, no 9,3314–3323, 2013.

[41] L. Thanh, N. Van Nong, G. J. Snyder, M. Hoang, B. Balke, L. Han, E. Stamate, S. Linderoth, N. Pryds, “High performance p -type segmented leg of misfit-layered cobaltite and half-Heusler alloy”, ENERGY Convers. Manag., vol 99, 20–27, 2015.

[42] B. C. Stuart, M. D. Feit, S. Herman, A. M. Rubenchik, B. W. Shore, M. D. Perry, “Optical ablation by high-power short-pulse lasers”, J. Opt. Soc. Am. B, vol 13, no 2, 459–468, 1996.

[43] J. Hohlfeld, S. Wellershoff, J. Gudde, U. Conrad, V. Jahnke, E. Matthias, “Electron and lattice dynamics following optical excitation of metals”, Chemical Physics 251, 237–258, 2000.

[44] Z. Lin, L. V Zhigilei, “Electron-phonon coupling and electron heat capacity of metals under conditions of strong electron-phonon nonequilibrium”, PHYSICAL REVIEW B 77, 075133, 2008.

[45] A. Kaiser, “Ultrafast dynamics of nonequilibrium electrons in metals under femtosecond laser irradiation”, PHYSICAL REVIEW B, vol 65, 1–11, 2002.

[46] L. D. Landau, “Timescales in the response of materials to femtosecond laser excitation”, Appl. Phys.A, vol 769, 767–769, 2004.

[47] T. J. Y. Derrien, T. Sarnet, M. Sentis, T. E. Itina, “Application of a two-temperature model for the investigation of the periodic structure formation on Si surface in femtosecond laser interactions”, JOURNAL OF OPTOELECTRONICS AND ADVANCED MATERIALS Vol.

12, No. 3, , p. 610 - 615, 2010.

[48] B. Rethfeld, D. S. Ivanov, M. E. Garcia, “Modelling ultrafast laser ablation”. J. Phys. D: Appl. Phys. 50 193001, 2017.

[49] B. N. Chichkov, C. Momma, S. Nolte, F. von Alvensleben, A. Tünnermann, “Femtosecond, picosecond and nanosecond laser ablation of solids”, Appl. Phys. A Mater. Sci. Process., vol 63, no 2, 109–115, 1996.

[50] J. Thorstensen, S. Erik Foss, “Temperature dependent ablation threshold in silicon using ultrashort laser pulses”, J. Appl. Phys., vol 112, no 10, 2012.

[51] N. M. Bulgakova, “Theoretical Models and Qualitative Interpretations of Fs Laser Material Processing”, J. Laser Micro/Nanoengineering, vol 2, no 1, 76–86, 2007.

[52] T. Zier, E. S. Zijlstra, A. Kalitsov, I. Theodonis, M. E. Garcia, “Signatures of nonthermal melting”, Struct. Dyn. 2, vol 54101, 1–9, 2015.

[53] N. M. Bulgakova, I. M. Bourakov, “Phase explosion under ultrashort pulsed laser ablation: Modeling with analysis of metastable state of melt”, Appl. Surf. Sci., vol 197–198, 41–44, 2002.

[54] G. Raciukaitis, M. Brikas, P. Gecys, M. Gedvilas, “Accumulation effects in laser ablation of metals with high-repetition- rate lasers Gediminas”, Proc. of SPIE Vol. 7005, 2008.

[55] J. B. J. Savolainen, M. Snogdahl, C. Peter, “Ultra-short pulse laser ablation of metals : threshold fluence , incubation coefficient and ablation rates”, Appl Phys A, 97–101, 2010.

[56] P. T. Mannion, J. Magee, E. Coyne, G. M. O. Connor, T. J. Glynn, “The effect of damage accumulation behaviour on ablation thresholds and damage morphology in ultrafast laser micro-machining of common metals in air”, Applied Surface Science 233, vol 233, 275–287, 2004.

[57] F. Di Niso, C. Gaudiuso, T. Sibillano, F. Paolo, A. Ancona, P. M. Lugarà, “Role of heat accumulation on the incubation effect in multi-shot laser ablation of stainless steel at high repetition rates”, Optic Express, vol 22, no 10, 2230–2236, 2014.

[58] J. Bonse, S. Baudach, J. Krüger, W. Kautek, M. Lenzner, “Femtosecond laser ablation of silicon - modification thresholds and morphology”, Appl. Phys. A, vol 74, no 1, 19–25, 2002.

[59] C. S. R. Nathala, A. Ajami, W. Husinsky, B. Farooq, S. I. Kudryashov, A. Daskalova, I. Bliznakova, A. Assion, “Ultrashort laser pulse ablation of copper , silicon and gelatin : effect of the pulse duration on the ablation thresholds and the incubation coefficients”, Appl. Phys. A, vol 122, no 2, 1–8, 2016.

[60] S. Xiao, E. L. Gurevich, A. Ostendorf, “Incubation effect and its influence on laser patterning of ITO thin film”, Appl.Phys. A, 333–338, 2012.

[61] D. Ashkenasi, R. Stoian, A. Rosenfeld, “Single and multiple ultrashort laser pulse ablation threshold of Al2O3 (corundum) at different etch phases”, Applied Surface Science 154–155, 2000.

[62] D. Ashkenasi, M. Lorenz, R. Stoian, A. Rosenfeld, “Surface damage threshold and structuring of dielectrics using femtosecond laser pulses : the role of incubation”, Applied Surface

Science 150, 101–106, 1999.

[63] A. Rosenfeld, D. Ashkenasi, E. E. B. Campbell, M. Lorenz, R. Stoian, H. Varel, "MATERIAL PROCESSING WITH FEMTOSECOND LASER PULSES.

[64] M. Birnbaum, "Semiconductor Surface Damage Produced by Ruby Lasers", Journal of Applied Physics 36, 3688, 1965.

[65] J. Cui, A. Nogales, T. A. Ezquerra, E. Rebollar, "Influence of substrate and film thickness on polymer LIPSS formation", Appl. Surf. Sci., vol 394, 125–131, 2017.

[66] B. Tan, K. Venkatakrishnan, A femtosecond laser-induced periodical surface structure on crystalline silicon. J. Micromech.Microeng. 16, 1080–1085, 2006.

[67] T. J. Y. Derrien, R. Koter, J. Krüger, S. Höhm, A. Rosenfeld, J. Bonse, "Plasmonic formation mechanism of periodic 100-nm-structures upon femtosecond laser irradiation of silicon in water", J. Appl. Phys., vol 116, no 7, 2014.

[68] M. S. Trtica, B. M. Gakovic, B. B. Radak, D. Batani, T. Desai, M. Bussoli, "Periodic surface structures on crystalline silicon created by 532nm picosecond Nd:YAG laser pulses", Appl. Surf. Sci., vol 254, no 5, 1377–1381, Des 2007.

[69] T. T. D. Huynh, N. Semmar, "Dependence of ablation threshold and LIPSS formation on copper thin films by accumulative UV picosecond laser shots", Appl. Phys. A Mater. Sci. Process., vol 116, no 3, 1429–1435, 2014.

[70] S. I. Kudryashov, E. V. Golosov, A. A. Ionin, Y. R. Kolobov, A. E. Ligachev, L. V. Seleznev, D. V. Sinitsyn, A. R. Sharipov, "Nanostructuring of solid surfaces by femtosecond laser pulses", AIP Conf. Proc., vol 1278, no March 2017, 156–164, 2010.

[71] T. Tavera, N. Pérez, A. Rodríguez, P. Yurrita, S. M. Olaizola, E. Castaño, "Periodic patterning of silicon by direct nanosecond laser interference ablation", Appl. Surf. Sci., vol 258, no 3, 1175–1180, 2011.

[72] N. Destouches, N. Crespo-Monteiro, G. Vitrant, Y. Lefkir, S. Reynaud, T. Epicier, Y. Liu, F. Vocanson, F. Pigeon, "Self-organized growth of metallic nanoparticles in a thin film under homogeneous and continuous-wave light excitation", J. Mater. Chem. C, vol 2, no 31, 2014.

[73] S. K. Das, H. Messaoudi, A. Debroy, E. Mcglynn, R. Grunwald, "Multiphoton excitation of surface plasmon- polaritons and scaling of nanoripple formation in large bandgap materials", Opt. Mater. Express 3, 1705-1715, 2013.

[74] J. Bonse, A. Rosenfeld, J. Krüger, "On the role of surface plasmon polaritons in the formation of laser-induced periodic surface structures upon irradiation of silicon by femtosecond-laser pulses", J. Appl. Phys., vol 106, no 10, 2009.

[75] J. Bonse, J. Krüger, "Pulse number dependence of laser-induced periodic surface structures for femtosecond laser irradiation of silicon", J. Appl. Phys., vol 108, no 3, 2010.

[76] T. T. D. Huynh, A. Petit, N. Semmar, "Picosecond laser induced periodic surface structure on copper thin films", Applied Surface Science, vol 302, 109–113, 2014.

[77] A. Talbi, C. T. Tameko, A. Stolz, E. Millon, C. Boulmer-Leborgne, N. Semmar, "Nanostructuring of titanium oxide thin film by UV femtosecond laser beam: From one spot

to large surfaces", Appl. Surf. Sci., Volume 418, 425-429, 2017.

[78] H. Mei, C. Wang, J. Yao, Y. C. Chang, J. Cheng, Y. Zhu, S. Yin, C. Luo, "Development of novel flexible black silicon", Opt. Commun., vol 284, no 4, 1072–1075, 2011.

[79] A. Y. Vorobyev, C. Guo, "Direct femtosecond laser surface nano/microstructuring and its applications", Laser Photonics Rev., vol 7, no 3, 385–407, 2013.

[80] A. Serpenguzel, A. Kurt, I. Inanç, J. Carey, E. Mazur, "Luminescence of black silicon", J. Nanophotonics, vol 2, no 1, 2008.

[81] T. Sarnet, J. E. Carey, E. Mazur, "From black silicon to photovoltaic cells, using short pulse lasers", AIP Conf. Proc., vol 1464, 219–228, 2012.

[82] M. Halbwax, T. Sarnet, P. Delaporte, M. Sentis, H. Etienne, F. Torregrosa, V. Vervisch, I. Perichaud, S. Martinuzzi, "Micro and nano-structuration of silicon by femtosecond laser: Application to silicon photovoltaic cells fabrication", Thin Solid Films, vol 516, no 20, 6791–6795, 2008.

[83] O. Varlamova, F. Costache, M. Ratzke, J. Reif, "Control parameters in pattern formation upon femtosecond laser ablation", Appl. Surf. Sci., vol 253, no 19, 7932–7936, 2007.

[84] J. Bonse, J. Krüger, S. Höhm, A. Rosenfeld, "Femtosecond laser-induced periodic surface structures", J. Laser Appl., vol 24, no 4, 2012.

[85] J. Reif, F. Costache, O. Varlamova, G. Jia, M. Ratzke, "Self-organized regular surface patterning by pulsed laser ablation", Phys. Status Solidi Curr. Top. Solid State Phys., vol 6, no 3, 681–686, 2009.

[86] S. Gräf, F. A. Müller, "Polarisation-dependent generation of fs-laser induced periodic surface structures", Appl. Surf. Sci., vol 331, 150–155, 2015.

[87] E. L. Gurevich, S. V. Gurevich, "Laser Induced Periodic Surface Structures induced by surface plasmons coupled via roughness", Appl. Surf. Sci., vol 302, 118–123, 2014.

[88] J. F. Young, J. S. Preston, H. M. Van Driel, J. E. Sipe, "Laser induced periodic surface structure. II. Experimens on Ge, Si, Al and brass", Physical Review B, vol 27, no 2. 1155–1172, 1983.

[89] J. Bonse, A. Rosenfeld, J. Kruger, "On the role of surface plasmon polaritons in the formation of laser-induced periodic surface structures upon irradiation of silicon by femtosecond-laser pulses", J. Appl. Phys., vol 106, no 10, 2009.

[90] H. Sandra, S. V Kirner, A. Rosenfeld, "Laser-Induced Periodic Surface Structures — A Scientific Evergreen", IEEE JOURNAL OF SELECTED TOPICS IN QUANTUM ELECTRONICS, VOL. 23, NO. 3, 2017.

[91] E. L. Gurevich, "On the influence of surface plasmon-polariton waves on pattern formation upon laser ablation", in Applied Surface Science, vol 278, 52–56, 2013.

[92] V. I. Emel, "Mechanisms of the formation of low spatial frequency LIPSS on Ni / Ti reactive multilayers", J. Phys. D: Appl. Phys. 49 365103, 2016.

[93] O. Varlamova, Self-organized Surface Patterns Originating from Laser-Induced Instability.

thesis dissertation, Cottbus university, 2013.

[94] S. Yazidi, A. Fafin, S. Rousselet, F. Pailloux, S. Camelio, D. Babonneau, Structure and far-field optical properties of self-organized bimetallic Au_xAg_{1-x} nanoparticles embedded in alumina thin film, Phys. Status Solidi C 12, No. 12, 1344–1348, 2015.

[95] E. Rebollar, M. Castillejo, T. A. Ezquerra, "Laser induced periodic surface structures on polymer films : From fundamentals to applications", Eur. Polym. J., vol 73, 162–174, 2015.

[96] J. Reif, O. Varlamova, S. Uhlig, S. Varlamov, M. Bestehorn, "On the physics of self-organized nanostructure formation upon femtosecond laser ablation", Appl. Phys. A Mater. Sci. Process., vol 117, no 1, 179–184, 2014.

[97] O. Varlamova, J. Reif, S. Varlamov, M. Bestehorn, "Self-organized Surface Patterns Originating from Laser-Induced Instability", Nano-Optics and Nanophotonics, 3–30, 2015.

Chapter II: Ultrashort laser-matter interaction: case of picosecond laser beam

I. Introduction

Ultrashort laser-matter interaction has been extensively investigated in the last two decades, due to the high accuracy and precision on materials processing offered. The ultrashort pulse duration makes the investigation of fundamental physical phenomenon during laser radiation very complicated. For example, laser induced periodic surface structure formation mechanisms are not yet fully understood and the proposed approaches explaining these mechanisms are still under discussion. In this context, this chapter deals with a fundamental study of micro and nanostructures generation on mesoporous silicon surfaces under a picosecond regime. Because of the particular surface morphology of the target with nanosized pores and very low roughness, the use of picosecond laser beam as an intermediate time regime, the working under UV radiation and the very specific experimental conditions, original results are obtained that could be fruitful to help in understanding the physical mechanisms involved in surface structuring.

The following experiments have been carried out in two main regimes of laser dose (number of pulses N and beam fluence F (mJ/cm^2)) (Fig.II.1.):

- First regime corresponds to the generation of nanostructures where the fluence was limited to relatively very low values (few tens of mJ/cm^2) and the number N of pulses was increased to high values (several thousands).
- Second regime leading to the formation of microstructures where the fluence employed was in the range of ablation thresholds and N was limited to several hundred of pulses.

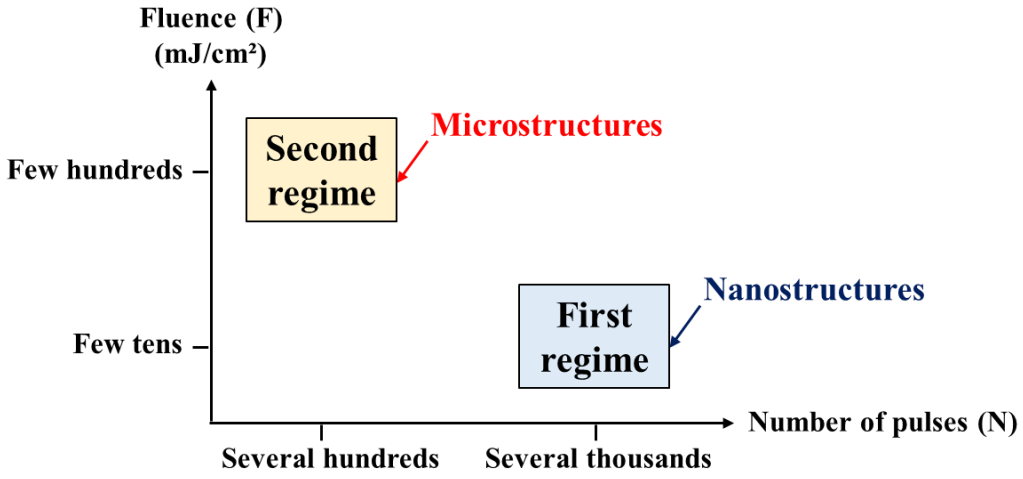

Figure.II.1. Schematic of experiments strategy.

II. Picosecond laser

	Nd:YAG Picosecond laser (GREMI)
Pulse duration	40 ps
Possible wavelengths	1064, 532 and 266 nm
Working wavelength used in this study	266 nm
Maximum frequency	10 Hz
Polarization	linear

Table.II.1. Characteristics of picosecond laser used in this chapter

A picosecond Nd:YAG laser irradiating at fundamental wavelength of 1064 nm with a pulse duration close to 40 ps is employed in this investigation (its main features are summarized in table.III.1). After passing through an automated shutter, the laser beam is perpendicular to the sample and focused into a circular spot of 600 µm diameter by a plan-convex lens (75 mm focal length) as shown in fig.II.2.

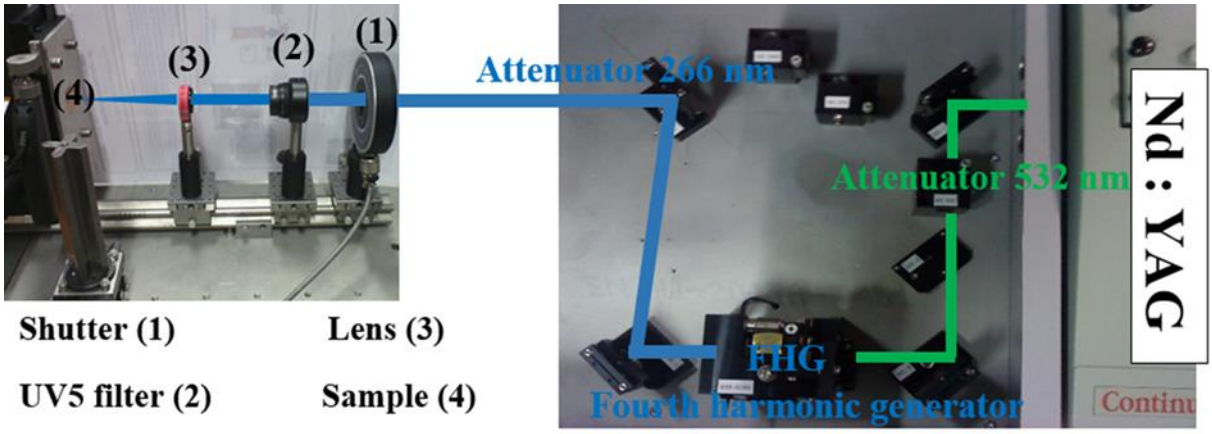

Figure.II.2. Schematic view of the experimental set up: left) focusing of the laser beam on the sample, a UV5 filter is used to cut the residual 532nm wavelength emission; right) 266 nm ps Nd: YAG laser beamforming.

The determination of laser spot size is ideally performed according to Liu's method [1] which is demonstrated in chapter III. However, to employ this method, the laser beam must exhibit a good Gaussian distribution and a high energy stability (pulse to pulse energy) which is not the case for our picosecond laser as shown in fig.II.3, which demonstrate a huge fluctuation of pulse energy between 28 and 50 mJ for an average energy of 42 mJ (energies measured @ 532 nm). Thus the spot diameter value given above is determined through a direct estimation from SEM images.

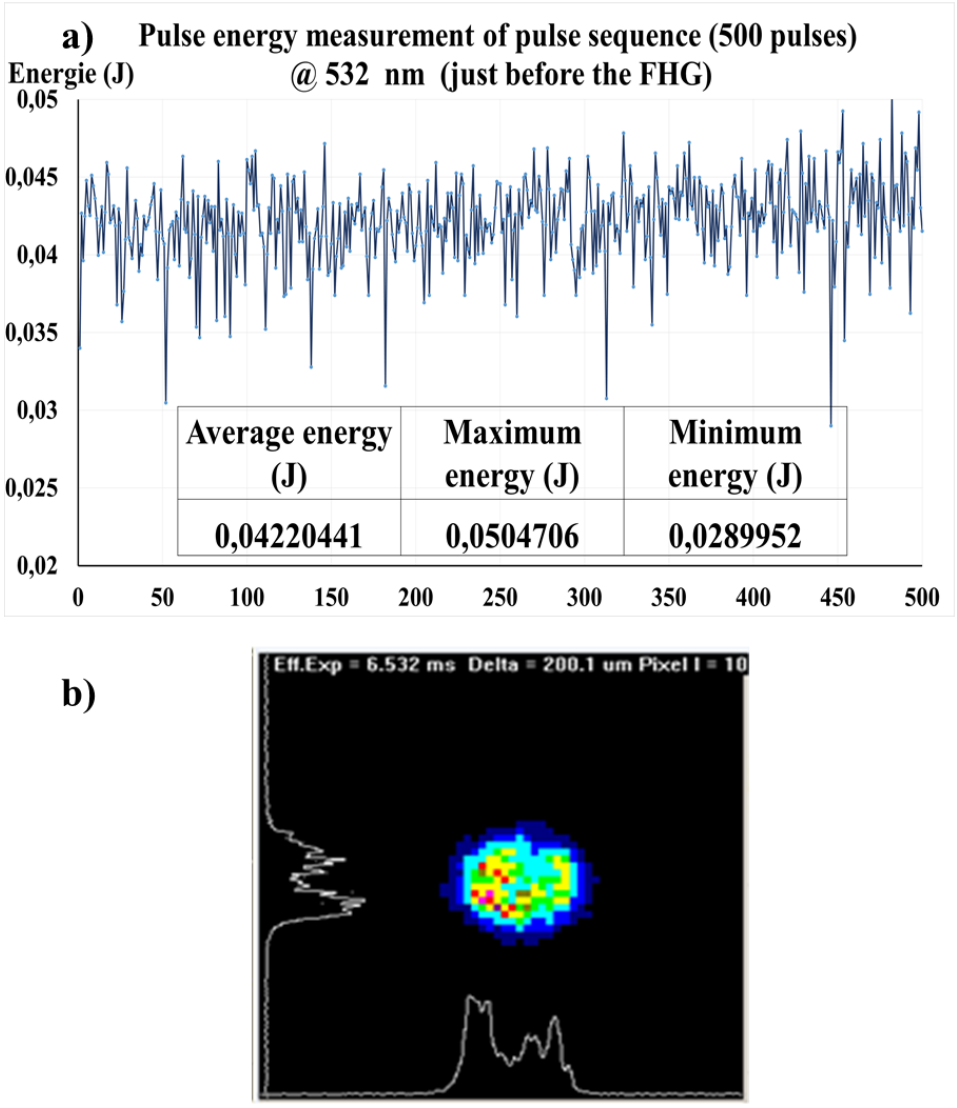

Figure.II.3. a) fluctuation of pulse energy of ps laser beam measured by powermeter @ 532 nm, b) Spatial distribution of ps laser beam characterized by WinCam D camera.

III.Elaboration of mesoporous silicon (MeP-Si) samples

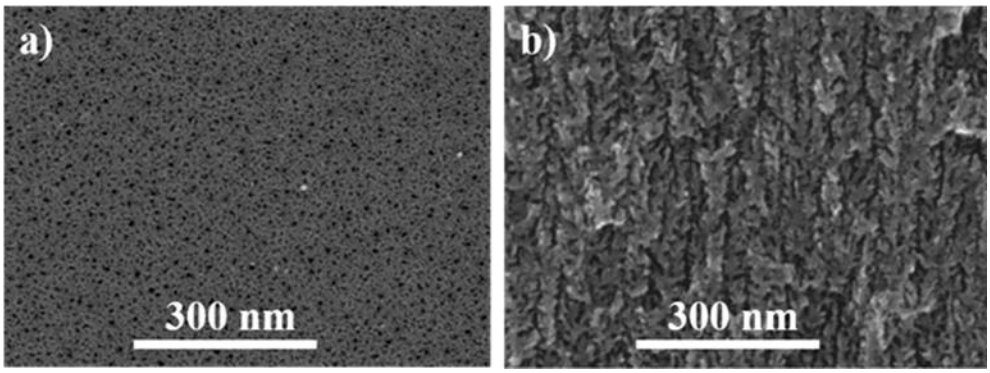

Figure.II.4. SEM views of MeP-Si, a) surface morphology, b) cross-section morphology.

MeP-Si substrates were provided by SiLiMiXT Company and fabricated via electrochemical etching process on 500 µm thick p-type silicon wafers <100>. Electrical resistivity is in the range of 10-20

mΩcm, with a porosity of about 40%, pore size in the range of 1-10 nm and a porous thickness close to 50 µm. Scanning Electron Microscopy (SEM) view of p-type MeP-Si surface morphology is presented in Fig.II.4. The principle of the etching process is based on electrochemical corrosion of silicon wafer in presence of an electrolyte solution containing hydrofluoric acid (HF). Electrochemical reactions remove the silicon in form of SiF_6^{-2} yielding to pore formation (experiment setup is illustrated in Fig.II.5.)[2]. The optimizing of pore size, distribution, porosity and thickness is possible through varying the process parameters (electrolyte solution (HF concentration), current intensity and time process).

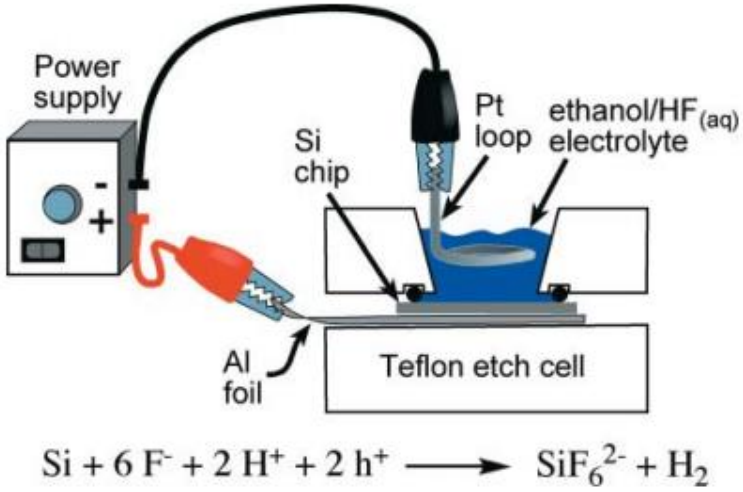

Figure.II.5. Illustration of experimental setup used for fabrication of MeP-Si from Si wafers via electrochemical etching [2]**.**

IV. Laser Induced Periodic Surface Structures on MeP-Si surfaces

As widely reported in the literature, the LIPSS generation is strongly depending on the laser dose which is a combination of beam fluence F and number of pulses N. Thus, in this paragraph the effect of these parameters is investigated.

1. Effect of laser beam fluence

The laser fluence, or so called energy density, refers to the amount of laser energy received by the treated area (laser spot). Thus, the variation of fluence could be conducted through either the variation of beam energy at unvaried spot size or the variation of laser spot size at constant energy by changing the distance lens-target. The dependence between the fluence threshold (ablation and induced damage) and the laser spot size on different materials by nanosecond [3] and femtosecond [4][5] irradiations, and in either case, it has been found that threshold fluence decreases as the laser spot increases. Similar behavior can be expected when using picosecond laser since its pulse duration ranging within nanosecond and femtosecond time scale. In this present work, the spot size was fixed

to 600 µm in diameter in all experiments in order to avoid the direct dependence of ablation threshold with spot size.

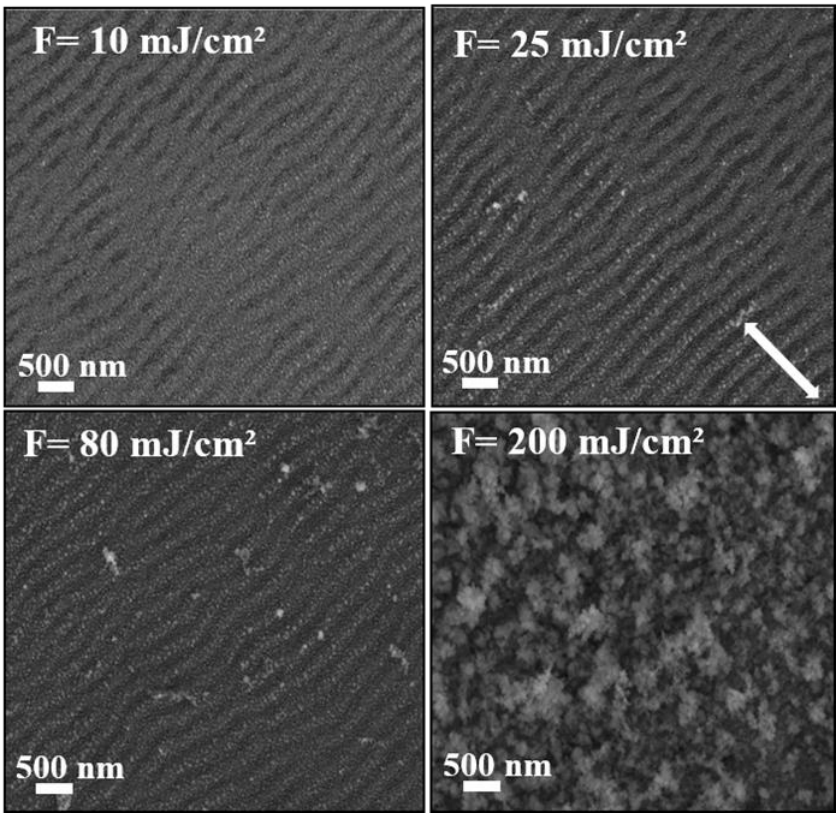

Figure.II.6. SEM views of MeP-Si surfaces irradiated by different laser fluences (F = 10 to 200 mJ/cm²) and for N = 3000 for laser spot of 600 µm in diameter.

Fig.II.6. displays the MeP-Si surface morphologies after irradiation by a picosecond laser beam at a fixed pulse number of 3000 and for fluences varying from 10 to 200 mJ/cm². For relatively low fluence ranging in 10 to 25 mJ/cm², LIPSS with a period close to 266 nm and with a perpendicular orientation to the laser beam polarization are produced. An enhancement of the SEM image contrast could be noticed when F is increased from 10 to 25 mJ/cm² which may imply the formation of deeper LIPSS with increasing F. For F close to 80 mJ/cm², similar LIPSS organization could still be observed. However, the presence of several impurities on the MeP-Si surface as removal features and clusters could be obviously noticed that may refer to the initiation of removal material process (ablation mechanism) at this fluence. Finally at high fluence of 200 mJ/cm², the smooth mirror surface of MeP-Si is transformed into a pretty rough surface covered by a tremendous amount of redeposited material formed through a strong ablation process that starts at 80 mJ/cm² and increases drastically when F reaches 200 mJ/cm² by increasing N to 3000. Therefore, the fluence required for clean LSFL formation on MeP-Si at 3000 pulses, without inducing a surface damage, is about 25

mJ/cm² which seems to be relatively very low in comparison with the values reported in literature (ranging in 100-500 mJ/cm²) with semi-conductors target especially silicon [6][7][8].

Because the non-existence of data about ablation and LIPSS formation of MeP-Si in literature and since the electrical properties of MeP-Si are very similar to those of Si (semi-conductor behavior) [9], a comparative investigation between MeP-Si and Si seems to be essential to better understand the physical phenomenon leading to the LIPSS formation.

It is found in several studies that when silicon target is irradiated by IR femtosecond laser, LSFL are generally formed for laser fluence in the range of 120 to 520 mJ/cm² depending on the number of pulses [10][7][8][11][12]. Indeed, to observe LIPSS generation after a single pulse or few laser pulses, the fluence employed has to be slightly above the single pulse ablation threshold fluence (500 mJ/cm²). In contrast, other studies have shown the possibility of LSFL formation at limited laser fluence (~100 mJ/cm²) obviously below the single-pulse ablation threshold by increasing the laser dose through cumulative amount of number of pulses. In other words, the LIPSS formation and ablation threshold fluences are reduced by increasing the number of pulses. This phenomenon was explained in literature by the accumulation effect or incubation effect [12][13] (for more details see chapter I).

Despite the availability of numerous studies on the LIPSS formation on silicon surface under IR irradiations, there is only few papers published on the same topic but under UV irradiations. An important reduction of the threshold fluence under UV has been noticed. S. Hohm et al [14], have reported a reduction of ablation threshold fluence of silicon from 120 to 80 mJ/cm² for wavelengths of 800 and 400 nm respectively. A.A. Ionin et al [15], have shown that LSFL-formation threshold fluence decreases from 240 to 60 mJ/cm² when the working wavelength changes from 744 to 248 nm. Also, it appears that the incubation coefficient S depends on the wavelength: S decreases from 0.86 (wavelength 744 nm) to 0.76 (wavelength 248nm). The reduction of LIPSS threshold fluence under UV can be explained by the enhancement of the photon absorption process, which yields to a strong excitations of electrons. This is clearly achieved by the huge enhancement of absorption coefficient (α) in the UV range ($\alpha = 1.84.10^6$ cm^{-1} at 250 nm compared to $1.3.10^3$ cm^{-1} at 750 nm) [16].

Thus, the LIPSS formation on MeP-Si at low fluence values (25 mJ/cm²) could be attributed to UV photons absorption and the ‘primordial’ role of incubation effect (over 3000 pulses).

2. Effect of laser pulse number

As mentioned in the previous paragraph, a 'strong' ablation process of MeP-Si started for F > 80 mJ/cm². Thus, in order to avoid this phenomenon, all the next experiments are conducted within the (10 – 25 mJ/cm^2) fluence range.

2.1. LIPSS evolution

The laser fluence is limited to 20 mJ/cm². Fig.II.7 shows the evolution of MeP-Si surfaces with increasing values of N. After 100 or 250 pulses, a random distribution of nanoparticles is unexpectedly generated under uncontrolled atmosphere (ambient air). For N = 500, unclear quasi-periodic patterns oriented horizontally could be observed. These structures are probably formed through the organization of nanoparticles and/or the modulation of surface. As increasing N up to 1000 - 3000, agglomeration and/or coalescence of nanoparticle processes yield to the generation of clearer LIPSS organization, maybe deeper but with many shortcuts and bifurcations as seen in fig.II.6. Lastly, for a larger number of pulses N=12000, very clear LIPSS organization is observed with a period roughly equal to the beam wavelength (266 nm) with perpendicular orientation to the beam polarization typically low spatial frequency LIPSS (LSFL). Fig.II.8. presents the high magnified SEM views of MeP-Si surface after 12000 pulses. These images show the organization and agglomeration of nanoparticles along regular lines leading to the formation of NPs based LSFL. Between these NPs lines the initial mesoporous silicon morphology appears very clean and smooth, as it has not been irradiated. This suggests the key role played by the NPs played in the formation of these LSFL whereas MeP-Si stays as received.

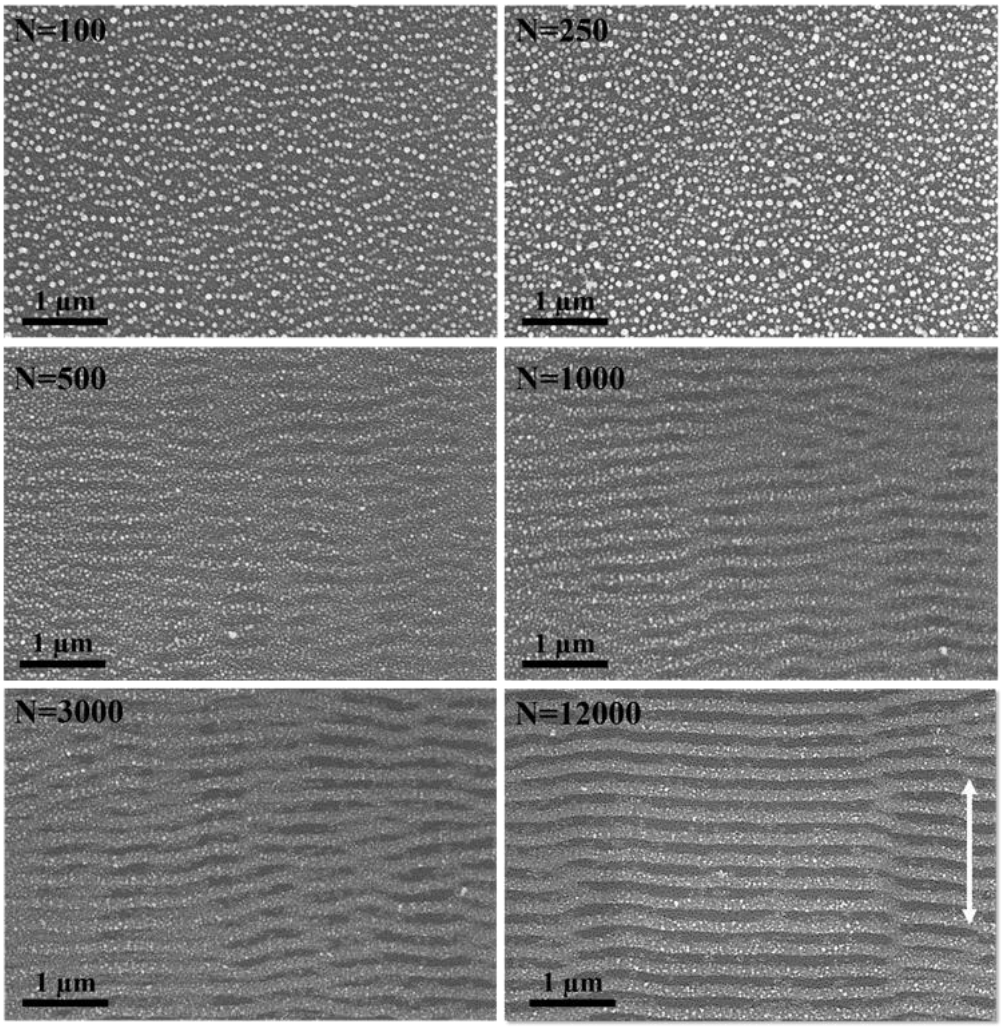

Figure.II.7. SEM images of the evolution of surface morphologies with increasing N at fixed F=20mJ/cm²

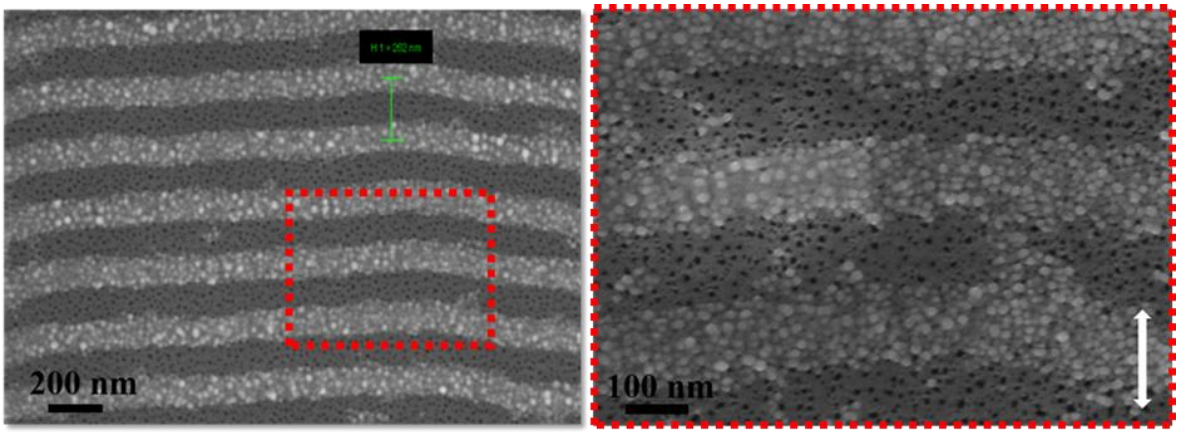

Figure.II.8. SEM high-magnified images of LIPSS obtained at 20 mJ/cm² and 12000 shots @ 266 nm ps.

The observed LIPSS on silicon surface appeared as periodic reliefs and valleys or surface modulation. In addition, it is widely accepted that these nanostructures are produced due to the interferences generated between the incident beam and the light scattered from the surface resulting

in inhomogeneous energy deposition leading to material ablation at non uniform depth [17]. However, J. D. Fowlkes *et al*[18], have shown the possibility to form "exotic LIPSS" on silicon surface by ordering nanoparticles formed under special conditions that are very similar to those used to grow nanoparticles by pulsed-laser deposition (PLD) as described in [18] with a UV-nanosecond laser (25 ns laser pulse at 248 nm), fluences ranging in 1000 to 3000 mJ/cm² and under controlled environment (SF_6 and He). Two ablation steps are used. Firstly, the silicon target is irradiated by 1500 laser pulses at 3 J/cm² under controlled environment of ~ 510^5 Pa of SF_6, and microstructures such as cone/hole are obtained. This step is followed by 200 laser pulses at 1000 mJ/cm² in ~ 70 Pa of He inducing the ordered nanoparticles as shown in fig.II.9. It has been also shown that silicon surface irradiated by 1000 pulses at a fluence lower than 1 J/cm², presents NPs (30 - 40 nm in diameter) aggregated randomly in curvilinear strings only under He background pressure of 10 to 10^4 Pa. Otherwise, when employing the same fluence under vacuum, no NPs are formed. This indicated the important role of background pressure in these nanoparticles formation in such conditions. Fig.II.9. shows an example of NP ordering morphologies obtained by J. D. Fowlkes et al on Si surface [18].

This question on the origin of nanoparticles based LIPSS formation on MeP-Si is discussed in the present work. The formation of nanoparticles and LIPSS, may be due to the special experimental conditions (low fluence, high number of pulse working under air ambient) or due to the intrinsic properties of MeP-Si. Then it has been decided to irradiate a silicon target in similar conditions than the MeP-Si to compare the surface modifications.

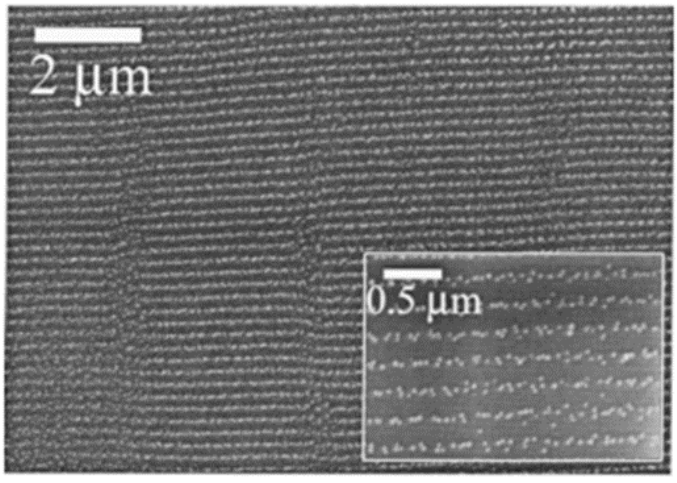

Figure.II.9. SEM views of long range nanoparticle ordering on Si surface irradiated in 5 10^5 Pa of SF_6 by nanosecond laser [18].

Fig.II.10. illustrates the surface morphologies of crystallized silicon irradiated under the same conditions than those applied for MeP-Si (picosecond @ 266 nm and F = 20 mJ/cm²). The results show the LSFL generation on Si surface with a period close to the beam wavelength and an orientation perpendicular to the beam polarization. These LSFL are formed like modulated surface or periodic reliefs and valleys as widely observed in literature [6][19]. Furthermore the Si surface appeared very clean and smooth without the formation of any tiny nanoparticles or impurities as a result of ablation or evaporation process. This means that despite the formation of LIPSS organization on Si and MeP-Si surfaces under similar experimental conditions, the physical mechanisms occurred are very different. Although, silicon and mesoporous silicon have approximatively the same electronic properties (electrical conductivity and band gap), their surface responses under laser irradiation in similar conditions are very different. This difference could be explained on the one hand by the particular morphology of mesoporous silicon (presence of nanopores distribution) and on the other hand by its relatively very low thermal conductivity which is 10 to 20 times lower than for silicon [20].

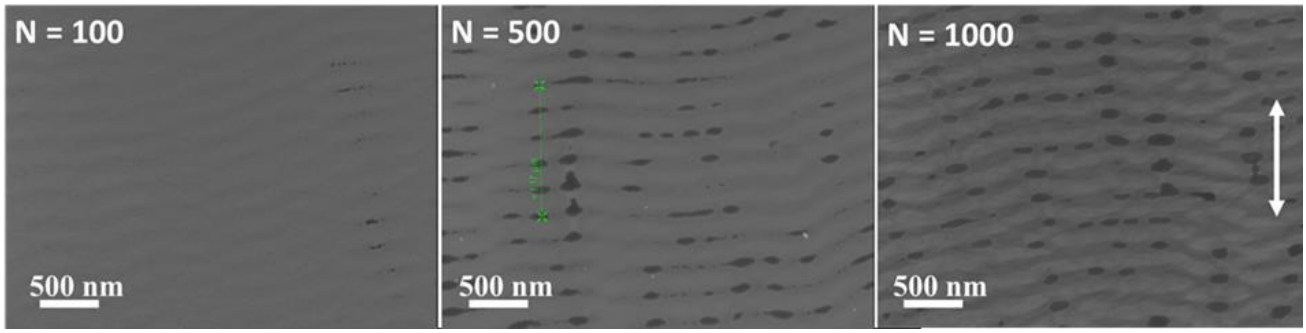

Figure.II.10. SEM views of silicon surfaces irradiated by picosecond beam at 20 mJ/cm² @ 266 nm for 3 different N values of laser shots.

The formation of LSFL on silicon surface at this low fluence (20 mJ/cm²) seems to be in good agreement with the work of A.A. Ionin et al [15], estimating a LSFL threshold around 60 mJ/cm² for a single pulse becoming to respectively ~ 15 mJ/cm² and 2 mJ/cm² after 100 and 1000 pulses (for spot diameter of 370 µm). The comparison of our experimental results with the literature confirms that the LIPSS threshold fluence can be reduced by working in UV wavelength range (which leads to an improvement of the absorption coefficient), increasing the number of pulses (resulting to an incubation effect) and employing a large spot sizes. The decreasing of F_{th} as N and ω (beam spot radius) increased has been recently evidenced by A. Naghilou *et al*[5]. They have shown the strong dependence between F_{th}, N and ω on polystyrene sample irradiated 30 fs laser beam @ 790 nm (see Fig.II.11.).

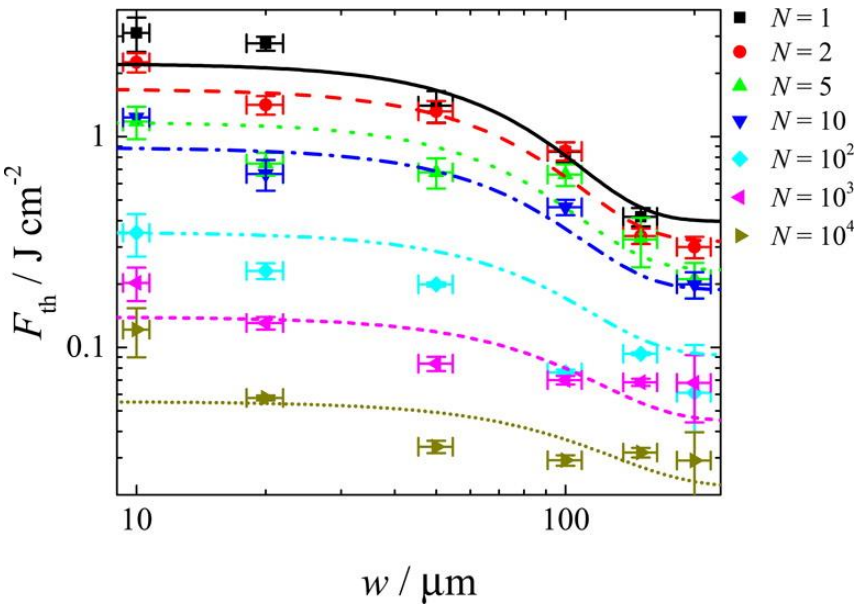

Figure.II.11. F_{th} evolution as function of N and ω (waist radius) of polystyrene sample under fs radiation @ 790 nm [5].

2.2. Nanoparticles generation and evolution

For better understanding of the mechanisms leading to the nanoparticle generation on the MeP-Si and the evolution of the nanoparticle size with number of shots. ImageJ Software was used for SEM images treatment in order to determine the NPs size.

Fig.II.12. displays the SEM images of NPs generated on MeP-Si after treatment by ImageJ. For N = 100 - 250, the NPs are formed with a typical diameter of 55 nm. After 500 pulses, the NPs typical diameter decreases to 33 nm. For N > 500, the ImageJ processing of SEM images (magnification of 20000) is not as easy as coalescence and agglomeration processes seem to be initiated then distinct NPs cannot be visible anymore. For N = 12000 pulses, a SEM image (with 100000 of magnification) has been successfully treated showing NPs with a typical diameter of 15nm (Fig.II.13.).

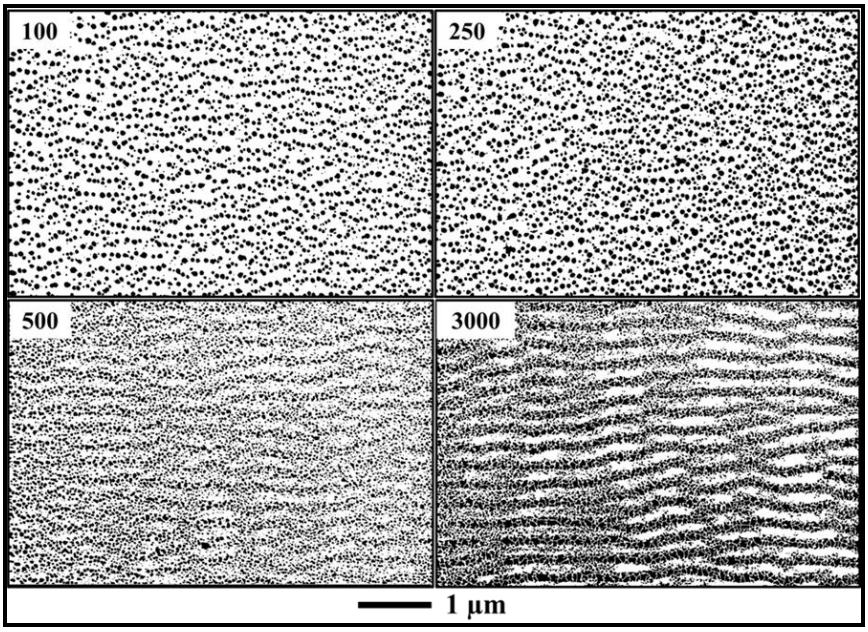

Figure.II.12. SEM images of MeP-Si treated by ImageJ for different values of N (100, 250, 500, and 3000).

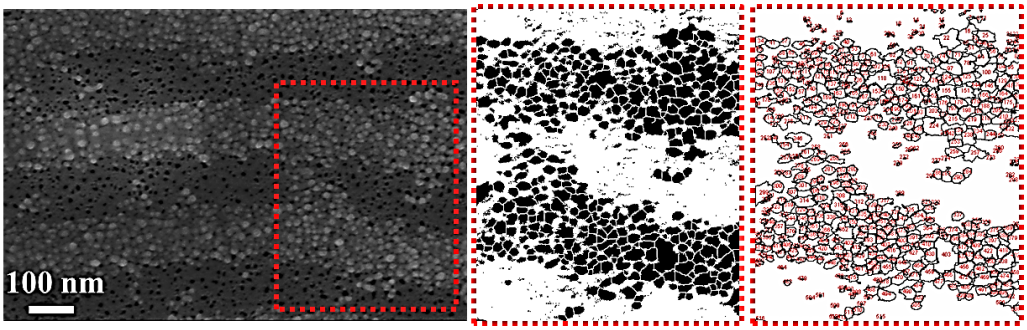

Figure.II.13. SEM image of NPs based LSFL treated by ImageJ for N=12000.

Ultrashort laser ablation, offers a great control of NPs size distribution and chemical composition with optimized laser parameters and good environment (liquid solution, gas) [21]. The main mechanisms potentially responsible of ablation process are the Coulomb explosion, phase explosion, mechanical fragmentation and thermal vaporization-condensation [21][22][23] In this present work, MeP-Si is irradiated by a 266 nm picosecond laser. The laser energy (photons) is first absorbed by electrons in the valence band therefore directly excited to the conduction band (direct band gap of silicon = 3.43 eV corresponding to 362 nm wavelength). Then, free electrons win energy by successive photon absorption and relax their energy to the lattice through electron-lattice coupling [24]. This yields to the lattice heating within 1 ps [25]. The resulting heating leads to high temperatures that may reach the evaporation point. Then, NPs can form through condensation from the vapor phase [26][27][28]. These processes occur at relatively low laser dose (20 mJ/cm^2) called "soft" or "gentle" ablation process. Indeed, in these conditions, no clusters or impurities are observed (that would be the signature of a strong ablation process). After, the formation of thin film of NPs

(55 nm diameter) on MeP-Si surface, NPs are submitted to laser irradiation by the increase of the number of pulses. NPs are supposed to undergo the same physical mechanisms than melting and evaporation that lead to decrease their size to 33 and 15 nm diameter after respectively 500 and 12000 laser pulses.

Despite MeP-Si is fabricated from electrochemical etching of Si wafers, the presence nanopores, hydrogen and oxygen bonding (Si-H, Si-H_2 and Si-O_2) formed on the MeP-Si after the etching process that can yield to a high UV photons absorption and a decreasing of thermal conductivity[20], may explain the huge difference noticed between the behavior of MeP-Si and Si irradiated in similar conditions.

2.3. Formation mechanisms of LIPSS

In order to determine the average amplitude and period of obtained NPs-based LIPSS above the surface at 20 mJ/cm² and after 12000 pulses, AFM characterization were performed and results are shown in Fig.II.14. The profile obtained reveals an average period of 255 nm (close to the working wavelength of 266 nm) and an average amplitude close to 54 nm.

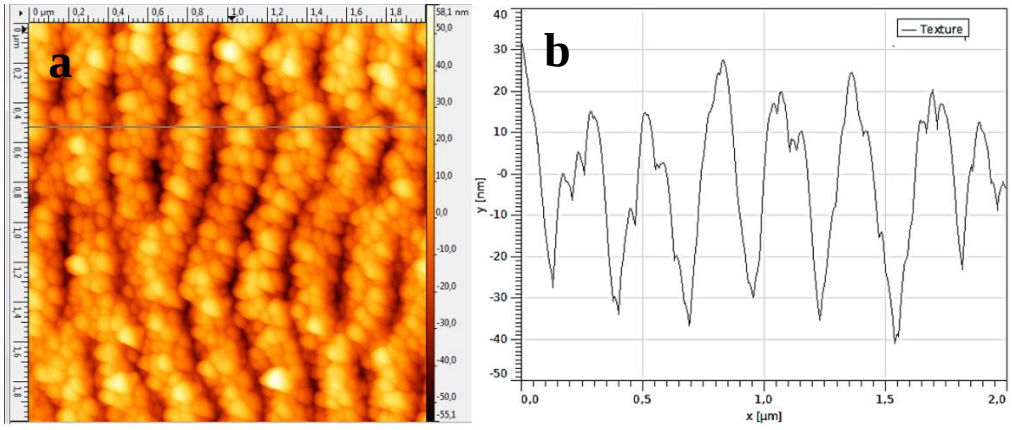

Figure.II.14. (a) AFM image of LIPSS formed on the MeP-Si surface after 12000 laser pulses at 20 mJ/cm² and (b) the profile analysis of LIPSS height and period measured with AFM.

Regarding the previous results showing a uniform and clear NPs-based LSFL obtained at 20 mJ/cm^2 for 12000 pulses, it can be supposed that NPs formation process is due to a surface modulation phenomenon including NPs or just a NPs agglomeration arranged in well-defined lines without surface modulation (Fig.II.15).

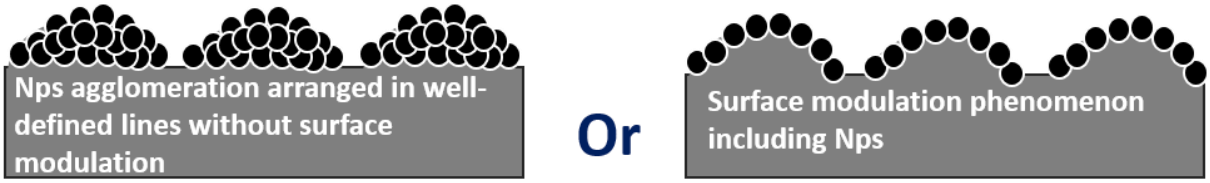

Figure.II.15. Schematics of (left) NPs agglomeration arranged in well-defined lines without surface modulation, and (right) surface modulation phenomenon including NPs.

To help the understanding, SEM characterizations of the LIPSS cross section obtained for 20 mJ/cm² and 12000 pulses were performed. Fig.II.16. shows the SEM cross-section images at different magnifications. Image (a) presents a periodic nanostructure (period close to 247 nm) that is very similar to the average period measured by AFM (Fig.II.14.b). The width of these LIPSS is about 120 nm and their amplitude (defined as the height above of MeP-Si surface) is about 54 nm, close to the value measured by AFM. Images in Fig.III.16. show that no pore could be observed below the formed LIPSS while the pores located between two ripples are still open as previously seen in fig.II.8. This result implies the formation of a localized molten phase filling the pores in 100 nm depth below the formed LIPSS.

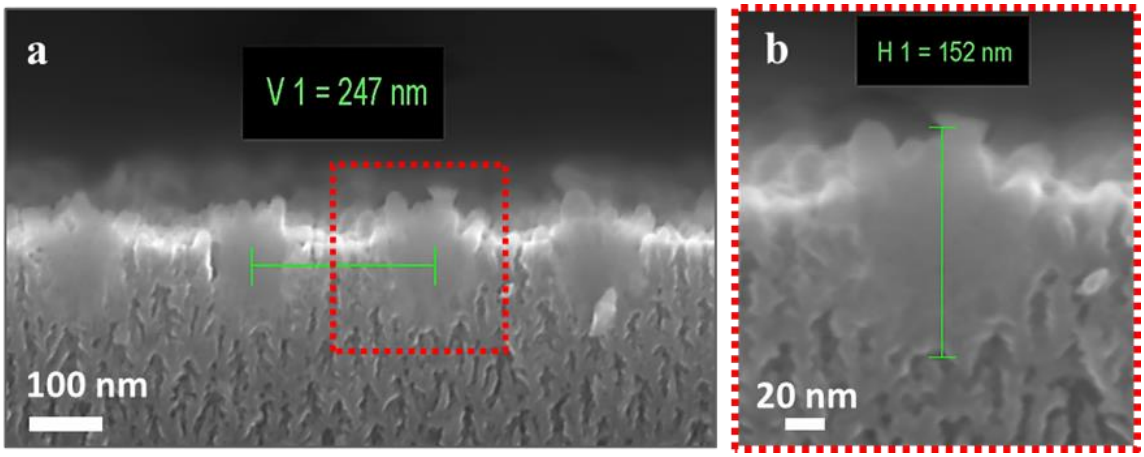

Figure.II.16. LIPSS SEM cross-section views formed at 20 mJ/cm² after 12000 pulses.

Regarding these experimental observations, LIPSS formation mechanism may be attributed to the interference model assuming that LIPSS formed as result of non-uniform laser energy deposition. In fact, pulse after pulse the non-uniform laser energy deposition, interacting with MeP-Si surface, leads to form localized regions with melting. Therefore two hypothesis can be proposed:

(a) The regions where NPs are agglomerated and molten phase is produced, are the regions that have received the higher amount of laser energy (Fig.II.17.).

(b) The regions localized between the LIPSS are those that received the higher amount of energy (Fig.II.18.).

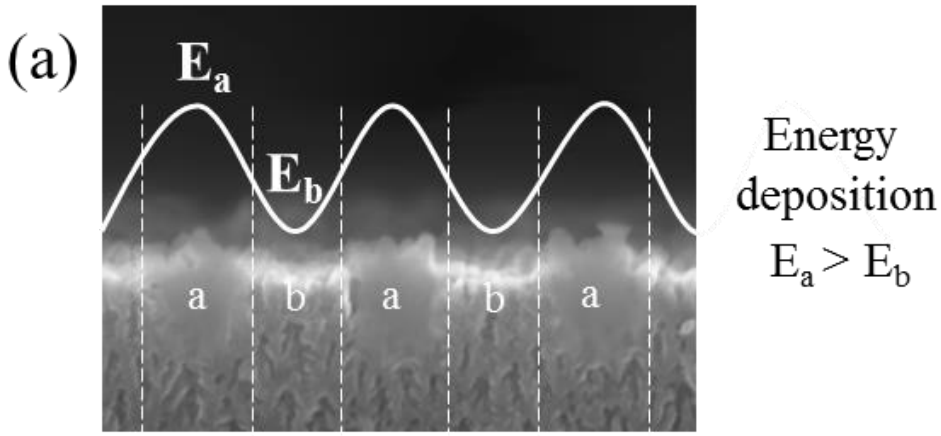

Figure.II.17. Illustration of hypothesis (a) proposed to explain the LIPSS formation mechanisms.

The first hypothesis supposes that the formed LIPSS regions correspond to the hot local regions (identified as (a) regions in fig.II.17) receiving the higher amount of energy (E_a). This induces a melting process in those regions. In contrast, the regions located between LIPSS (identified as (b) regions in fig.II.17) have received a limited amount of energy (E_b) which was not enough to trigger the melting process. However, this hypothesis seems to be in contradiction with Marangoni convection and thermal capillarity processes, assuming that molten phase moves from the hot regions towards colder ones. Moreover, these effects are probably contributed to organize the NPs generated randomly on the surface of MeP-Si (after 250 pulses) into well-defined NPs agglomerations by moving them from hot regions to cold ones. For these reasons, this hypothesis seems to be not compatible with the physical mechanisms.

The second hypothesis supposes that regions located between LIPSS ((a) regions in fig.II.18) have received the higher amount of energy E_a (Fig.II.18.). This can yield to two other scenarios as following:

- ✓ (b-1) The higher energy E_a leads to the formation and then the redistribution of molten material toward the cold regions (b) in parallel of NPs organization. This supposes that molten material moves from (a) regions to fill the nanopores of (b) regions. However, this is far from happening because the presence of NPs agglomeration covering the (b) regions and the very small size of pores (1-10 nm).
- ✓ (b-2) Because (b) regions are considered as the cold regions that receive the low amount of energy (E_b), the NPs move from (a) regions to them (Marangoni and thermal capillarity effects). Pulse by pulse, the heat accumulates and thus yields to a melting process confined in

(b) regions. However, due to the relatively high energy deposited in (a) regions, ablation, and NPs generation evaporation processes can occur. According to our experimental observations, this is the most likely hypothesis to happen.

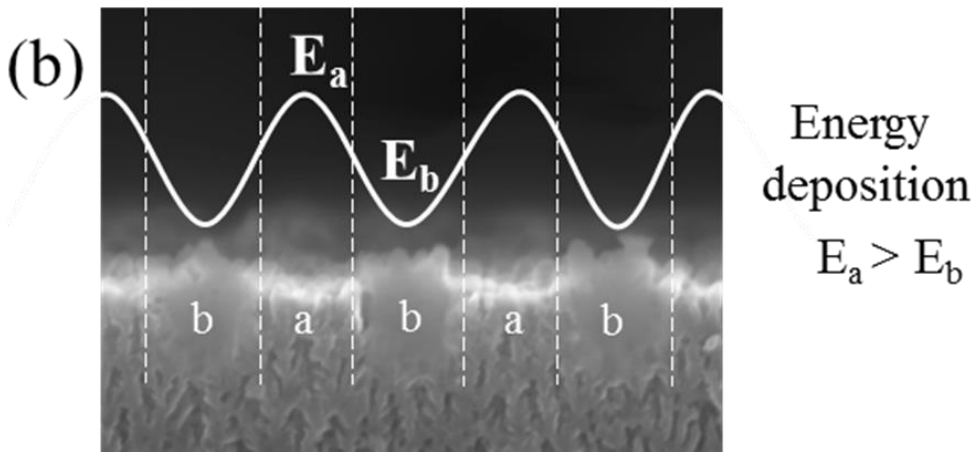

Figure.II.18. Illustration of hypothesis (b) proposed to explain the LIPSS formation mechanisms.

The formation of the molten phase during short and ultra-short irradiation has been studied using pump-probe method and transmission electron microscopy [29][25]. During ultra-fast irradiation of semiconductors, the laser energy generates free electrons via different mechanisms of absorption such linear or multiphoton absorption (as detailed in the first chapter) depending on the gap energy value, the beam wavelength (incident photon energy), the pulse duration and the laser fluence. As a result of this electronic excitation, several physical mechanisms can take place such as, strong non-equilibrium between electrons and lattice subsystems and ultrafast melting, electron-lattice temperature relaxation and thermal melting [24]. In literature, the solid-liquid transformation generally occurs for a large amount of energy. The formation of LSFL and molten phase at such low fluence (20 mJ/cm²) may be possible by increasing the laser dose that means by incubation effect. Even if the fluence is too low for melting, evaporation or ablation (below the single pulse threshold), some chemical and structural defects are induced inside the material. The accumulation of these defects by the next coming pulses, facilitates the melting of material (for more details see chapter 1) [13].

It is widely accepted that the non-thermal effects, such as non-thermal melting and non-thermal ablation, take place during ultra-fast laser irradiation with a pulse duration shorter than 10 ps (thermalization time) while thermal effects are observed with laser pulses larger than 10 ps in the case of silicon based material. In addition, Liquid phase is obtained by thermal process. Therefore, the melted material formed below the LIPSS by using 40 ps laser is produced through a typical thermal melting process. It should be pointed out that the relatively low thermal conductivity of

MeP-Si can contribute to confine the laser heating into these localized regions (the thermal heated zone of MeP-Si irradiated by single ps laser pulse is estimated to be ~ 16 nm).

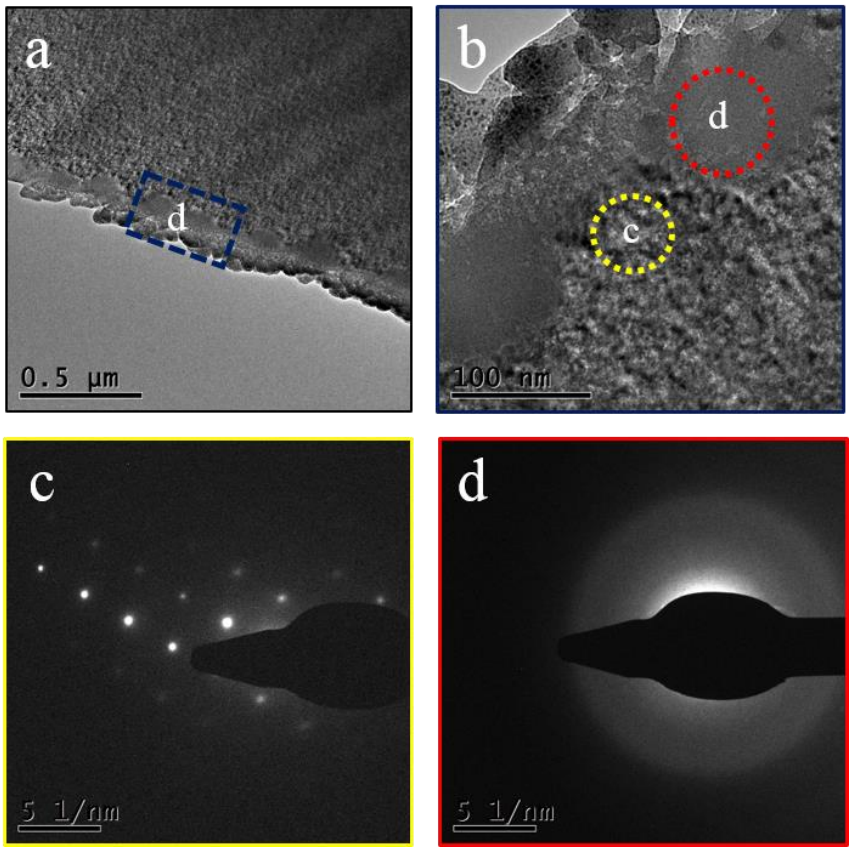

Figure.II.19. TEM analyses of LSFL formed by 266 nm ps irradiation at 20mJ/cm² and after 12000 pulses.

After laser irradiation and lattice heating and melting, the molten material is fastly cooled in the nanosecond timescale through thermal conduction into the cold bulk. J. Jia et al, propose a cooling rate as high as 10^{13} - 10^{15}K/s [30] . As a result of melting, resolidification and due to the high cooling rate, some phase transformations such as amorphization or recrystallization of material could take place [31][32]. In this present study, TEM analyses reported in fig.II.19. indicate that picosecond laser irradiations induce a localized phase transformation from crystalline to amorphous phase inside and below the LSFL as shown in diffraction micrograph presenting only a hallow and no diffraction rings (fig.II.19.d) while the mesoporous silicon between the LIPSS stays crystallized as shown in fig.II.19.c which displays the presence of spotlights as signature of crystallized phase. This change from crystalline to amorphous phase implies a severe undercooling of molten phase due to a high cooling rate [33].

To resume this part, a scenario based on experimental observations is proposed in four steps as shown in Fig.II.20.

For UV ps irradiation of MeP-Si at low fluence (20 mJ/cm²).

(1): Random generation of NPs after relatively low number of pulses,

(2): Organization of NPs to form regular LSFL,

(3): NPs and MeP-Si keep receiving the laser energy leading to introduce a localized melting below the LIPSS,

(4): Melting depth increases versus the number of shots to form tubular periodic amorphous phase (100 nm in depth).

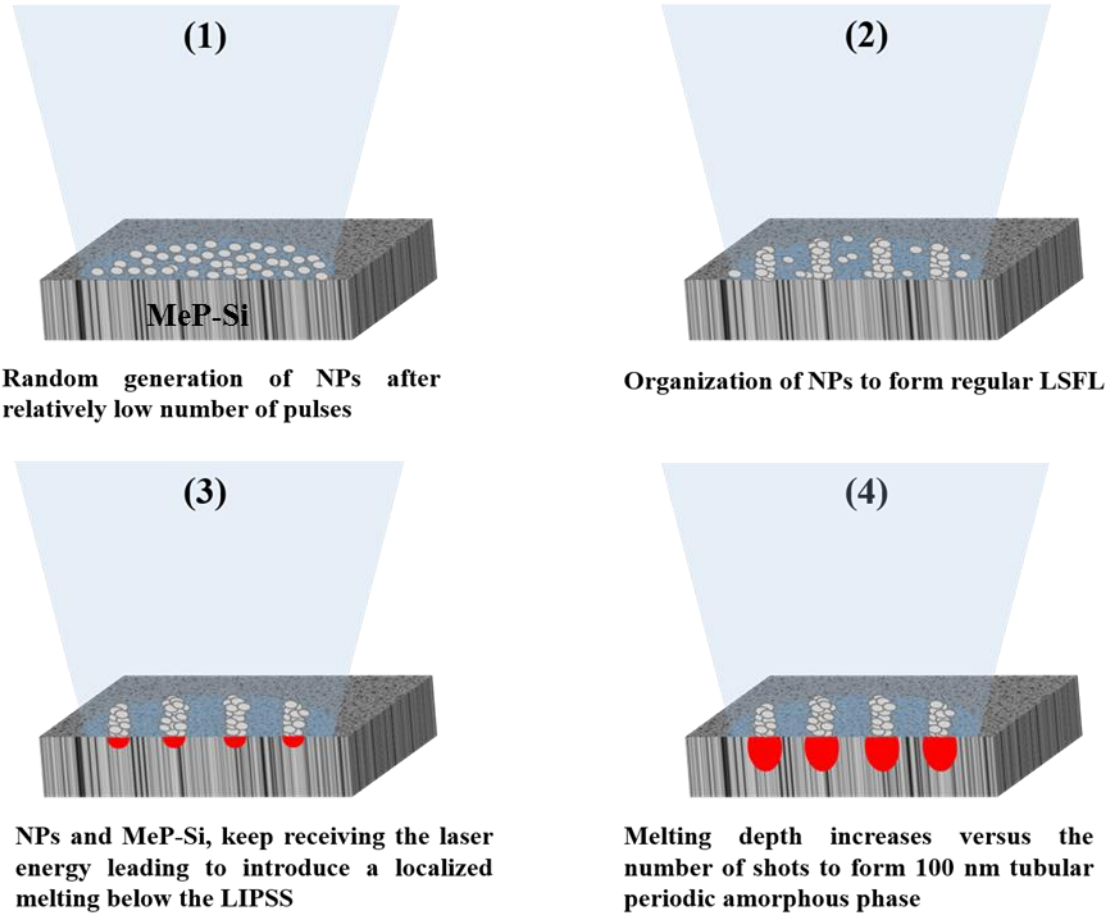

Figure.II.20. Proposed scheme of LIPSS formation (on MeP-Si by 266 nm 40ps laser) scenario based on experimental observations.

V. Microstructure formation on MeP-Si (50 µm)/Si

As shown in the first part of this chapter, by irradiating the MeP-Si by 266 nm ps laser at 20 mJ/cm², NPs formation through soft ablation process is achieved after few hundred of pulses. Then, a LSFL formation and the apparition of a molten phase have been observed after 12000 pulses. In the second part of this chapter, a different kind of structure formation is investigated by using the same picosecond laser but under very different experimental conditions as relatively high fluence (few hundred of mJ/cm²), resulting in the formation of quasi-periodic micro-spikes on MeP-Si and Si.

1. Strong ablation process on MeP-Si (50 µm)/Si

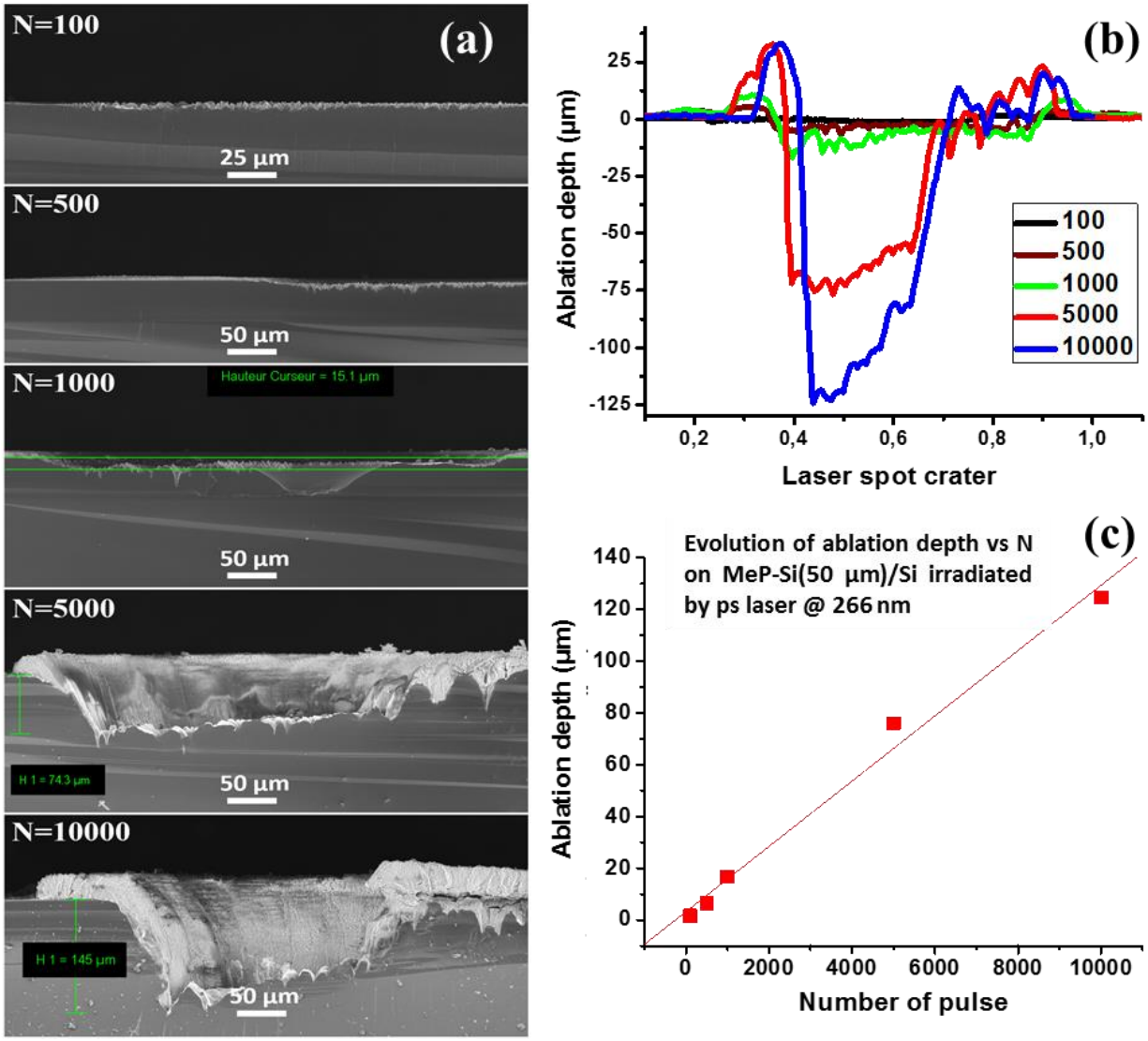

Figure.II.21. (a) SEM cross sectional images of MeP-Si (50 µm)/Si irradiated by 266 nm ps laser at 400 mJ/cm² for N varied from 100 to 10000. (b) The laser spot crater dimensions characterized by mean of a profilometer. (c) Evolution of ablation depth versus the number of pulse.

Fig.II.21. displays the strong ablation process occurred for MeP-Si and on Si surfaces. The irradiated target can be considered as a bi-layer of MeP-Si (50 µm) on Si (as described above). First, only

MeP-Si is exposed to laser pulses during 3000 pulses (value given by the ablation rate fit-curve which corresponds to 50 µm of etching depth). For N over 3000 pulses, all MeP-Si layer is removed and Si becomes irradiated by photons. The strong ablation process is obviously achieved through relatively high ablation depths (for example after 1000 pulses, approximately 16 µm of material is removed). For N =5000 and 10000, a deep laser crater is formed (130 µm depth for 10000 pulses) with huge amount of removal material redeposited around (the amplitude of redeposited material reaches roughly 35 µm above the initial surface).

These investigations yield to average values of ablation rate per pulse of 16 nm/pulse and 10 nm/pulse for respectively MeP-Si and Si. The fluence employed is limited to 400 mJ/cm² that seems to be not enough large to cause this severe etching and ablation processes. The laser irradiation under UV and the large laser spot size could explain these strong effects as demonstrated previously in the first part. It should be pointed out that the used fluence value is 20 times higher than the required fluence for NPs formation on MeP-Si and LSFL formation on Si after 1000 pulses.

2. Spikes formation on MeP-Si and Si surfaces

Fig.II.22. presents a sequence of SEM top views of MeP-Si and Si surface morphologies obtained after picosecond laser irradiation at 400 mJ/cm² with increasing the number of shots N from 10 to 10000 pulses. After 10 laser shots, different irregular structures appear (fig.II.22.a). They are randomly distributed on the MeP-Si surface, their diameters are estimated to be in the range of 0.8 to 3 µm (values given by ImageJ software). When N increases up to 100 pulses, the formation of larger structures sized in the range of 0.8 to 4 µm diameter is observed (fig.II.22.b). In addition, some fringes are noticed as a result of energy modulation due to the use of a diaphragm. After 500 pulses, the MeP-Si surface is covered by a regular quasi-uniform spike distribution (fig.II.22.c). With increasing N to 1000 pulses, similar organization of larger spikes is observed showing an average value of apparent diameter about 2.4 µm (fig.II.22.d). When N > 5000 pulses, the MeP-Si layer is totally, removed as said previously, and then micro-spikes are formed on Si surface with a larger size about, 10 µm in diameter (fig.II.22.e), than those formed on MeP-Si. Finally after 10000 pulses, larger structures are formed on Si with diameter close to 20 µm (fig.II.22.f).

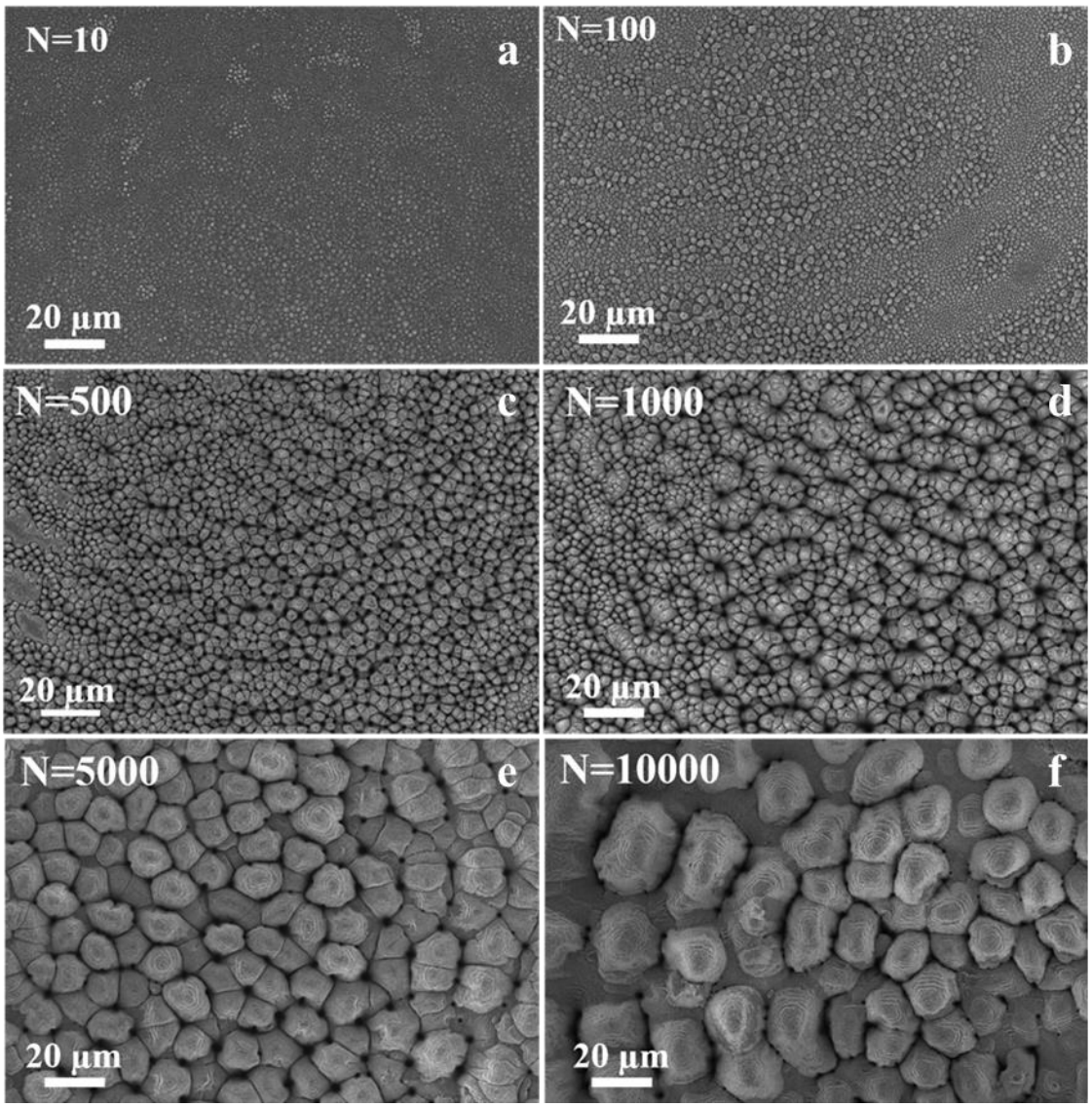

Figure.II.22. SEM top views of surface morphologies of MeP-Si and Si irradiated by 266 nm ps laser at 400 mJ/cm² for N varied from 10 to 10000 shots.

SEM top views provide a good investigation on the homogeneity and the size of formed spikes. In order to examine the shape of these spikes, a tilted SEM characterization has been performed of laser spot irradiated by 100 to 10000 shots as shown in fig.II.23. As mentioned previously, the cross-section views show an increase of spike size and the enhancement of their homogeneity and distribution on the surface with increasing N. In the 500 to 1000 pulse range, quasi-uniform conical-spikes are developed on the entire surface of MeP-Si. Between 5000 and 10000 pulses, their shapes and sizes are modified.

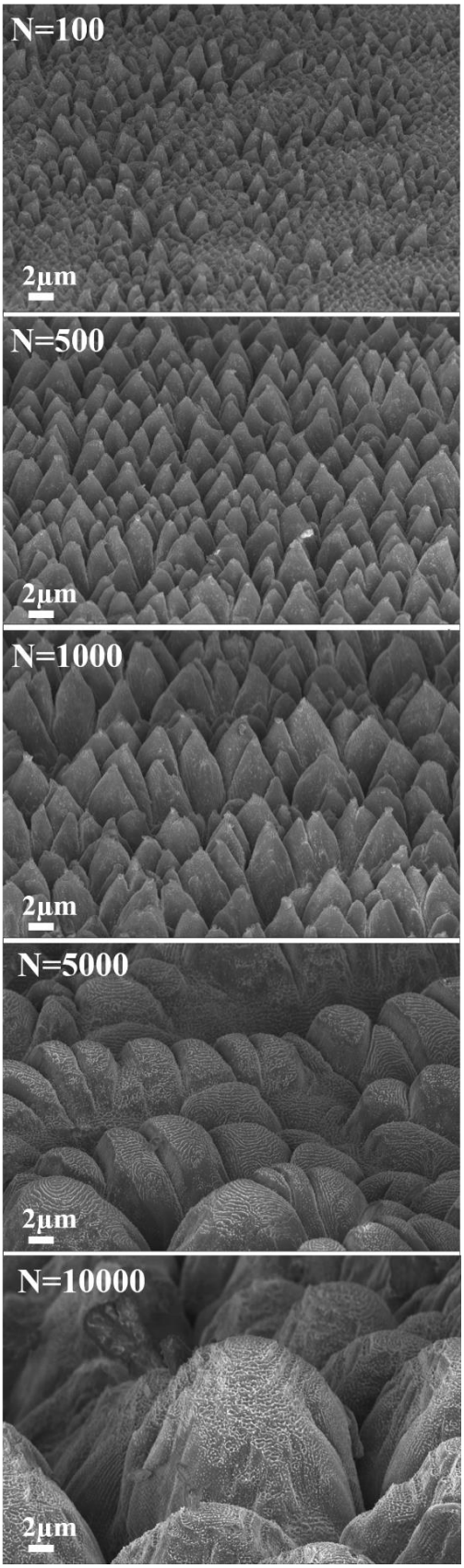

Figure.II.23. SEM tilted cross section views of spikes formed on MeP-Si/Si by ps at 400 mJ/cm².

Despite several studies achieved on the spikes formation on silicon by fs laser irradiation, the formation mechanisms of these structures have not been fully understood yet[35][36][37]. T. Sarnet and co-authors have proposed the following scenario to describe the spikes formation steps [34]. First, at low laser dose, small structures (LIPSS) are formed, similar to capillary waves with periodicity close to the beam wavelength. When laser dose is increased, the capillary waves tend to form larger and more hydrodynamically stable structures. The absorption of laser energy by structures is not uniform. The ablation process is maximized in the valley between these structures which leads to amplify the phenomena and form quasi-uniform spikes distribution on the surface.

In the case of MeP-Si, the use of relatively low fluence leads to LIPSS formation through the organization of nanoparticles generated after few shots as reported in the previous part of this chapter. A periodic melted material was formed after a high number of laser shots. In contrast, LIPSS do not form when employing a relatively high fluence of 400 mJ/cm² in comparison with the ablation threshold of silicon (60 mJ/cm² at 248nm for pulse duration of 100 fs)[15]. However, a strong ablation process takes place even after only 10 shots modifying the initial flat and smoothed surface of MeP-Si into this roughened surface mainly covered by higher amount of irregular structures sized between 0.4 and 1µm (Fig.II.22.a).

With increasing N from 10 to 100 shots, the non-uniform ablation process is steadily occurring and maximized around the valley of initial formed structures (at 10 shots). This leads to a preferential material removal occurring around the initial small structures, while ablation process continues to spring up the spikes in the flat areas (where no structures are formed after 10 shots due to a low laser dose). As a result of this process the amount of small structures (size ranging between 0.4 and 1µm) decreases with increasing N (because they are transformed into bigger structures) and in contrast the amount of bigger structures increases (1 and 2.2 µm). By the next coming shots, the shape and uniformity of spikes is enhanced until the surface becomes covered by quasi-uniform spikes with growing diameter up to 8 µm (Fig.II.22.c and d) for 500-1000 shots. Finally, for the largest N values, the MeP-Si is completely removed and the ablation process continues only on Si surface leading to the formation of bigger structures reaching 20 µm in diameter.

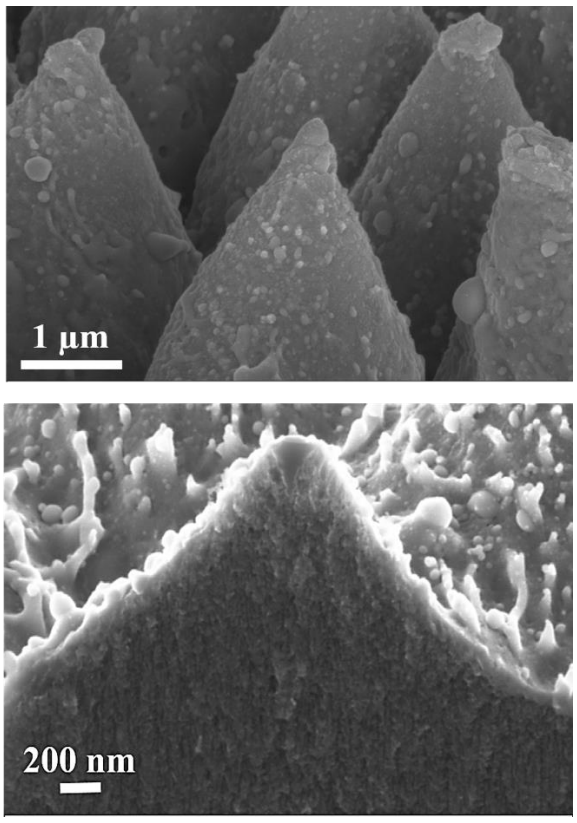

Figure.II.24. The core of spike obtained at 400 mJ/cm² and 1000 shots on MeP-Si.

Fig.II.24. shows the cross section of a spike exhibiting almost the same morphology that untreated mesoporous silicon. Moreover, a very thin melted phase covering valleys and spikes can be observed. This thin film presents irregular nanostructures. This result confirms that ablation process plays the main role on the spikes formation mechanism through material removal. However, some thermal effect like melting could also occur.

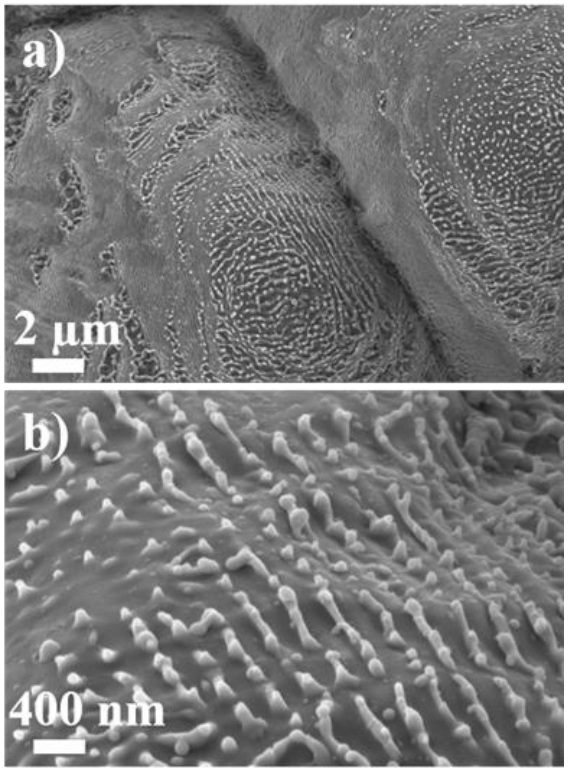

Figure.II.25. High-magnified SEM tilted cross section views of spikes formed on Si after "10000 pulses" at 400 mJ/cm² (the MeP-Si film was completely removed).

Fig.II.25. displays the formation of some nanostructures on spikes surface on Si. Different structures are formed from random dots to regular valleys with a period close to the beam wavelength (266 nm) and an orientation perpendicular to the beam polarization as typical LSFL. These LSFL are present in the thin molten phase formed on the surface of spike as a result of thermal melting and they are self-organized to form hydrodynamically stable structures as classically observed on Si.

VI. Conclusion

In this chapter, the irradiation of MeP-Si by UV picosecond laser in comparison with Si is investigated. Despite similar properties of the both materials, the laser beam interaction leads to very different results. At relatively low beam fluence (20 mJ/cm²), the LSFL formation is observed on both materials due to the high absorption coefficient of Si under 266 nm irradiation, the large spot size and the incubation effect takes place with the relatively high number of pulses (up to 12000 pulses). In the case of MeP-Si, unexpected NPs generation is obtained when experiments were carried out in ambient air. In contrast, no NPs formation was observed on Si surface when it was irradiated in similar conditions. Moreover, a periodic localized molten phase is produced on MeP-Si through thermal melting process. A phase transformation from crystalline to amorphous is resulting of a severe cooling rate. When MeP-Si (50 µm)/Si sample are irradiated by a relatively high laser fluence (400 mJ/cm²), a strong ablation process occurs with a high ablation rate when N is increased up to 10000 (~ 140 µm). Micro-structures as conical spikes were formed through this ablation process first on MeP-Si then on Si surface. An enhancement of spikes homogeneity is noticed with increasing N. The generation of these spikes especially on MeP-Si may lead to enhance its optical properties (absorption of IR radiations) that could be promising for different application in solar cells and photodetectors as reported for black silicon [34].

References

[1] J. M. Liu, "Simple technique for measurements of pulsed Gaussian-beam spot sizes", Opt. Lett., 7, 196-198, 1982.

[2] J. R. Dorvee, J. Sailor, G. M. Miskelly, "Digital microfluidics and delivery of molecular payloads with magnetic porous silicon chaperones", Dalton Trans., 721–730, 2008.

[3] G. Mann, S. Pentzien, J. Krüger, "Applied Surface Science Beam diameter dependence of surface damage threshold of fused silica fibers and preforms for nanosecond laser treatment at 1064 nm wavelength", Appl. Surf. Sci., vol 276, 312–316, 2013.

[4] S. Martin, A. Hertwig, M. Lenzner, K. Krüger, W. Kautek, "Spot-size dependence of the ablation threshold in dielectrics for femtosecond laser pulses", Appl. Phys.A 77, 883–884, 2003.

[5] A. Naghilou, O. Armbruster, M. Kitzler, W. Kautek, "Merging Spot Size and Pulse Number Dependence of Femtosecond Laser Ablation Thresholds: Modeling and Demonstration with High Impact Polystyrene", J. Phys. Chem. C, vol 119, no 40, 22992–22998, 2015.

[6] J. Bonse, A. Rosenfeld, J. Krüger, "On the role of surface plasmon polaritons in the formation of laser-induced periodic surface structures upon irradiation of silicon by femtosecond-laser pulses", J. Appl. Phys., vol 106, no 10, 2009.

[7] M. Guillermin, F. Garrelie, N. Sanner, E. Audouard, H. Soder, "Single- and multi-pulse formation of surface structures under static femtosecond irradiation", Appl. Surf. Sci., vol 253, no 19, 8075–8079, 2007.

[8] J. Bonse, J. Krüger, "Pulse number dependence of laser-induced periodic surface structures for femtosecond laser irradiation of silicon", J. Appl. Phys., vol 108, no 3, 2010.

[9] J. Ryu, Y. J. Jang, S. Choi, H. J. Kang, H. Park, J. S. Lee, S. Park, "All-in-one synthesis of mesoporous silicon nanosheets from natural clay and their applicability to hydrogen evolution", NPG Asia Materials, vol 8, no 3, 248-9, 2016.

[10] J. Bonse, A. Rosenfeld, J. Krüger, "On the role of surface plasmon polaritons in the formation of laser-induced periodic surface structures upon irradiation of silicon by femtosecond-laser pulses", J. Appl. Phys., vol 106, no 10, 2009.

[11] E. L. Gurevich, S. V. Gurevich, "Laser Induced Periodic Surface Structures induced by

surface plasmons coupled via roughness", Appl. Surf. Sci., vol 302, 118–123, 2014.

[12] J. Bonse, S. Baudach, J. Krüger, W. Kautek, M. Lenzner, "Femtosecond laser ablation of silicon - modification thresholds and morphology", Appl. Phys. A, vol 74, no 1, 19–25, 2002.

[13] G. Raciukaitis, M. Brikas, P. Gecys, M. Gedvilas, "Accumulation effects in laser ablation of metals with high-repetition- rate lasers Gediminas", Proc. of SPIE Vol. 7005, 2008.

[14] S. Höhm, M. Herzlieb, A. Rosenfeld, J. Krüger, J. Bonse, "Dynamics of the formation of laser-induced periodic surface structures (LIPSS) upon femtosecond two-color double-pulse irradiation of metals, semiconductors, and dielectrics", Appl. Surf. Sci., vol 374, 331–338, 2016.

[15] A. I. Andrei, E. V Golosov, R. K. Yu, I. K. Sergei, A. E. Ligachev, V. M. Sergei, N. N. Yurii, L. V Seleznev, D. V Sinitsyn, "Formation of quasi-periodic nano- and microstructures on silicon surface under IR and UV femtosecond laser pulses", Quantum Electron., vol 41, no 9, 829, 2011.

[16] Martin A. Green, "Solar Energy Materials & Solar Cells Self-consistent optical parameters of intrinsic silicon at 300 K including temperature coefficients", Solar Energy Materials & Solar, vol 92, 1305–1310, 2008.

[17] H. M. Van Driel, J. E. Sipe, J. F. Young, "Laser-induced periodic surface structure on solids: A universal phenomenon", Phys. Rev. Lett., vol 49, no 26, 1955–1958, 1982.

[18] J. D. Fowlkes, A. J. Pedraza, D. A. Blom, H. M. Meyer, "Surface microstructuring and long-range ordering of silicon nanoparticles", Appl. Phys. Lett., vol 80, no 20, 3799–3801, 2002.

[19] R. Le Harzic, D. Dörr, D. Sauer, F. Stracke, H. Zimmermann, "Generation of high spatial frequency ripples on silicon under ultrashort laser pulses irradiation", Appl. Phys. Lett., vol 98, no 21, 8–11, 2011.

[20] A. Melhem, D. De Sousa Meneses, C. Andreazza-Vignolle, T. Defforge, G. Gautier, N. Semmar, "Structural, Optical and Thermal Analysis of n-type Mesoporous Silicon Prepared by Electrochemical Etching", J. Phys. Chem. C, 2015.

[21] L. Delfour, T. E. Itina, "Mechanisms of Ultrashort Laser-Induced Fragmentation of Metal Nanoparticles in Liquids: Numerical Insights", J. Phys. Chem. C, vol 119, no 24, 13893–13900, 2015.

[22] M. E. Povarnitsyn, T. E. Itina, M. Sentis, K. V. Khishchenko, P. R. Levashov, “Material decomposition mechanisms in femtosecond laser interactions with metals”, Phys. Rev. B - Condens. Matter Mater. Phys., vol 75, no 23, 1–5, 2007.

[23] N. M. Bulgakova, I. M. Bourakov, “Phase explosion under ultrashort pulsed laser ablation: Modeling with analysis of metastable state of melt”, Appl. Surf. Sci., vol 197–198, 41–44, 2002.

[24] N. M. Bulgakova, “Theoretical Models and Qualitative Interpretations of Fs Laser Material Processing”, J. Laser Micro/Nanoengineering, vol 2, no 1, 76–86, 2007.

[25] T. T. D. Huynh, M. Vayer, A. Sauldubois, A. Petit, N. Semmar, “Evidence of liquid phase during laser-induced periodic surface structures formation induced by accumulative ultraviolet picosecond laser beam”, Appl. Phys. Lett., vol 107, no 19, 2015.

[26] M. E. Povarnitsyn, T. E. Itina, P. R. Levashov, K. V Khishchenko, “Mechanisms of nanoparticle formation by ultra-short laser ablation of metals in liquid environment.”, Phys. Chem. Chem. Phys., vol 15, no 9, 3108–14, 2013.

[27] K. Gouriet, T. E. Itina, S. Noel, J. Hermann, M. Sentis, L. Zhigilei, “Formation of nanoparticles by short and ultra-short laser pulses”, Proc. SPIE - Int. Soc. Opt. Eng., vol 7005, 1–8, 2008.

[28] T. E. Itina, A. Voloshko, “Nanoparticle formation by laser ablation in air and by spark discharges at atmospheric pressure”, Appl. Phys. B Lasers Opt., vol 113, no 3, 473–478, 2013.

[29] A. Rousse, C. Rischel, S. Fourmaux, I. Uschmann, S. Sebban, G. Grillon, P. Balcou, E. Förster, J. P. Geindre, P. Audebert, J. C. Gauthier, D. Hulin, “Non-thermal melting in semiconductors measured at femtosecond resolution”, Nature, vol 410, no 6824, 65–68, 2001.

[30] J. Jia, M. Li, C. V. Thompson, “Amorphization of silicon by femtosecond laser pulses”, Appl. Phys. Lett., vol 84, no 16, 3205–3207, 2004.

[31] M. S. Rogers, C. P. Grigoropoulos, A. M. Minor, S. S. Mao, “Absence of amorphous phase in high power femtosecond laser-ablated silicon”, Appl. Phys. Lett., vol 94, no 1, 2007–2010, 2009.

[32] Y. Izawa, Y. Izawa, Y. Setsuhara, M. Hashida, M. Fujita, R. Sasaki, H. Nagai, M. Yoshida, “Ultrathin amorphous Si layer formation by femtosecond laser pulse irradiation”, Appl. Phys.

Lett., vol 90, no 4, 1–3, 2007.

[33] J. M. Liu, R. Yen, H. Kurz, N. Bloembergen, J. M. Liu, R. Yen, H. Kurz, N. Bloembergen, "Phase transformation on and charged particle emission from a silicon crystal surface , induced by picosecond laser pulses", Appl. Phys. Lett. 39, 755, 1981.

[34] T. Sarnet, J. E. Carey, E. Mazur, "From black silicon to photovoltaic cells, using short pulse lasers", International Symposium on High Power Laser Ablation. 219–228, 2012.

[35] Z. Huang, J. E. Carey, M. Liu, X. Guo, E. Mazur, J. C. Campbell, "Microstructured silicon photodetector", Appl. Phys. Lett., vol 89, no 3, 3–5, 2006.

[36] C. H. Crouch, J. E. Carey, M. Shen, E. Mazur, F. Y. Génin, "Infrared absorption by sulfur-doped silicon formed by femtosecond laser irradiation", Appl. Phys. A Mater. Sci. Process., vol 79, no 7, 1635–1641, 2004.

[37] M. Y. Shen, C. H. Crouch, J. E. Carey, E. Mazur, "Femtosecond laser-induced formation of submicrometer spikes on silicon in water", Appl. Phys. Lett., vol 85, no 23, 5694–5696, 2004.

Chapter III: Ultrashort laser-matter interaction: case of femtosecond laser beam

I. Introduction

In the previous chapter, laser induced structure formation on MeP-Si was investigated mainly based on an experimental approach. A wide range of unexpected results are obtained under picosecond regime from the formation of LSFL by NPs organization, localized molten phase formation to quasi-periodic conical spikes generation that could be attracting for many applications in micro-electro-mechanical systems, tribology, structural color, wetting, cell growth, etc [1][2]. Due to their wide field of applications, LIPSS have paid a great attention recently. J. Bonse et al [2] have reported that the number of publications per year on LIPSS topic has impressively grown in the last decades to reach approximatively 80 publications in 2015 (fig.III.1.). Among the different type of lasers employed in these papers (continuous, nanosecond, picosecond and femtosecond), femtosecond laser was the most used one in these publications. This is probably due to the reduction of thermal effects in such regime that facilitates the micromachining with a high level of accuracy. Therefore, in this present chapter, we aim to investigate the LIPSS formation on single laser spot as well as on large surface under femtosecond regime.

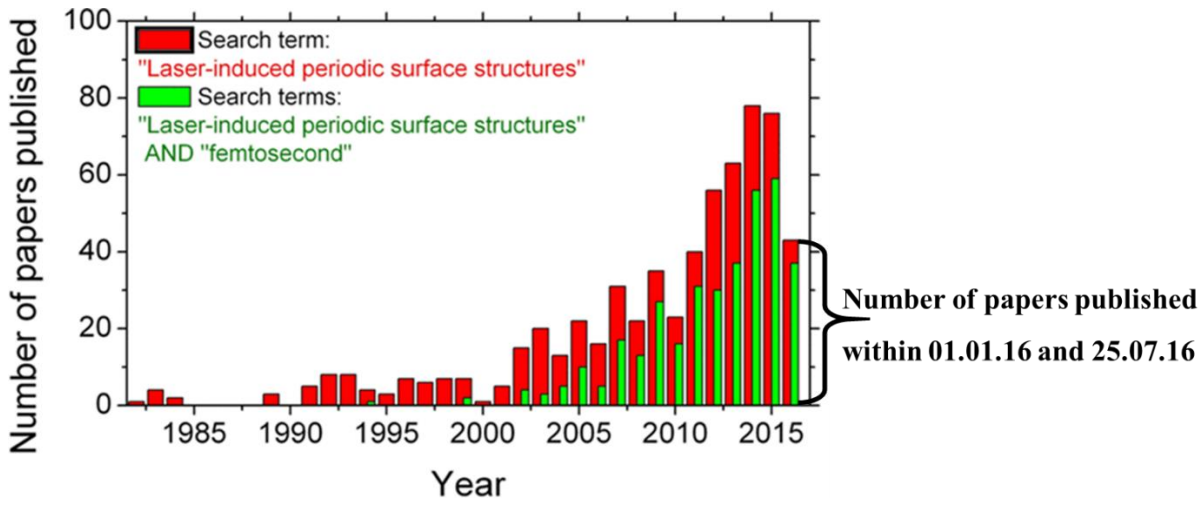

Figure.III.1. Number of publications appeared per year on LIPSS field [1].

First, this chapter deals with a comparative investigation of LIPSS formation on MeP-Si surface under femtosecond laser irradiation with those formed under picosecond ones in the previous chapter. Then, a large surface laser nanostructuring of MeP-Si is investigated by the help of two fs lasers irradiating respectively at 266 and 1030 nm.

Several studies are available on LIPSS formation on different bulk materials[3][4][5], but only few studies are focused on thin films (most of them are concerning the metallic thin films[6][7]). In order to explore the LIPSS formation on thin films using a fs laser irradiating at 266 nm., titanium oxide thin film was chosen for this investigation due to its promising application on different fields such as thermoelectricity, photovoltaic and photocatalysis effects [8][9][10].

II. Femtosecond laser sources

Two different ultra-short laser systems were employed. From GREMI laboratory, Titanium-Sapphire (Ti: Al_2O_3) femtosecond laser with a pulse duration of 100 fs and irradiating at 800 nm was used. A third harmonic generator was used to generate the working wavelength of 266 nm. Due to its limited repetition rate (1000 Hz), a second laser system, based on potassium yttrium tungstate (YKW) crystal available in NCLA laboratory offering a pulse duration of 500 fs at 1030 nm and repetition rate reaching 300 kHz, was used. The main features of both lasers are summarized in the following table:

	Ti:Al_2O_3 Femtosecond laser (GREMI)	Yb:YKW Femtosecond laser (NCLA)
Pulse duration	100 fs	500 fs
Possible wavelengths	800, 400 and 266 nm	1030, 515 and 343 nm
Working wavelength used in this study	266 nm	1030 nm
Maximum frequency	1000 Hz	300000 Hz
Polarization	linear	linear

Table.III.1. Characteristics of the used lasers in this work

All experiments were carried out in ambient air. The laser nanostructuring process was performed via two modes as following:

- ✓ Statistic mode (single laser spot);
- ✓ Dynamic mode (large surface area);

For both configurations, the laser beams (Ti: Al_2O_3 and Yb: YKW) were focused onto the surface of samples using a scanner galvo with F-theta lens (f= 100 mm) as illustrated in fig.III.2.

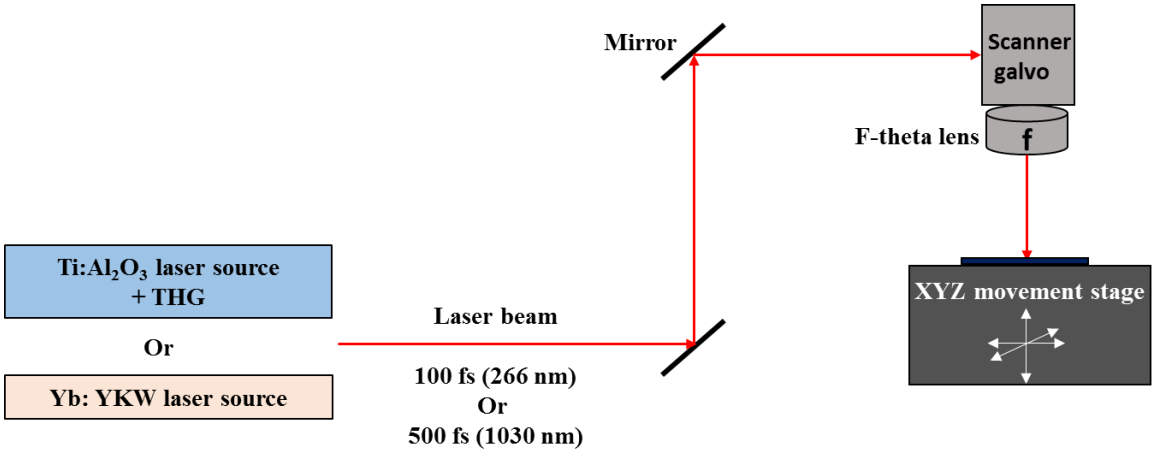

Figure.III.2. Schematic of the experimental set up.

Liu's method was used to determine the laser beam diameter parameter of Ti: YKW (see section III.2.1). However, in the case of Ti: Al2O3, the laser spot diameter was directly estimated from the SEM images (350 µm) because its affected Gaussian distribution as shown in fig.III.3.

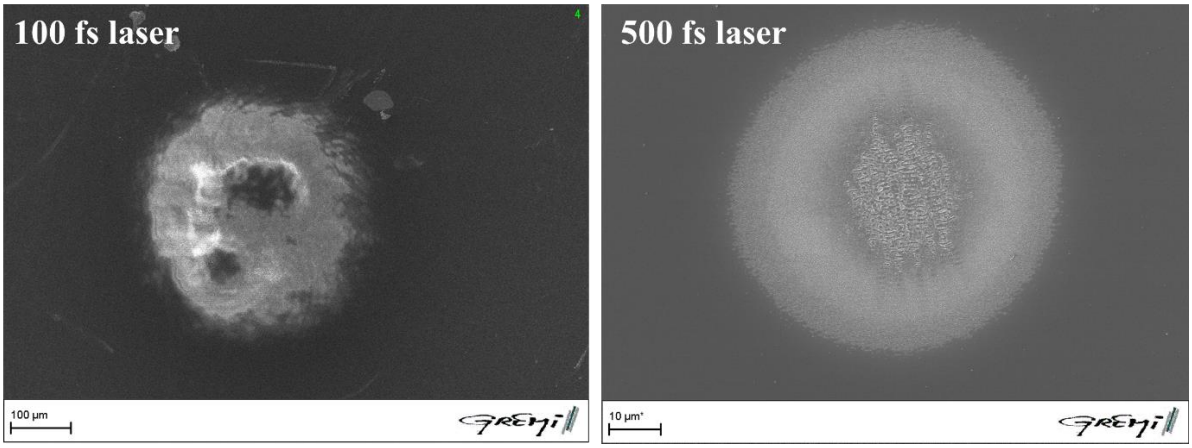

Figure.III.3. SEM views of laser spots formed on MeP-Si irradiated by 100 fs (left) and 500 fs (right).

III. Mesoporous silicon MeP-Si

This part deals with a comparative study of LIPSS formation in femtosecond and picosecond regimes (chapter II).

1. Results obtained with the fs laser having a pulse duration of 100 fs and irradiating at 266 nm

1.1. Evolution of MeP-Si surface morphology with the pulse number N

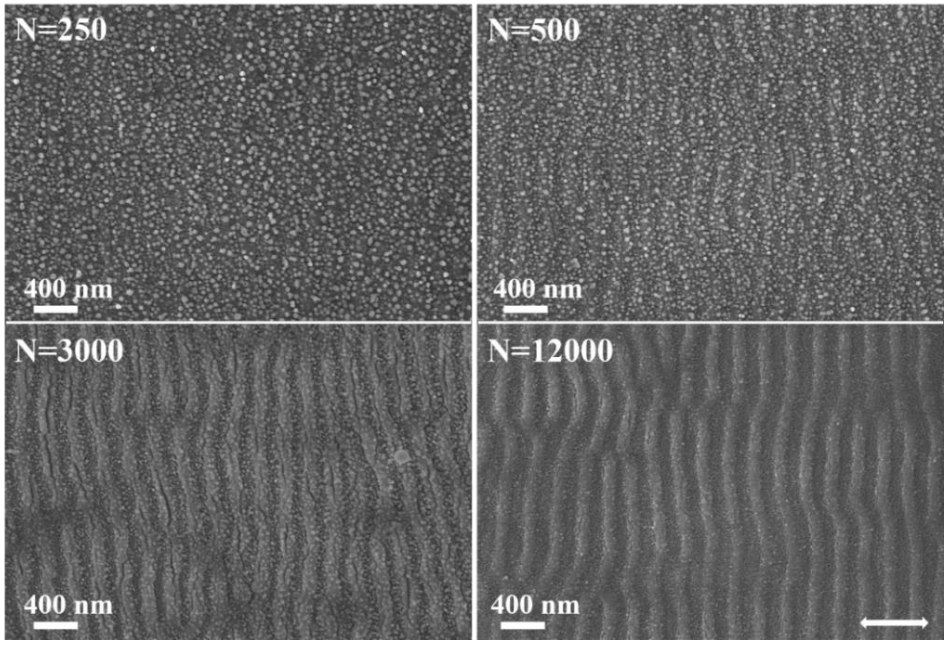

Figure.III.4. SEM top views of MeP-Si surface morphologies irradiated by UV femtosecond laser at different N at 20 mJ/cm²

Fig.III.4. displays the evolution of MeP-Si surface morphologies irradiated by femtosecond laser beam at 20 mJ/cm² at different numbers of pulses (N). This fluence (F) was chosen to be the same as the one used with the picosecond laser beam (chapter II). As observed on the SEM views under picosecond laser beam irradiation (Fig.II.7.), NPs appear at the beginning of laser irradiation followed by the LIPSS formation through NPs coalescence and organization. At relatively low N value (250 pulses), the MeP-Si surface is covered by a random distribution of NPs with a mean size close to 35 nm (value extracted from a numerical analysis through ImageJ software) resulting from gentle ablation (as discussed in chapter II).

When N increases up to 3000 pulses, unclear LIPSS are formed with a 260 nm SEM-estimated period close to the working wavelength and their orientations are perpendicular to the laser polarization. At relatively high N = 12000 (Fig.III.4. and Fig.III.5.), the LIPSS are better defined and NPs are well arranged. The typical morphology of MeP-Si re-appeared between two ripples as the as-received MeP-Si surface before laser irradiation with the initial pores distribution (as seen in fig.III.5.).

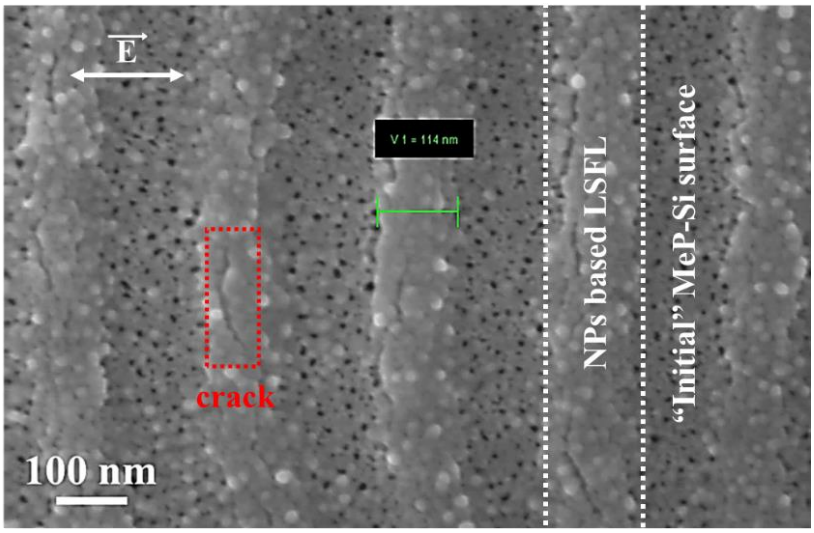

Figure.III.5. High magnified SEM image of LIPSS formed on MeP-Si surface after 12000 pulses

Despite the difference in the pulse duration time scale between the ps and fs lasers. SEM characterizations showed roughly the same stages of LSFL formation in the two regimes (ps and fs). However, some differences should be noticed. At the first stage after 250 shots, the mean size of NPs generated in ps regime was about 55 nm in diameter, which is larger than the mean size of NPs formed in fs regime (about 35 nm in diameter). The reduction of NPs size by the use of femtosecond beam was expected. It was reported that laser pulse duration influences directly the size of NPs [11]. For example, the irradiation of silicon by nanosecond laser beam involves a substantial melting as well as the generation of cavitation bubbles that generally lead to the production of large NPs. Conversely laser irradiation with shorter laser pulses (ps and fs) results in the formation of ultra-small NPs by the reduction of thermal effects and cavitation bubbles especially after a relatively low number of pulses (250 shots). Even under ultra-short laser pulse irradiation (ps and fs pulse duration times), it has been shown that NPs sizes obtained with ps laser are larger than those produced with fs one.

In addition, it has been noticed in fig.III.4. that nano-cracks appear on LIPSS surface after 3000 shots only on samples irradiated by femtosecond laser (no cracks were observed under the ps irradiation). The following mechanisms for nano-cracks formation have been widely discussed in the literature. Firstly, the photons of a fs laser pulse are absorbed and the sample surface temperature increases then strongly decreases at the end of the laser pulse. Thus, thermal stress due to heating and cooling processes induces a tiny crack on the sample surface. During the next pulse the electric field is enhanced around the tiny crack in the perpendicular direction to the laser polarization, causing an

intense thermal stress that enhances the damage (this supposes that LSFL are very dense) [11][12][13].

Furthermore, Fig.III.4. reveals that the LIPSS formed after 12000 pulses by femtosecond laser are not always straight and show bifurcations from one LSFL to two LSFL bending the LIPSS located around this bifurcation. The bifurcation formation mechanism and bending phenomenon could be attributed to the progressive inhomogeneous surface absorption, resulting from localized defects due to electronic excitation and subsequent self-organization processes [14].

1.2. Molten phase formation

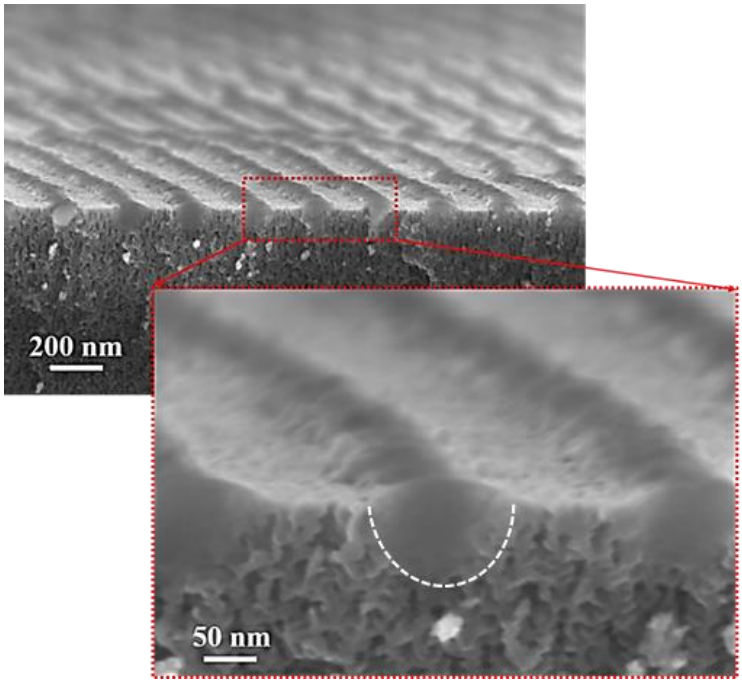

Figure.III.6. SEM tilted (14°) cross-section views of LIPSS formed at 20mJ/cm2 and after 12000 shots, by UV 100 fs laser beam.

Fig.III.6. shows 14°-tilted cross-section views of LIPSS obtained after 12000 shots by 100 fs laser beam. These views showed that no pores could be observed below the formed LIPSS while the pores located between two ripples are still open as observed previously with the picosecond. This result implies the formation of a localized molten phase that fills the pores in 100 nm depth below the formed LIPSS. Furthermore, the LSFL (observed in Fig.III.6.) seem to be very smooth and dense in comparison with those obtained with ps presenting a granular morphology (chapter II).

In the case of femtosecond irradiation, it is generally accepted [15][16] that the formation of molten phase is induced through non-thermal melting due to the short pulse duration (shorter than the electron-phonon relaxation time). However these non-thermal effects take place at relatively high

fluences, about 2.2 times larger than the thermal effects threshold [17] (about 60 mJ/cm² in the case of silicon irradiated by femtosecond laser at 248 nm [18]). In the present study, the working fluence was too low to melt the material after few pulses (through non-thermal melting). However it could cause some chemical and structural changes in the material. By increasing N, the accumulation of these defects by the next coming pulses, facilitates the evaporation, ablation or melting of material through incubation effect [19].

Another very important point that should be noticed is that the melt depth obtained by irradiation by picosecond and femtosecond lasers is similar in both cases i.e. around 100 nm. This result confirms that the liquid phase was formed through the same mechanism (thermal melting) because the depth of molten phase formed through thermal melting should be ten times thicker than the melt depth produced by non-thermal melting [17].

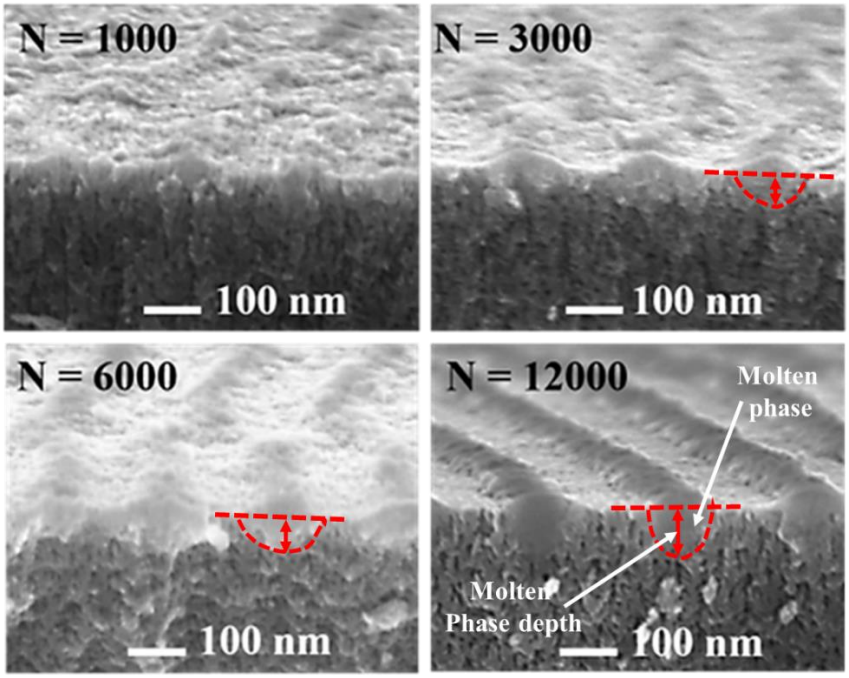

Figure.III.7. Cross sectional SEM images of MeP-Si irradiated at 20 mJ/cm² for N varying from 1000 to 12000.

Fig.III.7. displays the SEM cross section of MeP-Si irradiated at different N. This shows clearly the role of the incubation effect on the melting phase depth evolution located below LSFL. For N < 3000 the melted phase appears just in surface. For N > 3000, the quasi-periodic melting started to be formed below the ripples. For N > 6000 to 12000 shots, the periodicity of localized molten phase is enhanced and the thickness of the melted phase below the regular LIPSS reaches a maximum of ~100 nm. This confirms two concluding remarks. On the one hand the fluence employed was not sufficient to produce a molten phase in one laser shot then we cannot speak of ultra-fast melting [17].

On the other hand the incubation effect has a key role on the LIPSS formation, this means we observe a thermal melting process in fs regime at low fluence.

TEM analyses have also been performed for LSFL formed by fs laser beam at 20 mJ/cm² and after 12000 shots. The results are closely similar to those obtained in ps case (fig.III.8.). The molten phase formed below LIPSS became amorphous after re-solidification whereas the MeP-Si between LIPSS stays crystallized. This phase transformation is attributed to the severe undercooling of molten phase.

To summarize this part, it has been observed that an unexpected similar behavior by incubation phenomenon, despite the difference of the pulse duration between the picosecond and femtosecond lasers, is responsible of LIPSS formation on MeP-Si. LSFL with orthogonal orientation to the laser polarization were formed after a high number of pulses, due to coalescence and organization of unexpected nanoparticles produced at the first stage of beam interaction. SEM and TEM techniques demonstrate the formation of a liquid phase that became amorphous after the re-solidification process. It is found that at such low laser fluences (about 20 mJ/cm²) and after a large number of pulses (about 12000), like-thermal effects could occur by melting diffusion in picosecond as in femtosecond regime through incubation.

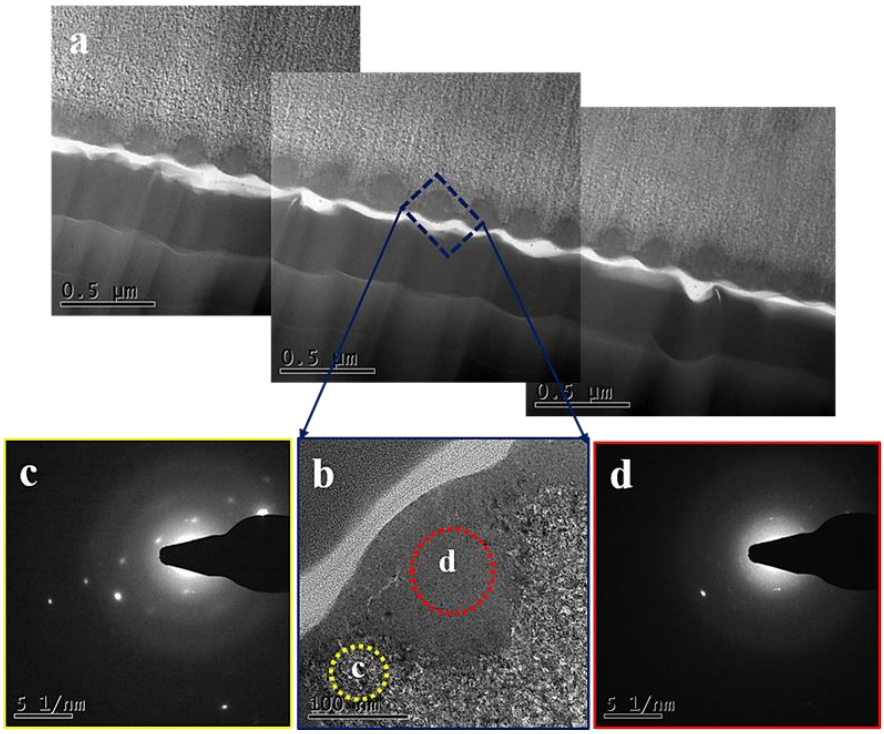

Figure.III.8. TEM analysis of LSFL formed by 266 nm fs irradiation at 20mJ/cm² and after 12000 pulses.

1.3. Large surface nanostructuring

The fundamental study of LIPSS formation on MeP-Si by ps and fs laser irradiations shows a very similar finding and formation processes. The next step of this study aims to perform a large surface treatment in order to obtain similar nanostructures organization on a relatively large scale of 5x5 mm² in order to investigate the role of such structures in the evolution of thermoelectric properties (the goal of the next chapter). Although, the similar results obtained with ps as well as fs laser, the study of large surface nanostructuring is performed using only fs laser due to reduce the processing time (because the relatively high repetition rate of our fs laser which reaches 1000 Hz compared to the frequency of ps which is limited to 10 Hz).

In the case of Ti:Sapphire laser system (GREMI), the samples were fixed and a scanner galvo reflecting the laser beam onto the sample taking into account the laser pulse number by adjusting the translation step s as shown in Fig.III.9. In this configuration the step of translation is the same in both axis. The average number N of pulses received by each point of material surface can be estimated through the following relation:

$$N = \left(\frac{d}{s}\right)^2 \qquad Eq.III.1$$

Where d is the laser spot diameter and s is the step of translation.

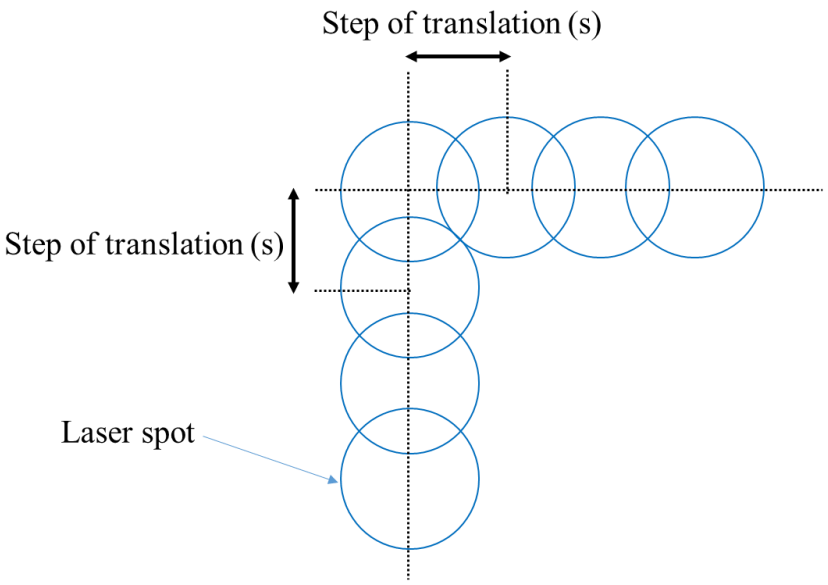

Figure III.9. Laser scanning scheme (100 fs laser).

Fig.III.10. illustrates the different morphologies obtained at various laser doses. The fluences were varied in the 12 to 30 mJ/cm² range, the step of sample translation changing from 3 to 6 µm, corresponding to a pulse number of 13000 and 3300. For F=12 mJ/cm², mainly NPs are formed and their density increases with N. For N = 13000, vertical periodic organization of NPs could be observed as seen before on single laser spot (fig.III.4. for N=250). Thus, despite of the relatively high N value, the formation of clear LSFL is not obtained for this fluence of 12 mJ/cm². When F increases up to 20 mJ/cm², LSFL are generated after 13000 pulses with the presence of some clusters. Otherwise, at 3300 pulses, NPs distribution covers the surface of MeP-Si. Lastly, for F = 30 mJ/cm², ablation regime is reached leading to cluster, random nanostructures formation.

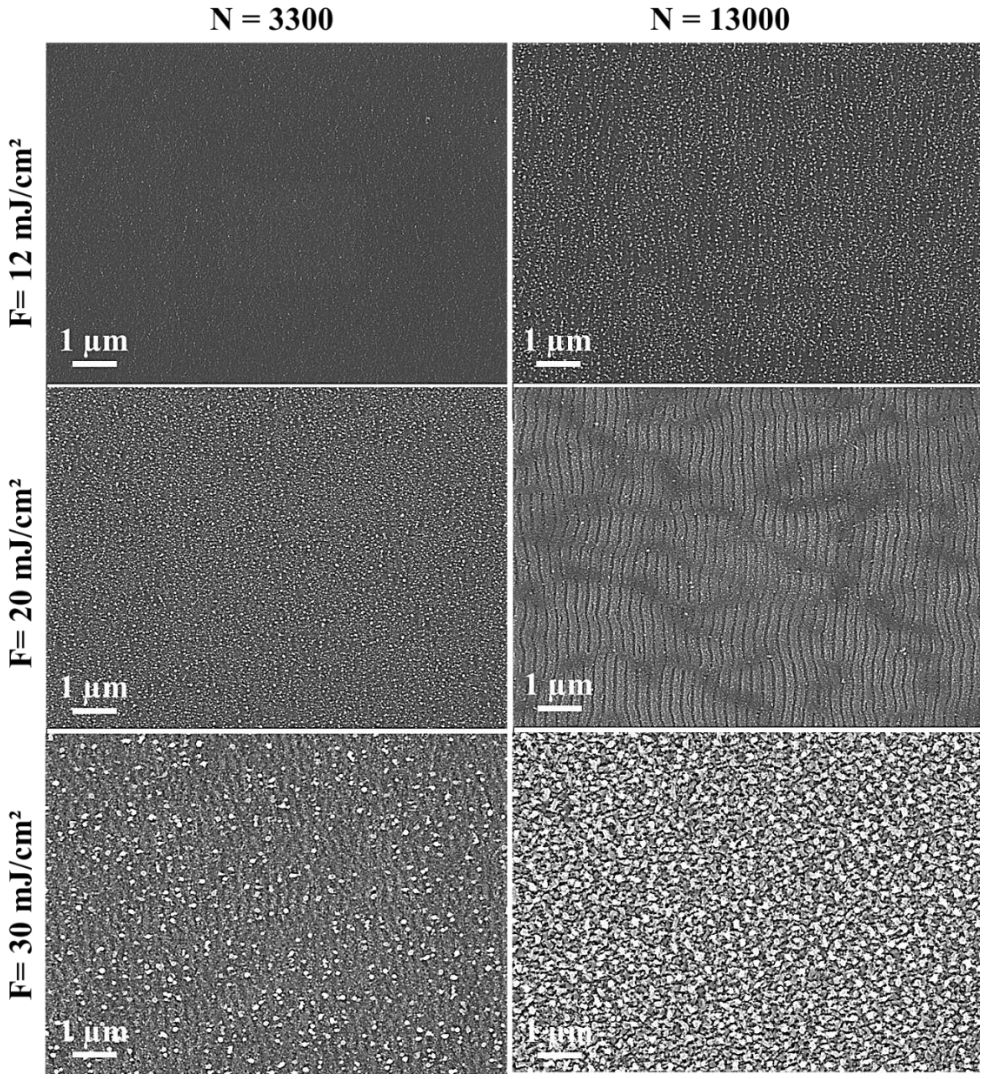

Figure.III.10. SEM top views of different morphologies obtained on MeP-Si by fs laser scanning.

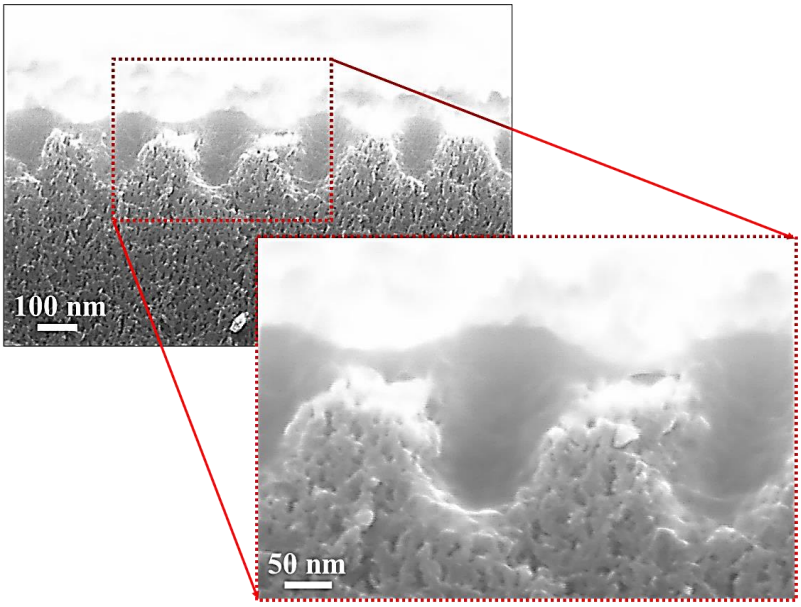

Figure.III.11. SEM cross-section views of LIPSS formed by laser scanning at 20mJ/cm² and after 13000 shots, by 266 nm fs beam.

Thus, experimental results obtained by large laser nanostructuring of MeP-Si seem to be very similar to those obtained on a single laser spot. That means LSFL are expected to be formed through NPs organization in parallel to the localized molten phase production. However the cross section view of LSFL obtained at 20 mJ/cm² and after 13000 pulses (fig.III.11.) exhibits the formation of periodic valleys and crests produced as a result of localized etching and ablation mechanisms probably due to the interferences generated between the incident beam and the electromagnetic surface wave (can be the light scattered from the surface roughness and/or surface plasmons polaritons) resulting in a modulation of laser energy deposition. This implies that under dynamic mode (laser scanning), LIPSS are formed through ablation process that started by NPs generation and then achieved by periodic localized ablated zones. In comparison with the previous result for steady state no molten phase and no agglomeration of NPs above the initial surface could be observed Finally, a clean large nanostructured MeP-Si surface without any cluster or impurity has been obtained when employing an intermediate fluence of 15 mJ/cm² with N = 13000, that will be suitable for thermoelectricity application (Fig.III.12.).

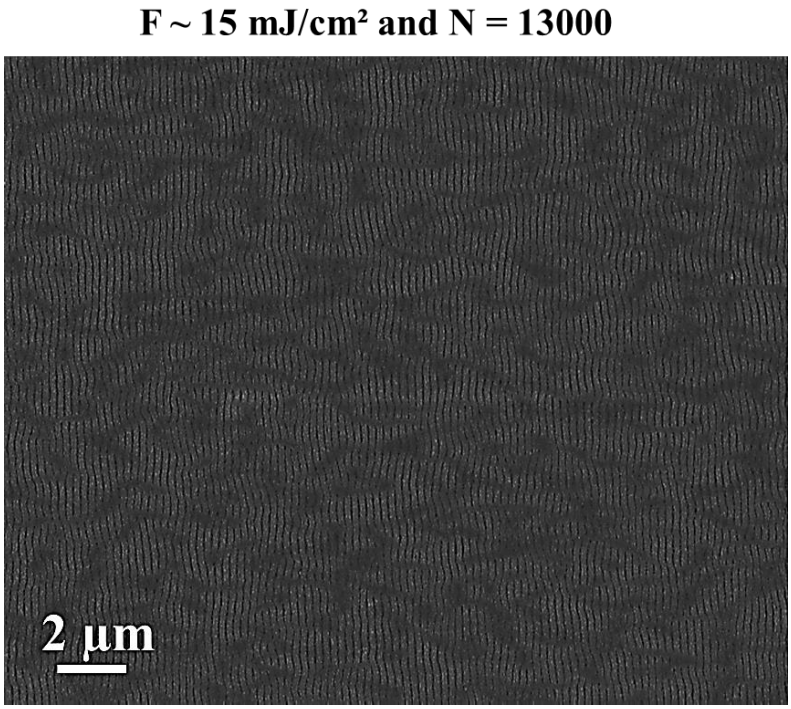

Figure.III.12. Large nanostructured MeP-Si surface performed under fs irradiation.

2. Results obtained with the fs laser having a pulse duration of 500 fs and irradiating at 1030 nm

In spite of the promising findings obtained on the nanostructuring of large surfaces of MeP-Si by the use of 100 fs laser at 1000 Hz, the processing times reaches roughly 112 seconds per 1 mm² for N = 13000 pulses seems to be too long. This duration value was estimated using the formula given below:

$$Processing\ time\ (s/mm^2) = \left(\frac{1}{Step\ of\ translation}\right)^2 \times \frac{1}{Frequency} \qquad (\text{Eq. } III.2)$$

Therefore, to obtain a nanostructured surface (as shown in Fig.III.12.) of 25x25 mm², ~ 20 hours was needed. This duration time is obviously too high and makes this process not suitable for applications. In order to reduce the processing time, a 500 fs laser operating at 1030 nm, devoted to industrial micromachining applications, was utilized because its high repetition rates (300 kHz).

2.1. Threshold ablation fluence and incubation coefficient

The determination of ablation threshold F_{th} of MeP-Si under 500 fs irradiation at 1030 nm after N pulses, is performed according to the method of Liu [20] which consists to vary the beam energy at fixed focal spot (the distance target-lens is unvaried) as shown in Fig.III.13.

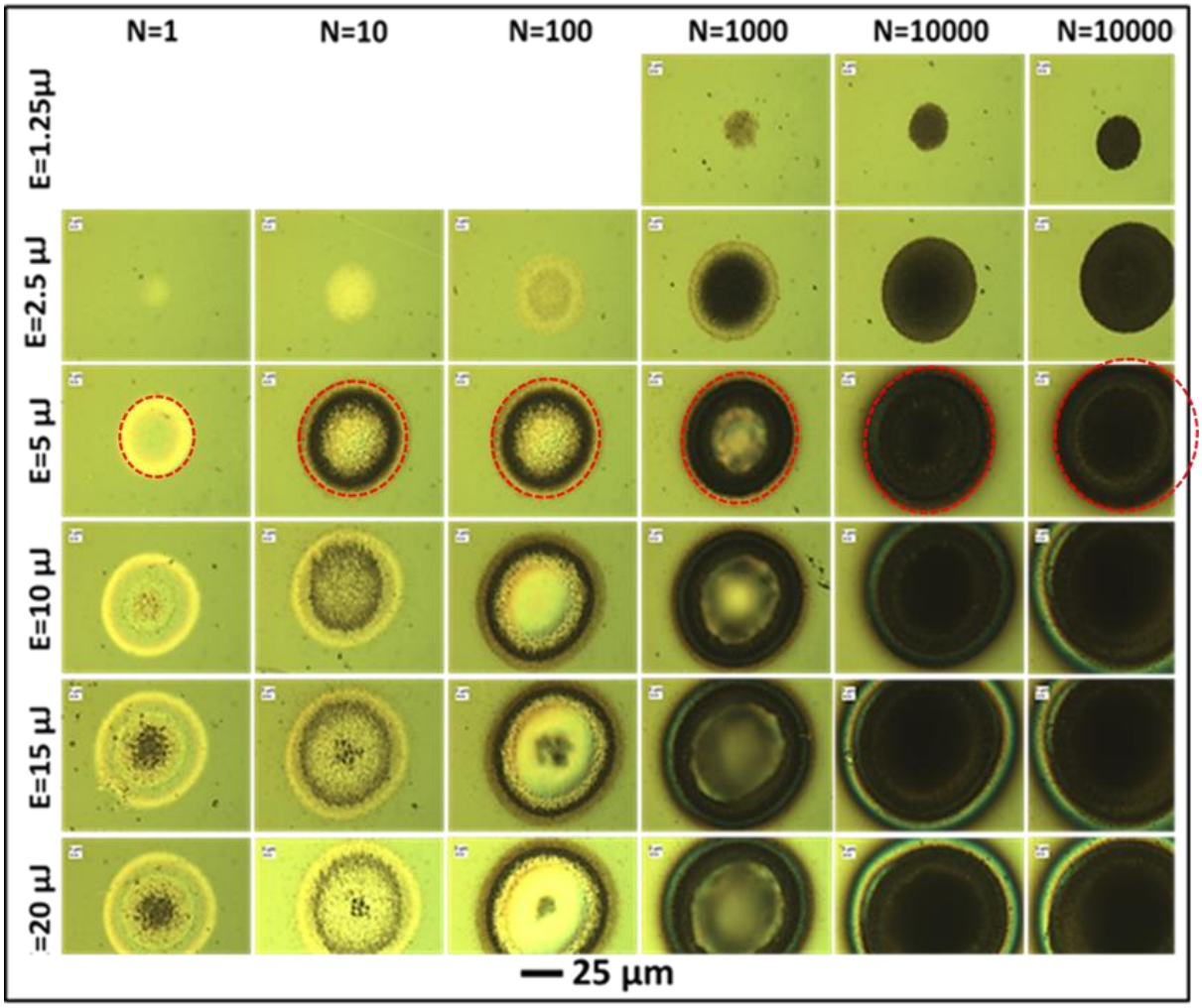

Figure.III.13. Optic microscopy characterization of laser spot formed on MeP-Si irradiated by 500 fs laser @ 1030 nm for different energies E and number of pulses N.

The crater diameter of each spot was measured and plotted versus laser pulse fluence used to ablate the crater (Fig.IV.11). The threshold was deduced from equation (Eq.III.3) showing the relationship between the laser fluence F and the crater diameter D.

$$D^2 = 2\omega_0{}^2 \ln\left(\frac{F}{F_{th}}\right) \qquad Eq.III.3$$

Where ω_0 refers to the waist beam radius parameter (measured at 1/e) which can be estimated through the slope of linear fitting of curves plotted according the following equation:

$$D^2 = 2\omega_0{}^2 \ln\left(\frac{E}{E_{th}}\right) \qquad Eq.III.4$$

The beam waist radius was found to be about 32 µm.

The ablation thresholds are thus determined from the intercepts of these linear curves (D^2~ln (F)) with the fluence axis (horizontal axis) as displayed in Fig.III.14.

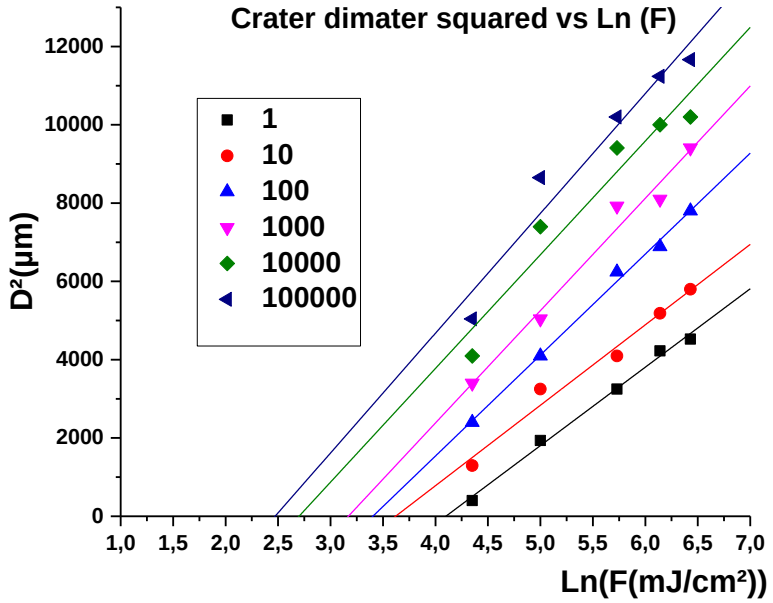

Figure.III.14. Semi-log plots of laser spot square diameter D^2 versus laser fluence F.

The ablation threshold measured for single pulse is roughly 60 mJ/cm² @ 1030 nm (Fig.III.14.). This value seems to be relatively low compared to the ablation threshold of silicon reported in literature, 200-300 mJ/cm², for IR fs laser with a pulse duration times varying from 5 to 500 fs [21]. However, such value is expected since a different physical processes have been achieved at very low fluence (20 mJ/cm²) with MeP-Si (as observed in the previous chapter).

Fig.III.15. presents the evolution of ablation threshold decreasing with the number of pulses N. For example the F_{th} calculated after 1000 pulses is around 23 mJ/cm² compared to 60 mJ/cm² for the single threshold value. This reduction in threshold value is widely observed in literature and generally attributed to the incubation effect as discussed in chapters I and II. In the case of metal and semiconductors, it is found that incubation phenomenon presents a linear behavior relating the ablation threshold with the number of pulses by the following equations [22][21]:

$$F_{th}(N) = F_{th}(1)N^{S-1} \qquad (Eq.\ III.5)$$

$$Ln[F_{th}(N)] = Ln[F_{th}(1)] + (S-1)Ln[N] \qquad (Eq.\ III.6)$$

Where S is the incubation or accumulation coefficient. A typical value for silicon irradiated by IR fs laser is S = 0.8-0.85[19][21]. A similar behavior is observed for MeP-Si (Fig.III.15.) with an incubation coefficient of S ~ 0.86. The incubation effect of MeP-Si could be considered very similar to Si.

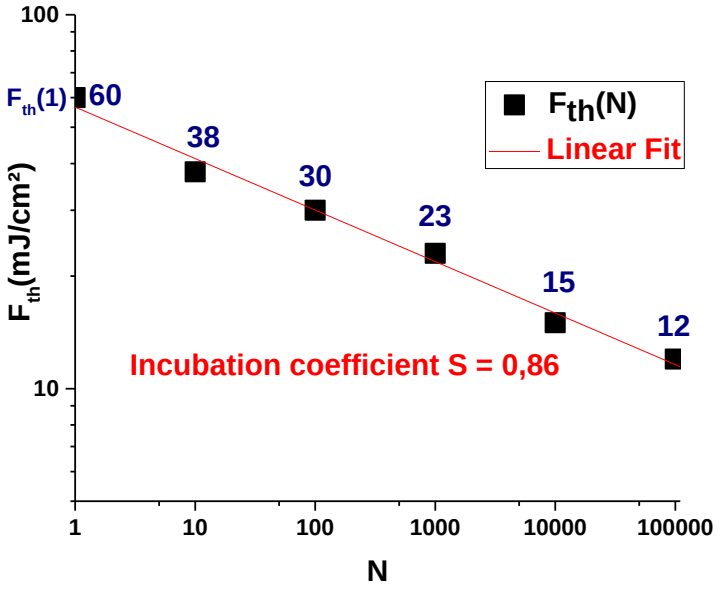

Figure.III.15. Evolution of threshold ablation fluence F_{th} of MeP-Si versus number of pulses N for a 500 fs laser @ 1030 nm.

2.2. Large surface nanostructuring

The second laser scanning configuration performed with the 500 fs laser system (NCLA) is illustrated in fig.III.16. Parallel lines are drawn on the material surface (to treat homogenous surfaces, these lines must be overlapped). The number of pulses can be controlled through the velocity V of drawing, spot diameter d, repetition rate F and spacing between lines s (see Eq.III.7).

$$N = \frac{d^2.F}{V.s} \qquad Eq.III.7$$

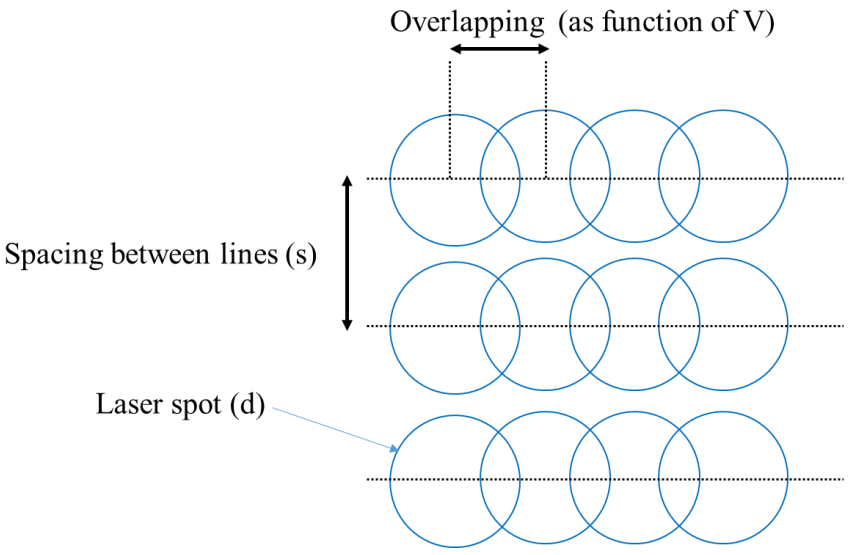

Figure III.16. Laser scanning scheme (500 fs laser).

As example of lines drawn by laser, the optic microscopy image (fig.III.17.) shows a line draw by 500 fs laser @ 1030 nm with a speed of 25 mm/s at 100 kHz of repetition rate (resulting to an average number of pulses of 256 pulses) and a fluence of 62 mJ/cm². This image shows the formations of regular LIPSS oriented perpendicular to the beam polarization with a period ~ 1 µm (resolution limit of optic microscopy). The applied fluence (62 mJ/cm²) is slightly above the ablation threshold.

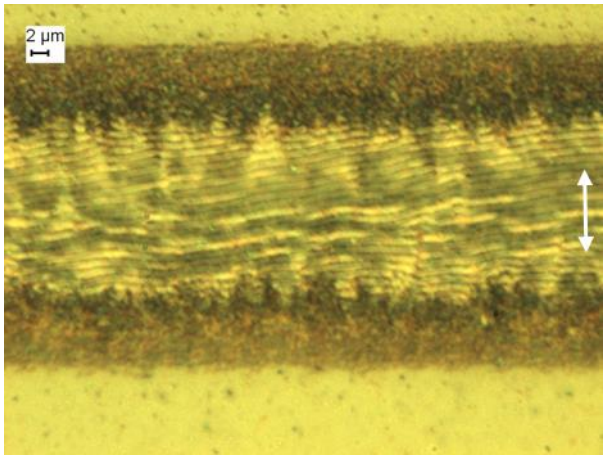

Figure.III.17. LSFL organization formed along of line drawn by 500 fs laser @ 1030 nm (V=25 mm/s and F= 62 mJ/cm²).

For large surface nanostructuring of MeP-Si by 500 fs laser, the distance sample-lens kept constant resulting in a laser radius parameter ~ 32 µm). The repetition rate was also fixed to 100 kHz. For target moving, the spacing between lines is chosen to be 5 µm, this low value compared to the spot size insuring the getting of homogenous surface. However, the laser fluence and the speed scan, which indicates the number of pulses, were varied.

Fig.III.18. illustrates the different MeP-Si morphologies obtained for F ranging in 75 to 105 mJ/cm² and for N varied from 80 to 200 pulses. For F = 75 mJ/cm², clear LIPSS organizations can be observed for N = 80-100 pulses. The applied fluences have been chosen to be higher than the threshold ablation in order to form LIPSS organization as reported in several studies [23][24] showing that LIPSS are generated for laser fluence close to the ablation threshold for a limited number of pulses typically few tens, in accordance with the value N (80-100) for our experiments. Under such experimental conditions, it is accepted that LIPSS formation mechanism can be explained by interference model.

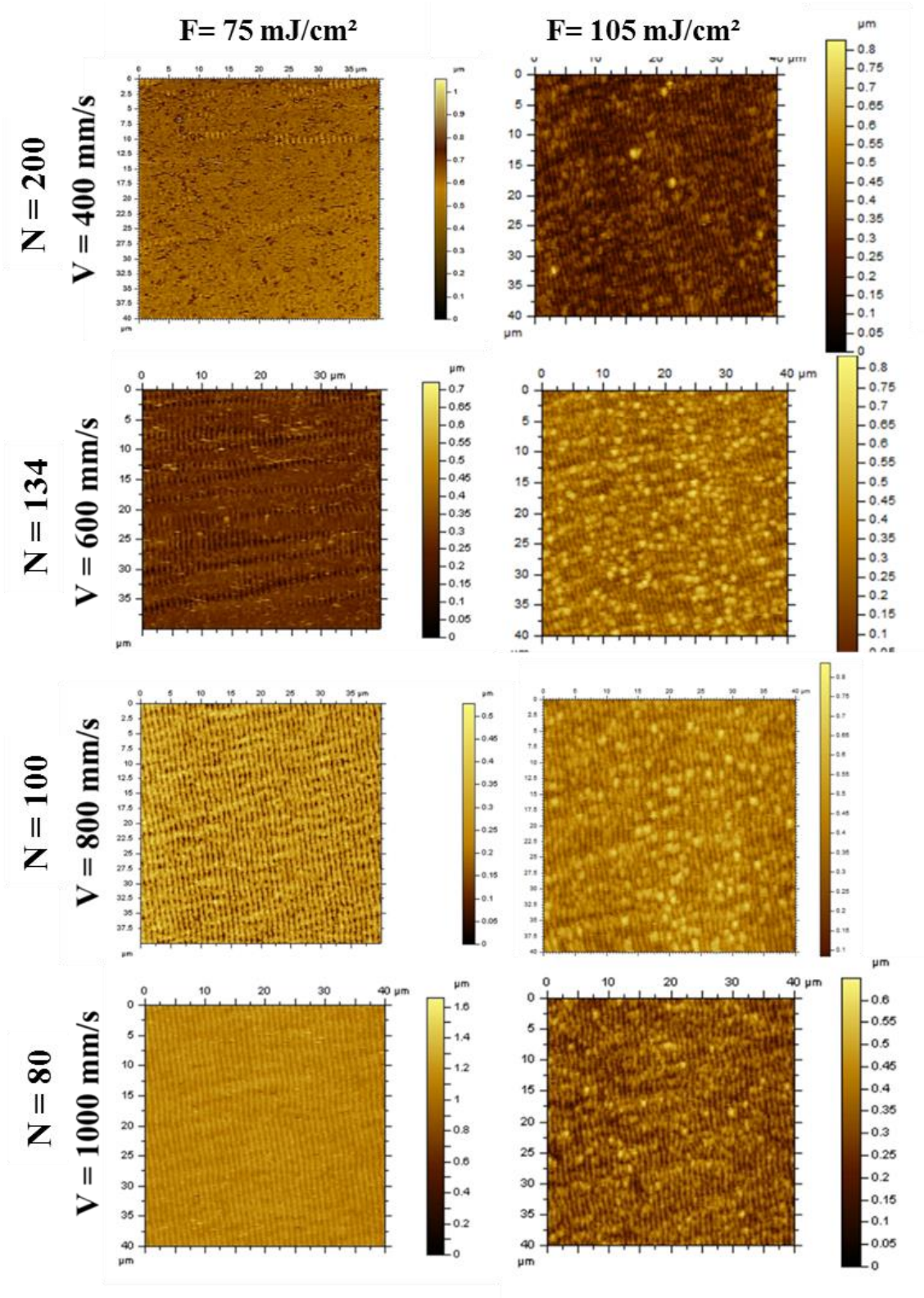

Figure.III.18. AFM views of MeP-Si morphologies after fs irradiation @ 1030 nm at different F and N.

Here, the average period of LIPSS formed (for F = 75 mJ/cm² and N in the range of 80-100) is ~ 950 nm which is slightly smaller than the working wavelength 1030 nm (Fig.III.19.). Their orientation is perpendicular to the beam polarization as shown in Fig.III.20. For the same fluence, when N is

higher than 134 pulses, the LSFL organization start to be destroyed and only short LSFL could be observed. A strong ablation process starts to damage the LIPSS, there is a deposit of removal material on the surface that perturbs the AFM characterization leading to low resolution-quality images. The AFM images obtained for samples irradiated at 105 mJ/cm² confirm the initiation of an ablation process leading to a surface covered by random distribution of nanoparticles from re-deposition.

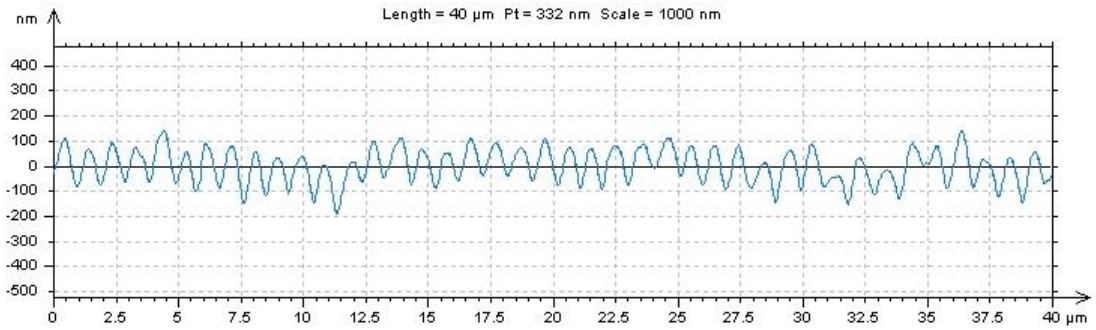

Figure.III.19. AFM Surface profile of MeP-Si irradiated by 500 fs @ 1030 nm (F = 75 mJ/cm² and N = 80).

Large homogenous MeP-Si surfaces of 25×25 mm² covered by LSFL with a period of ~ 1030 nm has been be obtained for a fluence near or slightly above to the ablation threshold at a relatively low number of pulses that implies a reduction of processing time especially for high repetition rate. The processing time needed to obtain a LSFL organization (as shown in Fig.III.20.) is estimated to be 0.2 s/mm². This means that the time required to treat a surface of 25 ×25 mm² is roughly 2 minutes.

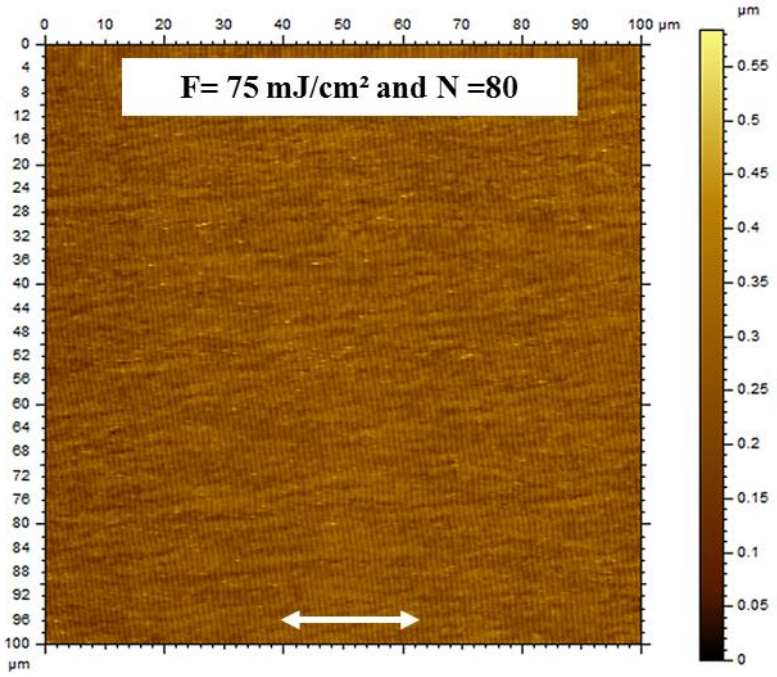

Figure.III.20. LSFL organization formed on 25×25 mm² MeP-Si surface by 500 fs laser @ 1030 nm.

IV. Titanium oxide thin film

1. Elaboration of titanium oxide thin film samples

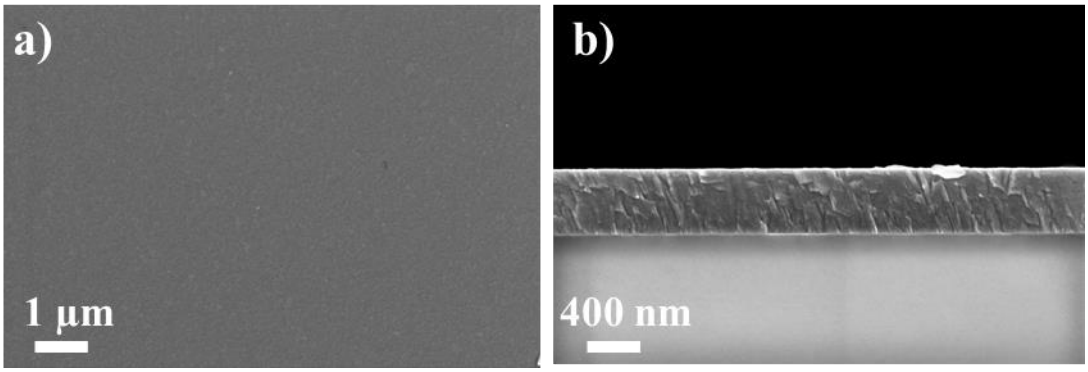

Figure.III.21. SEM characterization of $TiO_{1.6}$ thin film: a) top view and b) cross section.

Pulsed-laser deposition (PLD) method has been used to grow titanium oxide thin films with a thickness of 500 nm onto SiO_2/Si substrate (Fig.III.21.). A KrF excimer laser beam (248 nm, 10Hz) was focused onto a stoichiometric ceramic TiO_2 target located in a PLD chamber under a 10^{-6} mbar vacuum. This low ambient pressure produces a lack of oxygen in the deposited material and then O/Ti ratio of thin films is not 2 as expected but rather 1.6 to 1.8 (as reported in [18]).

The laser beam (4 J/cm² in fluence) is focused onto the target. The plasma plume transports the target species towards the substrate (located at a distance of 50 mm in front of the target). The substrate was hold at 700°C during the growth in order to induce a better crystallinity of the films. A schematic and view of PLD reactor is given in Fig.III.22.

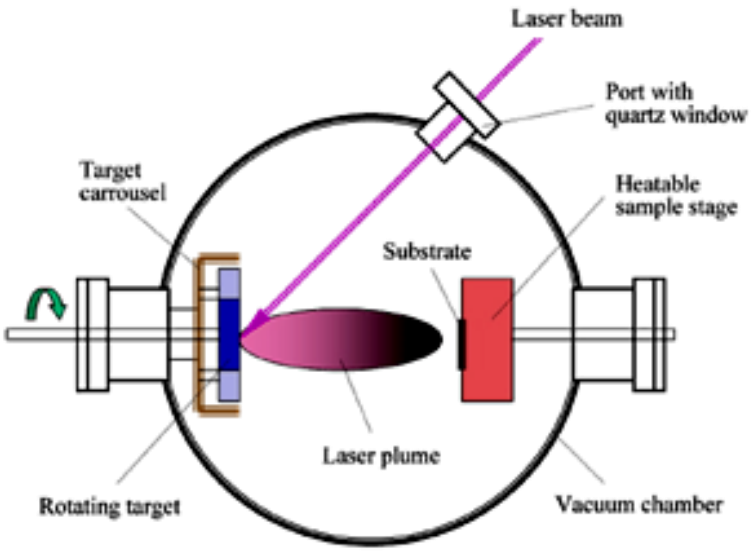

Figure.III.22. Scheme of PLD reactor used for TiO_x thin film deposition in GREMI.

2. LIPSS formation on titanium oxide thin films

In this section, we were interested to investigate the LIPSS formation on titanium oxide thin films grown by pulsed laser deposition method. The nanostructuring of TiO_x thin films is explored from a single laser spot to a large homogenous surfaces, typically 5x5 mm² in our case, depending on the laser dose (i.e. beam fluence and pulse number). The results are obtained by the use of 100 fs laser @ 266 nm and for a repetition rate fixed to 1000 Hz. The samples were placed before the focal plan of the lens leading to a relatively large spot size of ~ 350 µm in diameter.

1. Single laser spot

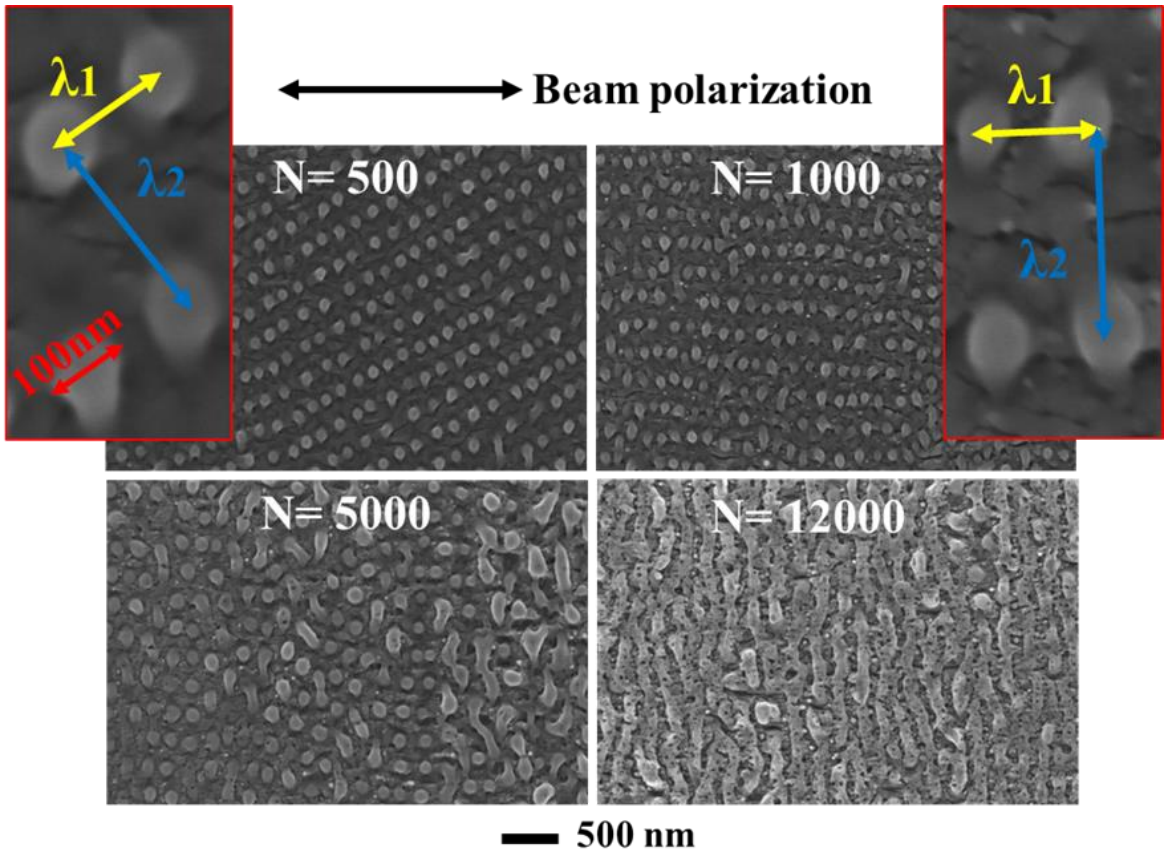

Figure.III.23. SEM characterizations of TiO1.6 thin film surfaces irradiated by GREMI fs laser beam at 100 mJ/cm² for various N.

Fig.III.23. shows the SEM views of the surface morphology of $TiO_{1.6}$ depending on the number of laser pulses N ranging from 500 to 20000 at a fixed fluence of 100 mJ/cm². At N = 500, regular periodic dots (circles) as 2D nanostructures organization are formed. These regular dots are 100 nm in diameter and are aligned in well-defined lines that could be considered as a typical LIPSS organization with two periods depending on the orientation of the lines. The first period (λ1) estimated by SEM is close to 160 nm, which corresponds to the half of the UV laser wavelength. It is

widely accepted in the literature [25][26]that nanostructures with such a period can be considered as HSFL(High Spatial Frequency LIPSS). The second period ($\lambda 2$) is close to the working wavelength of 266 nm, which is attributed to LSFL. At this number of shots, these 2D nanostructures present an intermediate orientation which is neither perpendicular nor parallel to the beam polarization, but tilted at a angle of 30° with respect to the beam polarization. A similar 2D organization was also observed by increasing N to 1000 shots, resulting in a slight deformation of the shape of the dots. Some nanostructures started to coalesce in the direction perpendicular to the laser beam polarization. This result evidences a good control of the orientation by the beam polarization, since the orientation of LSFL became parallel to the beam polarization while the orientation of HSFL became perpendicular to the beam polarization. When N increases up to 5000 shots, this surface morphology was modified: previous dots were transformed into irregular structures due to the coalescence of the dots formed at $N < 1000$. Lastly, after $N = 20000$ shots, a new shape of nanostructures with a period of around 240 nm was formed perpendicular to the polarization, typical for LSFL.

The formation mechanisms of these nanostructures are still unclear. As discussed in the first chapter, two models are currently under discussion, interference (coupled with excitation of surface Plasmon polaritons) and free-surface energy minimization [27]. In the present study, the formation of nanostructures could be attributed to free-surface energy minimization, well-known as "the self-organization approach". LIPSS may develop in the melt phase, which appears on the sample surface after laser radiation. Therefore, the surface organization is a result of melt phase redistribution. Under ultra-short laser irradiation, several phenomena could occur such as heating, melting and boiling due to the high absorption of energy. This is especially true under UV irradiation (high absorption coefficient and low penetration depth) which induces an increase in surface temperature where molten material could be formed [17][15][28]. This molten material is subjected to different thermo-dynamic forces such as surface tension gradient (due to the non-uniform heating), thermal capillarity and/or Plateau-Rayleigh instability [29] leading to changes in the surface morphology. The minimization of surface energy due to hot liquid material transport towards cold regions results in the agglomeration of melt material in regular dots as shown in Fig.III.23.[30][31]. To the best of our knowledge, these droplets are only visible on thin film samples, which clearly evidences the role of the free surface energy in the formation of these nanostructures, particularly in nanomaterials, where the surface-to-bulk ratio is much larger than in bulk materials. As reported in the case of copper thin films irradiated by a picosecond laser beam, regular dots (200 nm in diameter and 270 nm in period) with an orientation perpendicular to the laser beam polarization were evidenced [6][32].

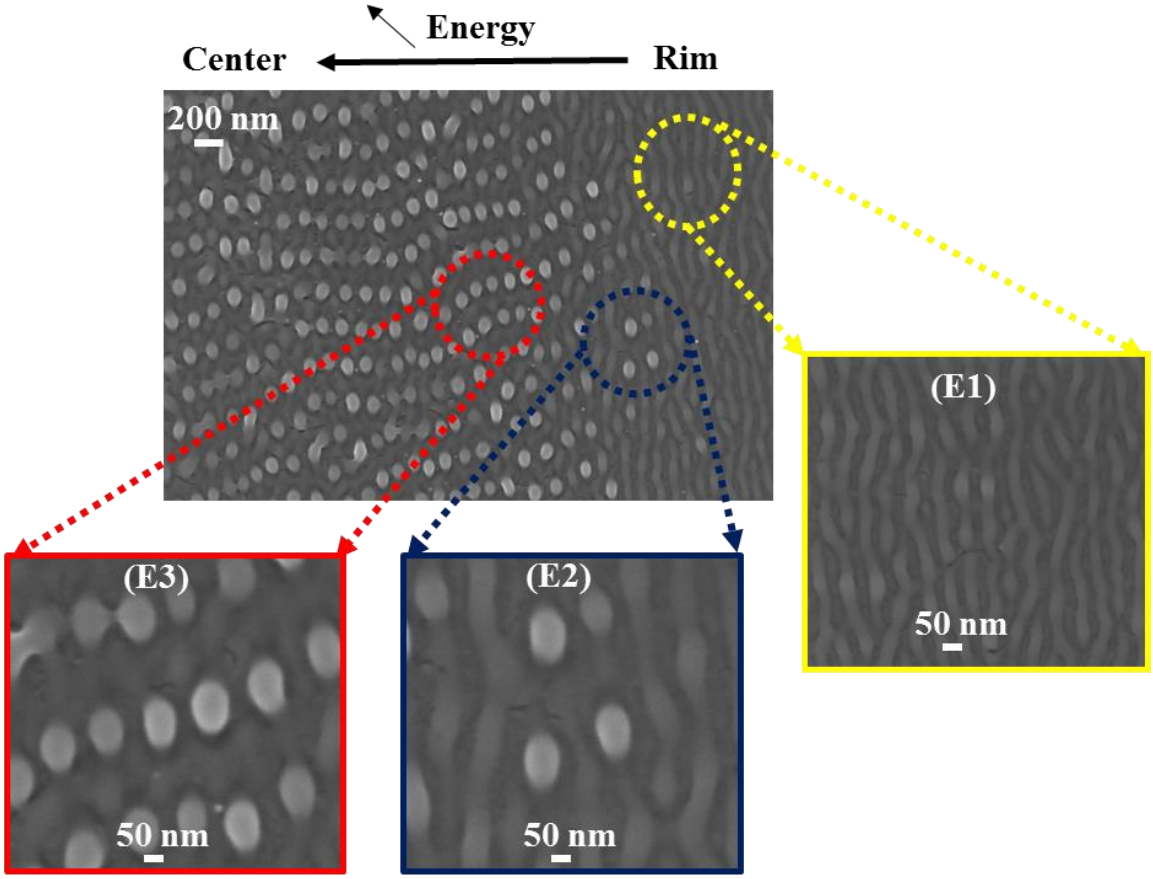

Figure.III.24. SEM views of the rim of the laser spot at 100 mJ/cm² and after 1000 shots.

Fig.III.24. presents the image of $TiO_{1.6}$ morphology at the rim of the irradiated zone at 100 mJ/cm² and after 1000 shots. This illustrates the various stages in the formation of dots at the same N value but at different localized fluences. Due to the pseudo-Gaussian shape of the laser beam, the energy increases from the outer region toward the center region of the laser spot, which means that the localized energy are distributed as follows : E1 <E2 < E3. This induces two types of nanostructures. The outer region (E1 zone) shows the earlier stage of evolution while the inner region (E3) corresponds to the more fully evolved surface organization. Therefore, the intermediate (E2 zone) displays the transition surface morphology between E1 and E2. Zone E1 shows nano-ripples (HSFL) with a period close to 130 nm and an orientation perpendicular to the beam polarization formed at low local fluence [25]. When the local energy increases steadily from the E1 to the E3 zone, the HSFL organization becomes unstable under the influence of hydrodynamic instabilities and surface tension at high temperature. These forces move and redistribute the melt material inside the HSFL into short and discontinuous quasi-periodic ripples in order to minimize the surface energy (in E2). Then thermal capillarity forces move the hot melt material toward cold region, leading to the formation of circular droplets in zone E3. Therefore the second period of observed dots comes from the first HSFL formed at low fluence. This result is in good agreement with previous one published

on ZnO thin films, assuming that low fluences promote HSFL formation whereas higher fluences promote LSFL formation [25].

By increasing the pulse number, thermodynamic forces lead to different surface morphologies. This evolution, presented in Fig.III.23. For different N values, suggests the formation of nanostructures due to the relaxation of hydrodynamic instabilities controlled by the laser fluence. It is difficult to link the orientation of these structures with the beam polarization since, as shown previously, the orientation of these nanostructures changes with the number of pulses and local fluences from a random orientation (for N = 500) to an orientation parallel to the polarization (for N = 1000) and an orientation perpendicular to the polarization after 20000 shots.

The formation mechanism of LIPSS on $TiO_{1.6}$ during fs irradiation in such conditions seems to be the result of molten material relaxation mechanisms. In order to confirm this observation, a simple experiment in which a $TiO_{1.6}$ film has been irradiated by 40 ps laser @ 266 nm under the same conditions (F = 100 mJ/cm² and N =1000) has been performed. The results of this experience are presented in Fig.III.25. The first SEM image shows the generation of at least four different morphologies on the same laser spot (same laser dose). However, due to the quasi-Gaussian distribution of the beam, the local energy deposition is not uniform. The zone (a) shows a typical LSFL with period ~ 250 nm and orientation parallel to the beam polarization. In contrast, within few micrometers, a LSFL organization with shorter period ~ 225 nm is formed with polarization perpendicular to the polarization. Therefore, linking the orientation of LIPSS with the beam polarization seems to be very complicated here. Further, a dot organization similar to those observed with fs laser, appears in the ps regime but with larger diameters ranging from 150 nm to 215 nm (zone a and b). Assuming the role of molten material in the LIPSS generation, the formation of larger dots in ps regime is an expected result since the thermal melting could occur much easier in ps time scale than in fs time due to a pulse duration larger than the thermalization time. This means that, under ps regime the amount of molten material is more important than those formed under femtosecond regime. This leads to the formation of larger dots after relaxation and cooling, but also to the formation of a wide variety of different morphologies that cannot be explained.

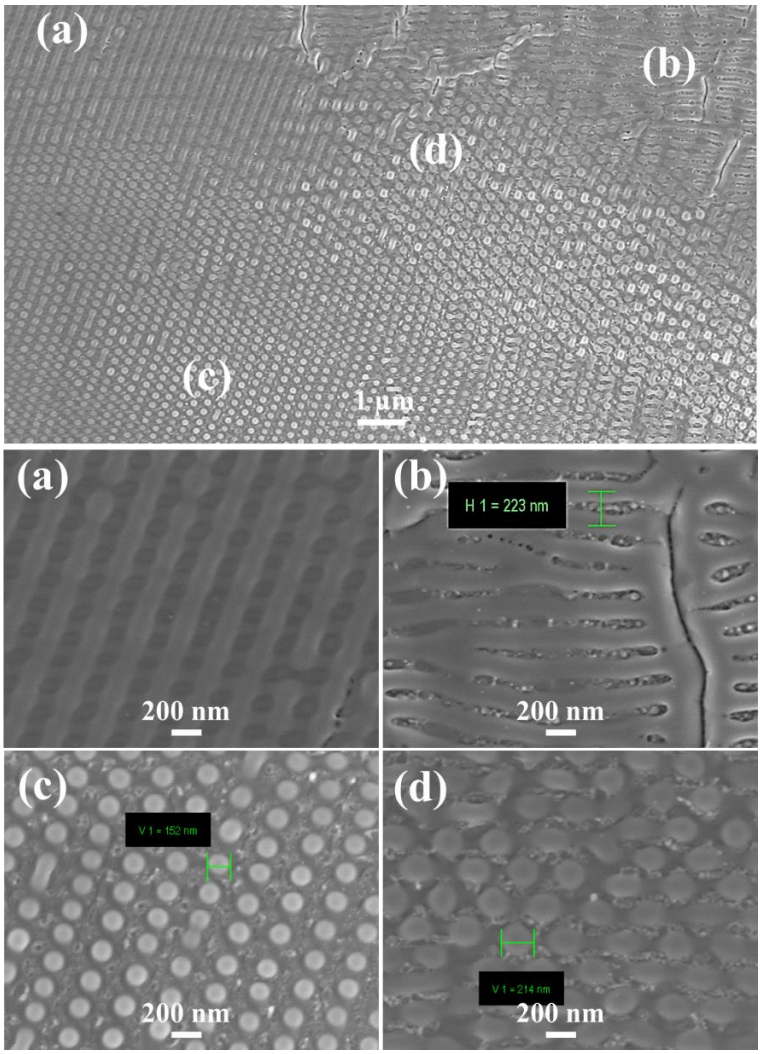

Figure.III.25. SEM views of TiO1.6 irradiated by 40 ps laser @ 266 nm for F=100 mJ/cm² and after 1000 shots.

As example of hydrodynamic forces that can contribute in the mechanisms of dots formation from HSFL, Plateau-Rayleigh instability model[33][31] (Fig.III.26) could match very well with the experimental results presented in Fig.III.24.

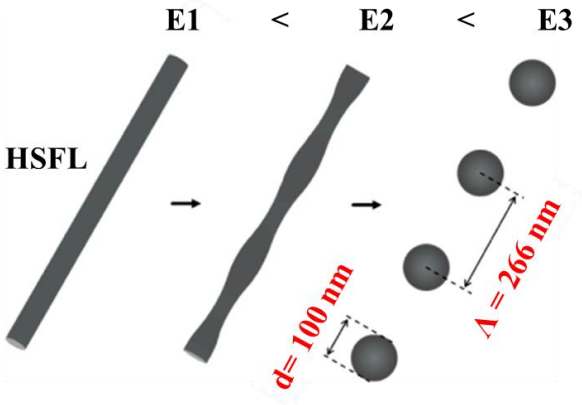

Figure.III.26. Schematic of Plateau-Rayleigh instability model showing a HSFL transformed into circular dots.

3. Large surface nanostructuring

In this part, a $TiO_{1.6}$ surfaces of 5×5 mm² were treated with the 100 fs laser @ 266 nm (as previously for MeP-Si). The fluences were varied in the 15 to 30 mJ/cm² range with a translation step from 3 to 6 µm, corresponding to pulse numbers of 13000 and 3300 (estimated by formula (Eq. IV.1)). Fig.III.27. (fluence 15 mJ/cm² and 13000 shots) shows a homogenous surface covered by regular dots with two periods at 266 nm and 160 nm, identical to the nanostructures obtained at 100 mJ/cm² and 1000 shots on a single laser spot.

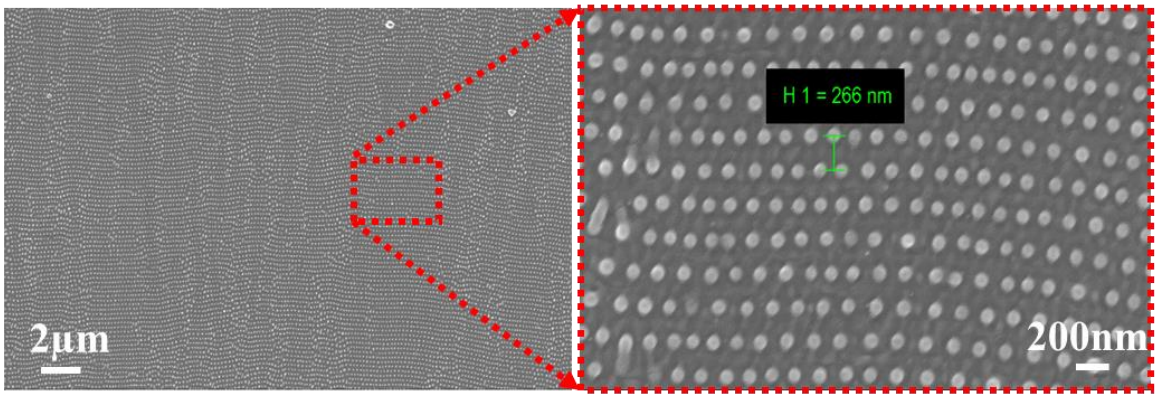

Figure.III.27. Periodic dots formed on 5×5 mm² TiO1.6 surface by 100fs laser @ 266 nm (F=15 mJ/cm² and N~13000).

Decreasing the laser pulse number to 3300 and increasing the fluence to 30mJ/cm^2 (Fig.III.28.), short LIPSS with a period of 230 nm close to the working wavelength and an orientation parallel to the beam polarization are formed.

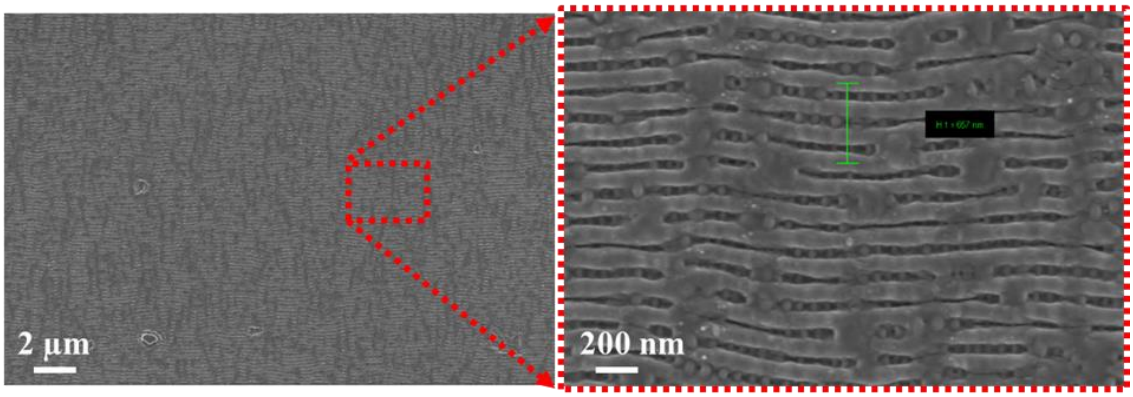

Figure.III.28. LSFL organization formed on 5×5 mm² TiO1.6 surface by 100fs laser @ 266 nm (F=30 mJ/cm² and N~3300).

An intermediate morphology is formed (Fig.III.29.) when reducing the fluence to 25 mJ/cm² at the same number of pulses (3300). Periodic dots are obtained inside LSFL at these laser parameters. Small structures are formed between LSFL lines like small "bridges" linking LSFL. No dots are

observed in these regions. However, HSFL and LSFL organization could coexist and interconnect in the same zone. The origin of the small bridges is coming from the HSFL formed probably at low laser dose. This morphology could be considered like a 3D organization. Three morphologies are formed as function of amplitude. First HSFL are formed, then LSFL and lastly dots. This "complex" morphology assumes that the liquid phase formed was subjected to the different forces leading to such organization after relaxation and cooling, but also indicates there is a continuous evolution of the surface morphology from regular periodic drops to regular LSFL which confirms also the self-organization model proposed to explain the nanostructures formation mechanisms.

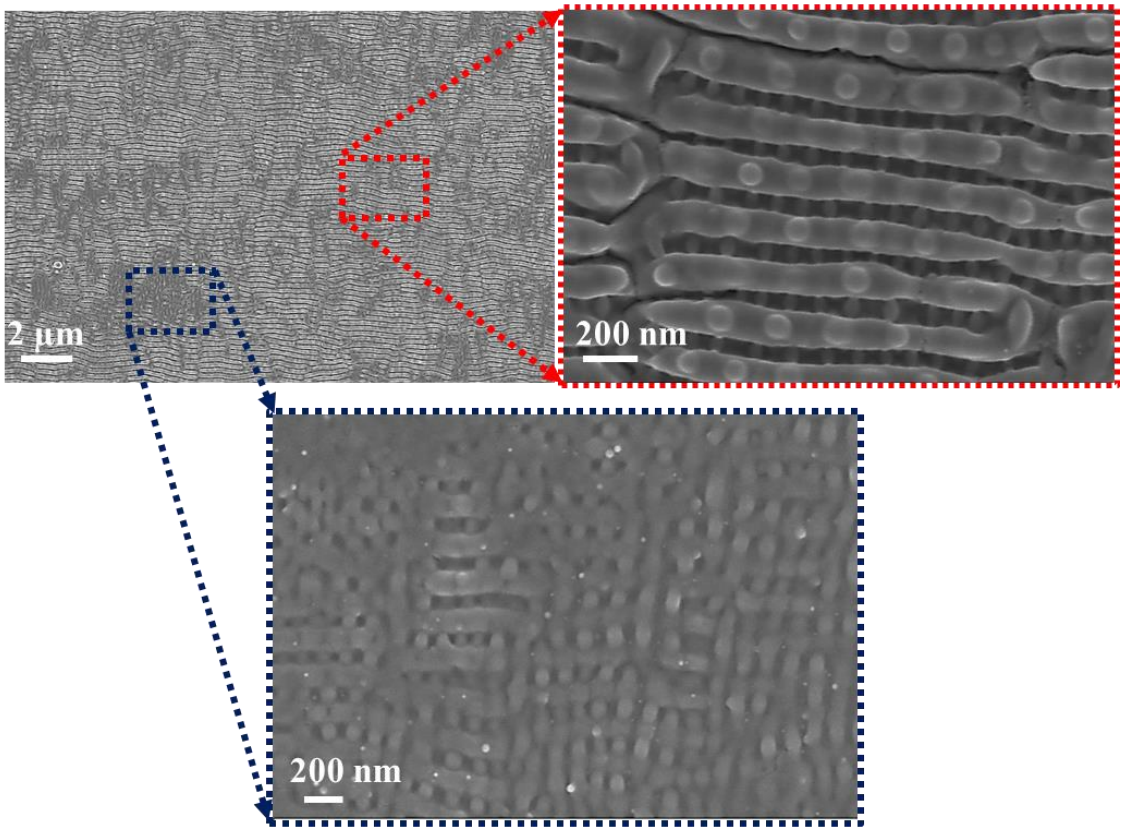

Figure.III.29. LSFL and dots organizations generated on 5×5 mm² TiO1.6 surface by 100fs laser @ 266 nm (F=25 mJ/cm² and N~3300).

For F = 30 mJ/cm² and 13000 laser pulses (Fig.III.30.), the laser dose becomes high enough to completely destroy the previous nanostructures and to create new microstructures via ablation-evaporation process. The chemical composition at the surface may be altered especially by reduction of the oxygen contained inside these microstructures, indicated by the change of contrast in the SEM image, as already reported for ZnO irradiated by a KrF laser [34].

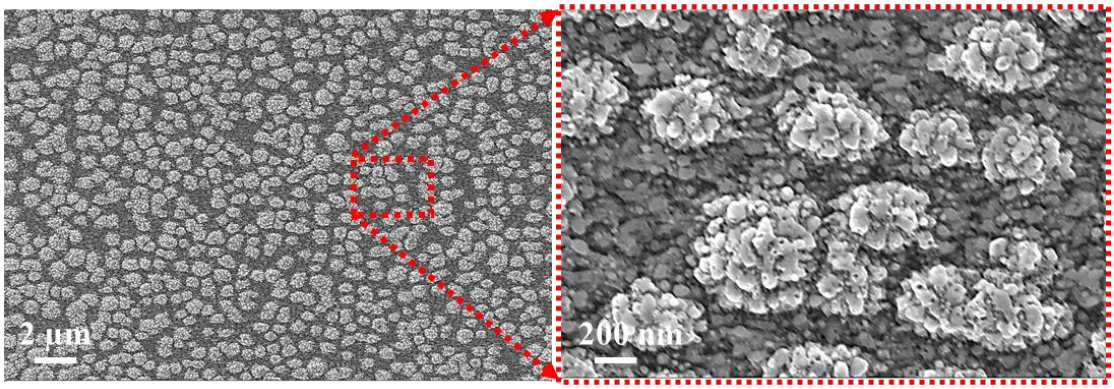

Figure.III.30. Ablated large surface of TiO1.6 irradiated by 100fs laser @ 266 nm (F=30 mJ/cm² and N~13000).

The use of relatively low fluences < 30 mJ/cm² (ablation threshold of bulk TiO_2 ~ 240 mJ/cm² after 1000 pulses) for large surface treatment was helpful to obtain homogeneous structured surfaces without locally ablated zones. The nanostructures formed at a large scale seem to be more periodic and uniform than those formed without using scanning (fig.III.23. vs .fig III.27.). This could be explained by a better homogeneity of the laser beam energy deposited. When the beam is focused onto a single laser spot (stationary regime), the local energy absorbed by the surface is not the same at each point of the laser spot surface due to the quasi Gaussian distribution which induces nanostructured zones and ablated zones on the same spot. The translation of the beam in x,y directions enables a graded distribution of energy on the whole surface (each point in the scanned surface receives the same amount of energy) and the increase in the laser dose is achieved by the accumulation of laser pulses. In addition it can be observed that a similar dots organization is obtained with a laser fluence of 100 mJ/cm² after 1000 shots and with a fluence of 15 mJ/cm² after 13000 shots. This phenomenon can be explained by the reduction in the energy threshold of these dots due to the incubation effect.

The processing times are varied in the range of 28 to 112 s/mm² for respectively N = 3300 and 13000. These relatively long processing times are due to the low fluences, the inhomogeneity of the laser beam and the limited repetition rate of the used laser (as explained previously in the case of MeP-Si).

Conclusion

The LIPSS formation on MeP-Si and $TiO_{1.6}$ thin films under femtosecond irradiation has been investigated. Under low fluence and high number of pulse, the experimental findings obtained by fs laser are very similar to those observed with ps laser. This assumes that under such conditions, thermal effects like thermal melting could occur even in the fs scale.

The nanostructuring of large surface of MeP-Si was successfully performed with 100 fs laser (@ 266 nm) as well as with 500 fs laser (1030 nm). The processing time is also successfully reduced from 112 to 0.2 mm²/s for respectively100 fs (1 kHz) and 500 fs (100 kHz).

The formation of different nanostructure morphologies (dots, HSFL, LSFL) on non-stoichiometric titanium oxide thin films was displayed. The experimental observations of the evolution of the $TiO_{1.6}$ surface morphology suggest the free-surface energy minimization as a formation mechanism of these organizations. The micro-nanostructuring of a large area surface of $TiO_{1.6}$ was also successfully performed by the use of relatively low laser fluences with a large number of pulses.

The main results shown in this chapter are summarized in the following table:

<table>
<tr><td rowspan="6">Mesoporous Silicon

MeP-Si</td><td>100 fs laser @ 266 nm (1 kHz)</td><td>500 fs laser @ 1030 nm (100kHz):</td></tr>
<tr><td>LSFL are generated from organization of NPs generated after few hundred pulses and for low fluence ~ 20 mJ/cm².</td><td>Ablation threshold is determined to be 60 mJ/cm² for 1 pulse.</td></tr>
<tr><td>Periodic localized molten phase is produced 100 nm in depth.</td><td rowspan="2">Incubation coefficient is estimated to be 0.86.</td></tr>
<tr><td rowspan="2">The experimental findings obtained with fs laser seem to be very similar to those observed with ps laser (chapter II).</td></tr>
<tr><td rowspan="2">The nanostructuring of large surfaces, up to 25x25 mm², is performed.</td></tr>
<tr><td>Incubation effect plays a very important role in LIPSS formation and melting processes.</td></tr>
</table>

	The nanostructuring of large homogenous surfaces is successfully performed.	The processing time is greatly reduced
	The LSFL formation mechanism in dynamic mode is very different than in the stationary mode, and seems to be like a lithography process.	
Titanium oxide thin films (500 nm) TiO1.6	100 fs laser @ 266 nm (1 kHz)	
	Different types of nanostructures are generated from HSFL, LSFL to regular dots.	
	The formation mechanisms of these nanostructures is attributed to the free-surface energy minimization.	
	Hydro-thermodynamic forces and especially Plateau-Rayleigh instability model are satisfying to explain the transition from HSFL to regular dots.	
	Nanostructuring of large surface is also performed at low fluences.	
	The processing time is relatively long as the laser has a limited repetition rate.	

Table.III.2. main findings shown in this chapter.

V. References

[1] A. Y. Vorobyev, C. Guo, “Direct femtosecond laser surface nano/microstructuring and its applications”, Laser Photonics Rev., vol 7, no 3, 385–407, 2013.

[2] Jorn Bonse, Sandra Hohm, Sabrina V. Kirner, Arkadi Rosenfeld, Jorg Kruger, “Laser-Induced Periodic Surface Structures — A Scientific Evergreen”, IEEE JOURNAL OF SELECTED TOPICS IN QUANTUM ELECTRONICS, vol 23, no 3, 2017.

[3] S. Höhm, A. Rosenfeld, J. Krüger, J. Bonse, “Laser-induced periodic surface structures on titanium upon single- and two-color femtosecond double-pulse irradiation”, Opt. Express, vol 23, no 20, 25959–25971, 2015.

[4] T. J. Y. Derrien, R. Koter, J. Krüger, S. Höhm, A. Rosenfeld, J. Bonse, “Plasmonic formation mechanism of periodic 100-nm-structures upon femtosecond laser irradiation of silicon in water”, J. Appl. Phys., vol 116, no 7, 2014.

[5] M. Martínez-Calderon, A. Rodríguez, A. Dias-Ponte, M. C. Morant-Miñana, M. Gómez-Aranzadi, S. M. Olaizola, “Femtosecond laser fabrication of highly hydrophobic stainless steel surface with hierarchical structures fabricated by combining ordered microstructures and LIPSS”, Appl. Surf. Sci., vol 374, 81–89, 2016.

[6] T. T. D. Huynh N. Semmar, “Dependence of ablation threshold and LIPSS formation on copper thin films by accumulative UV picosecond laser shots”, Appl. Phys. A Mater. Sci. Process., vol 116, no 3, 1429–1435, 2014.

[7] F. Ruffino, A. Pugliara, E. Carria, L. Romano, C. Bongiorno, G. Fisicaro, A. La Magna, C. Spinella, M. G. Grimaldi, “Towards a laser fluence dependent nanostructuring of thin Au films on Si by nanosecond laser irradiation”, Appl. Surf. Sci., vol 258, no 23, 9128–9137, 2012.

[8] S. Harada, K. Tanaka, H. Inui, “Thermoelectric properties and crystallographic shear structures in titanium oxides of the Magnli phases”, J. Appl. Phys., vol 108, no 8, 1–7, 2010.

[9] I. Vaiciulis, M. Girtan, A. Stanculescu, L. Leontie, F. Habelhames, S. Antohe, “on Titanium Oxide Spray Deposited Thin Films for Solar Cells Applications”, Proc. Rom. Acad. Ser. A, vol 13, no 4, 335–342, 2012.

[10] T. Watanabe, Nakajima, R. Wang, M. Minabe, S. Koizumi, A. Fujishima, K. Hashimoto,

"Photocatalytic activity and photoinduced hydrophilicity of titanium dioxide coated glass", Thin Solid Films, vol 351, 260–263, 1999.

[11] O. I. Eroshov, P. Perminov, S. V. Zabotnov, M. B. Gongal'skii, A. A .Ezhov, L. A. Golovan, P. K. Kashkarov, "Structural properties of silicon nanoparticles formed by pulsed laser ablation in liquid media", Crystallogr. Reports, vol 57, no 6, 831–835, 2012.

[12] N. G. Semaltianos, S. Logothetidis, W. Perrie, S. Romani, R. J. Potter, S. P. Edwardson, P. French, M. Sharp, G. Dearden, K. G. Watkins, "Silicon nanoparticles generated by femtosecond laser ablation in a liquid environment", J. Nanoparticle Res., vol 12, no 2, 573–580, 2010.

[13] R. Intartaglia, K. Bagga, F. Brandi, "Study on the productivity of silicon nanoparticles by picosecond laser ablation in water: towards gram per hour yield.", Opt. Express, vol 22, no 3, 3117–27, 2014.

[14] S. Gräf, F. A. Müller, "Polarisation-dependent generation of fs-laser induced periodic surface structures", Appl. Surf. Sci., vol 331, 150–155, 2015.

[15] A. Rousse, C. Rischel, S. Fourmaux, I. Uschmann, S. Sebban, G. Grillon, P. Balcou, E. Förster, J. P. Geindre, P. Audebert, J. C. Gauthier, D. Hulin, "Non-thermal melting in semiconductors measured at femtosecond resolution", Nature, vol 410, no 6824, 65–68, 2001.

[16] N. Medvedev, Z. Li, B. Ziaja, "Thermal and nonthermal melting of silicon under femtosecond x-ray irradiation", Phys. Rev. B - Condens. Matter Mater. Phys., vol 91, no 5, 1–10, 2015.

[17] N. M. Bulgakova, "Theoretical Models and Qualitative Interpretations of Fs Laser Material Processing", J. Laser Micro/Nanoengineering, vol 2, no 1, 76–86, 2007.

[18] A. I. Andrei, E. V Golosov, R. K. Yu, I. K. Sergei, A. E. Ligachev, V. M. Sergei, N. N. Yurii, L. V Seleznev, D. V Sinitsyn, "Formation of quasi-periodic nano- and microstructures on silicon surface under IR and UV femtosecond laser pulses", Quantum Electron., vol 41, no 9, 829, 2011.

[19] G. Raciukaitis, M. Brikas, P. Gecys, M. Gedvilas, "Accumulation effects in laser ablation of metals with high-repetition- rate lasers Gediminas", Proc. of SPIE Vol. 7005, 2008.

[20] J. M. Liu, "Simple technique for measurements of pulsed Gaussian-beam spot sizes", Opt. Lett., 7, 196-198, 1982.

[21] J. Bonse, S. Baudach, J. Krüger, W. Kautek, M. Lenzner, “Femtosecond laser ablation of silicon - modification thresholds and morphology”, Appl. Phys. A, vol 74, no 1, 19–25, 2002.

[22] J. B. J. Savolainen, M. Snogdahl, C. Peter, “Ultra-short pulse laser ablation of metals : threshold fluence , incubation coefficient and ablation rates”, Appl Phys A, 97–101, 2010.

[23] X. Ji, L. Jiang, X. Li, W. Han, Y. Liu, A. Wang, Y. Lu, “Femtosecond laser-induced cross-periodic structures on a crystalline silicon surface under low pulse number irradiation”, Appl. Surf. Sci., vol 326, 216–221, 2015.

[24] J. Bonse, A. Rosenfeld, J. Kruger, “On the role of surface plasmon polaritons in the formation of laser-induced periodic surface structures upon irradiation of silicon by femtosecond-laser pulses”, J. Appl. Phys., vol 106, no 10, 2009.

[25] D. Dufft, A. Rosenfeld, S. K. Das, R. Grunwald, en J. Bonse, “Femtosecond laser-induced periodic surface structures revisited: A comparative study on ZnO”, J. Appl. Phys., vol 105, no 3, 2009.

[26] R. Le Harzic, D. Dörr, D. Sauer, M. Neumeier, M. Epple, H. Zimmermann, F. Stracke, “Formation of Periodic Nanoripples on Silicon and Germanium Induced by Femtosecond Laser Pulses”, Phys. Procedia, vol 12, 29–36, 2011.

[27] J. Reif, O. Varlamova, S. Uhlig, S. Varlamov, M. Bestehorn, “On the physics of self-organized nanostructure formation upon femtosecond laser ablation”, Appl. Phys. A, vol 117, no 1,179–184, 2014.

[28] T. T. D. Huynh, M. Vayer, A. Sauldubois, A. Petit, N. Semmar, “Evidence of liquid phase during laser-induced periodic surface structures formation induced by accumulative ultraviolet picosecond laser beam”, Appl. Phys. Lett., vol 107, no 19, 2015.

[29] S. Strobel, C. Kirkendall, J. Chang, “Thermal stability of electrodeposited platinum nanowires and morphological transformations at elevated temperatures”. Nanotechnology 23, 475710, 2012.

[30] T. T. D. Huynh, A. Petit, N. Semmar, “Picosecond laser induced periodic surface structure on copper thin films”, Appl. Surf. Sci., vol 302,109–113, 2014.

[31] M. Gedvilas, G. Raiukaitis, V. Kuikas, K. Regelskis, “Driving forces for self-organization in thin metal films during their partial ablation with a cylindrically focused laser beam”, AIP

Conf. Proc., vol 1464, no 2012, 229–243, 2012.

[32] T. T. D. Huynh, A. Petit, N. Semmar, “Picosecond laser induced periodic surface structure on copper thin films”, in Applied Surface Science, vol 302,109–113, 2014.

[33] K. Jacobs, U. Saarlandes, “Influence of Slip on the Rayleigh-Plateau Rim Instability in Dewetting Polymer Films”, PRL 113, 014501, 2014.

[34] N. Semmar, M. Tebib, J. Tesar, N. N. Puscas, E. Amin-chalhoub, “Applied Surface Science Direct observation of phase transitions by time-resolved pyro / reflectometry of KrF laser-irradiated metal oxides and metals”, Applied Surface Science, vol 255, 5549–5552, 2009.

Chapter IV: New micro-ZT-meter for thermoelectric properties measurement and evaluation of nanostructuring effect on the evolution of TE properties of materials

I. Introduction

Electrical conversion of residual and environmental heat is still in progress for scientists and engineers throughout new materials and original architectures, combining micro and nanoscale to large area thermoelectric generators. Identification of the intrinsic properties of the assembled materials is also of a high interest and needs more and more valuable means for accurate measurements. In the two last chapters, we have focused in the investigation of the laser-matter interaction through studying the different physical phenomena allowing the formation of different micro-nano structures on mesoporous silicon and titanium oxide under ps and fs radiations. In this chapter, the use a modulated CO_2 laser beam is described as a new tool to probe the thermoelectric properties of materials through optimizing the laser heating process.

The present chapter is divided in two parts. In the first part a new homemade micro ZT-Meter (ZT refers to the thermoelectric figure of merit) is presented in details for the characterization of several type of materials (bulk or thin film). This setup allows a simultaneous measurement of basic thermoelectric parameters: thermal conductivity (k), electrical conductivity (σ) and Seebeck coefficient (S), from room temperature to 250°C. In the second part, this setup is used in order to evaluate the effect of laser nanostructuring of mesoporous silicon on the evolution of its thermoelectric properties.

II. ZT meter: Presentation and validation

Thermoelectric evaluation of material properties are often achieved using industrial modules e.g. ZEM3, LSR3, SeebSys, PPMS, MMR, SRX etc.[1][2][3][4][5][6] . Alleno et al[7] presented recently a test of uncertainties on these measurements and found that the accuracy on the Seebeck measurement is the main part of the metrology problem. Moreover, a lot of tentative Seebeck effect measurements on thin films are submitted to additional disadvantages like the mechanical stress, the thermal behavior of the whole system (film and substrate) and the incorrect position of sensors (electrical and thermal). A detailed review on measuring thermoelectric properties of a wide type of materials are now well detailed and easily reported in the literature according to the physic-chemistry of the thermoelectric materials [8][9][10][11][12]. Due to the phonon confinement and the thermal conductivity decrease, additional arrangements more specific to thin film configuration, as in plane and cross plane properties are also detailed in references [13][14]. Also, few homemade ZT-meter setups are specifically designed for the direct and simultaneous measurement of the Seebeck

coefficient and the electrical conductivity of a wide material state, from bulk to thin substrate and/or thin film materials for instance [15][16]. Often, the thermal conductivity measurement is additionally estimated using one of the adapted techniques like 3omega (3ω) and thermos-reflectance [17][18], or the time-domain pulsed photo-thermal [19][20][21], and rarely designed to be included in the same setup. In GREMI laboratory, a novel measurement setup is built in order to estimate simultaneously under the same thermodynamic conditions the main parameters for thermoelectricity. Electrical conductivity and Seebeck coefficient will be measured through an integrated four probe Van der Pauw method in a specific sample holder. In addition a heat flux sensor could be added and adapted to get real-time thermal conductivity measurement on bulk and coating materials.

III. Design and operating principle

In this section the design scheme of the thermoelectric property measurement device (ZT-meter) is presented. The operating principle of the micro-ZT-meter is detailed.

1. Design of the sensor-integrated sample holder

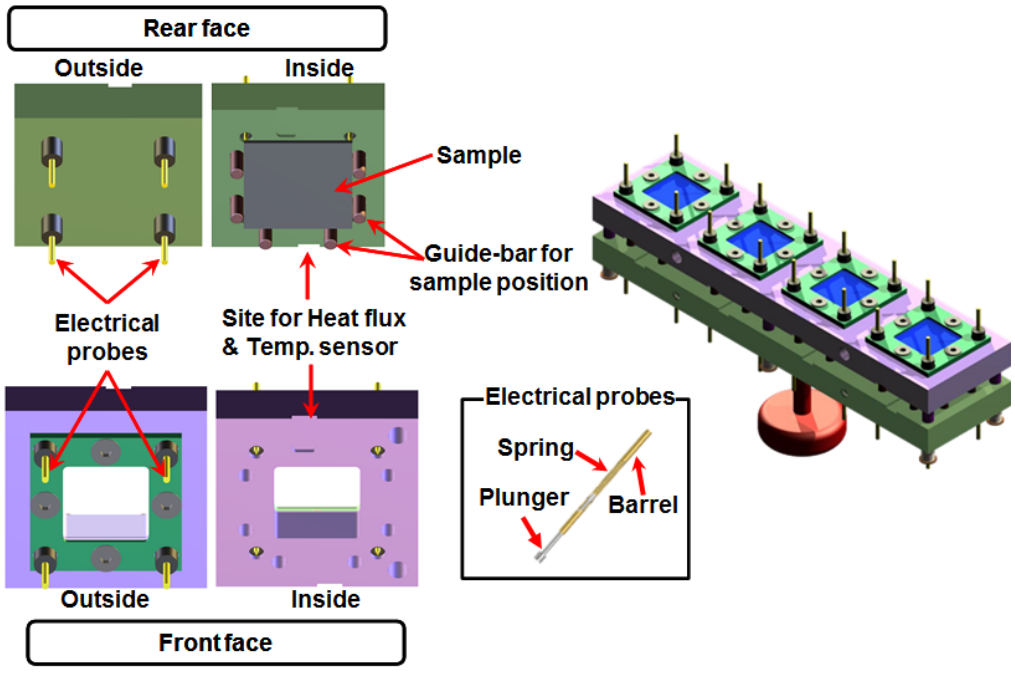

Figure.IV.1. ZT-meter design schematic view. Four sample holders are available. Each one is composed from two pieces with electrical probes on one-side and heat flux and temperature sensors on the other side. Six guide-bars are able to support the sample. Electrical probes are mounted on a spring close to the holder, maintaining the sample and facilitating all the contacts.

The ZT-meter illustrated in Fig.IV.1. is manufactured substantially from Poly-Ether Ether Ketone (PEEK) to ensure a good electrical insulating of the sample to be characterized with the remainder of ZT-meter components. It has four identical cells, mounted on triaxial travel system. Each cell is opened in front face to let pass the laser beam (heating source). Four electrical probes are mounted with square shape geometry on the front face and also four others on the rear face of each cell. These

electrical probes allow the measurement of voltage in order to determine the Seebeck coefficient (S). They serve also to determine the electrical resistivity (ρ) by four probes measurement technique, according to Van der Pauw method with square distributing of points [22]. Two heat flux sensors (Captec production®) with integrated thermocouples are installed at the top and the bottom of the front face and also two others on the rear face. Their roles are to measure the temperature and the heat flux density on the front and rear faces of the sample. These two physical quantities will allow us to determine the thermal conductivity (κ) of the samples. The sample is sandwiched between the front face and the rear one. By means of a guidance system, we ensure a good placement of the sample on the electrical probes and heat flux sensor into ZT-meter. In order to respect the geometric shape of Van der Pauw method, the samples must be of square shape with side of 25 mm. The electrical probes are springs probes (Fig.IV.1.). The plunger is made of beryllium-copper and the barrel is made of phosphor-bronze with gold plated. The spring allows plunger to be at the same level of heat flux sensor on the sample that ensures a good electrical and thermal contact.

2. Sample preparation

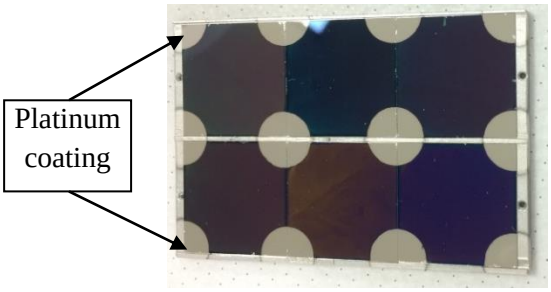

Figure.IV.2. Image of six samples after the deposition of platinum thin films by PVD on the four corners of each sample.

In order to improve the electrical contact between samples and electrical probes [23], a 50 nm platinum contact electrode was deposited at the four corners of the samples by PVD magnetron sputtering at 200W-DC power under an argon pressure of 10 µbar (Fig.IV.2.). The patterning of these electrodes is obtained through a metallic mask fixed on the sample during the sputtering process.

3. Operating principle

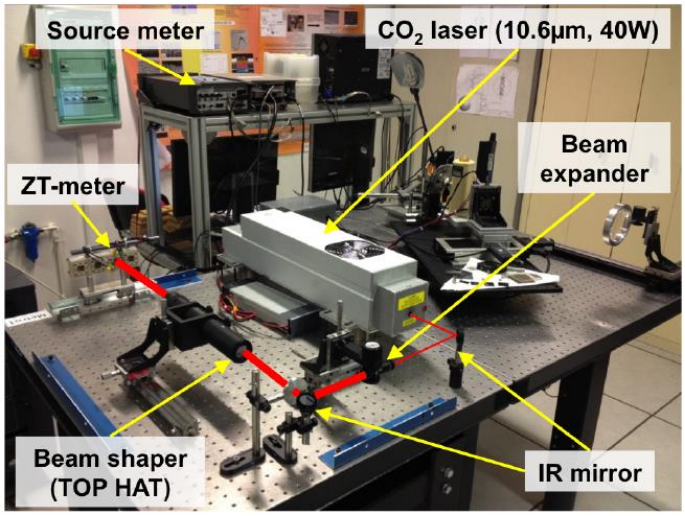

Figure.IV.3. Photography of the thermoelectric (TE) measurement station including the micro ZT-meter.

Fig.IV.3. shows the TE measurement station which includes: a CO_2 source laser (10.6 µm, 40 W and 4 mm of size laser beam) used as heating source, a beam expander to widen the diameter of laser beam up to 10mm of diameter, and a beam shaper to homogenize the beam energy in order to obtain a top-hat distribution instead of Gaussian one. Also, source-meter (Tektronix Company) 2450 last generation is dedicated to electrical resistivity measurement which can generate the current and make a very fast measurement of voltage with law noise. Multi-meter 2700 (Tektronix Company) equipped with multiplexer card (20 channels), for the measurement of the voltage and the temperature in order to determine the Seebeck coefficient and the flux density.

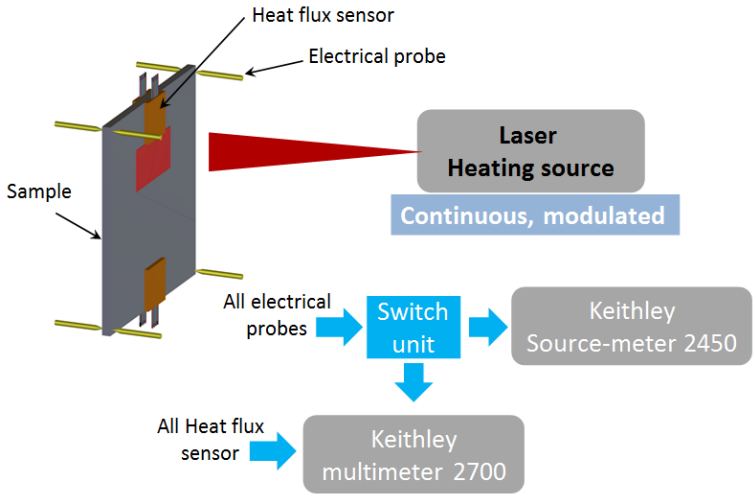

Figure.IV.4. Schematic representation of ZT-meter operation principle.

The operation principle of ZT-meter is illustrated on Fig.IV.4. The heating of the sample is provided by the CO_2 laser beam that can operate in continuous and modulated mode up to 1MHz (in our case the sample is not cooled). The top of the sample is heated on the front face creating a temperature difference between the top and the bottom of the sample on this face, but also between front and rear

faces. The beam laser is passing through a diaphragm with 10x5 mm of aperture the recording of temperature, heat flux and potential difference data of electrical probes and heat flux sensor are ensured by keithley multimeter 2700 equipped with 20 input channel card. These measurements allow to determine the Seebeck coefficient and the thermal conductivity. Through the switch unit and when the sample temperature becomes stable, the electrical probe is switched from multimeter 2700 to keithley source-meter 2450 in order to determine the electrical resistivity by four probes technique. The source-meter is able to impose a current from a few nA to 1 A and to measure a voltage from a few µV to 200 V.

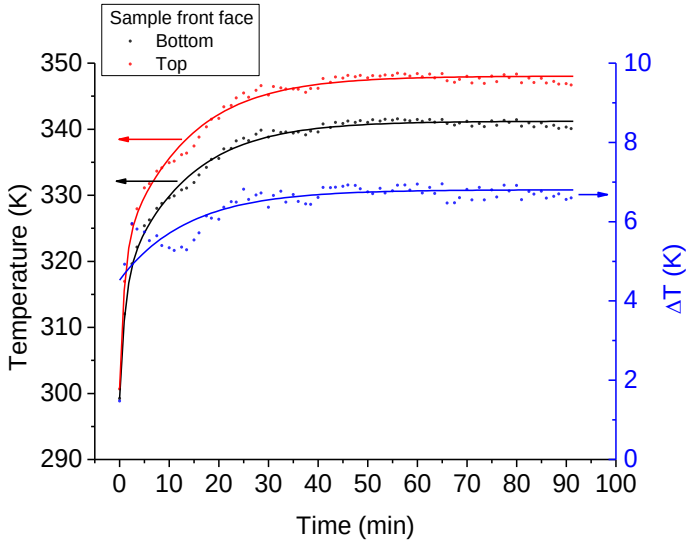

Figure.IV.5. Temperature evolutions on top and bottom of sample front face versus measurement time in the case of bulk p-type c-silicon.

Fig.IV.5. shows the temperature evolution on the top (red curve) and the bottom (black curve) of the sample front face and also the temperature difference (ΔT blue curve)) between the top and the bottom. The heating is stopped when the sample temperature becomes stable. The potential difference measurement is made at the left and right side of the sample front face (Fig.IV.6.), it is important to note that the potential difference must be the same at the left and right side to consider that the temperature difference (which generate the potential difference) at both sides is the same.

In addition in Fig.IV.6, the evolution of the Seebeck coefficient is plotted versus time. We notice that Seebeck coefficient becomes stable when the temperatures of the top and the bottom of sample become stable. It can be concluded that to properly assess the Seebeck coefficient of materials, the heating temperature should be in steady state mode.

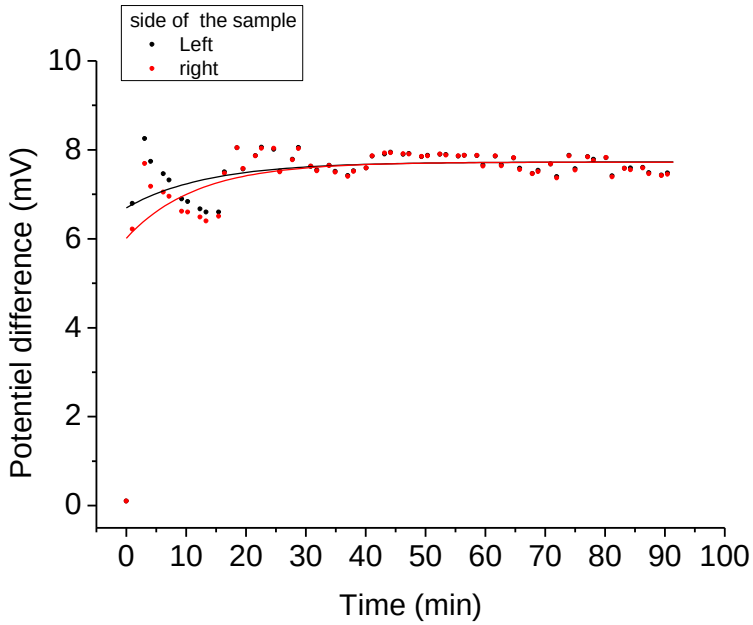

Figure.IV.6. Measured voltage at the left and right side of sample front face and evolution of Seebeck coefficient versus time in the case of bulk p type c-Si.

3.1. Seebeck coefficient measurement

Over the duration time of stabilization, the average of the temperature at the top and at the bottom of the sample have been calculated then the temperature difference (ΔT) between the top and the bottom is deduced. Moreover the average of the potential difference at the left ($\bar{U}_{left}$) and at the right ($\bar{U}_{right}$) side of the sample and the average ($\bar{U}$) between the left potential differences ($\bar{U}_{left}$) and right one ($\bar{U}_{right}$) have been calculated. The Seebeck coefficient is determined by dividing the averaged potential difference ($\bar{U}$) by the temperature difference (ΔT):

$$S = \frac{\overline{U}}{\Delta T} \text{ With } \overline{U} = \frac{\overline{U}_{left} + \overline{U}_{right}}{2},\ \Delta T = \overline{T}_{top} + \overline{T}_{bottom} \qquad \text{Eq.V.1}$$

3.2. Electrical resistivity

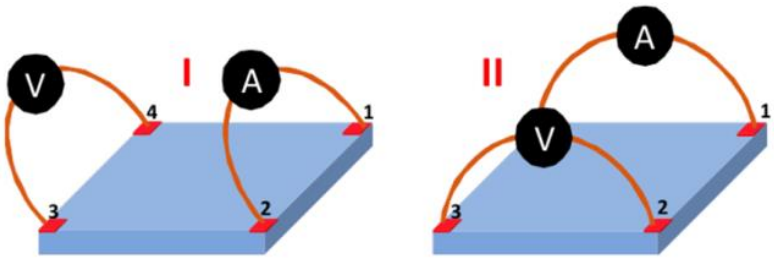

Figure.IV.7. Schematic representation of measurement technique of electrical resistivity according to Van der Pauw method.

When the temperature on the sample becomes stable, the four electrical probes at the front face from the Multi-meter are switched to the source meter using an electronic module homemade, in order to determine the electrical resistivity of the sample by Van der Pauw method. The principle of this technique is shown in Fig.IV.7. It consists to impose the current on a side of the sample and to measure the voltage on the parallel one (configuration-I), then it is done on the two other sides (configuration-II). The two resistances R_I and R_{II} which characterize respectively the configuration I and II, are related to the sample resistance (R_{sample}) through Van der Pauw equation

$$\exp(-\pi \frac{R_I}{R_{Sample}}) + \exp(-\pi \frac{R_{II}}{R_{Sample}}) = 1 \qquad \text{Eq.V.2}$$

The resistance sample (R_{sample}) is determined numerically, and then the electrical resistivity of the sample is calculated by multiplying R_{sample} by the sample thickness (d):

$$\rho = R_{sample} d \qquad \text{Eq.V.3}$$

There is four possibilities for each configuration. For example, in the case of configuration I, we can apply the current I_{12} into contact 1 and out of contact 2 then measure the voltage V_{43} from contact 4 to contact 3 as shown in Fig.V.7. Likewise for I_{21}-V_{34}, I_{43}-V_{12}, I_{34}-V_{21}. And, R_I will be equal to the average of four resistances:

$$R_I = \frac{1}{4}(\frac{V_{43}}{I_{12}} + \frac{V_{34}}{I_{21}} + \frac{V_{12}}{I_{43}} + \frac{V_{21}}{I_{34}}) \qquad \text{Eq.V.4}$$

Likewise for configuration II:

$$R_{II} = \frac{1}{4}(\frac{V_{23}}{I_{14}} + \frac{V_{32}}{I_{41}} + \frac{V_{14}}{I_{23}} + \frac{V_{41}}{I_{32}}) \qquad \text{Eq.V.5}$$

4. Validation of ZT meter

4.1. Bulk material

4.1.1. Case of bulk silicon

In order to evaluate the reliability and accuracy of the experimental setup, test measurements have been performed on reference materials, which are n-type and p-type silicon single crystals (c-S). The n-type c-Si is doped with phosphorus, the thickness of the samples is 300 µm (±20µm) and the electrical resistivities given by the manufacturer (ρ_m) are >1.4 Ω.cm and 20-30 Ω.cm. For p-type c-

Si, the doping element is boron; the sample thickness is 508 µm (+-35µm) and the electrical resistivity (ρ_m) is 1.5-4 Ω.cm.

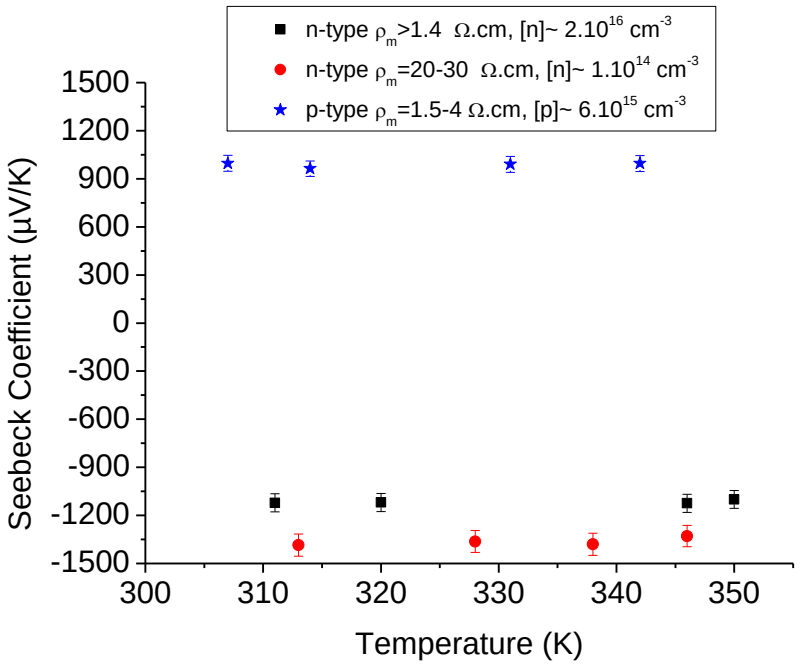

Figure.IV.8. Seebeck coefficient of n-type and p-type c-Si bulk materials as a function of the temperature (ρm is the manufacturer value).

Fig.IV.8. shows that Seebeck coefficient measurement versus temperature for p-type and n-type silicon single crystals. It can be noticed that negative sign for n-type and positive sign for p-type are obtained meaning that measurement have been done in the right direction and is addressed to the true carriers. In addition the measured Seebeck coefficient of n-type increases with the electrical resistivity which is consistent with the theory of thermoelectricity [24]. For the both case p-type and n-type, the measurement of Seebeck coefficient shows that it does not vary so much for the temperature range from 300 to 350K. For n-type, the Seebeck coefficient is between -1.3 to -1.45 mV/K for ρ_m = 20 to 30 Ω.cm of electrical resistivity and from -1.05 to-1.15 mV/K for ρ_m > 1.4 Ω.cm and in the case of p-type, it is around 1 mV/K (± 0.1 mV/K).

According to the literature [24], the Seebeck coefficient for n-type is from -1.3 to -0.9 mV/K for [n] = 10^{14} -10^{16} cm^{-3}, and for p-type is from 0.9 to 1.1 mV/K for [p] =10^{15}- 10^{16} cm^{-3}. This shows that our measurements are consistent with the literature and allows the validation of the reliability and accuracy of our ZT-meter on bulk material.

The evolution of electrical resistivity versus the temperature determined by ZT-meter is given in Fig.IV.9. It is noted that the electrical resistivity for both n- and p-types varies slowly in this range of temperature. But more important is the measurement values at room temperature which are consistent with manufacturer values (ρ_m).

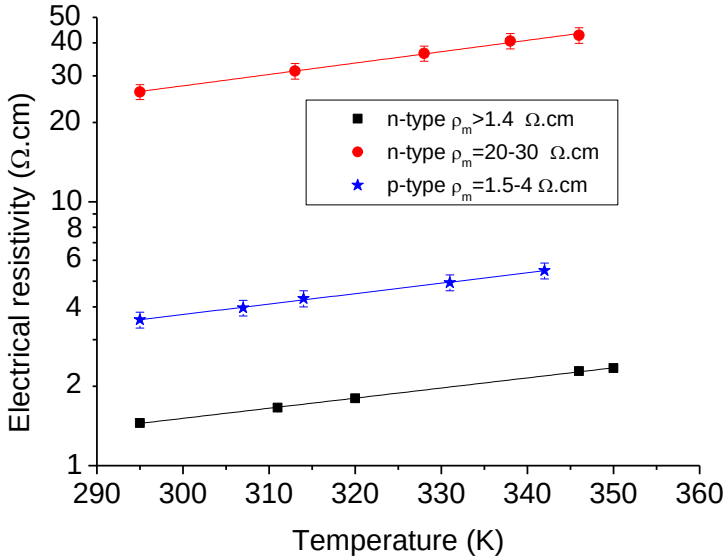

Figure.IV.9. Electrical resistivity of n-type and p-type c-Si bulk material as a function of the temperature (ρm is the manufacturer value).

4.1.2. Case of mesoporous p-type c-silicon

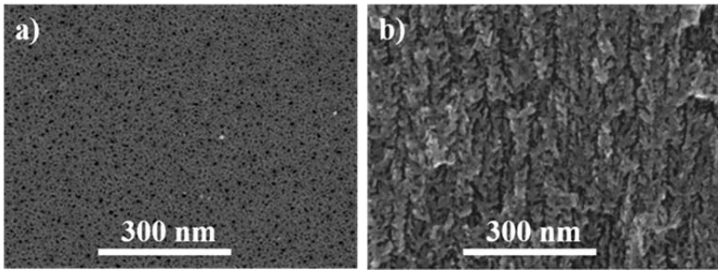

Figure.IV.10. Cross (a) and top (b) view of mesoporous p-type c-Si realized by SEM.

The Mesoporous Silicon (MeP-Si) substrate was provided by SiLiMiXT. Its electrical resistivity is in the range of 10-20 mΩ.cm, with a porosity of about 40 %, pore size is in the range of 1-10 nm and a porous thickness close to 50 µm (Fig.IV.10.).

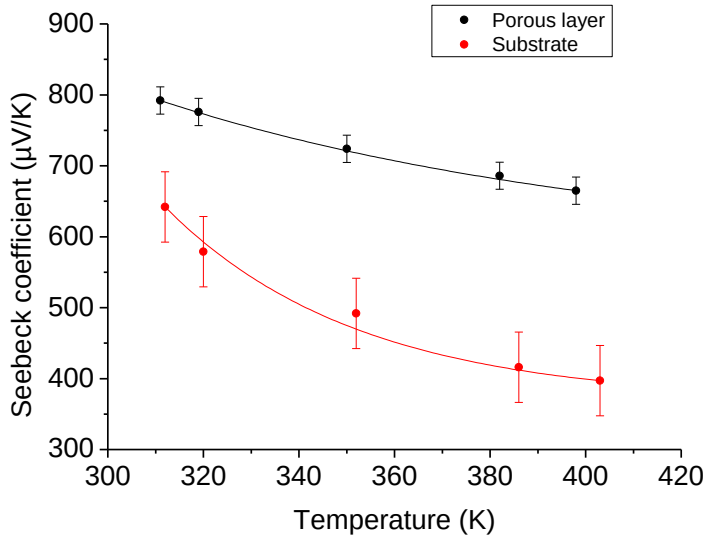

Figure.IV.11. Evolution of Seebeck coefficient of the porous layer and substrate versus of temperature in the case of p-type c-silicon sample.

In order to evaluate the effect porosification of silicon on the evolution of its Seebeck coefficient, the Seebeck measurement of Si sample before and etching (MeP-Si (50 µm)) are performed. The evolution of Seebeck coefficient of the porous layer and substrate versus of temperature is given by Fig.IV.11. We notice that the Seebeck coefficient increases one and a half times after etching.

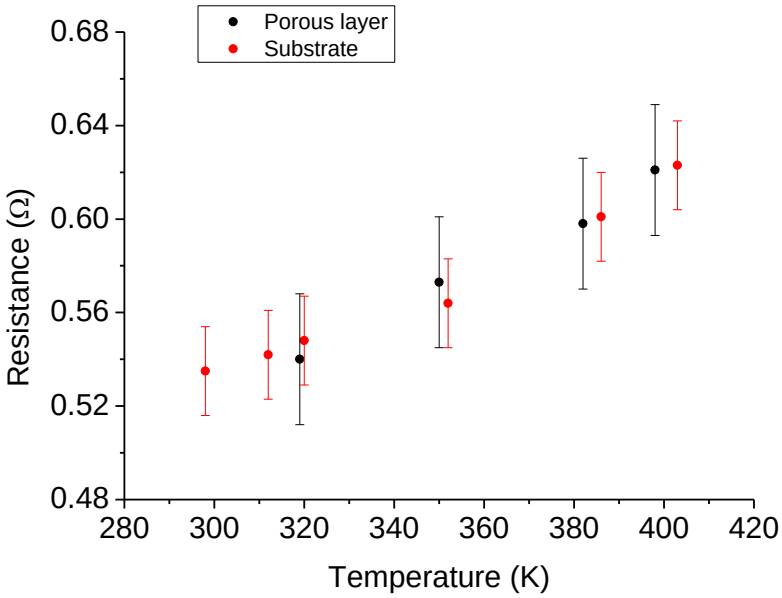

Figure.IV.12. Evolution of electrical resistance of the porous layer and the whole substrate versus temperature in the case of p-type c-silicon sample.

Fig.IV.12. shows the evolution of electrical resistance for porous layer and whole substrate versus temperature. It can be noticed that the measured electrical resistance is the same for porous layer and whole substrate.

4.2. Thin film materials

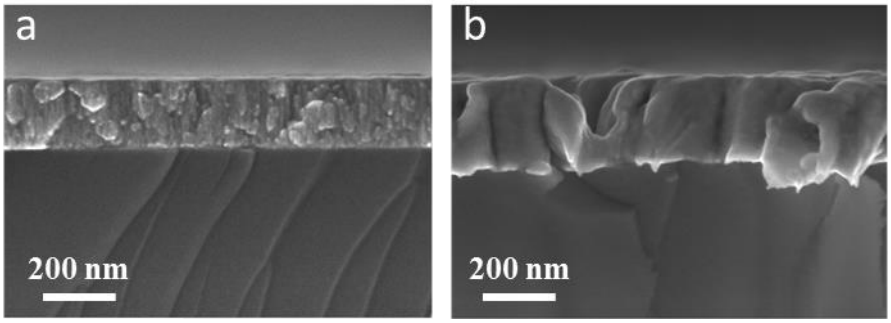

Figure.IV.13. Cross view realized by SEM of copper (a) and constantan (b) thin films deposited on SiO2/Si substrate by PVD magnetron.

As the ZT-meter is dedicated to evaluate the thermoelectric properties of thin film materials, we have made measurements on copper thin film and constantan thin film deposited by PVD (magnetron sputtering) on SiO_2/Si substrate with 2.2 µm of SiO_2 film thickness (Fig.IV.13.). The thickness of the layer has been determined by SEM and is 250 nm for constantan layer and 200 nm for copper one.

The EDX analysis on the constantan layer has shown that there is 73 % by weight of copper and 27 % of nickel in the deposited layer (Fig.V.14).

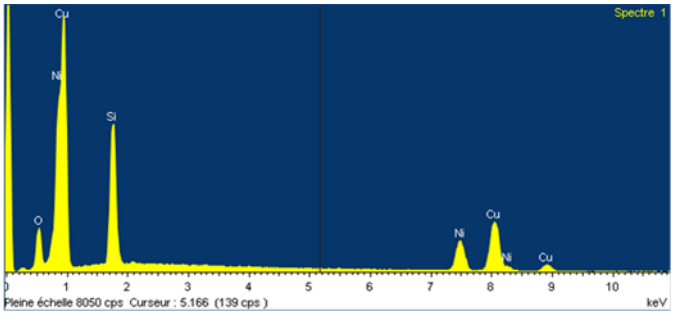

Figure.IV.14. EDX analysis Spectrum of constantan thin film.

As all metallic materials, the constantan and copper are highly reflective in the IR range and a small part of IR laser beam has been absorbed. As seen on Fig.V.15. showing the evolution of Seebeck coefficient versus temperature, there is a limitation in temperature. The maximum attainable temperature is 310 K for constantan and 312 K for copper.

As mentioned previously, the potential difference must be the same at the left and right sides for a proper assessment of the Seebeck coefficient. In the case of constantan layer Fig.V.15, the Seebeck measurement at the left is very close to the right one. However in the case of copper layer the measured the Seebeck value at the left is around 1 µV/K with positive sign and for the right side, it is around -4µV/K (negative sign). This can be explained by the limits of our ZT-meter for the materials exhibiting similar thermoelectric properties that copper ones. This measurement allows to define the sensitivity of our device at 4 µV/K. It is important to note that in literature, no measurements of the Seebeck coefficient for nano-metric thin films of copper are available, and we refer to the bulk copper whose Seebeck coefficient is around 1.9 µV/K @ room temperature [25]. In the literature [25], the Seebeck coefficient of Constantan (55% Cu, 45 %Ni) is -39 µV/K at room temperature, that is two times larger than our measured value (~ 23 µV/K). This is not due to our measurement system but to the percentage of Ni in Cu that is lower, more copper in the layer (Fig.IV.15) has caused the drop of Seebeck coefficient.

However this effect is less pronounced for electrical resistivity of constantan thin film : measured value by ZT-meter for this temperature range is around 58±10 µΩ.cm to be compared to 50 µΩ.cm in literature [26]. The electrical resistivity of copper thin film is almost constant for this temperature range and it is equal to 30 ± 5 µΩ.cm. Compared to the literature [27], the electrical resistivity of pure bulk copper is 1.7 µΩ.cm i.e. eighteen times lower than the copper thin film deposited in our reactor.

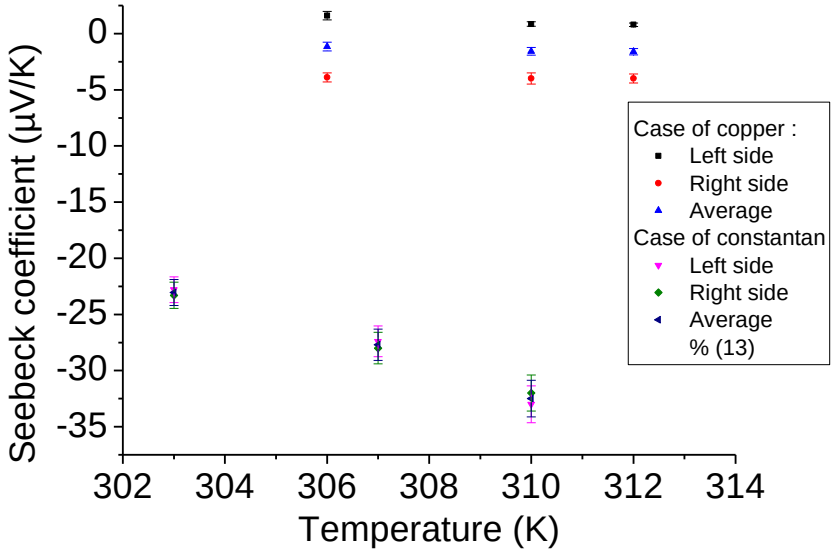

Figure.IV.15. Seebeck coefficient versus temperature in the case of constantan and copper thin film deposited by PVD magnetron on SiO_2/Si substrate.

IV. Effect of laser nanostructuring on the evolution of Seebeck coefficient and electrical resistivity of materials

The main purpose of this thesis is to investigate the effect of laser nanostructuring of materials on the evolution of their TE properties

1. Case of MeP-Si

1.1. Seebeck coefficient

The sample chosen for this section is the nanostructured MeP-Si (Fig.IV.15.) obtained by laser irradiating (500 fs @ 1030 nm and 100 kHz repetition rate) as shown in the previous chapter. The sample surface is homogenously covered by periodic ripples (1D structures). Thus, to measure the Seebeck coefficient of nanostructured MeP-Si, the sample can be placed in two different configurations depending on the LIPSS orientation in relation with the laser heating gradient direction. The first configuration (1) is presented in Fig.V.16 and is obtained when the orientation of LIPSS covering the surface is parallel to the heat gradient direction. The second one (2), is obtained when the heat gradient direction is orthogonal to the LIPSS orientation (fig.IV.16.).

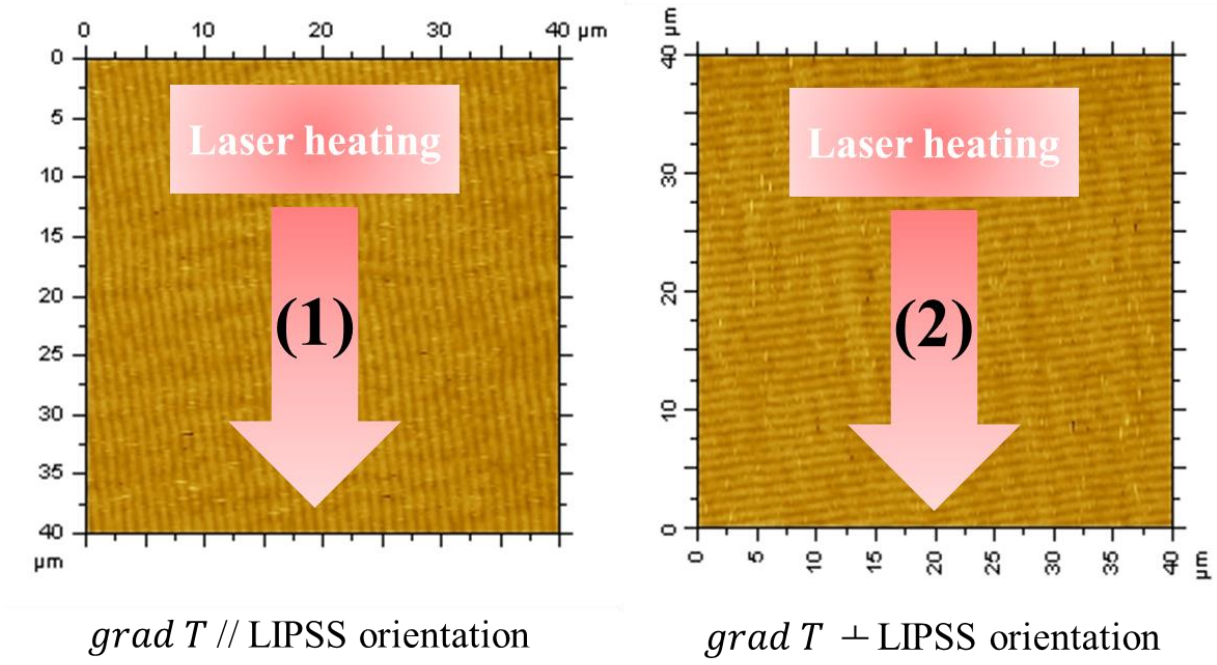

Figure.IV.16. Schematic of the two configurations used for Seebeck measurement of nanostructured MeP-Si.

The determination of Seebeck coefficient evolution versus temperature of nanostructured MeP-Si (for the two configurations) in comparison with the untreated one is presented in Fig.IV.17. This figure shows clearly on the one hand the enhancement of S due to laser nanostructuring and on the other hand the very different S values obtained for the same sample (nanostructured MeP-Si) depending on (1) and (2) configurations. In the first configuration, a huge enhancement of Seebeck coefficient can be noted reaching almost 200 % at 310 k. In contrast, in the second configuration, a low improvement of S about 15% at the same temperature is observed. The enhancement of S can be attributed to the carrier quantum confinement effect achieved by laser nanostructuring (as explained in chapter 1). The obvious difference of Seebeck values achieved between the two configurations can be explained by the different heat gradient behaviors depending on the configuration. In the first configuration, the heat (absorbed from the laser beam) propagates throughout the structures. Whereas, in the second one, the heat propagates through a modulated surface, and the ripples can play as thermal barrier leading to large difference of temperatures between the top and the bottom of sample. Because S is inversely proportional to the temperature gradient, its values in configuration (2) will be lower than in configuration (1).

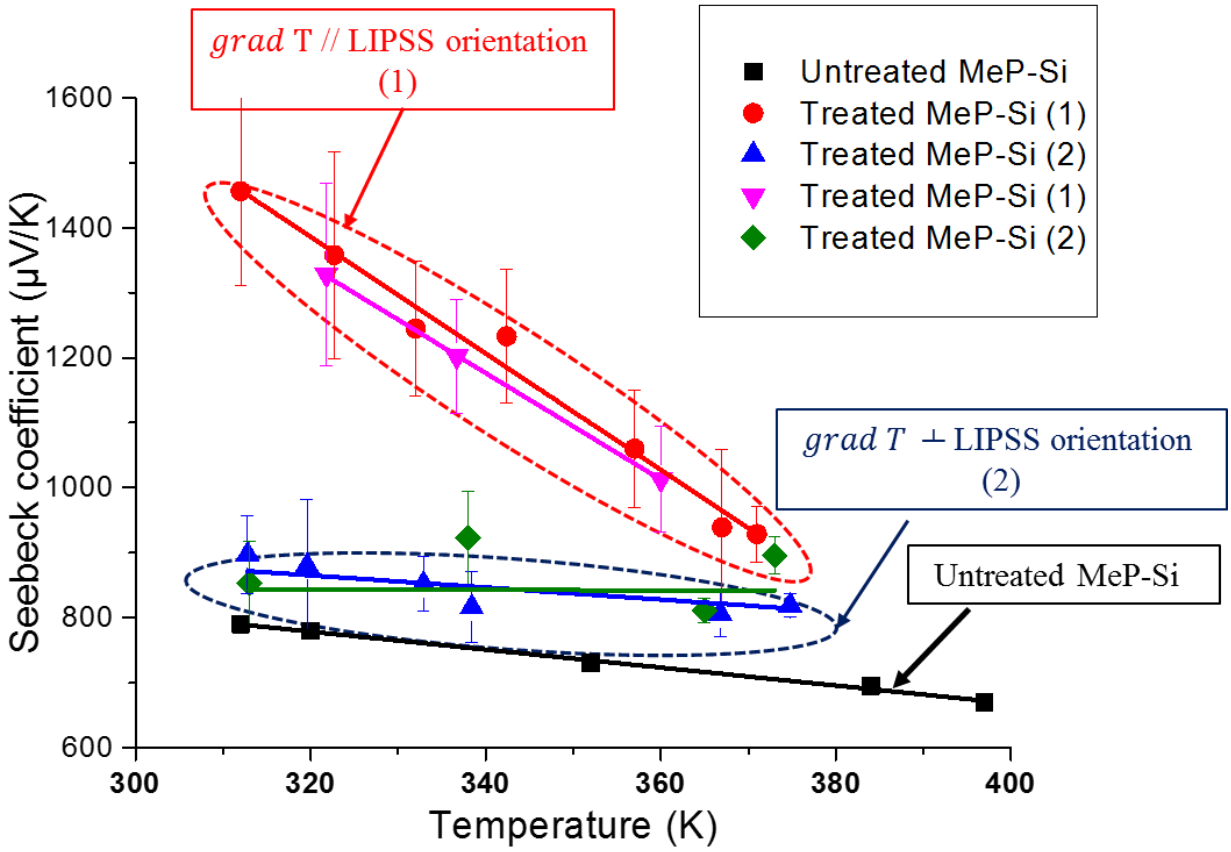

Figure.IV.17. Seebeck coefficient measurement (on nanostructured MeP-Si and untreated MeP-Si) vs temperature.

1.2. Electrical resistivity

The electrical resistivity of MeP-Si before and after nanostructuring is measured through Van der Pauw method as discussed previously and the results are given is Fig.IV.18. This figure shows a large reduction of the resistance with nanostructuring. The electrical resistivity of nanostructured sample (~60 μΩ.cm) is reduced to roughly 50 % of the untreated one (120~μΩ.cm). This means that electrical conductivity of nanostructured sample is two times larger than the un-nanostructured one.

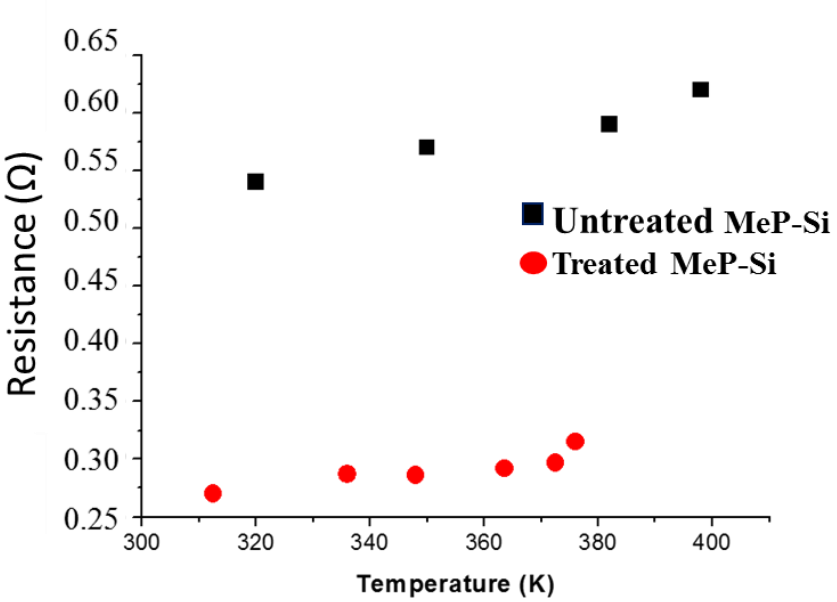

Figure.IV.18. Electrical resistance measured for MeP-Si before (black squares) and after (red circles) laser treatment.

1.3. Figure of merit

The measurement of Seebeck coefficient and electrical conductivity showed a large enhancement of these properties with nanostructuring. To estimate the ZT value of nanostructured MeP-Si, we still require the third TE property which is the thermal conductivity. Unfortunately, this property was not measured yet (the addition of thermal conductivity measurement in ZT device is in progress). However, the thermal conductivity of MeP-Si has been determined in our group by the use of photo thermal pulsed laser as reported in [19]. This value is depending on the thickness of MeP-Si layer. For our sample (50 µm of thickness), the thermal conductivity is found to be about 5 W/m.K [19]. This value will certainly change after nanostructuring and probably it will decrease according to a theoretical prediction expecting the reduction of lattice contribution of thermal conductivity with nanostructuring as explained in the first chapter. However, if we suppose that the thermal conductivity does not change after nanostructuring. This allows to an estimated values of ZT varying in the range of 0.08 to 0.2 at 310 K of nanostructured MeP-Si compared to 0.03 for MeP-Si as presented in Tab.IV.1. This presents a huge enhancement reaching almost 600 % with nanostructuring.

		Seebeck coefficient	Electrical conductivity	Thermal conductivity	Figure of Merit
Untreated MeP-Si		800 µV/K	0.810^3 S/m	5 [19] W/m.K	0.03 @ 310 K
Nanostructured MeP-Si	(1)	1400 µV/K	$1.6\ 10^3$ S/m	5 W/m.K	0.2 @ 310 K
	(2)	900 µV/K	1.6 103 S/m	5 W/m.K	0.08 @ 310 K

2. Case of $TiO_{1.6}$ thin film

In spite of the various morphologies observed with large area nanostructuring of TiO1.6 thin film (see chapter III), the long processing time (for nanostructuring) and the poor pulse energy stability of 100 fs laser made the obtaining of 25x25 mm² nanostructured surface of TiO1.6 very complicated. Thus, only the following surface morphology has been investigated here:

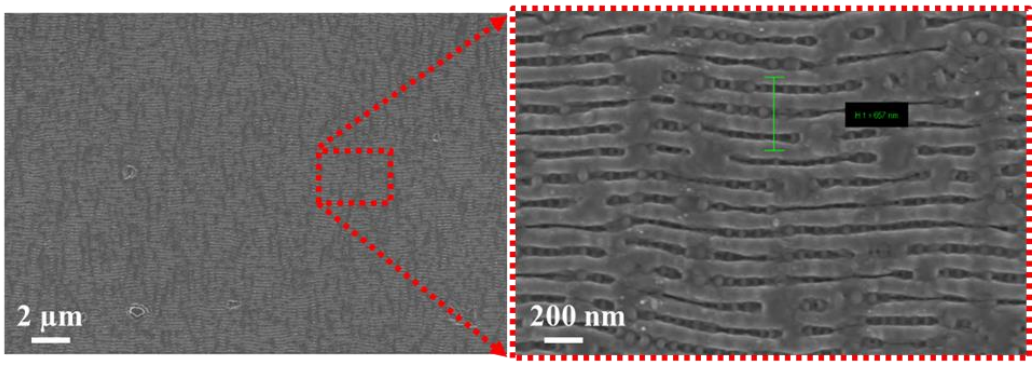

Figure.IV.19. LSFL organization formed on 5×5 mm² TiO1.6 surface by 100fs laser @ 266 nm (F=30 mJ/cm² and N~3300).

As seen with MeP-Si, due to the 1D symmetry of LIPSS, the measurement of seebeck coefficient can be performed through two configurations that depend on the orientation of LIPSS in relation with the laser heating gradient direction. The first configuration (1) is presented in Fig.IV.20 and is obtained when the orientation of LIPSS covering the surface is parallel to the heat gradient direction. The second one (2), is obtained when the heat gradient direction is orthogonal to the LIPSS orientation (fig.IV.20).

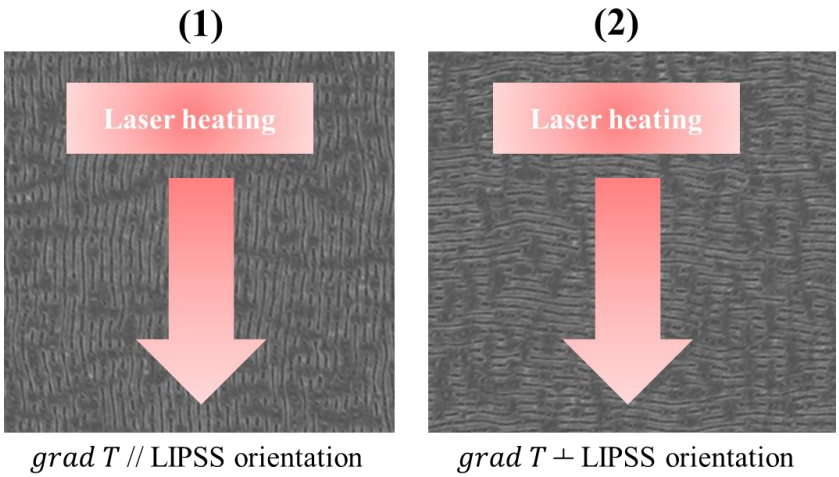

Figure.IV.20. Schematic of the two configurations used for Seebeck measurement of nanostructured TiO1.6.

The determination of Seebeck coefficient evolution versus temperature of nanostructured $TiO_{1.6}$ thin film (for the both configurations) in comparison with the untreated one is presented in Fig.IV.21. This figure shows clearly the enhancement in the absolute term of S due to laser nanostructuring and the very different S values obtained for the same sample (nanostructured $TiO_{1.6}$) depending on (1) and (2) configurations. In the first configuration, a very huge enhancement in the absolute term of Seebeck coefficient reaching roughly 1000% is achieved (from 40 to 390 µV/K at 305 K). In contrast, in the second configuration, a huge improvement in the absolute term of S exhibiting a values 5 to 6 times higher than the untreated one (240 compared to 40 µV/K at 305 K). The enhancement of S can be attributed to the carrier quantum confinement effect achieved by laser nanostructuring (as explained in chapter I). The obvious difference of Seebeck values achieved between the two configurations can be explained by the different heat gradient behaviors depending on the configuration. In the first configuration, the heat (absorbed from the laser beam) propagates throughout the structures. Whereas, in the second one, the heat propagates through a modulated surface, in this case ripples may play as thermal barrier leading to a large gradient of temperatures between the top and the bottom of sample as seen with MeP-Si. Similarly, the measurement of electrical conductivity shows a great improvement from ~0.46 to 2.5 $S.m^{-1}$ for respectively untreated and nanostructured $TiO_{1.6}$ thin film. Thus, according to those measurements (Seebeck coefficient and electrical conductivity), the power factor shows an important improvement from 0.74 10^{-3} (untreated) to 0.15 and 0.38 $\mu W.K^{-2}.m^{-1}$ @ 305 K (for nanostructured sample depending on the configuration (2) and (1) respectively). This means that the power factor on nanostructured thin film can reach a value 500 times higher than the untreated one. The enhancement of power factor observed with titanium oxide thin film is extremely huge compared to the one observed with MeP-Si. This can be attributed to the fact that MeP-Si studied here is a bulk sample (50 µm), therefore nanostructuring its surface

may limit the enhancement of its TE properties only on thin film of approximatively 200 nm (amplitude-depth of nanostructures). Otherwise, in the case of $TiO_{1.6}$ thin film (500 nm), the nanostructuring of its surface can clearly modify the TE properties of the whole thin film.

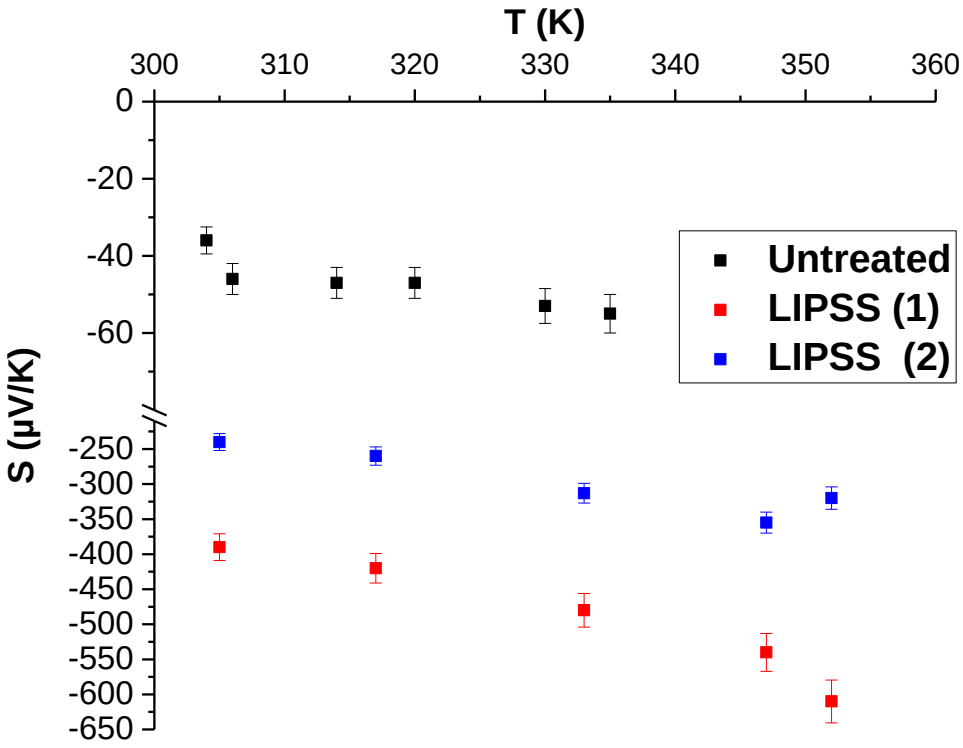

Figure.IV.21. Seebeck coefficient measurement (with nanostructured and untreated $TiO_{1.6}$) vs temperature.

V. Conclusion

In this chapter, a new experimental homemade device, dedicated to TE property characterization (Seebeck coefficient and electrical conductivity) of bulk and thin film samples, has been validated. A good accuracy for Seebeck measurement down to 4.0 µV/K has been achieved. Moreover, a preliminary finding evidencing the evolution of TE properties with laser nanostructuring have shown a huge enhancement of Seebeck coefficient and electrical conductivity.

In the case of MeP-Si an important improvement on Seebeck coefficient and electrical conductivity has been achieved yielding to a figure of merit value six times higher than the value measured with the untreated sample.

Concerning, the results reported with $TiO_{1.6}$ thin film, Seebeck coefficient and electrical conductivity have shown an important improvement leading to a power factor value extremely enhanced (500 times higher than the power factor of untreated sample).

According to those results, the laser nanostructuring process can provide a very promising approach in the enhancement of TE properties which requires a further validation through studying other different TE materials, and the evaluation of the global output thermoelectric power.

References

[1] K. Wang, A. Wang, A. Tomic, L. Wang, A. M. M. Abeykoon, E. Dooryhee, C. Petrovic, "Enhanced thermoelectric power and electronic correlations in $RuSe_2$", APL Materials 3, 041513, 2015.

[2] G. Ren, S. Butt, C. Zeng, Y. Liu, B. I. N. Zhan, J. Lan, Y. Lin, C. Nan, "Electrical and Thermal Transport Behavior in Zn-Doped BiCuSeO Oxyselenides", Journal of ELECTRONIC MATERIALS, 2014.

[3] M. Battabyal, B. Priyadarshini, D. Sivaprahasam, N. S. Karthiselva, R. Gopalan, "The effect of Cu_2O nanoparticle dispersion on the thermoelectric properties of n-type skutterudites", J. Phys. D. Appl. Phys., vol 455309, 2014.

[4] S. Demirel, E. Altin, E. Oz, S. Altin, A. Bayri, E. Altin, E. Oz, S. Altin, A. Bayri, "An enhancement ZT and spin state transition of $Ca_3Co_4O_9$ with Pb doping", Journal of Alloys and Compounds 627 430–437, 2015.

[5] X. Chen, P. Lin, K. Zhang, H. Baumgart, B. Geist, "Seebeck Coefficient Enhancement of ALD PbTe / PbSe Nanolaminate Structures Deposited inside Porous Silicon", ECS Journal of Solid State Science and Technology, vol 5, no 9, 503-508, 2016.

[6] J. Luo, D. Billep, T. Waechtler, T. Otto, M. Toader, O. Gordan, E. Sheremet, J. Martin, M. Hietschold, D. R. T. Zahn, T. Gessner, "Enhancement of the thermoelectric properties of PEDOT:PSS thin films by post-treatment ", J. Mater. Chem. A, 2013.

[7] E. Alleno, D. Bérardan, C. Byl, C. Candolfi, R. Daou, R. Decourt, E. Guilmeau, S. Hébert, J. Hejtmanek, P. Masschelein, V. Ohorodnichuk, M. Pollet, S. Populoh, D. Ravot, O. Rouleau, M. Soulier, "Invited Article : A round robin test of the uncertainty on the measurement of the thermoelectric dimensionless figure of merit of $Co_{0.97}Ni_{0.03}Sb_3$". Review of Scientific Instruments 86, 011301 (2015).

[8] P. F. P. Poudeu, J. D'Angelo, A. D. Downey, J. L. Short, T. P. Hogan, M. G. Kanatzidis, "High thermoelectric figure of merit and nanostructuring in bulk p-type $Na_{1-x}Pb_mSb_yTe_{m+2}$", Angew. Chemie - Int. Ed., vol 45, no 23, 3835–3839, 2006.

[9] R. Venkatasubramanian, T. Colpitts, E. Watko, M. Lamvik, N. E-masry, "MOCVD of Bi_2Te_3 , Sb_2Te_3 and their superlattice structures for thin-film thermoelectric applications", Journal of Crystal Growth, vol 170, 817–821, 1997.

[10] S. Walia, S. Balendhran, H. Nili, S. Zhuiykov, G. Rosengarten, Q. H. Wang, M. Bhaskaran, S. Sriram, M. S. Strano, K. Kalantar-zadeh, "Transition metal oxides – Thermoelectric properties", Prog. Mater. Sci., vol 58, no 8, 1443–1489, 2013.

[11] M. Yasukawa, Y. Shiga, T. Kono, "Electrical conduction and thermoelectric properties of perovskite-type", Solid State Communications, vol 152, 964–967, 2012.

[12] Q. Wei, M. Mukaida, K. Kirihara, Y. Naitoh, T. Ishida, "Recent Progress on PEDOT-Based Thermoelectric Materials", Materials, 732–750, 2015.

[13] A. Zhou, W. Wang, X. Yao, B. Yang, J. Li, Q. Zhao, C. Wang, D. Xu, P. Ziolkowski, E. Mueller, Impact of the film thickness and substrate on the thermopower measurement of thermoelectric films by the potential-Seebeck microprobe (PSM), Applied Thermal Engineering, 107, 552–559, 2016.

[14] R. Singh, Z. Bian, A. Shakouri, G. Zeng, J. Bahk, J. E. Bowers, J. M. O. Zide, A. C. Gossard, R. Singh, Z. Bian, A. Shakouri, G. Zeng, J. Bahk, "Direct measurement of thin-film thermoelectric figure of merit", Applied Physics Letters, 94, 212508, 2009.

[15] P. K. Rawat, B. Paul, "Simple design for Seebeck measurement of bulk sample by 2-probe method concurrently with electrical resistivity by 4-probe method in the temperature range 300 - 1000 K", Measurement 91 613–619, 2016.

[16] Q. Li, X. Yin, "Effects of Phase Composition on Microstructure and Mechanical Properties of Lu 2 O 3 -doped Porous Silicon Nitride Ceramics", J. Mater. Sci. Technol., vol 27, no 6, 529–533, 2011.

[17] Y. K. Koh, S. L. Singer, W. Kim, J. M. O. Zide, H. Lu, Y. K. Koh, S. L. Singer, W. Kim, J. M. O. Zide, H. Lu, D. G. Cahill, A. Majumdar, A. C. Gossard, "Comparison of the 3ω method and time-domain thermoreflectance for measurements of the cross-plane thermal conductivity of epitaxial semiconductors", J. Appl. Phys. 105, 054303, 2009.

[18] C. A. Paddock, G. L. Eesley, C. A. Paddock, G. L. Eesley, "Transient thermoreflectance from thin metal films Transient thermoreflectance from thin", Journal of Applied Physics 60, 285, 1986.

[19] A. Melhem, D. De Sousa Meneses, C. Andreazza-Vignolle, T. Defforge, G. Gautier, N. Semmar, "Structural, Optical and Thermal Analysis of n-type Mesoporous Silicon Prepared

by Electrochemical Etching", J. Phys. Chem. C, 119, 21443−21451, 2015.

[20] K. A. Aissa, N. Semmar, A. Achour, Q. Simon, A. Petit, J. Camus, "Achieving high thermal conductivity from AlN films deposited by high-power impulse magnetron sputtering", J. Phys. D: Appl. Phys. 47, 2014.

[21] E. Amin-Chalhoub, N. Semmar, L. Coudron, G. Gautier, C. Boulmer-Leborgne, A. Petit, M. Gaillard, J. Mathias, E. Millon, "Thermal conductivity measurement of porous silicon by the pulsed-photothermal method", J. Phys. D. Appl. Phys., vol 44, no 35, 355401, 2011.

[22] O. N. Lamellae, O. F. Arbitrary, "A method of measuring the resistivity and Hall coefficient on lamellae of arbitrary shape", PTechReview vol 20, no I, 220–224, 1958.

[23] O. Abbes, A. Melhem, C. Boulmer-leborgne, N. Semmar, "Establishment of optimized metallic contacts on silicon for thermoelectric applications", vol 6, no 11, 961–964, 2015.

[24] M. Wagner, "Simulation of thermoelectric device", Thesis dissertation, University of Vienna, 2007.

[25] Robin E. Bentley, Handbook of Temperature Measurement Vol. 3: The Theory and Practice of Thermoelectric Thermometry. Springer-Verlag Singapore, 1998.

[26] Samuel J. Rosenberg, "Nickel and Its Alloys", Inst. Mater. Res. Natl. Bur. Stand., 1968.

[27] D. F. W. M. A. Laughton, Electrical Engineer's Reference Book. 2002.

Chapter V: Complex pattern organizations generated on thin film surfaces under femtosecond radiations

I. Introduction

Laser induced periodic surface structure have been observed in wide variety of materials. Despite the great attention paid in studying the physical mechanisms leading to the formation of such structures, the existing models and explanations are still a matter of debate because the complex processes involving during the ultrashort-laser-matter interaction. Although, the experimental results, observed with bulk materials, are generally in good agreements with the theoretical explanations and proposed models such interference model including the excitation of surface plasmons polaritons, self-organization model and hydrodynamic approaches. In the case of thin films, supplementary physical effects have to be take into account such cavitation, bubble, delamination, role of substrate, thin film adhesion and thermos-elastic stresses. This may allow to very complicated phenomenon occurring during a laser radiation that can yield to complex and exotic surface organizations that can be observed only with thin films.

Thus, in this present chapter, we aim to present some complex surface organization of titanium oxide and polymer thin films generated under femtosecond irradiations (100 fs @ 266 nm and 500 fs @ 1030 and 343 nm). To our knowledge, these structures are seen for the first time reflecting the crucial role that thin film state plays in the formation of such structures.

II. Case of titanium oxide thin film deposited by magnetron sputtering

The results reported in chapter III and IV, concerning on the one hand the different surface morphologies obtained by laser treatment and on the other the huge enhancement on TE properties seen as result of these surface texturing, encourage us to more explore this work. The main limits of this process were the relatively long processing time (reaching 20 hours/ 25x25 mm^2) and the limited homogenous surfaces formed by PLD (roughly about 1 cm^2). Magnetron sputtering deposition method seems to be a useful method to solve the later problem since it allows the fabrication of large homogenous surface area (up to 10x10 cm^2). In order to reduce the laser nanostructuring processing time a 500 fs laser was used as done with MeP-Si in chapter III.

1. Thin film elaboration: Magnetron sputtering deposition method

The experimental device is a deposition chamber equipped with three circular 4-inch balanced magnetrons. One 101.6 mm in diameter and 4.0 mm thick titanium metallic target (Purity 99.995 %) powered by a Pinnacle + generator was used. The target surface is 30° titled with respect to the

substrate mechanically maintained on a circular rotating substrate holder. The draw distance between the center of the target and the center of the substrate holder is about 127 mm. The deposition chamber is pumped down to 10^{-4} Pa via a system combining a dry pump and a turbo-molecular pump. The flow rates of argon and oxygen are controlled by two flowmeters and the pressure in the deposition chamber is monitored by a cold-cathode and a capacitive gauge. During the deposition step, the rotation speed of the samples is about 26 rpm and shutters can be used to protect the un-sputtered targets or the samples (see fig.V.1.)

Figure.V.1. Photo of experimental setup used for magnetron sputtering deposition of titanium oxide thin film.

The different parameters involved in magnetron sputtering deposition (PVD) (pressures, Ar and O flows, current etc) were studied and optimized in order to grow homogenous titanium oxide thin films on SiO2 substrates (1.2 µm) with a Ti/O ratio in the range of 1.6 to 1.8 and thickness about 300 nm. The experimental conditions allowing to grow $TiO_{1.8}$ films (300 nm of thickness) are summarized in the following table:

Chamber vaccum (before injecting Ar and O gases)	Chamber pressure (in presence of Ar and O gases)	Ar flow	O flow	Décharge current	Processing time
$4.4\ 10^{-5}$ Pa	1 Pa	20 sccm	1,5 sccm	0,8 A	20 min

Tab.V.1. Experimental conditions applied for $TiO_{1.8}$ thin films deposition

The surface and cross section morphologies of TiO1.8 thin films (PVD) are given in fig.V.2. these SEM views showed a ~300 nm nanosized grain layer exhibing a rough surface (compared to the smooth surface obtained by PLD (see fig.III.)).

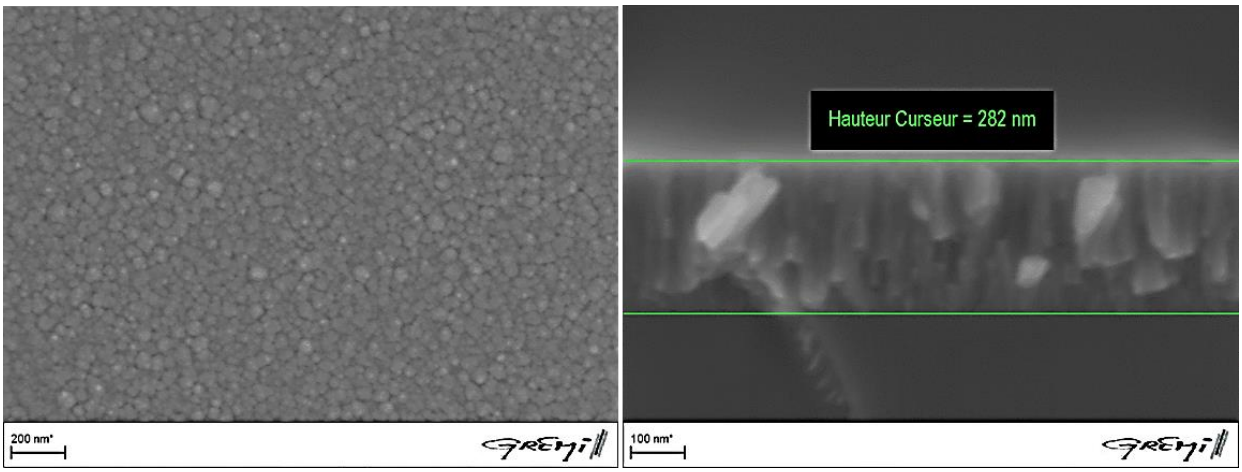

Figure.V2.SEM characterization of TiO1.8 thin film (PVD): left) top view and right) cross section.

2. Validation of 100 fs laser nanostructuring of $TiO_{1.8}$ (PVD)

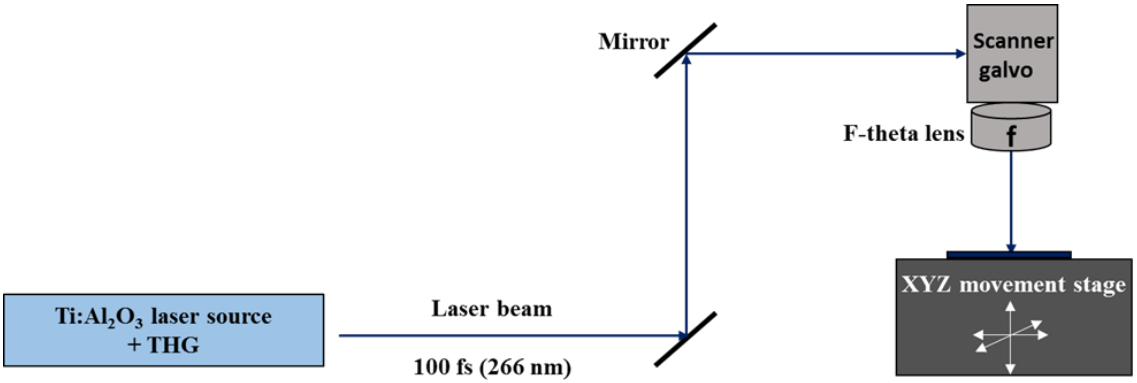

Figure.V.3.Schematic of the experimental set up using 100 fs laser @ 266 nm.

To study the laser nanostructuring of $TiO_{1.8}$ thin film (PVD), we aim to begin with a brief comparative investigation based on the experimental observations reported in chapter III with $TiO_{1.6}$ (PLD). 100 fs laser @ 266 nm is employed to treat large area (5x5 mm^2) of TiO1.8 (PVD) and TiO1.6 (PLD) under same experimental conditions (F and N). The results (shown in fig.V.4.) display a very similar surface organizations obtained with both samples. Dots and LSFL are formed for the same laser dose that validate our experimental process. However, despite these very similar results, the delamination of thin film (PVD) is noticed in some zones of the treated surface for a laser dose of 25 mJ/cm^2 and 3300 pulses (Fig.V.5.). Otherwise with PLD samples no delamination of thin film has been observed. The delamination of thin film under laser irradiation can be a result of ablation phenomena induced through thermal processes as vaporization and melting as reported in [1]. In our

case, after the removing of thin film, the substrate surface appears very clean without any damage and the removal film exhibits a LSFL pattern. This can suggest a clean delamination phenomena which occurs after the LSFL formation. Since, no delamination is observed in case of PLD thin film, the delamination of PVD thin film can be a result of the poor adhesion between the thin film and substrate and/or stress generated at the interface[2].

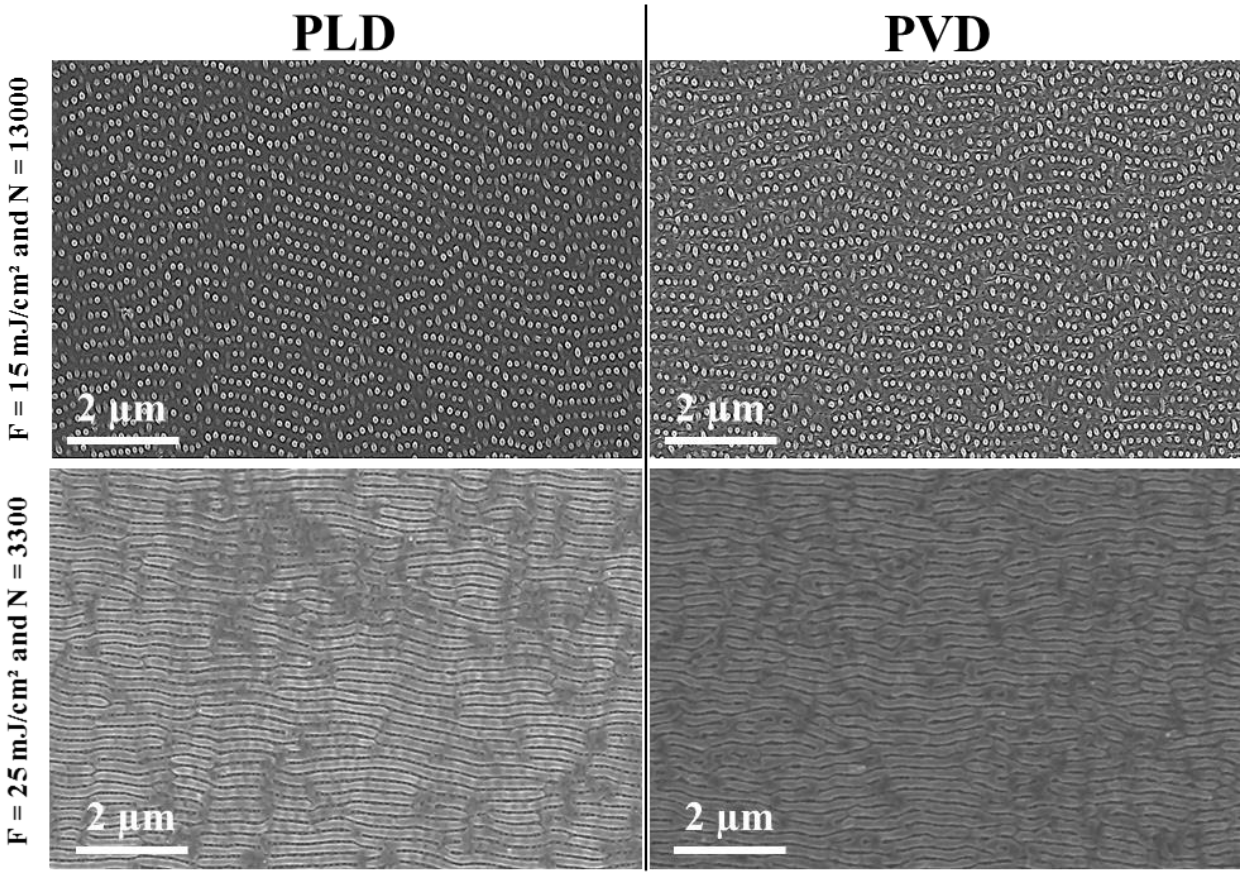

Figure.V.4. SEM views of 100 fs large area nanostructuring of PLD and PVD titanium oxide thin films under similar laser dose.

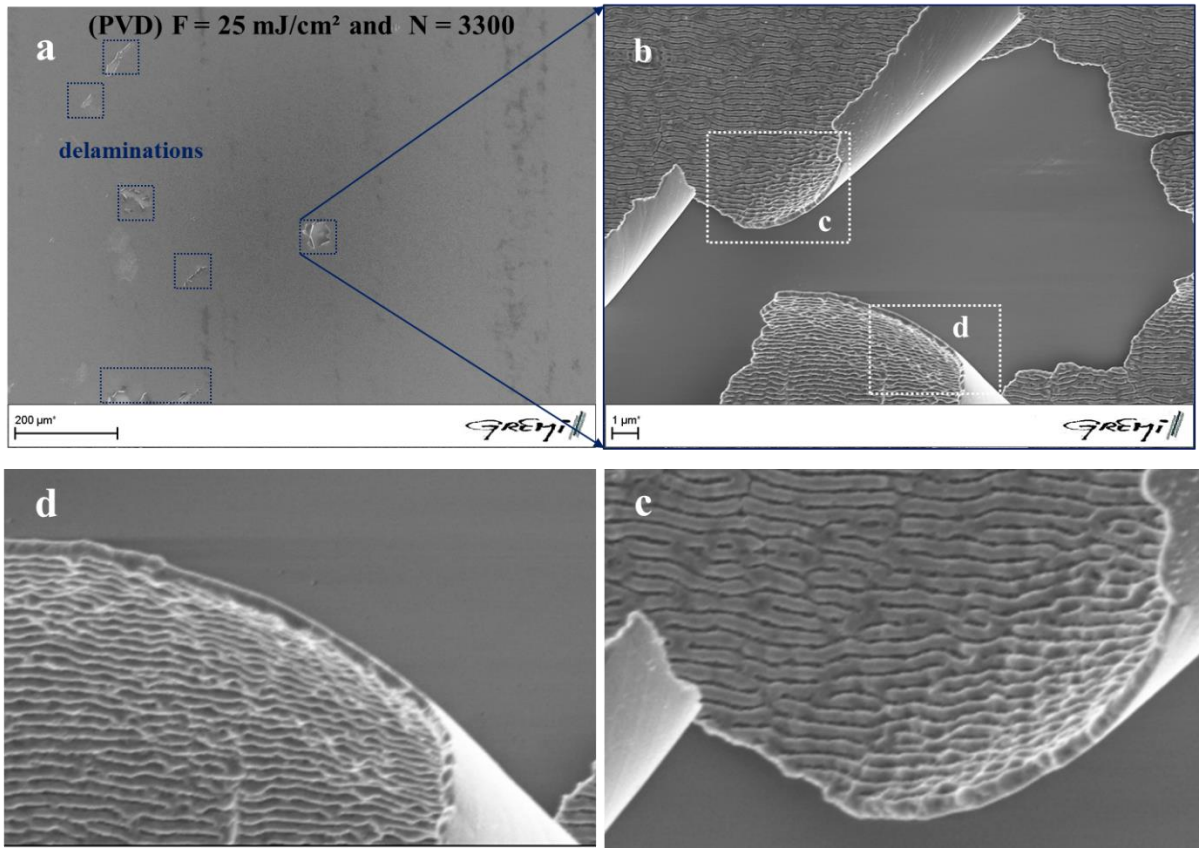

Figure.V.5 SEM characterization of TiO1.8 (PVD) irradiated by 100 fs @ 266 nm. a) Surface view at low magnification, b) zoomed image of a), c) and d) zoomed images of c and d zones.

3. $TiO_{1.8}$ thin film nanostrucutring using a 500 fs laser @ 1030 nm

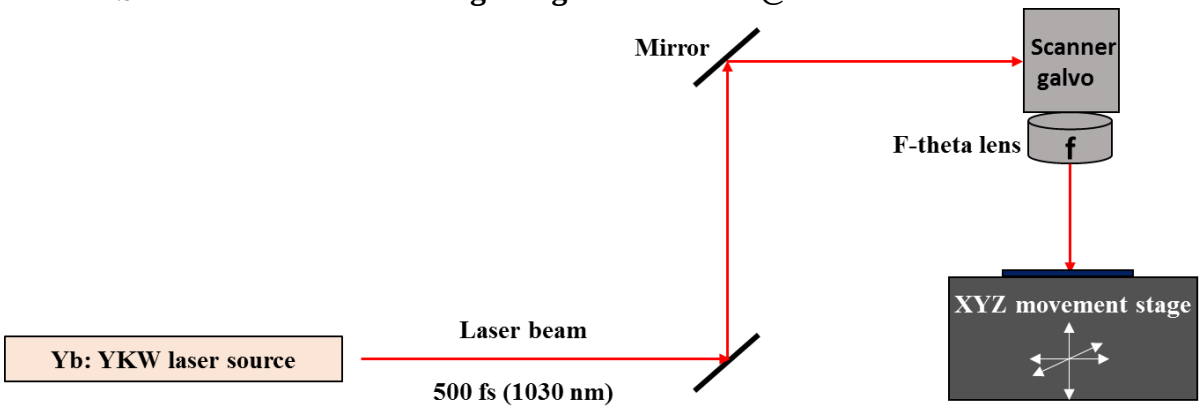

Figure.V.6. Schematic of the experimental set up using 500 fs laser @ 1030 nm.

3.1. Damage threshold

The determination of damage threshold fluences of $TiO_{1.8}$ thin film (PVD) under 500 fs irradiation at 1030 nm after different number of pulses (from 1 to 100000 pulses), is performed according to Liu's method [20] as explained in chapter III. We should point out that the crater diameter measured here corresponds to the diameter of the irradiated surface (surface morphology modification due to the laser radiation). Thus, the measured threshold fluence corresponds to the ablation threshold if the surface modification is induced by ablation process. Otherwise, if the ablation process does not take place, the measured threshold corresponds to the surface damage threshold (can be attributed to thin film specific processes: melting, cavitation, cracking (stress) and delamination).

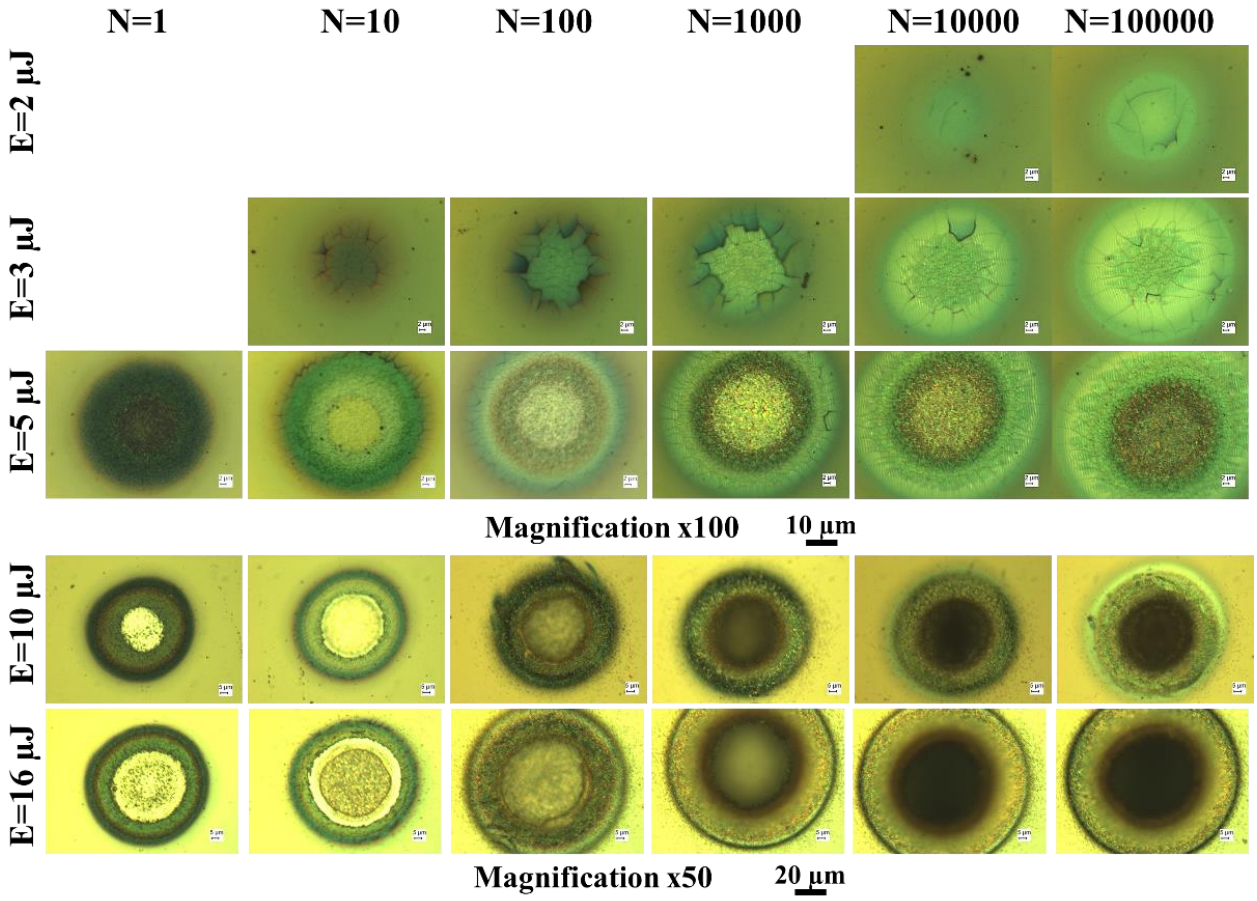

Figure.V.7. Optic microscopy characterization of laser spot formed on$TiO_{1.8}$ thin film irradiated by 500 fs laser @ 1030 nm for different energies E and number of pulses N.

The beam energy and the number of pulses were varied respectively in the range of 1.25 to 16 µJ and 1 to 100000 pulses as shown in fig.V.7. The beam waist radius was estimated to be 34 µm and the damage thresholds are thus determined as displayed in Fig.V.8.

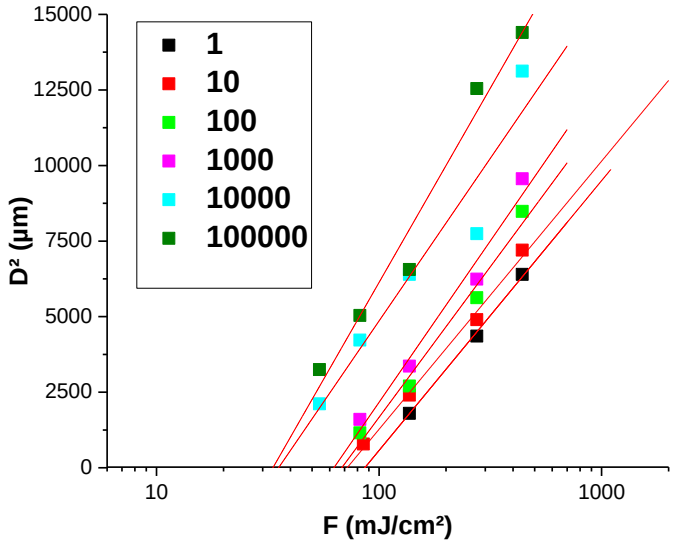

Figure.V.8. Semi-log plots of laser spot square diameter D^2 versus laser fluence F

The damage thresholds of $TiO_{1.8}$ measured for the different N are summarized in the following table. The single pulse ablation of TiO1.8 thin film is roughly 86 mJ/cm².

N	1	10	100	1000	10000	100000
F_{th} (mJ/cm²)	86	72	67	62	36	33

Table.V.2. Threshold ablation fluences estimated for each number of pulses.

3.2. Incubation effect

The evolution of damage threshold with the number of pulses N is plotted in fig.V.9. The damage threshold fluence decreases with increasing pulse number and then saturates at a value about 36 mJ/cm² at 10000 pulses. In spite of the fact that there are missing data in this curve especially between 1000 to 10000 pulses range, these observations are in agreement with the results reported in the literature suggesting very similar incubation behavior in case of dielectric thin films (HfO_2, Sc_2O_3, Ta_2O_2, Al_2O_3 , SiO_2 …) [3][4][5][6][7]. In those studies, several dielectric films have been investigated allowing to a similar incubation effect behavior characterizing by two regimes. The first regime shows a decreasing of threshold (ablation and damage) as function of number of pulses while the second one, exhibits the saturation (also called the stabilization) (see fig.V.10.). This saturations leads to $F_{th}(\infty)$ which reflects to the minimum fluence needed for which damage occurs. The ratio of this value to the single pulse threshold ($F_{th}(\infty)/F_{th}(1)$) is typically ranging in 0.1 to 0.9 for dielectric oxide films [4]. In our case, the $F_{th}(\infty) \sim 36$ which leads to a ratio of 0.4.

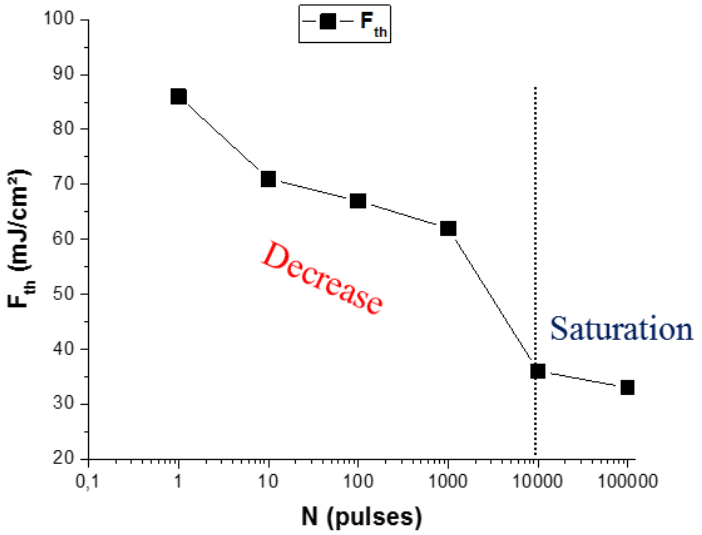

Figure.V.9. Evolution of threshold ablation fluence F_{th} of TiO1.8 thin film versus number of pulses N for a 500 fs laser @ 1030 nm.

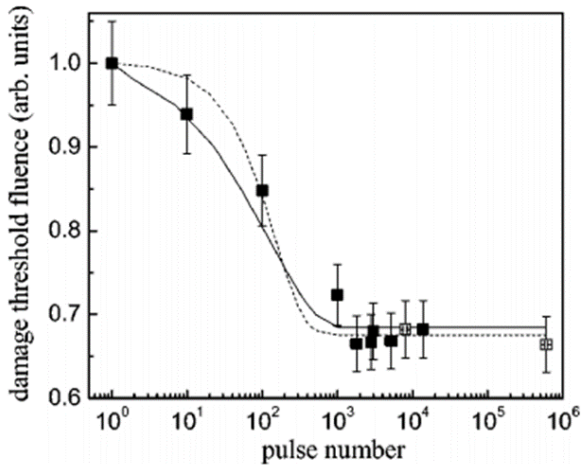

Figure.V.10. Damage threshold fluence as a function of the number of pulses for Ta_2O_2 irradiated by 30 fs laser @ 800 nm [6]**.**

In order to investigate the nature of surface damage, a SEM characterization of some laser spots isperformed. Fig.V.11. presents the evolution of spot surface morphology with increasing N from 10 to 10000 at fixed fluence of 85 mJ/cm². For N = 10, some micro-cracks appear on the entire surface but mainly around the rim of laser spot. For N > 100, we have almost the same surface morphology showing microcracks generated on the entire spot surface and some film parts were removed through delamination process clearly pronounced around the rim of laser spot. It is widely accepted In literature that, the cracking, fragmentation and delamination of material occurs due to the thermo-elastic stresses induced by laser irradiation [2][8]. As result of sub-picosecond pulse (500 fs), the laser energy absorption causes a confined heat in the irradiated volume. This thermal confinement

leads to an increasing of the irradiated zone temperature yielding to thermoelastic stresses generation [9]. Due to the repeated rapid heating/cooling processes, a very high density of thermoelastic stresses can be generated which causes to a fracture by fatigue and delamination of thin film. Also, The images, shown in fig.V.11, suggest that the induced damage threshold measured above is not based on the evaporation/melting processes but the surface damage through cracks and delamination processes.

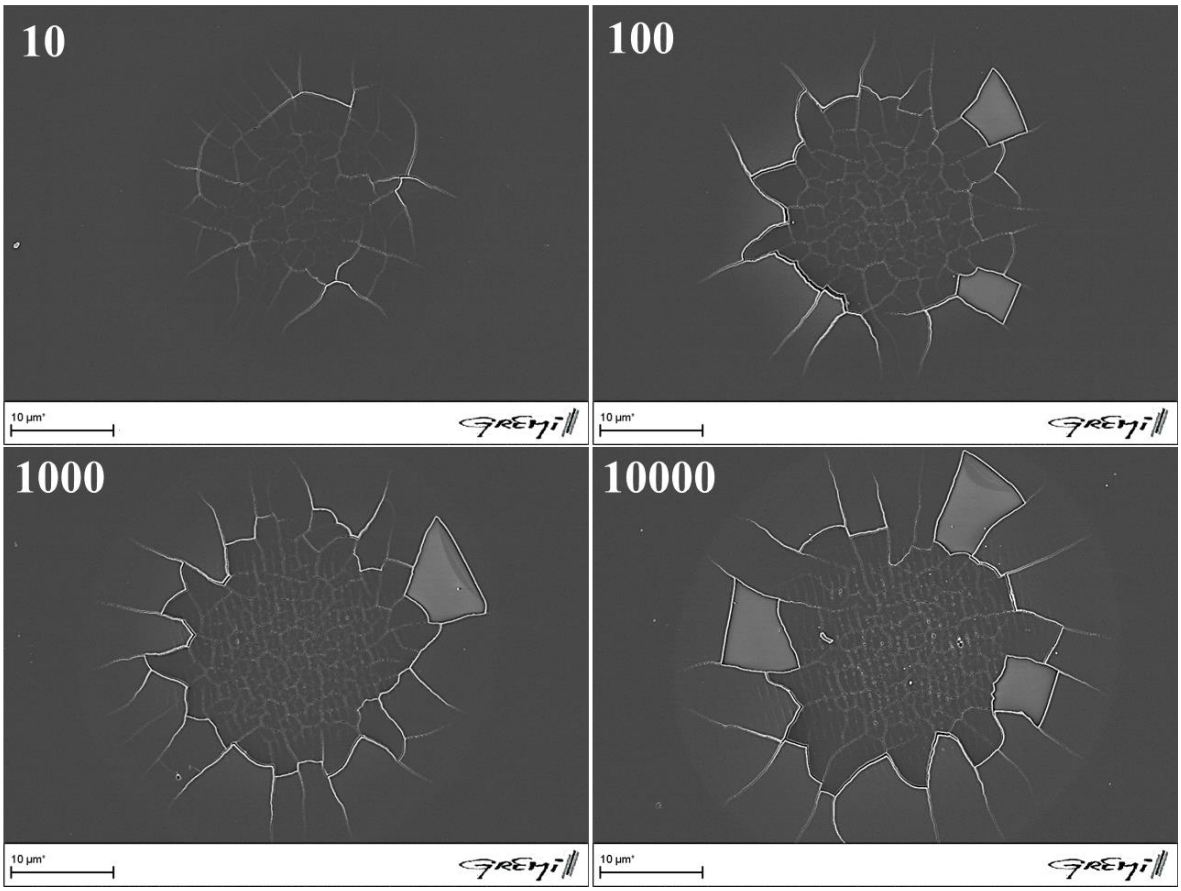

Figure.V.11. SEM views of laser spots formed on TiO1.8 thin film under 500 fs laser irradiation @ 1030 nm, the fluence was fixed to 85 mJ/cm² and N was varied from 10 to 10000.

3.3. Dynamic mode

The laser scan method used to treat large surface area with 500 fs laser was detailled in chapter III. In this paragraph, we aim to study the effect of laser fluence at fixed number of pulses on the evolution $TiO_{1.8}$ surface morphology. In fig.V.12, the SEM images of $TiO_{1.8}$ surface after 500 fs irradiation @ 1030 nm at different laser fluences are presented. The repetition rate, the scan speed and the spacing between lines were fixed to respectively 100 kHz, 4 mm/s and 5 µm leading to a number of pulses of 24000.

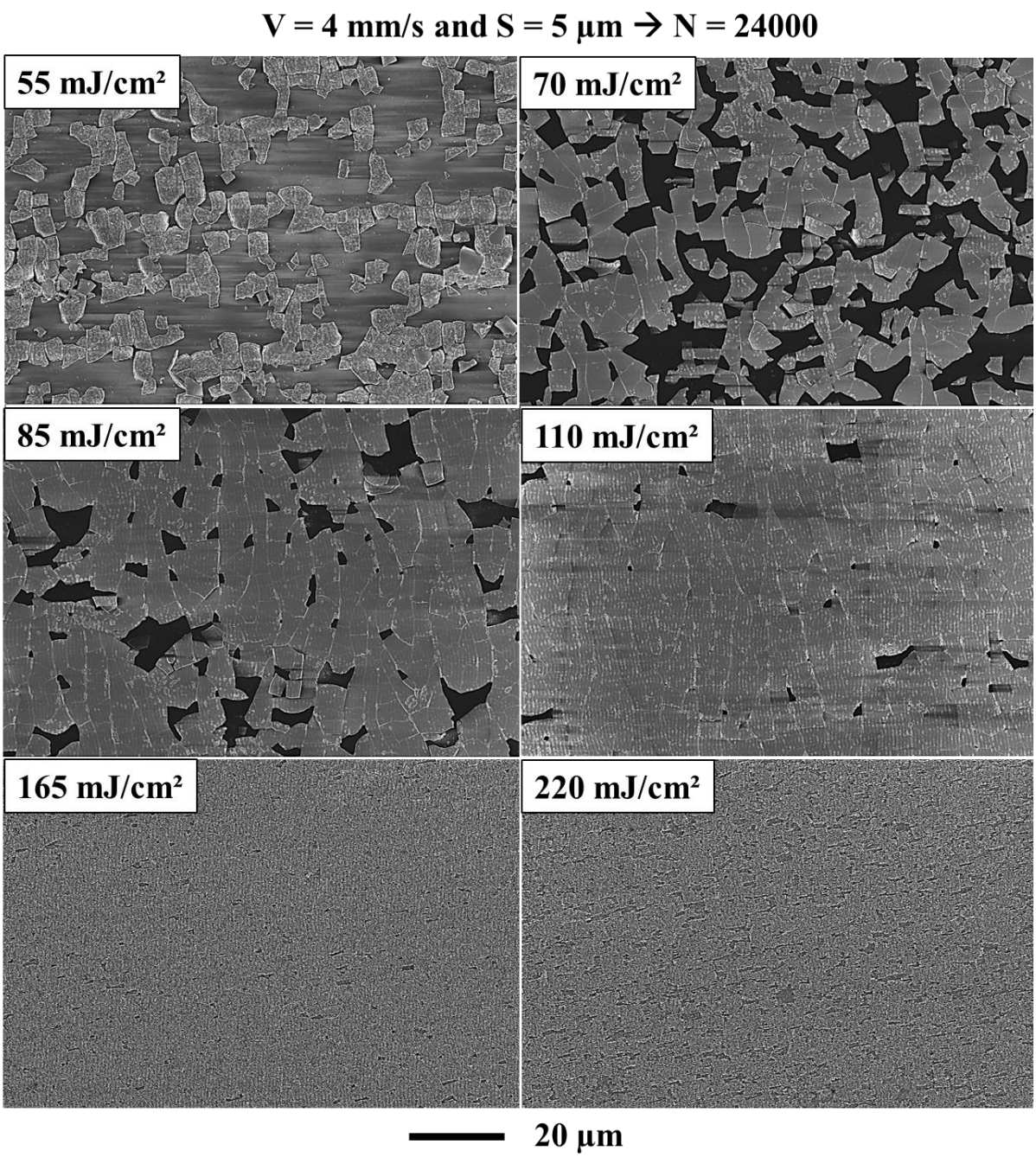

Figure.V.12. SEM views of TiO1.8 surface morphology evolution (after 500 fs laser irradiation @ 1030 nm) with increasing F and at fixed N

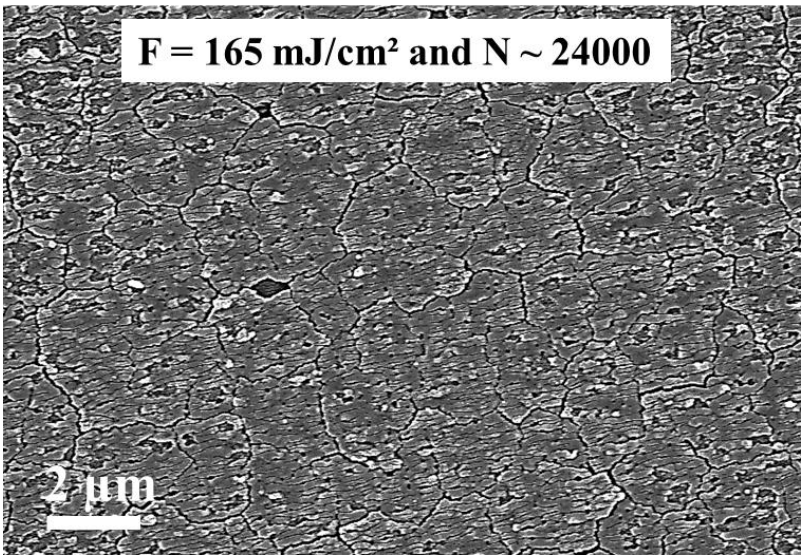

Figure.V.13. high magnified SEM view of TiO1.8 surface morphology shown in fig.V.13 @ 165 mJ/cm².

An unexpected behavior of surface morphology evolution, when the laser fluence increases, is noticed. The delamination effect seems to be drastically reduced by increasing F.

All applied fluences are above the surface damage threshold (36 mJ/cm² after 10000). For a fluence ranging in 55 to 85 mJ/cm², an important delamination process is achieved. However, for F higher than 110 mJ/cm², the delamination effect seems to be minimized and a micro-cracked surface morphology is observed (see fig.V.13). Thus, the following hypothesis is proposed in order to explain this result.

The surface can be damaged through two main processes:

- ✓ Cracks and delamination processes induced by thermo-elastic stresses.
- ✓ Ablation, evaporation and melting processes induced by the lattice heating due to heat accumulation.

If the applied fluence is over the cracking (stress) threshold but lower than the ablation (evaporation and melting) threshold, this can lead to significant removal of the film through cracking and delamination processes in form of flakes (this corresponds to a fluences lower than 110 mJ/cm²). Otherwise, if the applied fluence is above the melting and cracking threshold fluence but does not exceed the ablation (evaporation) threshold, the laser irradiation induces always a thermos-elastic stresses leading to cracks generation. However in parallel of this mechanism, melting process can take place which yields to stresses relaxation and may repair the surface damage induced by cracks and delamination. In other words, we suppose that cracking (stress) threshold is lower than thermal threshold (melting).

This hypothesis can be supported by the experimental observations of three laser spots formed after 10 pulses for three different fluence values (85, 140 and 280 mJ/cm²) (see fig.V.14).

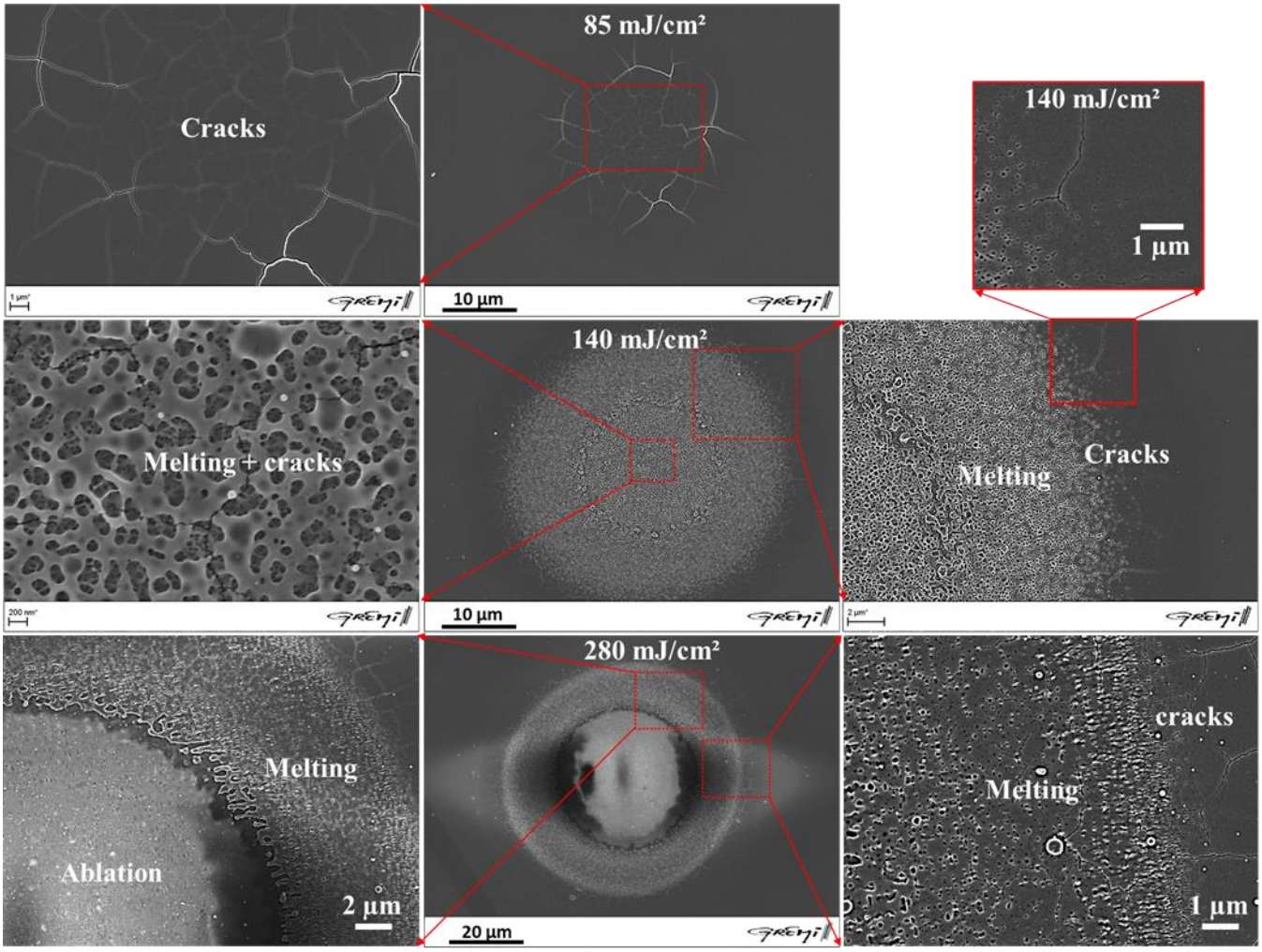

Figure.V.14. SEM images of laser spot formed on TiO1.8 surface under 500 fs irradiation @ 1030 nm after 10 pulses and at three different fluences.

For a fluence of 85 mJ/cm² near to the damage threshold, only some cracks are generated on the entire laser spot (28 µm in diameter). When F increases up to 140 mJ/cm², the spot center (18 µm) appears like a melted region with the presence of some cracks. Around this zone, cracks are developed (rim zone). Lastly, for relatively high fluence of 280 mJ/cm², three morphologies can be distinguished on laser spot of 75 µm (due to the Gaussian profile of our beam). In the center, the film is completely removed. Around this ablated zone, a melted ring can be seen. Some cracks can also been observed in the outer regions. Thus, these experimental results are in well agreement with the proposed hypothesis assuming that F_{th} (cracking) < F_{th} (melting) <F_{th} (ablation) as illustrated in fig.V.15.

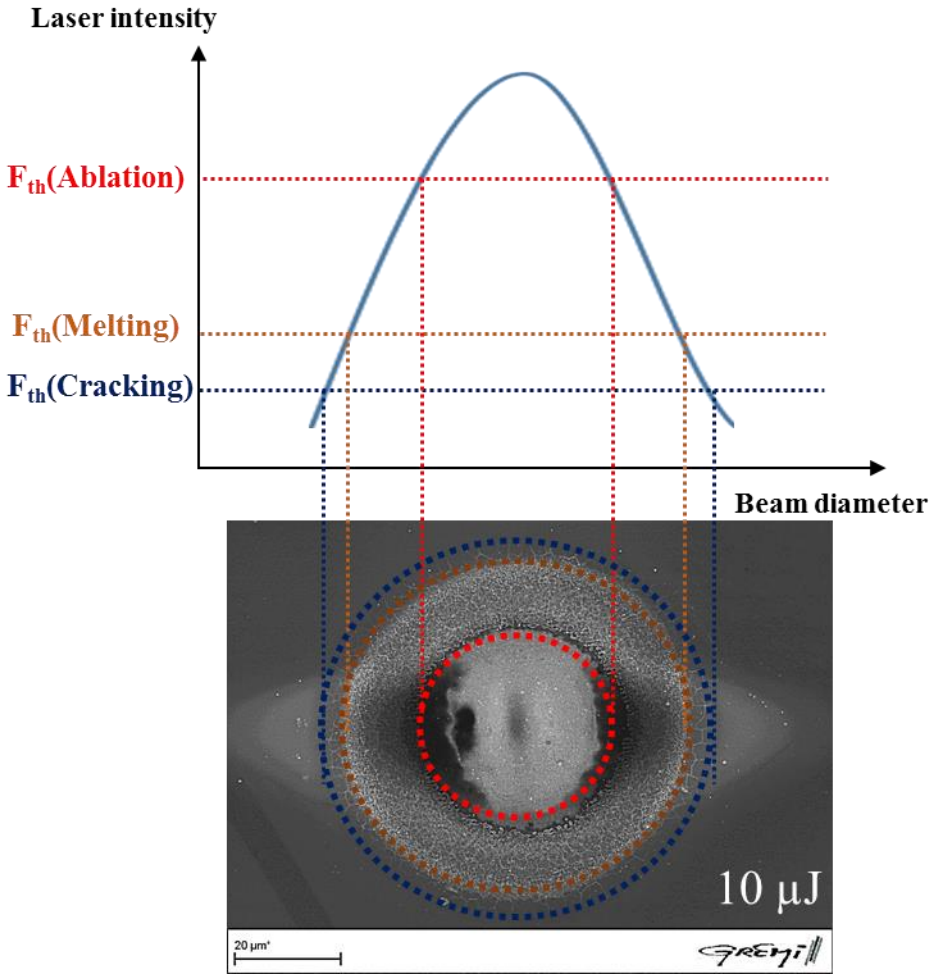

Figure.V.15. Illustration showing the different threshold fluence.

If we focus on the rim region of the treated surface obtained at 110 mJ/cm² from fig.V.11. The SEM characterization at different magnifications are given in fig.V.16. At the rim of the treated zone, some very periodic structures are observed in zone (a). This organization is formed at the beginning of the laser scan and thus the number of pulses will be lower than 24000 pulses. About 30 µm far from the rim, the delamination process start to take place yielding to the same morphology as shown in fig.V.11 for F= 110 mJ/cm². The magnified SEM image of zone (a) shows the formation of very periodic and regular vertical LIPSS with period of 850 µm (0.82 **λ**) and orientation parallel to the beam polarization. In the same image several micro-cracks are randomly developed. If we zoom in the image (a) we notice that the formed LIPSS are not formed due to the material transport and organization (leading the formation of crests and valleys or modulated surface) as widely observed in the LIPSS formed in the previous chapter and in the literature, but they are based in nano-cracks organized in well-defined periodic localized zones (with average period of 120 nm (ranging in **λ**/9 -

λ/8) and orientation perpendicular to the beam polarization). Regarding the discussion given above about the role of thermos-elastic stresses induced by laser irradiation on the formation of micro-cracks and thin film delamination. In the same context, the thermos-elastic stresses induced by laser, can be considered as a potential mechanism leading to nano-cracks generation. In other words, the cracks are formed in two different scales, nano and microscale (micro-cracks and nano-cracks) are produced due to the thermos-elastic stresses induced by laser.

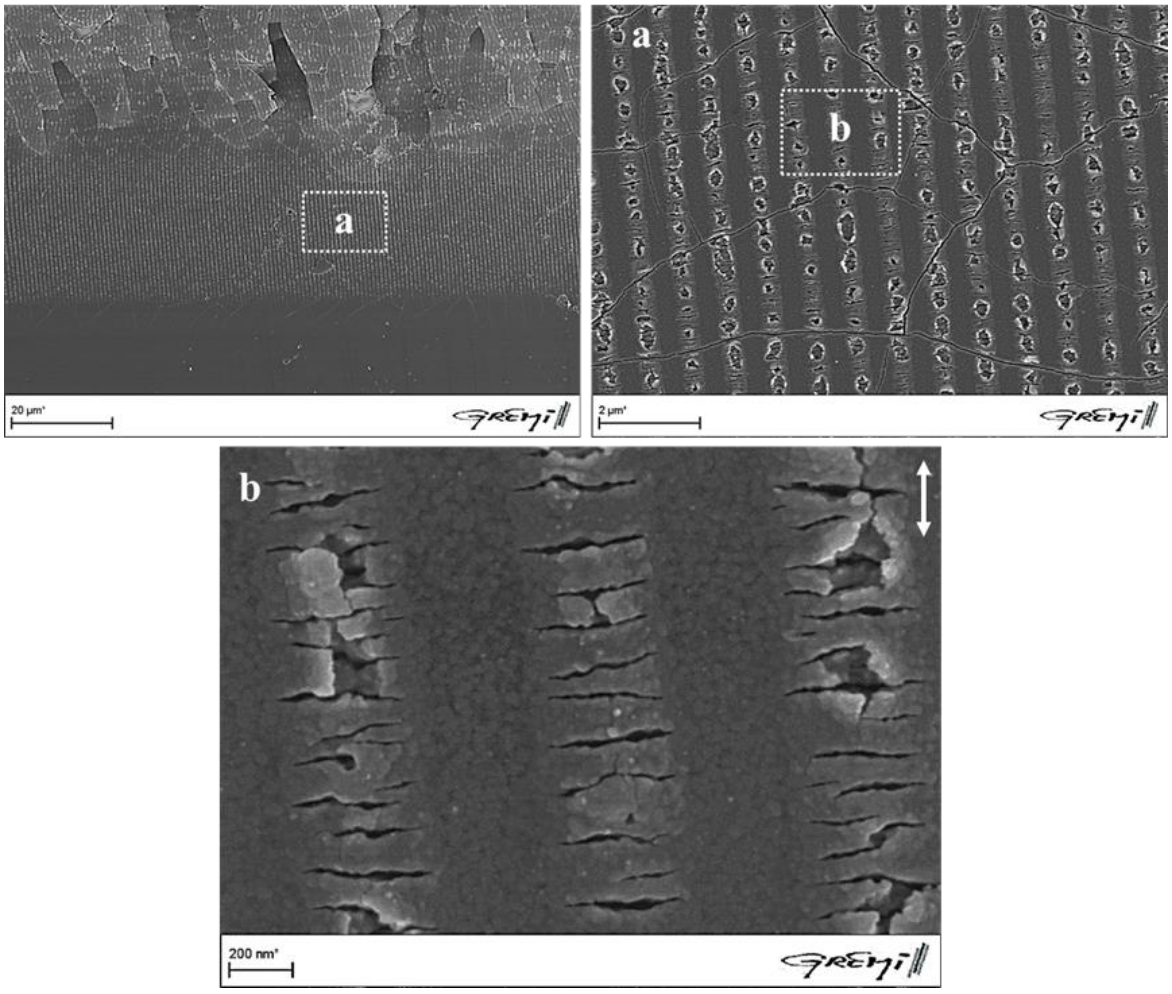

Figure.V.16.SEM images characterizing the rim of treated large surface area of TiO1.8 at N = 24000 and F = 110 mJ/cm².

So if we assume that micro and nano-cracks are both generated as result of stress induced by laser, the question arises thus is why the micro-cracks are generated randomly while the nano-cracks are produced and confined in well periodic zones?

Interference model (based on Sipe theory) may answer this question and can explain the LSFL organization. In general, this model predicts the formation of LIPSS as result of non-uniform laser energy deposition. Therefore, we can suppose that the nano-cracks based LSFL regions correspond

to the localized hot regions receiving the higher amount of laser energy that yields to generate thermos-elastic stress (leading to nano-cracks generation) in these particular regions. However, the regions localized between LSFL have not received enough of laser energy (higher as the local cracking threshold fluence) allowing to the generation of thermos-elastic stresses. Thus, these zones remain unmodified. An illustration of this explanation is given in fig.V.17.

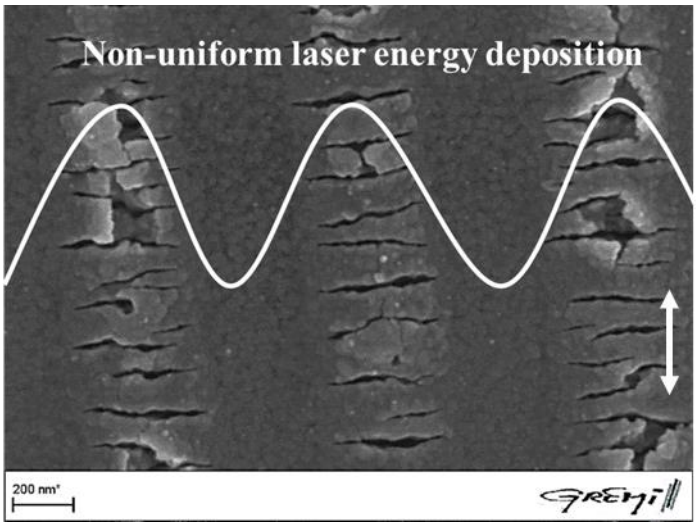

Figure.V.17. Illustration displays the non-uniform laser energy deposition proposed to explain nano-cracks based LIPSS formation.

Another explanation can support this interpretation is the local field enhancement [10][11]. In fact, we can assume that the first few laser pulses can cause the formation of some tiny nano-cracks (localized on the LSFL regions). These tiny nano-cracks can be considered as the scattering centers. By the next coming pulses, ionization processes can be reinforced by local field enhancement in the vicinity of these scattering centers. This lead to the generation of localized high electron density around these nano-cracks. The local field enhancement contributes to grow these nano-cracks in the direction perpendicular to the laser polarization (In our case, the generated nano-cracks are found to be perpendicularly oriented to the beam polarization). This explanation has been proposed recently by A. Rudenko et al [12], to explain the subwavelength nanostructure formation on the surface and in bulk of glasses. In their case, nano-pores and nano-voids induced by laser are considered as the scattering centers.

We showed that nano-cracks based LSFL are formed at the rim of irradiated area but for the rest of treated surface, these structures are destroyed by the delamination. However we can obtained homogenous surface covered by nano-cracks based LSFL at the same fluence but at a lower number of pulses down to 3000 pulses. For this, the speed scan was kept unvaried (4 mm/s) but the spacing

between lines was increased to 40 µm. Under these experimental conditions large surface area covered by very regular nano-cracks are formed (fig.V.18) simultaneously to randomly micro-cracks.

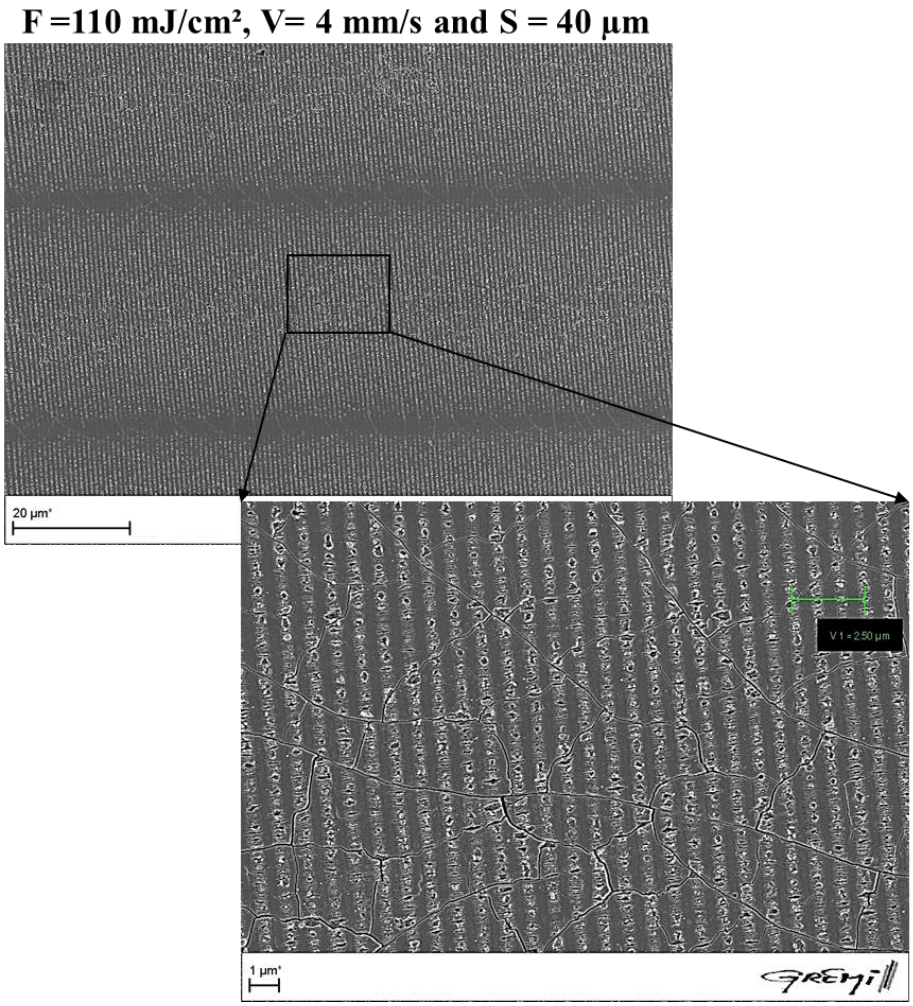

Figure.V.18. SEM images of TiO1.8 irradiated by 500 fs laser @ 1030 nm for N = 3000 and F = 110 mJ/cm².

III.Nano-cracks based LSFL formed on $TiO_{1.6}$ (PLD) spot by 500 fs laser @ 343 nm

Similarly to the previous study, a singular result of high periodic LSFL based on localized nano-cracks are presented. Those structures were obtained on a single laser spot of TiO1.6 thin film (deposited by PLD) irradiated by 500 fs laser beam, at 343 nm.

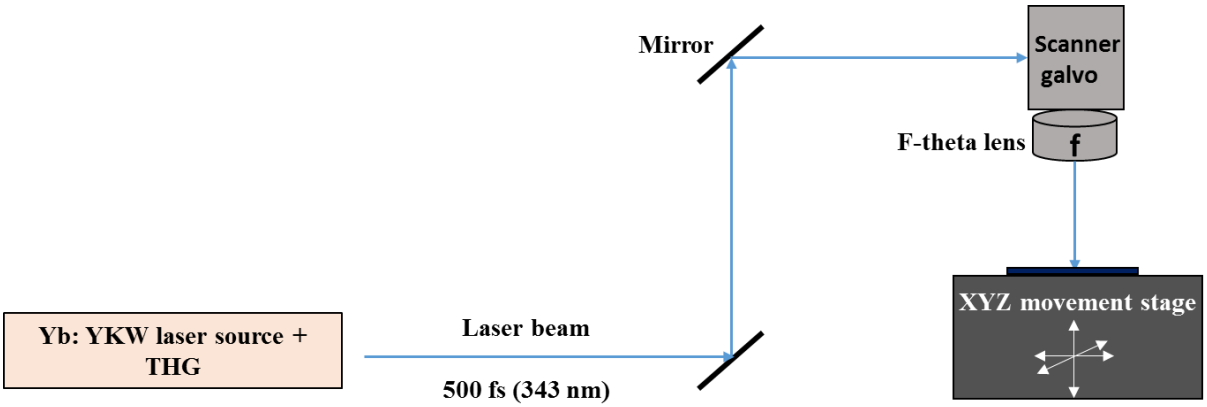

Figure.V.19. Schematic of the experimental set up using 500 fs laser @ 343 nm.

Under a fluence of 120 mJ/cm² and after 10000 pulses, very periodic nano-cracks based LSFL are formed without micro-cracks generation (Fig.V.20.). The period of these LSFL is roughly 340 nm (very close to the working wavelength of 343 nm) and their orientation is parallel to the beam polarization. The nano-cracks formed in these conditions appear very periodic with a period of 40 nm and orientation perpendicular to the beam polarization. Thus, the nano-cracks can be considered as short HSFL with period ranging in $\boldsymbol{\lambda}/9 - \boldsymbol{\lambda}/8$. So the surface organization can be described by periodic LSFL based on periodic localized nano-cracks).

The absence of micro-cracks can be explained by the good quality (dense growth and strong thin film adhesion) of TiO1.6 thin film deposited by PLD and/or the fact of using a UV wavelength (343 nm) (instead of 1030 nm wavelength). However, we cannot confirm for sure this because two parameters have been changed here, the deposition method and the working wavelength.

Therefore, further investigations seem to be necessary (such as the nanostructuring of TiO1.8 (PVD) under 343 nm and TiO1.6 (PLD) under 1030 radiations) to better understand why micro-cracks are not generated in the case of PLD film irradiated by fs laser at 343 nm.

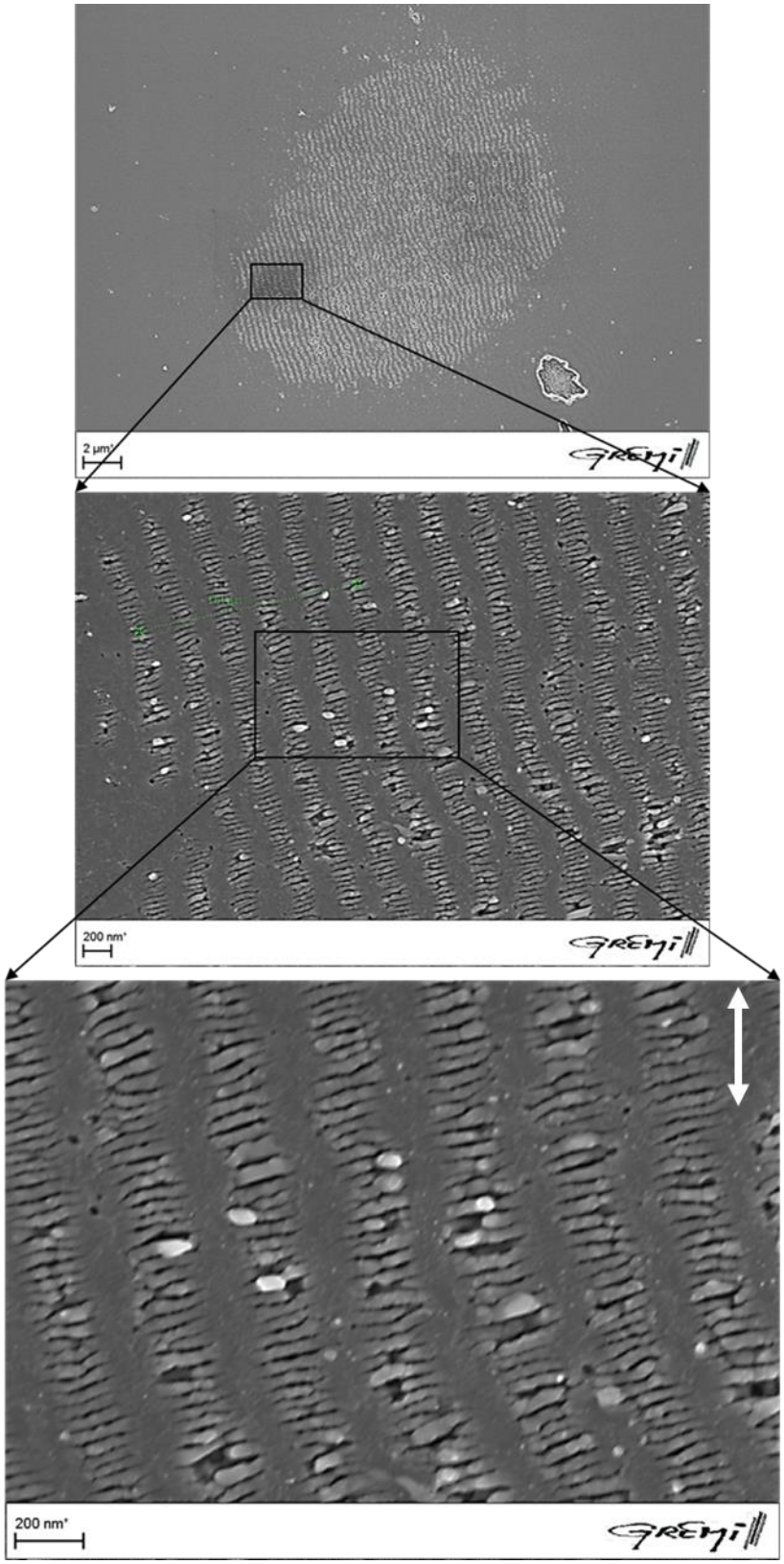

Figure.V.20. SEM images at different magnifications of laser spot formed on TiO1.6 (PLD) thin film under 500 fs irradiation @ 343 nm (F= 120 mJ/cm² and N= 10000).

IV. Polymers thin films

Although, inorganic materials are one of the most investigated as TE materials today, their high cost and complex synthesis restrict their wide application in TE modules. Organic materials (polymer) can be considered as potential alternatives due to their inexpensive processing, light weight and mechanical flexibility which provides promise for large-area flexible TEG [13]. Recent studies show that conducting polymers such as PPy:Tos, PEDOT:PSS, or PEDOT: PEDOT:TOS, exhibit attractive thermoelectric properties leading to a promising ZT of 0.25 at room temperature [14][15].

So far, we have already studied the nanostructuring of inorganic thermoelectric materials (MeP-Si and TiOx thin films) in order to improve their TE performance. In this last section, we aim to present some preliminary results obtained on polymers thin films nanostructured under 100 fs laser beam @ 266 nm. Our samples are based on polymer (polystyrene) thin films (200nm) prepared by spin coating of polymer solutions deposited on silicon substrates.

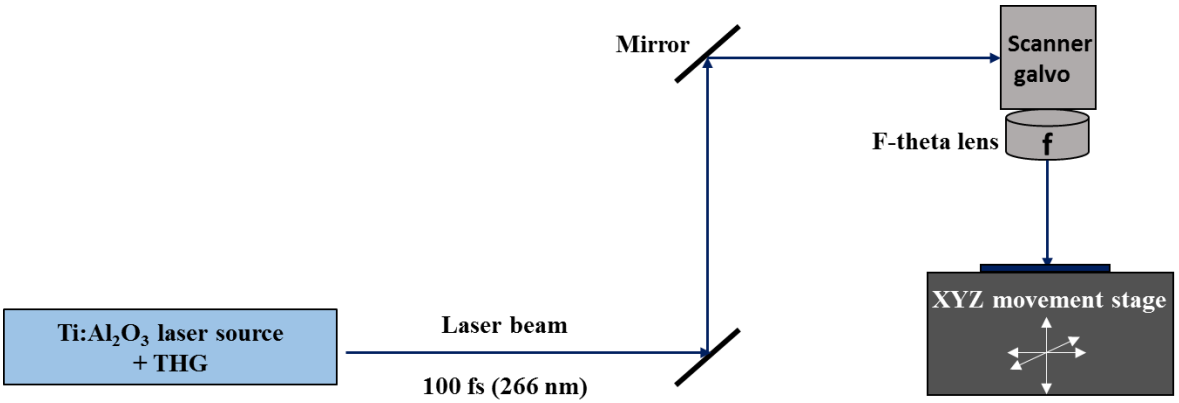

Figure.V.21. Schematic of the experimental set up using 100 fs laser @ 266 nm.

As reported in the literature, the ablation of polymer thin films occurs at very low fluences in order of few mJ/cm². E. Rebollar et al[16], have achieved that disruption and ablation of the polymer thin film takes place for a fluence above 2.6 mJ/cm² (for N=5000 pulses) under 120 fs laser beam at 265 nm (spot diameter of 10 mm). Therefore, in our experiments and in order to avoid the ablation of our polymer thin films, the fluence was limited to 8 mJ/cm² (for laser spot of 350 µm, value estimated from SEM images).

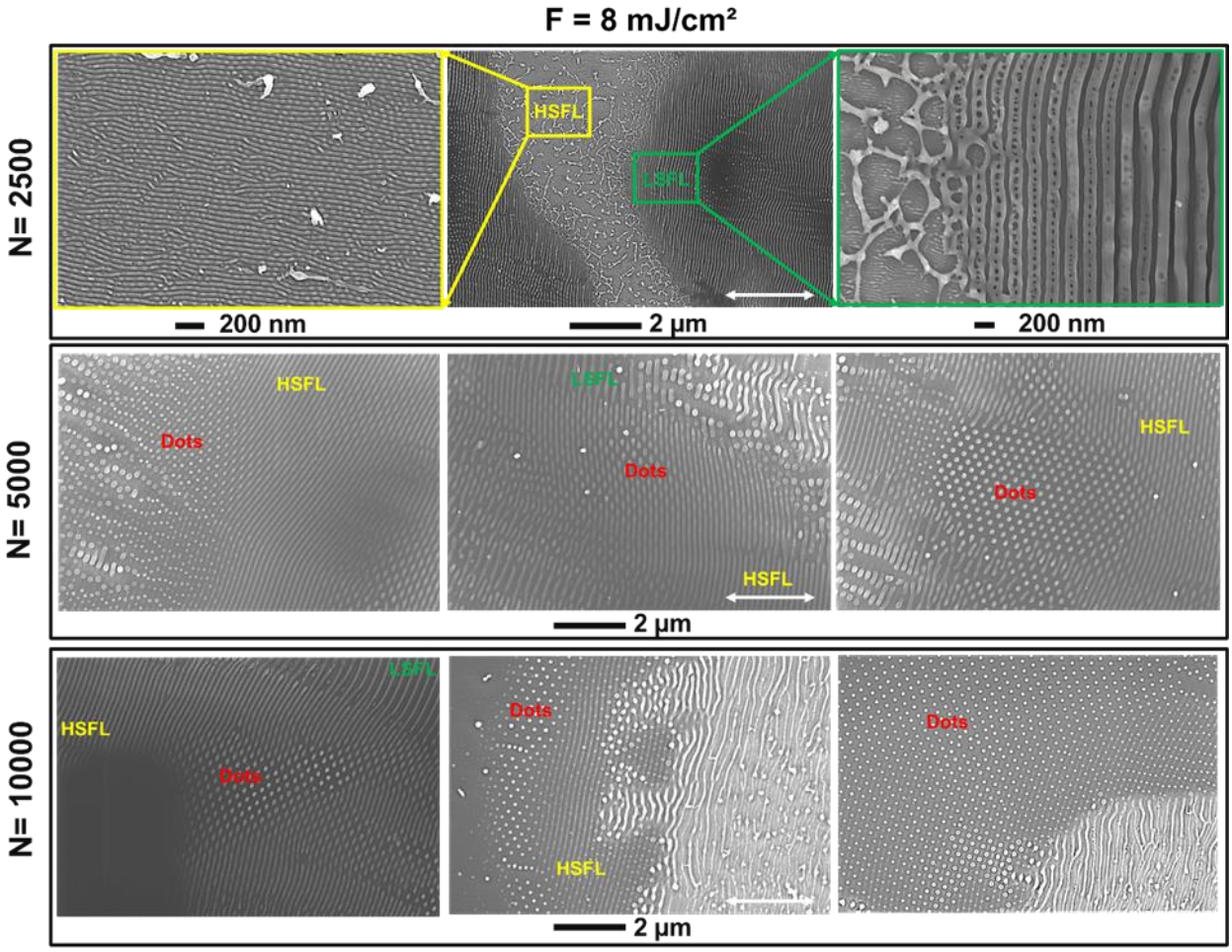

Figure.V.22. SEM views of polymer thin film surfaces irradiated by 100 fs @ 266 nm and after different number of pulses.

In fig.V.22. the evolution of polymer surface morphology with increasing N (for a fixed fluence of 8 mJ/cm²) is presented. Due to the inhomogeneous distribution of energy that laser beam exhibits, the surface morphology of irradiated polymer depends strongly on the received local energy. Up to 5 different surface structures could be observed in small area of 10x10 µm². For N = 2500 pulses, LSFL are formed with period ~ 260 nm and oriented perpendicular to the beam polarization. HSFL are also generated with period close to 40 nm and orientation parallel to the beam polarization. For N > 5000 pulses, a wide variety of nanostructures are identified, LSFL with period ~ 260 nm (beam wavelength = 266 nm), HSFL with period of 130 nm and orientation similar to the LSFL and periodic dot organization with diameter in the range 100 to 150 nm are also generated. The dots appear in a form of 2D lattices exhibiting a hexagonal symmetry. The formation of periodic dots was discussed previously on titanium oxide thin films surfaces and their formation mechanisms were attributed to the surface energy minimization under the effect of thermo-hydrodynamic forces (surface tension, Rayleigh instability plateau).

However, the dots formed on $TiO_{1.6}$ surface (and on copper thin film in the literature) were always appear organized and aligned in well define lines. In contrast, the dots formed on polymer are hexagonally patterned (fig.V.23).

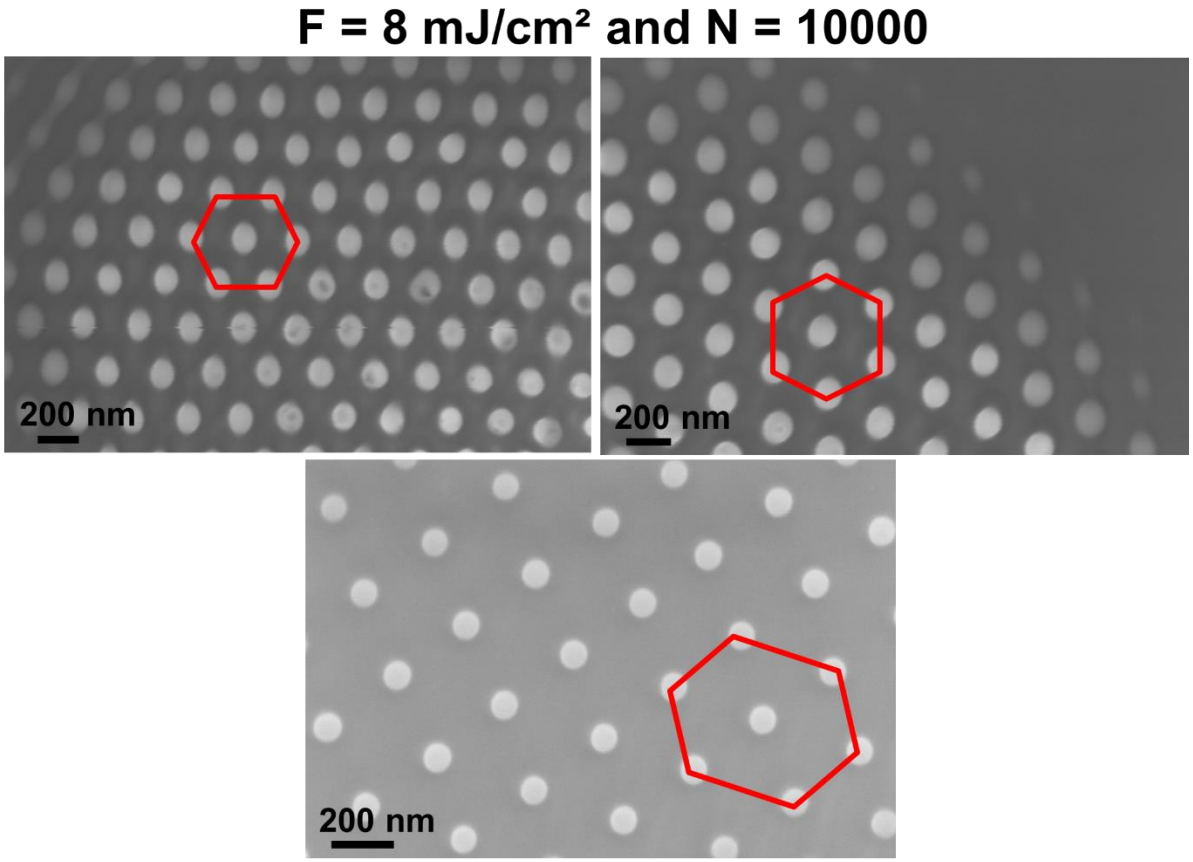

Figure.V.23. SEM views of 2D hexagonal dots organizations formed on polymer thin film surfaces irradiated by 100 fs @ 266 nm for F = 8 mJ/cm² and N= 10000).

V. Discussion

In this chapter, we have shown the formation of exotic and complex nanostructures results that have never been seen before in the literature. Despite extensive research has been focused in the investigation of LIPSS formation mechanisms, these mechanisms remain unclear and the understanding of the origin LIPSS formation still very challenged because of:

- ✓ The complex mechanisms occurring during the ultrashort laser-matter.
- ✓ The different parameters involved such material properties (metal, semi-conductor, dielectric, bulk or thin film) and the laser parameters (pulse duration and wavelength).
- ✓ The wide variety of LIPSS formation observed in the literature and even in this thesis such LSFL formed by nanoparticles organization (MeP-Si), LSFL and HSFL in form of periodic crests and valleys (Si, TiOx and polymer thin films), dots aligned in well-defined lines or hexagonal pattern (TiOx and polymer thin films), nano-cracks based LSFL (TiO_x thin films).

Regarding the results reported with titanium oxide thin film, the spatial modulated laser intensity pattern produced from interferences resulting between the incident laser and the excited surface electromagnetic wave (in form of surface plasmons polaritons, light scattered beam from the surface roughness...) can explain the formation mechanisms of formed LSFL and can predict their periodicity Λ from the classical formula :

$$\Lambda = \frac{\lambda}{1 \pm sin\Theta}$$

Where, λ is the laser wavelength and Θ determines the angle of incidence of the beam on the surface.

Although this model helps to explain the formation of quasi-periodic to very periodic nano-cracks localized in well-defined regions (correspond to the LSFL regions), since those regions have received the higher amount of energy yielding to induce thermo-elastic stresses. However, this model cannot predict the measured period of these nanostructures (40 and 120 nm respectively under 343 and 1030 nm irradiation).

Self-organization model which assumes the relaxation of laser induced instabilities as mechanism responsible for LIPSS formation (both LSFL and HSFL). In our case, thermo-elastic stresses can be considered as the instabilities generated by laser and then their relaxation leads to the formation of these periodic nano-cracks. However, this model remains very general and can be attributed to many different physical phenomenon but cannot predict the way in which the relaxation occurs and then how the surface is going to self-organize.

Similarly, In the case of polymers thin films, different surface organizations are observed from HSFL, LSFL to 2D dots organized on hexagonal pattern. Concerning LSFL and HSFL, the formation mechanisms of such structures are widely discussed in literature (interference and self-organization models). In contrast the complexity of pattern formed with dots seems to be very far from the predictions of these models (periodicity and symmetry).

For bulk materials, the LIPSS are generally formed in form of periodic crests and valleys (as result of local ablation or material transport under hydrodynamic forces). However, in the case of thin films, new physical phenomenon can contribute to form very complex structures like the periodic nano-cracks and hexagonal patterned dots as shown in this chapter.

The laser interaction with thin film materials recently emerging due to nanotechnology fields, should be revisited from the fundamental and basic point of view. The presence of thin film structure that is completely different from the substrate material and implying the presence of optical and thermal interface induce obviously more mechanisms during the processing (dual absorption by the film and the substrate, cavitation, delamination, microfluidics…) that are not present in bulk state material processing. Thus, more theoretical and modeling to investigate this emerging physics should complete our experimental investigation to propose some predictive models as those available for bulk state.

References

[1] S. Rapp, M. Domke, M. Schmidt, H. P. Huber, “Physical Mechanisms during fs Laser Ablation of Thin SiO2 Films”, Phys. Procedia, vol 41, 734–740, 2013.

[2] J. Lee, S. Kim, M. Lee, “Micro-scale patterning of indium tin oxide film by spatially modulated pulsed Nd:YAG laser beam”, Appl. Surf. Sci., vol 258, no 23, 9107–9111, 2012.

[3] D. Douti, L. Gallais, M. Commandré, “Laser-induced damage of optical thin films submitted to 343 , 515 , and 1030 nm multiple subpicosecond pulses”, Optical Engineering 53(12), 122509, 2014.

[4] L. A. Emmert, M. Mero, W. Rudolph, “Modeling the effect of native and laser-induced states on the dielectric breakdown of wide band gap optical materials by multiple subpicosecond laser pulses”, Journal of Applied Physics 108, 43523, 2010.

[5] D. N. Nguyen, L. A. Emmert, M. Mero, W. Rudolph, “The Effect of Annealing on the Subpicosecond Breakdown Behavior of Hafnia Films”, Proc. of SPIE Vol. 7132, 2008.

[6] M. Mero, K. Starke, J. C. Jasapara, “On the damage behavior of dielectric films when illuminated with multiple femtosecond laser pulses On the damage behavior of dielectric films when illuminated with multiple femtosecond laser pulses”, Optical Engineering 44(5), 051107, 2005.

[7] D. Ashkenasi, M. Lorenz, R. Stoian, A. Rosenfeld, “Surface damage threshold and structuring of dielectrics using femtosecond laser pulses : the role of incubation”, Applied Surface Science 150, 101–106, 1999.

[8] G. M. O. Connor, C. Mcdonnell, D. Milne, C. Prieto, H. Chan, D. Rostohar, G. M. O. Connor, “Laser patterning of very thin indium tin oxide thin films on PET substrates”, Appl. Surf. Sci., vol 359, no December, 567–575, 2015.

[9] N. Farid, H. Chan, D. Milne, A. Brunton, G. M. O. Connor, “Stress assisted selective ablation of ITO thin film by picosecond laser”, Appl. Surf. Sci., vol 427, no September, 499–504, 2017.

[10] F. Liang, S. L. Chin, “Physical evolution of nanograting inscription on the surface of fused silica”:, OPTICAL MATERIALS EXPRESS, vol 2, no 7, 1244–1250, 2012.

[11] G. Miyaji, K. Miyazaki, “Origin of periodicity in nanostructuring on thin film surfaces ablated with femtosecond laser pulses”, OPTICS EXPRESS, vol 16, no 20, 16265–16271, 2008.

[12] A. Rudenko, J. P. Colombier, S. Höhm, A. Rosenfeld, J. Krüger, J. Bonse, T. Itina, “Spontaneous periodic ordering on the surface and in the bulk of dielectrics irradiated by ultrafast laser : a shared electromagnetic origin”, SCIENTIFIC REPORTS, 7, 12306 , 2017.

[13] L. Wang, Y. Liu, Z. Zhang, B. Wang, J. Qiu, D. Hui, S. Wang, “Polymer composites-based thermoelectric materials and devices”, Compos. Part B, vol 122, 145–155, 2017.

[14] O. Bubnova, Z. U. Khan, A. Malti, S. Braun, M. Fahlman, M. Berggren, X. Crispin, “Optimization of the thermoelectric figure of merit in the conducting polymer poly (3 , 4-ethylenedioxythiophene)”, Nat. Mater., vol 10, no 6, 429–433, 2011.

[15] C. Gayner, K. K. Kar, “Recent advances in thermoelectric materials”, Progress in Materials Science, vol 83, 330–382, 2016.

[16] Esther Rebollar, Javier R. Vazquez de Aldana, Ignacio Martı n-Fabiani, Margarita Hernandez, Daniel R. Rueda, Tiberio A. Ezquerra, Concepcion Domingo, Pablo Moreno and Marta Castillejo “Assessment of femtosecond laser induced periodic surface structures on polymer films”, Phys. Chem. Chem. Phys., vol 15, no 27, 11287, 2013.

Conclusion

The main goal of this thesis work was to investigate the effect of ultrashort laser material surface nanostructuring on the evolution of thermoelectric properties. In order to accomplish this purpose, a fundamental study of laser induced periodic surface structure formation on the surface of two different materials (bulk mesoporous silicon and titanium oxide thin films) was needed.

In the case of mesoporous silicon sample (50 µm) and under particular conditions of low fluence ~ 20 mJ/cm² and large number of pulses (up to 12000), our experimental observations displayed the formation of LSFL organization very different than those reported in the literature (with silicon for example). These LSFL are formed as result of the organization of nanoparticles unexpectedly generated by the first few pulses. Well-periodic localized melted regions that transformed into amorphous phase after cooling are also observed below the LSFL organization suggesting the non-uniform energy deposition (resulting from the interferences generated between the incident beam and the surface electromagnetic wavelength) as a model that can potentially explain the origin of their formation. These results are obtained under both picosecond and femtosecond irradiations at 266 nm. In spite of the fact that under femtosecond irradiation, it is widely accepted that thermal effects leading to a thermal melting process are clearly reduced, our experimental observations showed almost the same behavior of mesoporous silicon melting under femtosecond regime as well as under picosecond regime. We thus supposed that under particular conditions of low fluence and large number of pulses, the incubation effect played a crucial role leading to the thermal effects occurring even when using a femtosecond laser beam. The ablation thresholds of MeP-Si under 500 fs laser at 1030 nm, were successfully estimated through Liu's method. The single pulse ablation threshold is found to be about 60 mJ/cm² which seemed to be relatively low value compared to the silicon threshold values reported in the literature (~ 120 – 500 mJ/cm²). However, this value is in good agreement with the results discussed above showing the initiation of nanoparticles formation (soft ablation), LIPSS generation and molten material formation at low fluence of 20 mJ/cm². The incubation effect of mesoporous silicon is also studied and showed a linear behavior as generally reported with metals and semiconductors. The nanostructuring of large mesoporous silicon area was also performed by using two femtosecond laser beams at 266 and 1030 nm and working at repetition rates of respectively 1 and 100 kHz. Homogeneous surfaces covered by periodic LSFL are obtained in both cases, although the long processing time achieved by the 100 fs laser operating at 1 kHz. This time was significantly reduced by using the 500 fs laser at 100 kHz. The LSFL formed on large surface with both lasers appeared like a periodic ablated (valleys) and un-ablated (crests zones) as

widely observed in the literature which implies a local ablation process occurring as result of the modulated energy deposition. Another different type of structures is developed on mesoporous silicon surface under the picosecond laser radiation, when relatively high fluence is employed that yields to a 'stronger' ablation process. Conical micro-spikes with diameter ranging from 0.8 – 4 µm are formed.

Concerning the titanium oxide thin film, this material was deposited through two technics: pulsed laser deposition (PLD) and sputtering deposition (PVD). The irradiation of TiO_x (PLD) by 100 fs laser, at 266 nm, leads to the formation of a wide variety of nanostructures such LSFL, HSFL and periodic circular dots. The generation of these nanostructures was strongly depending on the local fluence. The continuous evolution of the surface morphology from one structure to another one suggests the surface self-organization process, which takes place in order to minimize its energy, as plausible model explaining the formation of these nanostructures. Several thermo-hydrodynamic forces can be involved in such process like, thermal-capillary forces (Micro-Marangoni like effect, surface tension gradient). Among the different hydrodynamic forces, the Plateau-Rayleigh instability model matched very well with the experimental observations showing the continuous evolution of the surface morphology from HSFL to periodic dots. The nanostructuring of large surface of TiO_x (PLD) is performed under a very low fluence but with high number of pulses that implies a long processing time up to 112 s/mm². This yielded to homogeneous surfaces covered by nanostructures similar to those formed on single laser spot but clearly more periodic and more regular. This can be explained by the better distribution of beam energy insured by the laser scanning process. Further investigations on the nanostructuring of TiO_x are done with the sample fabricated by magnetron sputtering (PVD). The nanostructuring process of these samples by 100 fs laser radiations at 266 nm and under the same experimental conditions as those employed with (PLD) thin film showed a very similar surface morphologies but some delamination zones of the thin film are noticed. The irradiation of the same sample by 500 fs irradiating at 1030 nm, displayed a very different physical processes like the generation of random micro-cracks and delamination. Unexpected results are obtained with large surface nanostructuring experiments showing a 'strong' delamination of thin film when employing a relatively low fluences however this effect is gradually reduced by increasing the fluence. A hypothesis, based on the competition between the cracking (stress) and the melting processes, is proposed to explain this material behavior. The surface damage fluence threshold is determined according to method of Liu. The single pulse threshold found to be around 86 mJ/cm². Furthermore, a complex LIPSS organization is observed on the large nanostructured surface appeared as a very regular LSFL organization (period of 850 and orientation parallel to the beam

polarization) based on well-localized quasi-periodic nano-cracks generated in the perpendicular direction of the electric field. Interference, auto-organization (based on the relaxation of thermo-elastic stresses induced by laser) and the local field enhancement models are proposed to understand the LSFL formation as well as the nano-cracks generation. The irradiation of thin film (PVD) under 1030 nm, caused always the formation of micro-cracks although our efforts to avoid them by varying the irradiation conditions.

In parallel to these studies, the validation of new experimental homemade device dedicated to TE properties characterization of materials (in form of bulk and thin film) is performed. A good measurement accuracy of Seebeck coefficient with resolution down to 4 µV/K is achieved. Furthermore, the preliminary findings evidencing the evolution of TE properties with laser nanostructuring have shown a huge enhancement of Seebeck coefficient and electrical conductivity. In the case of MeP-Si an important improvement on Seebeck coefficient and electrical conductivity has been achieved yielding to a figure of merit value about six times higher than the untreated sample. While in the case of TiOx (PLD) thin film, Seebeck coefficient and electrical conductivity have shown a considerable improvement leading to a power factor value extremely enhanced (500 times higher than the power factor of untreated sample). This seems to be very promising since it can contribute to enhance the thermoelectric efficiency of TE devices especially for the MEMS based TE devices fabricated from the TE thin films.

Perspectives

Several complementary studies should be highly recommended in order to better understand and improve the results presented in this work.

The first study will be focused on studying the MeP-Si response under UV ultrashort laser radiation such as the investigation of the physical phenomenon responsible on the generation of nanoparticles and the effect of the working environment on their generation (Vacuum, Azote…), the determination of ablation/melting thresholds of MeP-Si and the effect of laser spot size variation on the evolution of these processes.

Because the different exotic and complex structures formed on thin film surfaces (titanium oxide and polymer), the second perspective of this work is to continue the investigation of LIPSS formation mechanism on TiO_x (PLD) under 500 fs at 343 nm which yielded to the generation of nano-cracks based LSFL without micro-cracks generation.

Due to the long processing time of large surface nanostructuring of TiO_x (PLD) by the 100 fs laser, only one surface organization (LSFL) was tested for thermoelectric properties evolution after nanostructuring. Thus, testing the evolution of TE properties of the other surface morphologies (dots and HSFL) is highly demanded and may lead to much better results.

The huge enhancement of TE properties of MeP-Si and especially with TiO_x thin film and the strong dependence between the measured Seebeck coefficient and the LIPSS orientation make the laser nanostructuring method a very promising approach for thermoelectric research. As this effect is first showed up in this work thesis, realizing additional studies in the same context (testing other potential thin films like TE oxides ($Ca_3Co_4O_9$ and ZnO) and TE polymers (PEDOT)) will be very interesting and fruitful for LIPSS and thermoelectric communities.

Abderazek Talbi

Effet de la nanostructuration par faisceaux laser ultra-courts sur l'évolution des propriétés thermoélectriques des matériaux

Résumé : Aujourd'hui, les énergies renouvelables comme l'énergie éolienne, l'énergie solaire, l'énergie hydroélectrique et la thermoélectricité jouent un rôle essentiel dans la couverture de nos besoins en énergie. Parmi ces différentes sources d'énergie, la thermoélectricité, qui permet de convertir la chaleur en électricité ou inversement, attire une grande attention grâce à son large champ d'application. Les actuelles avancées dans la recherche thermoélectrique visent l'amélioration du rendement de conversion des modules thermoélectriques, à travers l'optimisation des propriétés thermoélectriques intrinsèques des matériaux utilisés (coefficient de Seebeck, conductivité électrique et conductivité thermique). Pour cela, différentes approches ont été étudiées (dopage, nouveau alliages, nanostucturation …). Parmi ces approches, la nanostructration des matériaux a été largement étudiée pour mener à bien cet objectif. Dans ce travail de thèse, nous nous sommes intéressés à étudier l'effet de la nanostructuration de surface des matériaux (silicium mesoporeux et oxyde de titane déposé en couches minces) par faisceaux laser ultra-court (picoseconde et femtoseconde) sur l'évolution de leurs propriétés thermoélectriques. Dans un premier temps, nous nous sommes focalisés sur l'étude des différents phénomènes physiques impliqués durant l'interaction laser-matière ainsi que sur la formation des différentes nanostructures résultantes (en forme de ripples, spikes, dots et autres) en fonction de la dose laser appliquée (la fluence et le nombre de pulses). La formation de ces nanostructures a été étudiée suivant deux régimes (stationnaire et dynamique). Après l'optimisation des paramètres conduisant à la formation de ces nanostructures, la caractérisation du coefficient de Seebeck et la conductivité électrique avant et après la nanostructuration de ces matériaux a été réalisée grâce à un nouveau dispositif de mesure (ZT-meter) développé au laboratoire GREMI. Les résultats de mesures montrent une importante amélioration du coefficient de Seebeck et la conductivité électrique après la nanostrucutration. Un facteur d'augmentation de la puissance thermoélectrique a été observé pour les deux matériaux étudiés ; notamment dans le cas de couches minces d'oxyde de titane (jusqu'à 500 fois).
Mot clés : Thermoélectricité, nanostructuration, laser ultra-court, coefficient de Seebeck, conductivité électrique.

Effect of ultra-short laser nanostructuring of materials surfaces on the evolution of their thermoelectric properties

Abstract: Today, renewable energies such as wind, solar, hydropower and thermoelectricity play an essential role to cover our energy needs. Among these different sources of energy, thermoelectricity, which offers the ability to convert a heat into electricity or vice versa, has attracted a great attention due to its wide field of potential applications. The current advances in thermoelectric research are focusing on the improvement of the conversion efficiency of thermoelectric devices through optimizing and improving the thermoelectric properties of the thermoelectric materials (Seebeck coefficient, electrical conductivity and thermal conductivity). For this, different approaches (doping, new materials, nanostucturing...) have been investigated in the literature. Among these approaches, nanostructuring of materials is the most studied in the literature in order to improve the thermoelectric properties of materials. In this thesis work, we aimed to study the effect of surface nanostructuring of materials (mesoporous silicon and titanium oxide deposited in thin film) by ultra-short laser beams (picosecond and femtosecond) on the evolution of their thermoelectric properties. First, we focused on the study of various physical phenomena involved during the laser-matter interaction that yield to the formation of very different nanostructures in form of ripples, spikes, dots and others as function of the applied laser dose (fluence and number of pulses). The formation of these nanostructures has been studied in two regimes (stationary and dynamic). After optimizing the laser parameters leading to the formation of such nanostructures, a characterization of Seebeck coefficient and the electrical conductivity before and after the nanostructuring of these materials was carried out by using a new experimental setup (ZT-meter) designed and validated in GREMI laboratory. The results of measurements showed an important improvement of Seebeck coefficient and electrical conductivity after nanostructuring. This important improvement observed with the both materials leaded to a strong increase in the thermoelectric power factor (reaching roughly 50000%).

Keywords : Thermoelectricity, nanostructuring, ultra-short laser, Seebeck coefficient, electrical conductivity.

GREMI – Groupe de Recherche sur l'Energétique des Milieux Ionisées